Theoretical and numerical investigation of active suspensions: Determinism, chaos and intermittency

Theoretische und numerische Untersuchung aktiver Suspensionen: Determinismus, Chaos und Intermittenz
Zur Erlangung des akademischen Grades Doktor-Ingenieur (Dr.-Ing.)
Genehmigte Dissertation von Benjamin Deußen aus Kirchheimbolanden
Tag der Einreichung: 22.11.2022, Tag der Prüfung: 15.02.2023

1. Gutachten: Prof. Dr.-Ing. M. Oberlack
2. Gutachten: Prof. Dr.-Ing. Y. Wang
3. Gutachten: Prof. Dr. rer. nat. T. Speck

Darmstadt, Technische Universität Darmstadt

TECHNISCHE
UNIVERSITÄT
DARMSTADT

Fachbereich Maschinenbau
Fachgebiet für
Strömungsdynamik

Theoretical and numerical investigation of active suspensions: Determinism, chaos and intermittency
Theoretische und numerische Untersuchung aktiver Suspensionen: Determinismus, Chaos und Intermittenz

Accepted doctoral thesis by Benjamin Deußen

Date of submission: 22.11.2022
Date of thesis defense: 15.02.2023

Darmstadt, Technische Universität Darmstadt

Bitte zitieren Sie dieses Dokument als:
URN: urn:nbn:de:tuda-tuprints-242302
URL: http://tuprints.ulb.tu-darmstadt.de/24230
Jahr der Veröffentlichung auf TUprints: 2023

Für Carina

Erklärungen laut Promotionsordnung

§ 8 Abs. 1 lit. c PromO

Ich versichere hiermit, dass die elektronische Version meiner Dissertation mit der schriftlichen Version übereinstimmt.

§ 8 Abs. 1 lit. d PromO

Ich versichere hiermit, dass zu einem vorherigen Zeitpunkt noch keine Promotion versucht wurde. In diesem Fall sind nähere Angaben über Zeitpunkt, Hochschule, Dissertationsthema und Ergebnis dieses Versuchs mitzuteilen.

§ 9 Abs. 1 PromO

Ich versichere hiermit, dass die vorliegende Dissertation selbstständig und nur unter Verwendung der angegebenen Quellen verfasst wurde.

§ 9 Abs. 2 PromO

Die Arbeit hat bisher noch nicht zu Prüfungszwecken gedient.

Darmstadt, 22.11.2022

B. Deußen

Abstract

Active particles and active suspensions are a relatively new field of research. The study of such complex flows promises to yield interesting new results and possible applications range from medicine to the neutralisation of pollutants in water or soil. The term active particle refers in general to any object capable of self-driven motion. Thus, large animals such as the blue whale (*Balaenoptera musculus*) or technical devices such as planes are active particles, just like microscopic organisms capable of self-driven motion, e.g. *Escherichia coli*.

Active suspensions, i.e. a mixture of active particles and a fluid, are investigated from three different angles in the present work. The focus is on microscopic particles; the Reynolds number of the resulting suspension is therefore very small. This in turn allows the assumption of a Stokes flow, i.e. the convective term of the Navier-Stokes equation can be neglected. Despite the small Reynolds number, the behaviour of an active suspension under certain conditions is called active turbulence by some researchers. This designation inspires to apply methods from turbulence research to an active suspension. The aim is to reveal the nature of the collective behaviour of an active suspension. In particular, the question is whether the behaviour is more chaotic or more deterministic, or whether both types of behaviour occur and an intermittent system is present.

First, a model for active particles is developed that serves as the basis for all subsequent investigations. It is assumed that the fluid is Newtonian and described by the unsteady Stokes equation and the rigid particles are governed by the Newton-Euler equation. A special boundary condition at the particle surface is used to accelerate the particle. While one half of the particle surface is considered as passive, i.e. a no-slip condition is used, the other half is an active surface, where an active stress accelerates the surrounding fluid. Due to momentum conservation, the particle will move in the opposite direction of the active stress.

The model is used to derive Lie-symmetries, which are later used to analyse simulation data. Furthermore, a statistical description of an active suspension is derived based on the Lundgren, Monin and Novikov (LMN) hierarchy used in turbulence research. Additional symmetries arise for the resulting Probability Density Function (PDF) hierarchy, which transport important information about the physical system.

As already mentioned, the symmetries are used to analyse and interpret simulation data. To generate the data, a solver was developed on the basis of the eXtended Discontious Galerkin (XDG) methods implemented in the Bounded Support Spectral Solver (BoSSS) framework. The necessary extensions of the existing solver described in this paper include the implementation of a particle solver, the active boundary conditions and a collision model for the particles.

The third method for the analysis of active suspensions, which is examined in the present work, is a homogenised model. In contrast to the particle-resolved approach, which was realised in

the BoSSS framework, average values of the physical quantities are investigated. Similar to the Reynolds-Averaged Navier-Stokes (RANS) equations, unclosed terms arise in the model equations that describe statistical moments of higher order. These additional terms are modelled on a phenomenological basis, i.e. observations from the particle-resolved model are used to derive closure conditions.

Simulation results generated with both models are linked to the theoretical results of the symmetry analysis. It becomes apparent that the behaviour of an active suspension is determined in particular by the phenomenon of intermittency, i.e. a constant alternation between deterministic and chaotic behaviour exists.

Zusammenfassung

Aktive Partikel und aktive Suspensionen sind ein relativ neues Forschungsgebiet. Die Untersuchung solcher komplexen Strömungen verspricht interessante neue Ergebnisse, und die möglichen Anwendungen reichen von der Medizin bis zur Neutralisierung von Schadstoffen im Wasser oder im Erdreich. Der Begriff aktive Partikel bezieht sich im Allgemeinen auf jedes Objekt, das zu einer selbstständigen Bewegung fähig ist. So sind große Tiere, wie zum Beispiel der Blauwal (*Balaenoptera musculus*) oder technische Apparate wie Flugzeuge, aktive Partikel, ebenso wie Mikroorganismen, die sich selbst antreiben können, z. B. *Escherichia coli*.

Aktive Suspensionen, d. h. ein Gemisch aus aktiven Partikeln und einer Flüssigkeit, werden in der vorliegenden Arbeit aus drei verschiedenen Blickwinkeln untersucht. Der Schwerpunkt liegt dabei auf Suspensionen mit mikroskopisch kleinen Teilchen; die Reynoldszahl der resultierenden Suspension ist daher sehr klein. Dies wiederum erlaubt die Annahme einer Stokes-Strömung, d. h. der konvektive Term der Navier-Stokes-Gleichung kann vernachlässigt werden. Trotz der kleinen Reynoldszahl wird das Verhalten einer aktiven Suspension unter bestimmten Bedingungen von einigen Forschern als aktive Turbulenz bezeichnet. Diese Bezeichnung regt dazu an, Methoden aus der Turbulenzforschung auf eine aktive Suspension anzuwenden. Ziel ist es, die Natur des kollektiven Verhaltens einer aktiven Suspension aufzudecken. Insbesondere geht es um die Frage, ob das Verhalten eher chaotisch oder eher deterministisch ist, oder ob beide Verhaltensweisen auftreten und ein intermittierendes System vorliegt.

Zunächst wird ein Modell für aktive Partikel entwickelt, das als Grundlage für alle weiteren Untersuchungen dient. Es wird angenommen, dass ein Newtonisches Fluid vorliegt, welches durch die instationäre Stokes-Gleichung beschrieben wird. Die Partikel, welche als starre Körper angenommen werden, werden mit den Newton-Euler-Gleichungen modelliert. Spezielle Randbedingungen an der Partikeloberfläche beschleunigen die Partikel. Während die eine Hälfte der Partikeloberfläche als passiv betrachtet wird, d. h. es wird die Haftbedingung als Randbedingung verwendet, ist die andere Hälfte eine aktive Oberfläche, an der eine aktive Spannung das umgebende Fluid beschleunigt. Aufgrund der Impulserhaltung bewegt sich das Teilchen in die entgegengesetzte Richtung der aktiven Spannung.

Das Modell wird zur Bestimmung von Lie-Symmetrien verwendet, die später zur Analyse von Simulationsdaten herangezogen werden. Darüber hinaus wird eine statistische Beschreibung einer aktiven Suspension auf der Grundlage der in der Turbulenzforschung verwendeten Lundgren-Monin-Novikov (LMN) Hierarchie abgeleitet. Für die resultierende Hierachie von Wahrscheinlichkeitsdichtefunktionen ergeben sich zusätzliche Symmetrien, die wichtige Informationen über das physikalische System enthalten.

Die Symmetrien werden zur Analyse und Interpretation von Simulationsdaten verwendet. Um die Daten zu generieren, wurde ein Solver auf der Grundlage der eXtended Discontious Galerkin (XDG) Methode entwickelt, welche im Bounded Support Spectral Solver (BoSSS) Framework implementiert ist. Die notwendigen Erweiterungen des bereits vorhandenen Lösers, die in dieser Arbeit beschrieben werden, umfassen die Implementierung eines Partikellösers, der aktiven Randbedingungen und eines Kollisionsmodells für die Partikel.

Die dritte Methode zur Analyse von aktiven Suspensionen, die in der vorliegenden Arbeit untersucht wird, ist ein homogenisiertes Modell. Im Gegensatz zu dem partikelaufgelösten Ansatz, der im BoSSS Framework realisiert wurde, werden nun Mittelwerte der physikalischen Größen untersucht. Ähnlich wie bei den Reynolds-gemittelten Navier-Stokes Gleichungen entstehen in den Modellgleichungen ungeschlossene Terme, die statistische Momente höherer Ordnung enthalten. Diese zusätzlichen Terme werden auf phänomenologischer Basis modelliert, d. h. Beobachtungen aus dem teilchenaufgelösten Modell werden zur Ableitung von Schließungsbedingungen verwendet.

Die mit beiden Modellen erzeugten Simulationsergebnisse werden mit den theoretischen Ergebnissen der Symmetrieanalyse verknüpft. Es zeigt sich, dass das Verhalten einer aktiven Suspension insbesondere durch das Phänomen der Intermittenz bestimmt wird, d. h. es besteht ein ständiger Wechsel zwischen deterministischem und chaotischem Verhalten.

Acknowledgements

Since September 2018 I have been working at the Institute of Fluid Dynamics at the TU Darmstadt. The work and research during these four interesting, exciting and instructive years culminated in this thesis. In the process, I have received support from various sides, and I would like to use this opportunity to express my gratitude.

First of all, I would like to thank Prof. Martin Oberlack and Prof. Yongqi Wang for their supervision. Throughout my time at the institute, we had many interesting and beneficial discussions that helped to move the project forward. Thanks to the support of both professors, we have managed to publish three papers in high quality journals in addition to this thesis. Prof. Thomas Speck is our project partner within the TRR146. As a physicist, he was able to introduce me to different approaches to our problem. I would like to thank him for his additional feedback, suggestions to my work and for reviewing this thesis.

I was always able to count on the support of Dr. Florian Kummer for questions about numerics, especially with regard to the BoSSS code. I would like to express my sincere thanks for supervising the development of the solver used in this thesis. I would also like to thank Ruth Völker for her support in administrative and organisational matters and many encouraging conversations.

I would particular like to thank all colleagues at the Chair of Fluid Dynamics. It was a pleasure to work with all of you. Even when Corona restricted a lot of things, we still managed to work together and organise some socialising events. Especially I would like to mention my office colleagues Dominik Plümacher and Divya Praturi. In extended discussions we were able to shed light on individual topics of our work, which I enjoyed very much. I would also like to thank Ashreya Jayaram for the interesting exchange on the topic of active particles. Together we were able to realise a publication and through the constant exchange we were able to successfully work on the joint project. Furthermore, I would like to thank Lauritz Beck, Matthias Geisenhöfer, Juan Gutiérrez, Anne Kikker, Dario Klingenberg, Dennis Krause, Matthias Rieckmann, Martin Smuda and Jens Weber for the exchange with regard to the joint development of the BoSSS code. I would especially like to thank Dennis Krause for his research, the results of which form the basis for the development of the particle-resolved solver in my work.

For the feedback on this thesis I would like to thank Lauritz Beck, Lara De Broeck, Bärbel Deußen, Carina Deußen, Christoph Deußen, Toni Dokoza, Simon Görtz, Dario Klingenberg, Cat Nguyen, Jie Liu, Matthias Rieckmann, Martin Smuda and Weihang Sun

Finally, I would like to thank my family. Over the years, you have always encouraged and supported me, no matter whether it was the transfer from the Realschule to the Gymnasium or the move to Darmstadt. Apparently, the endless sessions of English vocabulary training

finally were successful, considering the language of this work. Last but not least, I would like to thank my wife Carina. Thanks to your support, this work became possible in the first place. You were always there and could motivate me even when the research did not progress. Especially in the last weeks and months before the completion of this thesis, you had my back. Of course I would also like to thank my daughter Clara Ylva. Listening to you speaking your first words, especially of course when you say “Papa!”, is always a great motivational boost for me.

Funding

This work was funded by the Deutsche Forschungsgemeinschaft (DFG, German Research Foundation)-Project No. 233630050-TRR 146.

Contents

List of Figures

List of Tables

List of Abbreviations

AMR Adaptive Mesh Refinement

BDF2 second-order Backward Differentiation Formula
BoSSS Bounded Support Spectral Solver

DG Discontinuous Galerkin
DNS Direct Numerical Simulations
DoF Degrees of Freedom

FEM Finite Element Method
FVM Finite Volume Method

GJK Gilbert-Johnson-Keerthi

HMF Hierarchical Moment Fitting
HPC High-Performance Computing

LBB Ladyženskaja-Babuška-Brezzi
LMN Lundgren, Monin and Novikov

MBR Minimal Bounding Rectangle
MSD Mean Squared Displacement

PARDISO PARallel DIrect Solver
PDF Probability Density Function

RANS Reynolds-Averaged Navier-Stokes

SIP Symmetric Interior Penalty

XDG eXtended Discontious Galerkin
XNSERO eXtended Navier-Stokes plus Rigid Object

Nomenclature

Differential operators

$\frac{\partial}{\partial x_i}$	Partial differential operator
$\frac{\mathrm{d}}{\mathrm{d}x_i}$	Material differential operator
$\frac{D}{Dx_i}$	Lie symmetry theory total differential operator

Dimensionless numbers

Pe	Péclet number
Re	Reynolds number
Re^M	Mixture Reynolds number
Re^P	Particle Reynolds number
St	Stokes number

Special functions

$\delta(x)$	Dirac delta distribution, unit impulse
$\mathcal{H}(x)$	Heaviside function

Greek letters

α, β, γ	Infinitesimal parameters
α_p	Volume fraction of a single particle
α^F	Volume fraction of the fluid phase
α^S	Volume fraction of the solid phase
α^S_{max}	Maximal volume fraction of the solid phase
β_{ip}	Particle orientation angles; reduces to a vector β_p in two dimensions
$\widetilde{\beta}_p$	Noise term applied to the particle orientation in the Vicsek model

β^{cluster}	Cluster orientation
β^{min}	Alignment, relative angle between to close particles
γ_p	Particle indicator function
γ^F	Fluid phase indicator function
γ^S	Solid phase indicator function
Γ_p	Surface of the particle p
Γ_p^{ac}	Active surface of a single Janus particle
Γ^{ac}	Active surface of all particles
Γ^D	External edge with Dirichlet boundary condition
Γ^{ext}	External edge of a cell
Γ^F	Surface of the entire fluid phase union of the particle surface and the external surface $\Gamma^F = \Gamma^S \cup \partial\Omega$
Γ^{int}	Internal edge of a cell
Γ^K	Edge of a cell
Γ^N	External edge with Neumann boundary condition
Γ_p^{pa}	Passive surface of a single Janus particle
Γ^{pa}	Passive surface of all particles
Γ^S	Surface of the entire solid phase, interface between the fluid and solid phase
δ_{ij}	Kronecker delta, unit tensor
ε	Aspect ration of the particles $\varepsilon = a/b$
ϵ_{ijk}	Levi-Civita symbol
ζ	Stokes friction coefficient
ζ_i	Local vector of the homogenised model $\zeta_i = x_i^* - x_i$
η	Penalty parameter of SIP
η_i	Infinitesimal for dependent variables
θ	Particle polar angle

Θ_{ij}^S	Non-dimensional moment of inertia tensor; reduces to a scalar $\Theta^S = \Theta_{33}^S$ in two dimensions
κ	Diffusion exponent
λ	Collision model distance threshold
μ^F	Fluid viscosity
μ^{int}	Intrinsic viscosity
μ^M	Mixture viscosity
ξ_i	Infinitesimal for indepedent variables
ρ^F	Fluid density
ρ^S	Solid density
τ_{ij}^F	Fluid stress tensor
τ^R	Diffusive time-scale
σ	Relaxation coefficient
ϕ	Function describing the surface of all particles
φ	Particle azimuth angle
ϕ_n	Orthogonal basis functions depend on Legendre polynomials
ϕ_p	Function describing the surface of the particle p
φ^I	Angle of incidence
ϕ^L, ϕ^U	New functions for the Saye-algorithm
Φ	Set of all particle functions ϕ_p
$\Phi_{\|\|}$	Sphericity of a particle
$\Phi_{\perp}$	Cross sectional sphericity of a particle
Φ_i	Transformation of the independent variables
χ_{ip}	Particle position
χ_p^{CP}	Centre of pressure
ψ	Function tangential to ϕ
$\psi\left(\mathfrak{U}\right)$	Shape function of a general sample space variable $\mathfrak{U}$

Ψ_i	Transformation of the dependent variables
$\Psi^{\mathfrak{P}}$	General flux of the phase $\mathfrak{P}$
ω_{ip}	Particle rotational velocity
ω^F	Fluid velocity rotation, vorticity
Ω	Global domain
Ω_p	Domain occupied by the particle p
Ω^F	Domain occupied by the fluid phase
Ω^S	Domain occupied by the solid phase

Latin letters

a	Long particle axis
$a\left(\cdot,\cdot\right)$	Bilinear viscous form
$a^{ac}\left(\cdot,\cdot\right)$	Bilinear active viscous form
a^p, a^q	Excentricity of the collision point on the particles p, q
$a_\perp$	Diameter of a cross sectional surface equivalent disk
a_s	Diameter of a surface equivalent sphere
a_v	Diameter of a volume equivalent sphere
A^c	Dimensionless active stress
$\mathfrak{A}^c$	Magnitude of the active force
A_i	Active stress source term
$\mathfrak{A}_i^c$	Active force
b, c	Short particle axis
$b\left(\cdot,\cdot\right)$	Bilinear form
$b^{\min}$	Sample space variable for the particle alignment
b_p	Two-dimensional particle orientation sample space variable
B_n	Legendre coefficients
c_{Ac}^D	Drag correction factor due to the active surface

c^D_{corr}	Correction factor for the drag force $c^D_{\text{corr}} = c^D_{Ac} c^D_H$
c^D_H	Drag correction factor due to the solid domain walls
c^{DT}_{corr}	Correction factor for the drag torque
c^e_1, c^e_2	Model parameter for the circulation lift force
C	Maximum number of child-nodes per parent node in the R-tree $\mathcal{R}$
$\mathcal{C}$	Minkowski-difference of two sets
C^D	Drag coefficient
C^L	Lift coefficient
D, D_κ, D^R, D^T	Diffusion coefficients
$\mathfrak{D}$	Density ratio between solid and fluid phase
e_{ip}	Particle orientation vector
$\widehat{e}_{ip}$	Sample space particle orientation vector
e^i_j	Basis vector of the coordinate system, $i = 1, 2, 3$
e^S	Length of the volume averaged orientation
e^{Sd}_i	Orientation of a Stokes dipole
e^{Sl}_i	Orientation of a Stokeslet
E_i	Event in probability theory
f^{ac}	Magnitude of the active stress
$f_{\text{G},i}$	Transformation function of the Galilei symmetry
f_i	Stress vector
$\mathfrak{f}_{i,j}$	Ansatz functions for the DG-method
f^{ac}_i	Active stress vector at the active particle surface Γ^{ac}_p
${}_K f$	K-point joint PDF of the three sample space variables b_p, V_i, X_{ip}
f^b	PDF of the particle orientation sample space variable b_p
$f^{b^{\text{min}}}$	Alignment PDF
$f^{\mathfrak{r}^{\text{min}}}$	Minimal distance PDF

$f^{\mathfrak{r}b}$	Joint PDF of the minimal distance and the alignment
$f^{\mathfrak{r}\mathfrak{v}}$	Joint PDF of the minimal distance and the relative velocity
$\widehat{f}^{\mathfrak{U}}$	Fine-grained PDF of the general sample space variable $\mathfrak{U}$
$f^{\mathfrak{U}}$	PDF of the general sample space variable $\mathfrak{U}$
f^{V}	PDF of the velocity sample space variable V_i
f^{X}	PDF of the partial position sample space variable X_{ip}
F	Index for the fluid phase
F_i	Force
$\mathfrak{F}_i$	Vector consisting of the hydrodynamic forces and torques acting on all particles
$\widetilde{F}_i$	Linear momentum exchanged during a binary collision
F_k	System of differential equations, where $k = 1, 2, ..., K$
$\langle F_i^A \rangle$	Averaged active force
$\langle F_i^B \rangle$	Averaged Basset-force
F_i^C	Contact force
$\langle F_i^D \rangle$	Averaged drag force
F_i^F	Force acting on the fluid phase
$\langle F_i^L \rangle$	Averaged lift force
$\langle F_i^{LC} \rangle$	Averaged circulation lift force
$\langle F_i^{LM} \rangle$	Averaged Magnus-force
$\langle F_i^{LS} \rangle$	Averaged Saffman-force
$\langle F_i^P \rangle$	Averaged pressure force
F_i^S	Force acting on the solid phase
F^{Sd}	Strength of a Stokes dipole
F^{Sl}	Strength of a Stokeslet
$\langle F_i^V \rangle$	Averaged virtual mass force
g_p	Sample space particle indicator function

g^{α}	Logistic function for the particle volume fraction
g^{e}	Logistic function for the particle orientation
g^{F}	Sample space fluid phase indicator function
G	Group
h	Sample space signed distance function
h^{Γ}	Mesh size at the particle surface $h^{\Gamma} \leq h^{K}$
h^{K}	Global mesh size
H_k	Auxiliary function to obtain an invariant solution
J_{ij}	Jacobian matrix
k	Coefficient of restitution
k^{eff}	Effective coefficient of restitution
K	Turbulent kinetic energy
K_j	Numerical cell
$K_{j,\mathfrak{P}}$	Cut-cell occupied by the phase $\mathfrak{P}$
$\mathfrak{K}_h$	Set of all cells covering the domain Ω
$\mathfrak{K}_h^X$	Set of all cut-cells
$\mathfrak{L}$	Mean squared displacement (MSD)
L^c	Characteristic length
M_{ij}	Mass matrix
M_j^i	MBR related to the node N_j^i in the R-tree $\mathcal{R}$
n_i	Normal vector at the surface of the solid phase, pointing from the particle to the fluid
n_{ip}	Tensor of the normal vectors at the surface of the particles, pointing from the particle to the fluid. The column vectors of n_{ip} are equivalent to the normal vector n_i.
n_i^C	Collision normal vector
$n_i^{\Gamma^K}$	Outward pointing normal vector at the edge Γ^K of a cell
N	Number of particles in the domain Ω
N'	Number of particles in a subdomain of Ω

N_j^i	Node of the R-tree $\mathcal{R}$
O_{ij}^p	Operator matrix
$\mathfrak{q}$	Scalar test function
p_i	A specific point
p^F	Fluid pressure
p^N	Prescribed pressure at a Neumann boundary
P, Q	Sets containing multiple particles
$\mathfrak{P}$	Index for a general phase, either takes the value F for the fluid phase, S for the solid phase
$\mathcal{P}$	Set of points describing the geometry of the particle p
$\mathcal{P}'$	Set of points describing the geometry of the particle p at the next time-step
P_i	Probability of an event E_i
P_{ij}	Tangential tensor $P_{ij} = \delta_{ij} - n_i n_j$
$\mathbb{P}_k$	Broken polynomial space
P_n	Legendre polynomials
$\mathcal{Q}$	Set of points describing the geometry of the particle q
Q_{ij}	Rotation matrix
r	Distance
$r(\cdot)$	Boundary conditions for the continuity equation
$r^{\min}$	Absolute value of the smallest minimal distance vector between two particles in a set P
$\mathfrak{r}^{\min}$	Sample space variable for the minimal particle distance
r_i	Distance vector
$r_i^{\min}$	Smallest minimal distance vector between two particles in a set P
$r_i^{p,q}$	Minimal distance vector between two particles p and q
R	Set of Voronoi-regions
$\mathfrak{R}$	Residual

$\mathcal{R}$	R-tree
s	Arc length variable along Γ_p
$s\left(\cdot\right)$	Boundary conditions for the Stokes equation
$s_i^{\mathcal{C}}$	Support mapping of the set $\mathcal{C}$
S	Entropy; As an index S refers to the solid phase
${}^nS$, ${}^n\widehat{S}$	Simplex in the nth iteration of the GJK algorithm
S^F	Generic fluid phase solver
S^S	Generic solid phase solver
t	Time
t^m	Simulation time at a specific time-step
t^{run}	Simulation runtime
Δt	Time-step
Δt^{acc}	Accumulated time-step
Δt^{safe}	Safe time-step during collision
t_i	Tangential vector at the surface of a particle
$t_i^{\perp}$	Perpendicular tangential vector at the surface of a particle
T_α	Global form of a symmetry
T_i	Torque
$\left\langle T_i^D \right\rangle$	Averaged drag torque
$\left\langle T_i^P \right\rangle$	Averaged pitching torque
$\mathfrak{u}$	General physical variable
$\widehat{\mathfrak{u}}$	Approximation of $\mathfrak{u}$
$\langle \mathfrak{u} \rangle$	Average of a physical variable $\mathfrak{u}$
$\overline{\mathfrak{u}}$	True physical volume average of a physical variable $\mathfrak{u}$
$[\![\mathfrak{u}]\!]$	Jump of the arbitrary physical variable
$\{\mathfrak{u}\}\left(\boldsymbol{x}\right)$	Average of the inner and outer value of $\mathfrak{u}$ at a cell boundary

u_i^D	Dirichlet velocity
$u_i^{\mathfrak{P}}$	Velocity of the phase $\mathfrak{P}$
u_i^{Sd}	Velocity induced by a Stokes dipole
u_i^{Sl}	Velocity induced by a Stokeslet
$\mathfrak{U}$	General sample space variable
U_i	Single-field velocity
U^c	Characteristic velocity
U^{cluster}	Cluster velocity
v	Absolute value of the particle velocity, particle speed
v_i	Support vector
$\mathfrak{v}_i$	Test function
v_{ip}	Particle translational velocity
$\mathbb{V}_k$	Function space of the ansatz and test functions
v^{ac}	Absolute value of the active velocity, induced by the propulsion mechanism
v^{pq}	Relative speed of the particles p and q
$\mathfrak{v}^{pq}$	Sample space variable for the relative speed of the particles p and q
V	Representative averaging volume element
$\mathfrak{V}$	Sample space variable of the particle speed
V_i	Velocity sample space variable
V^F	Volume occupied by the fluid phase
V^L, V^U	Dimensionally reduced region for the Saye-algorithm
V^P	Volume occupied by a single particle
V^S	Volume occupied by the solid phase
w_i^S	Relative velocity at the phase interface
${}_k x_i$	kth point of the global domain Ω
x_i	Eulerian coordinates, independent variables

x_i^*	Local Eulerian coordinates for the homogenised model
$\mathfrak{X}$	Lie operator
X_{ip}	Particle position sample space variable
$\mathfrak{X}_N$	Prolonged Lie operator
y_i	Dependent variables
Y_k	Solution of the system of differential equations F_k
z_i	Right hand side vector

1. Introduction

> But then the other machines gained the upper hand. [...] I consider them to be small pseudo-insects that can combine as needed, in the common interest so to speak, to form a superordinate system precisely in the form of clouds. This is how the evolution of mobile automatons took place. (Lem [133] pp. 83-85)

Small, autonomous machines - nano-robots - as described by Stanislaw Lem, are a long known and popular motif in science fiction literature. Such machines with their own propulsion mechanisms are, at their core, active particles. Research is still a long way from such advanced and according to science fiction literature even dangerous machines. However, active particles surround us in our daily lives, in fact we humans are active particles ourselves. In the most general definition, an active particle is an object capable of self-driven systematic motion [172]. In this work, swimming and flying active particles are investigated in particular. If such particles are combined with a fluid, an active suspension is obtained. In Fig. 1.1 a wide range of exemplary active particles is given. From the largest living animal on earth - the blue whale (*Balaenoptera musculus*) - to one of the smallest known organisms, the green algae *Micromonas pusilla* [6], many living organisms are capable of self driven motion. This trait is so important that it is often used to distinguish animals from other life forms, although there are stationary animals, e.g corals, as well as mobile plants, such as the green algae mentioned above.

On a macroscopic scale, artificial active particles are well known. Cars, trains, ships and planes transport people and goods every day. The focus of this work is, however, on microscopic particles similar to Lem's nano-robots, i.e. the particles are not visible by the naked eye. Such particles represent a new field of research, where various pioneering ideas and approaches exist. Possible applications, which are currently only investigated on a laboratory scale, range from medicine to the purification of polluted water and soil, combating the effects of climate change and neutralising chemical warfare agents. In medicine, active particles can be used as carriers for targeted drug delivery. Core idea is to deliver the medical agent, e.g. a cancer drug, directly to the origin of the disease [101]. Consequently, side effects of the medication can be alleviated. In addition to developing a reliable actuator capable of operation in vivo, biocompatibility and toxicity are a particular challenge [87, 176]. Artificial active particles might also be used to detect and degrade pollutants [115, 161, 192]. For example a TiO_2/Au coating at the surface of an active particle triggers a catalytic reaction, which degrades dye pollutants, while at the same time driving the particles forward [212].

Any microscopic active particle, whether artificial or biological in nature, has to cope with the special conditions resulting from its small size. To better understand these conditions one might define the Reynolds number

$$\mathrm{Re} = \frac{\rho^F U^c L^c}{\mu^F}, \tag{1.1}$$

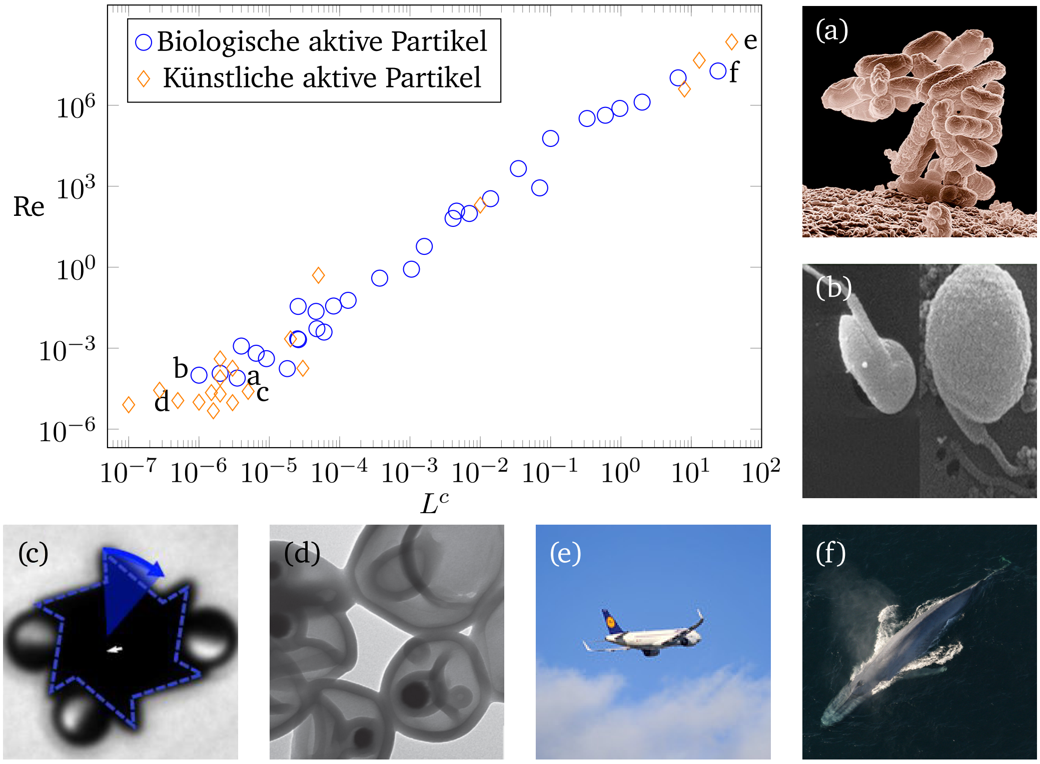

Fig. 1.1.: Active particle come in all sizes. The diagram shows the relationship between the length L^c and the Reynolds number Re of different biological and artificial active particles. (a) Motile strains of *Escherichia coli* are often used as model organism for active particles. Photo courtesy of USDA ARS [70]. (b) The green algae *M. pusilla* is one of the smallest known biological active swimmers. Reproduced from Alsante et al. [6]. (c) Silica Janus particles with platinum coating accelerate a micro-gear. Reproduced from Maggi et al. [144]. (d) Artificial stomatocytes are able to trap catalytical nano-particles, which are used as motor. Reproduced form Wilson et al. [207]. (e) Large swimming or flying artificial structures such as planes can be considered as active particles. Photo by Hope, M. [100]. (f) The largest biological active particle is the blue whale (*B. musculus*). Photo courtesy of NOAA [136].

where U^c is a characteristic velocity, L^c a characteristic length, ρ^F is the fluid mass density and μ^F the dynamic viscosity of the fluid. Assume a particle with a length $L^c = 10^{-6}$m swimming in water ($\rho^F = 10^3$kg m^{-3}, $\mu^F = 10^{-3}$kg m^{-1}s^{-1}) with a velocity of $U^c = 10^{-4}$m s^{-1}. The resulting Reynolds number Re $= 10^{-4}$ is small. By considering Fig. 1.1, a more precise definition of the term microscopic scale can be derived by means of the Reynolds number. The condition Re $\ll 1$ needs to be upheld, thus, all particles presented in the diagram with a characteristic length $a \ll 10^{-3}$m are in the microscopic range. Given that Re can be interpreted as the ratio between the inertial and viscous forces, a small Reynolds number indicates dominating viscous forces. Inertia is defined as the resistance towards a change in motion. Subsequently, in case of vanishing inertial forces no resistance exists and any velocity change is instantaneous. In other words, in a system with negligible inertia, time does not matter [171]. This has major implication for the motion of microscopic active particles. Purcell [171] explains the impact of the high viscous environment with the example of scallops. These swim by opening their shells slowly and closing them again quickly. The difference in speed of the two processes causes the scallop to move forward, a process which is called reciprocal motion [171]. The same process at small Reynolds numbers in a Newtonian fluid would have no effect, since the time in which the opening and closing process takes place does not matter. The scallop would merely oscillate about a stationary point. It should be noted, that a micro-scallop in a non-Newtonian fluid is quite capable of moving, since such fluids show non-linear and time-dependent behaviours [18].

Escherichia coli or *Bacillus subtilis* are often used as model organisms in experiments [59, 62, 191, 211]. They are able to propel themselves in Newtonian fluids at low Reynolds numbers by using a bundle of flagella, which are able to rotate continuously in one direction [181]. Hence, the propulsion is non-reciprocal and the bacteria can move forward. *Archaea* use a simpler structure, which is also capable of continuous rotation, the so-called archaellum [3]. Larger eukaryotic unicellular organisms use, among other mechanisms, a large number of cilia for locomotion. In contrast to the flagellum, these can only perform planar movements [214]. Due to their flexible structure, however, their motion is also non-reciprocal [171].

Probably the simplest way to artificially produce an active particle is the Janus particle approach. They were named after the two-faced Roman god Janus, who was supposed to represent the contradictions of the world. Following the naming, Janus particles have two or more surface regions with different optical, chemical, electronic or magnetic properties [197]. The different properties of the surfaces cause a flow of the surrounding fluid. For example, in case of the aforementioned particle with TiO_2/Au coating, where one half of the particle surface is coated with titanium dioxide and the other half with gold, the reaction which degrades the dye pollutants is responsible for an electric potential difference, which causes the fluid flow. Due to momentum conservation the particle will move in the opposing direction [212].

A different group of artificial active particles is driven by an external field, e.g. a magnetic field. The particles activated by this field follow a similar structure as their biological counterparts, where, both, the rotational movement of the flagella is mimicked as well as the rowing of the cilia [41, 117, 216]. Instead of only mimicking biological structures, bio-hybrid active particles directly employ the biological mechanism by modifying bacteria or eukaryotes [87]. One possibility to control bio-hybrid particle is to use the natural behaviour of bacteria to follow gradients of nutrients or pollutants. Another possibility is to genetically modify the bacteria to become sensitive to a certain mechanism. For example, Frangipane et al. [77] present photosensitive *E. coli* that can be made to reproduce complex two-dimensional structures like grayscale images.

Depending on their propulsion mechanism, active particles produce characteristic flow fields in their vicinity. Such fields can be approximated with singularities of different order. An active particle driven by an external force causes a flow field, which can be approximated by a Stokeslet, i.e. a force singularity in a viscous incompressible flow. The corresponding solution of the Stokes equation in three spatial dimension is [18, 25]

$$u_i^{\mathrm{Sl}}(\boldsymbol{r}) = \frac{F^{Sl}}{8\pi\mu^F r}\left(\frac{1}{r^2}e_j^{Sl} r_j r_i + e_i^{Sl}\right), \tag{1.2}$$

where u_i^{Sl} is the fluid velocity induced by the Stokeslet, F^{Sl} is the magnitude of the point force, e_i^{Sl} is the orientation of the Stokeslet, r_i is the distance vector towards the origin of the

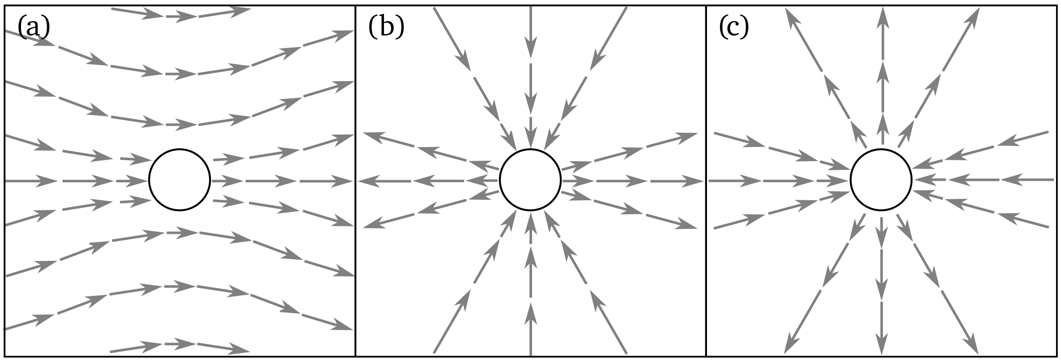

Fig. 1.2.: The flow in the vicinity of active particles can be approximated using singularities. All three particles in this figure move on the horizontal axis in the right direction. (a) A particle driven by an external force produces a flow field equivalent to a Stokeslet. (b) A pusher particle driven by a force exerted by the particle onto the fluid produces the flow field equivalent to a Stokes dipole. (c) An inversed Stokes dipole is produced by a puller particle. Illustration based on Bechinger et al. [18]

points force and r the length of the distance vector. The resulting flow field is given as a sketch in Fig. 1.2a.

In case of self-driven active particles, i.e. the particle exert a force on the fluid, one needs to distinguish two cases. Either the particle is pushed by its propulsion system, e.g. flagella, see Fig 1.3a or the particle is pulled, see Fig 1.3b. An approximation for the corresponding flow fields is a Stokes dipole, which is generated by two nearby opposing point forces [18]. The solution of the Stokes equation for a Stokes dipole in three dimensions is

$$u_i^{Sd}(\boldsymbol{r}) = \frac{F^{Sd}}{8\pi\mu^F r^3}\left(\frac{3}{r^2}\left(e_j^{Sd} r_j\right)^2 - 1\right) r_i, \tag{1.3}$$

where u_i^{Sd} is the fluid velocity induced by the dipole, F^{Sd} is the strength of the force dipole and e_i^{Sd} its orientation [18]. In case of the pusher particle F^{Sd} is positive, whereas in case of a puller particle the sign is negative. Both velocity fields are sketched in Fig. 1.2b+c.

In two dimensions the velocity of the singularities changes compared to three dimensions. The induced velocity u_i^{Sl} of the Stokeslet becomes [43]

$$u_i^{Sl}(\boldsymbol{r}) = \frac{F^{Sl}}{4\pi\mu^F} \ln\left(r^{-1}\right)\left(\frac{1}{r^2} e_j^{Sl} r_j r_i + e_i^{Sl}\right). \tag{1.4}$$

Furthermore, the induced velocity of the Stokes dipole is [43]

$$u_i^{Sd}(\boldsymbol{r}) = \frac{F^{Sd}}{4\pi\mu^F r^2}\left(\frac{3}{r^2}\left(e_j^{Sd} r_j\right)^2 - 1\right) r_i, \tag{1.5}$$

Notably, the order of the rate of decay with increasing distance r is reduced by one compared to the three dimensional case.

In order for the aforementioned new technologies to be used not only in the laboratory but also in medicine or industry, it is necessary to describe the collective behaviour of active suspensions. In general, the behaviour of an active suspension depends on its density [16, 149],

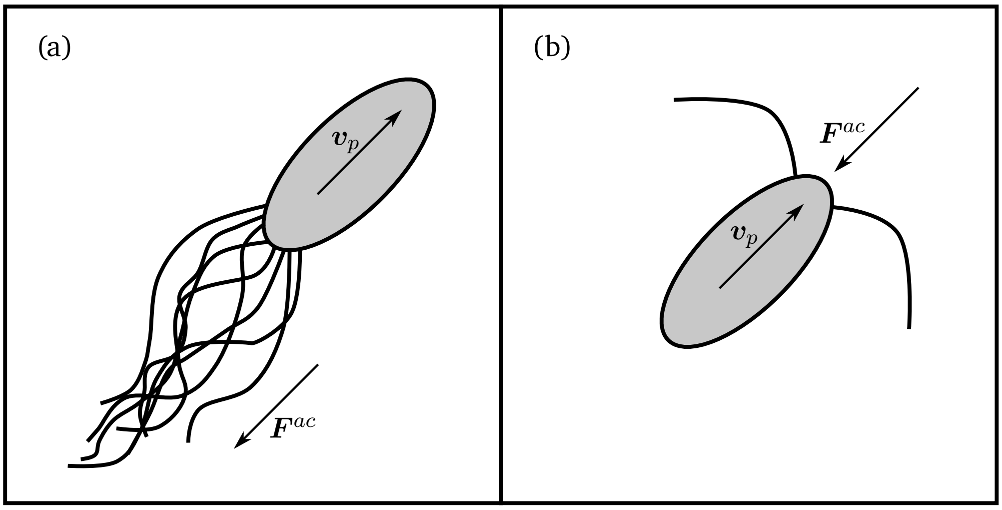

Fig. 1.3.: Two different categories of propulsion exists for self-driven active particles, i.e. particles with an internal source of force. In both images, $\boldsymbol{v}_p$ is the particle velocity and $\boldsymbol{F}^{ac}$ is the active force induced by the particle on the fluid. (a) A pusher particle, e.g. *E. coli* or *B. subtilis*, uses its a bundle of flagella to push the cell body forward. (b) The propulsion mechanism of a puller particle is mounted at the front of the particle and pulls the cell body through the fluid. An example for such a particle would be the algae *Chlamydomonas reinhardtii*. Illustration based on Bechinger et al. [18] and Saintillan [181].

the material law of the fluid phase [18, 155], the geometrical properties of the active particles [17, 73, 204] and of the enclosure [56, 210]. Due to the visual resemblance to turbulence at high Reynolds numbers, some authors established the term active turbulence for the chaotic behaviour of an active suspension for certain particle densities, e.g. Alert et al. [4], Bratanov et al. [34], Dombrowski et al. [59], and Sokolov and Aranson [191]. While both phenomena - hydrodynamic turbulence and active turbulence - share similarities, the differences are apparent. Classical hydrodynamic turbulence occurs at high Reynolds numbers and is driven by inertia. Energy is transferred from large to small scales and only at the smallest scales, viscosity becomes the dominant parameter, leading to the dissipation of energy. Such a process is described as energy cascade [123, 124]. In case of an active suspension, energy is injected at a certain scale, defined by the motor of the particles, and dissipated on any scale. Subsequently, no energy cascade is present [4]. Similarities between both phenomena can be found in the Probability Density Function (PDF) of the velocity. The PDF show non-Gaussian heavy tails, resembling the behaviour of the velocity and vorticity PDF in hydrodynamic turbulence [112, 205], a phenomenon which is also visible in the results of the present work.

Expanding the understanding of the collective behaviour and providing techniques to study active suspensions is the goal of the present work. The aim is to investigate the extent to which an active suspension behaves deterministically, chaotically in the sense of the aforementioned active turbulence, or as an intermittent system. The term intermittency describes a constant change between deterministic and chaotic behaviour and is known, for example, from the field of classical hydrodynamic turbulence research [135, 206]. Three different approaches, tools so to speak, are developed to describe an active suspension, which are all based on the same Janus particle model. Different modelling strategies for active suspensions are presented in

Sec. 2, including the Janus particle model used throughout this work. Despite the fact that the term active turbulence itself might be misleading due to the differences towards classical hydrodynamic turbulence, it is worthwhile to apply techniques known from turbulence research to active suspensions. Hence, classical and statistical Lie-symmetries of an active suspension are investigated in Sec. 3. In order to obtain statistical symmetries a probability theory is presented employing the joint PDF of the velocity, particle position and particle orientation. The theoretical results can be subsequently used to analyse simulation data. In Sec. 4 a particle-resolved solver is presented based on the eXtended Discontious Galerkin (XDG) method, employing high order ansatz polynomials. Simulations for large systems with this solver would exceed the available computation power. Hence, we introduce a second solver based on Eulerian volume averaging theory in Sec. 5. Results for both numerical approaches are given in Sec. 6. To analyse the data obtained by the simulations the classical and statistical symmetries are used. Subsequently, it will be shown, that it is possible to connect the phenomena visible in the simulations, such as the formation of particle clusters, to the theoretical foundations. In the final Sec. 7, the previously obtained results from theory and numerics are summarised and discussed.

2. Modelling active suspensions

Several different approaches exist to model complex organisms and apparatuses which are summarised under the term active particles. For a small number of particles it is possible to use detailed models. For example, for *E. coli* bacteria, models can be formulated that resolve the cell body and the flagellum in detail [104]. However, such detailed models are not useful for simulations of a suspension with many hundreds, thousands or even millions of particles. On the one hand, the available computing power is limited, and on the other hand, in the case of a suspension, one may not be interested in the detailed behaviour of the individual particles, but in the collective behaviour of the entire suspension. Hence, to examine the collective behaviour it is useful to simplify the model of the individual particles. The different structures of an active particle such as the cell body and the flagellum are replaced by a simpler geometrical structure.

In this section, first, a general introduction into the employed notations is given (Sec. 2.1), followed by an overview of different models for active particles (Sec. 2.2). While three different approaches to investigate active suspensions are examined in this work, the underlying model for an active particle is kept the same to ensure comparability. The model is an extension of the simpler models presented in Sec. 2.2. It is based on the assumptions to model the particles as rigid Janus particles and the fluid as a Newtonian fluid. A detailed presentation of the model assumptions and its derivation are presented in Sec. 2.3.

2.1. Notations

This section introduces notation conventions that will be used in the present work. An arbitrary scalar physical quantity is denoted by $\mathrm{u}^{\mathfrak{P}}$; bold characters $\mathbf{u}^{\mathfrak{P}}$ are used for tensor quantities. The superscript $\mathfrak{P}$ refers to the phase related to the physical quantity, having either the value F for the fluid phase or S for the solid particle phase. Moreover, subscripts are used to refer to elements of a tensor $\mathrm{u}^{\mathfrak{P}}_{i...j}$, where the number of indices $i...j$ indicates the tensor order of $\mathbf{u}^{\mathfrak{P}}$. The Einstein summation convention is always applied to such indices. Hence, if an index appears twice in a term, a summation is implied over the entire set of values of the specific index.

Variables describing particle properties are grouped into first and second order tensors, implying that they have two subscripts, where the first index refers to the spatial dimension and the second index to the number of particles. The tensor χ_{ip}, which describes the position of all N particles in the three dimensional space, has the from

$$\boldsymbol{\chi} = [\boldsymbol{\chi}_1, \ldots, \boldsymbol{\chi}_p, \ldots, \boldsymbol{\chi}_N] = \begin{bmatrix} \chi_{11}, & \ldots, & \chi_{1p}, & \ldots, & \chi_{1N} \\ \chi_{21}, & \ldots, & \chi_{2p}, & \ldots, & \chi_{2N} \\ \chi_{31}, & \ldots, & \chi_{3p}, & \ldots, & \chi_{3N} \end{bmatrix}. \tag{2.1}$$

Each column vector defines the position of a single particle. Similarly, quantities such as the particle orientation e_{ip} or the particle velocity v_{ip} are grouped together in tensors. In the case of two spatial dimensions, the tensor order of some of the particle quantities is reduced. In the three-dimensional space, the orientation of each particle is described by three angles of orientation, which are grouped together in the second order tensor β_{ip}. In the case of two dimensions, a single orientation angle is sufficient to describe the orientation of a particle, leading to a first order $1 \times N$ tensor β_p. Again, as the subscript p describes the element of a tensor, the summation convention is applied. If neither a superscript $\mathfrak{P}$ referring to the specific phase nor a subscript referring to the particles is given, the variable in question describes the entire system of both phases.

Furthermore, it is necessary to consider quantities at multiple points ${}_1x_i, \ldots, {}_kx_i, \ldots, {}_Kx_i$ of the global domain Ω. Such points are specified by a preceding index. The notation ${}_1\mathfrak{u} = \mathfrak{u}\left({}_1\boldsymbol{x}\right)$ denotes that the physical variable is evaluated at the point ${}_1x_i$, while ${}_k\mathfrak{u} = \mathfrak{u}\left({}_k\boldsymbol{x}\right)$ means evaluation at the point ${}_kx_i$. All variables in an equation are evaluated at the same point if no preceding index is used.

Most physical quantities $\mathfrak{u}$ depend on multiple independent variables such as one or multiple points ${}_1x_i, \ldots, {}_kx_i, \ldots, {}_Kx_i$ and the time t. Thus, to describe derivatives with respect to a single independent variable, the partial differential operator

$$\frac{\partial \mathfrak{u}}{\partial x_i}, \quad \frac{\partial \mathfrak{u}}{\partial t} \tag{2.2}$$

is used. To describe the change of a physical quantity of a material element alongside its path through the domain Ω, the material or total derivative is introduced [194]

$$\frac{\mathrm{d}\mathfrak{u}}{\mathrm{d}t} = \frac{\partial \mathfrak{u}}{\partial t} + U_i \frac{\partial \mathfrak{u}}{\partial x_i}, \tag{2.3}$$

where U_i is the velocity at the point x_i. Hence, it describes the local change $\partial\mathfrak{u}/\partial t$ of $\mathfrak{u}$ and the convective flux $U_i \partial\mathfrak{u}/\partial x_i$.

Generalised functions or distributions are used to describe different domains and interfaces. The multidimensional Dirac delta distribution $\delta\left(\boldsymbol{x}\right) = \prod_{i=1}^{d} \delta\left(x_i\right)$ is a generalised function, which allows to identify specific points of the domain Ω, such as the particle surface Γ. Its integral measure returns the value of a test function $f\left(\boldsymbol{x}\right)$ at the point $\boldsymbol{x} = 0$

$$\int_{\Omega} \delta\left(\boldsymbol{x}\right) f\left(\boldsymbol{x}\right) \mathrm{d}\boldsymbol{x} = f\left(0\right), \tag{2.4}$$

where the integration $\int_{\Omega} \mathrm{d}\boldsymbol{x} = \int_{\Omega} \mathrm{d}x_1 \ldots \mathrm{d}x_d$ is executed in the infinite domain Ω with the dimension d. The test function f is smooth and compactly supported, i.e.

$$\lim_{\boldsymbol{x} \to \infty} f\left(\boldsymbol{x}\right) = 0, \quad \lim_{\boldsymbol{x} \to -\infty} f\left(\boldsymbol{x}\right) = 0. \tag{2.5}$$

It should be noted that throughout this work most physical relations are given in a differential form, hence, the integration $\int_\Omega \mathrm{d}\boldsymbol{x}$ is not necessarily written down but implied. By shifting the argument of the Dirac delta distribution by some point ${}_1\boldsymbol{x}$ it is possible to retrieve the evaluation of $f(\boldsymbol{x})$ at a this point ${}_1\boldsymbol{x}$

$$\int_\Omega \delta\left(\boldsymbol{x} - {}_1\boldsymbol{x}\right) f\left(\boldsymbol{x}\right) \mathrm{d}\boldsymbol{x} = f\left({}_1\boldsymbol{x}\right). \tag{2.6}$$

Furthermore, we introduce a shortened notation for the evaluation of f at multiple different points. Let $\Gamma = \{{}_1\boldsymbol{x}, ..., {}_k\boldsymbol{x}, ..., {}_K\boldsymbol{x}\}$ be a set of K points, then the integration

$$\int_\Omega \delta\left(\boldsymbol{x} - \Gamma\right) f\left(\boldsymbol{x}\right) \mathrm{d}\boldsymbol{x} = f\left({}_k\boldsymbol{x}\right) \quad \forall\, {}_k\boldsymbol{x} \in \Gamma \tag{2.7}$$

yields the value of f at all points in Γ.

It is possible to derive the derivative of the Dirac delta distribution using integration by parts, which in the one-dimensional case reads

$$\int_\Omega \delta'\left(x\right) f\left(x\right) \mathrm{d}x = \left[\delta\left(x\right) f\left(x\right)\right]_{-\infty}^{\infty} - \int_\Omega \delta\left(x\right) f'\left(x\right) \mathrm{d}x = -f'\left(0\right), \tag{2.8}$$

where the first term on the right hand side vanishes due to (2.5). In the multidimensional case, one obtains

$$\int_\Omega \partial_d\left(\delta\left(\boldsymbol{x}\right)\right) f\left(\boldsymbol{x}\right) \mathrm{d}\boldsymbol{x} = -\int_\Omega \delta\left(\boldsymbol{x}\right) \partial_d\left(f\left(\boldsymbol{x}\right)\right) \mathrm{d}\boldsymbol{x} = -\left.\partial_d f\left(\boldsymbol{x}\right)\right|_{\boldsymbol{x}=0}, \tag{2.9}$$

where again the test function $f(\boldsymbol{x})$ vanishes at infinity due to (2.5) and the operator ∂_d is defined as

$$\partial_d = \frac{\partial}{\partial x_1}\frac{\partial}{\partial x_2}\cdots\frac{\partial}{\partial x_d}. \tag{2.10}$$

In order to derive the integral of the Dirac delta distribution, it is necessary to introduce the Heaviside function

$$\mathcal{H}\left(x\right) = \begin{cases} 1 & x > 0 \\ 0 & x < 0 \end{cases} \tag{2.11}$$

The d-dimensional Heaviside function is defined as the product

$$\mathcal{H}\left(\boldsymbol{x}\right) = \prod_{i=1}^{d} \mathcal{H}\left(x_i\right) \tag{2.12}$$

in analogy to the d-dimensional Dirac function (2.4). Integration by parts of the derivate of the Heaviside function yields

$$\begin{aligned}\int_\Omega \partial_d \mathcal{H}\left(\boldsymbol{x}\right) f\left(\boldsymbol{x}\right) \mathrm{d}\boldsymbol{x} &= -\int_\Omega \mathcal{H}\left(\boldsymbol{x}\right) \partial_d f\left(\boldsymbol{x}\right) \mathrm{d}\boldsymbol{x} \\ &= -f\left(\boldsymbol{x} \to \infty\right) + f\left(0\right) = \int_\Omega \delta\left(\boldsymbol{x}\right) f\left(\boldsymbol{x}\right) \mathrm{d}\boldsymbol{x},\end{aligned} \tag{2.13}$$

where (2.5) was used. Thus, the distributional derivative of the Heaviside function is the Dirac delta distribution.

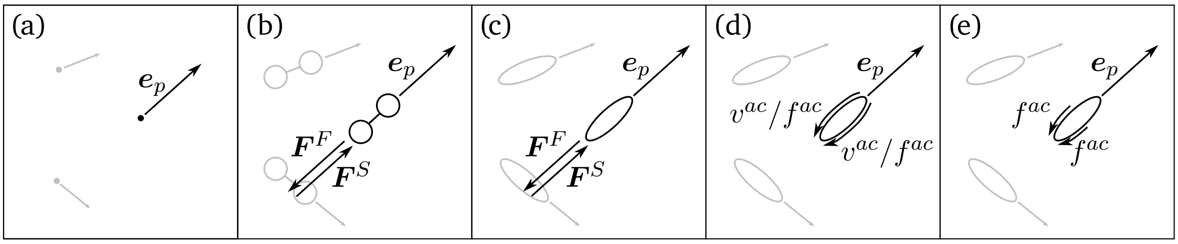

Fig. 2.1.: A selection of models for active particles. (a) Vicsek model: Each particle is represented by a point and the orientation vector e_{ip}. The velocity of the particles is the product of the orientation vector and a constant speed [200]. (b) Dumbbell model: Two connected beads form a dumbbell. The action of a flagellum is represented by the eccentric pair of forces $\boldsymbol{F}^F$ and $\boldsymbol{F}^S$. $\boldsymbol{F}^F$ is the force exerted by the flagellum onto the fluid, $\boldsymbol{F}^S$ is the reaction forces exerted by the fluid onto the particle [93, 94]. (c) Generalisation of the dumbbell model using an ellipsoidal particle [84, 85]. (d) Slip velocity and active stress models: The boundary conditions at the particle surface are modified by imposing a slip-velocity v^{ac} or by applying an active stress f^{ac} [27, 116, 143]. (e) Janus particle: This is the model used throughout the present work. One half of the particle surface is active, i.e. an active stress f^{ac} is applied to the particle surface, whereas the other half is passive, i.e. a no-slip boundary condition is applied [51, 116, 182]. Illustrations (a)-(e) are based on Saintillan and Shelley [182]

2.2. Models of active particles

Several different approaches exist to simplify the structure of complex active organisms. In this section an exemplary selection of models well-known in the literature is presented. Vicsek et al. [200] introduced a minimalist model where the particles are represented by a single point, the orientation e_{ip} and the velocity $v_{ip} = ve_{ip}$, see Fig. 2.1a. No fluid is considered in this model. The speed v, i.e. the absolute value of the velocity, is kept constant. Accordingly a change of the particle position χ_{ip} is described by

$$\chi_{ip}\left(t + \Delta t\right) = \chi_{ip} + ve_{ip}\Delta t, \tag{2.14}$$

where Δt is a single time-step. In the two-dimensional space, the orientation vector can be described by an angle β_p, i.e. the angle between the orientation vector and the first unit vector of the reference coordinate system. The orientation angle is obtained from

$$\beta_p\left(t + \Delta t\right) = \left\langle \beta_p \right\rangle_r + \widetilde{\beta}_p, \tag{2.15}$$

where $\left\langle \beta_p \right\rangle_r$ is the average orientation angle of all particles within a certain radius r around the particle p and $\widetilde{\beta}_p$ is a noise term [200]. Despite its minimal design, the model shows collective behaviour depending on the density of the suspension and the strength of the noise term $\widetilde{\beta}_p$. This includes unordered states, the formation of local clusters with similar orientation or a globally ordered suspension occurring in the case of high densities and low noise [200].

The dumbbell model (Fig. 2.1b) is a minimal swimmer model, considering both the fluid and the particle phase. Each rigid particle consists of two connected beads, resembling a dumbbell. A propulsion mechanism such as a flagellum is represented by an eccentric pair of forces, consisting of the force F_i^F acting on the fluid and the force F_i^S acting on the second bead [93]. Inertia is neglected, hence, the force balance on the second bead of the dumbbell reads

$$F_i^S - \zeta \left(\dot{\chi}_{i1} - u_i^F \left(\boldsymbol{\chi}_1\right)\right) + F_i^C = 0, \tag{2.16}$$

where $\zeta = 3\pi\mu^F a$ is the friction coefficient according to Stokes' law, a is the diameter of one bead, $\boldsymbol{\chi}_1$ is the position of the first bead, $u_i^F \left(\boldsymbol{\chi}_1\right)$ is the fluid velocity at $\boldsymbol{\chi}_1$ and F_i^C is the connection force between the two beads, ensuring the rigidity of the particles [93]. The force balance for the first bead is equivalent, however, the propulsion force F_i^S is only applied to the second bead. The fluid is described by the Stokes equation

$$0 = -\frac{\partial p^F}{\partial x_i} + \frac{1}{\text{Re}} \frac{\partial^2 u_i^F}{\partial x_j^2}, \tag{2.17}$$

where p^F is the fluid pressure and u_i^F the fluid velocity. By simulating a suspension of dumbbell particles, Hernandez-Ortiz et al. [93] found that particles agglomerate at the channel walls solely due to hydrodynamic interactions, an effect which can be theoretically explained by a mirror system at a no-slip wall, see Blake [25]. The model sketched in Fig. 2.1c is a generalisation of the dumbbell model used by Haines et al. [84, 85] to determine the effective viscosity of an active suspension, where the dumbbell was replaced by an ellipsoidal particle.

Models based on boundary conditions (Fig. 2.1d) do not rely on point forces. Instead, either a slip velocity v_i^{ac} or a mechanical active stress f_i^{ac} is prescribed at the particle surface. Thereby, such a model can be considered as a model for active particles driven by cilia, e.g. eukaryotic single cell organisms, and is also used as a general model for active particles [182]. Active particles of the type depicted in Fig. 2.1d are called squirmer and were first introduced by Blake [26] and Lighthill [141]. In this model the surface of the squirmer is impermeable, however, a slip velocity in tangential direction is prescribed. In case of an axisymmetric particle the tangential active slip velocity is given by

$$v^{ac}\left(\theta\right) = \sum_{n\geq 1} B_n \phi_n(\cos\left(\theta\right)) \tag{2.18}$$

where B_n are Legendre coefficients given by Lighthill [141] and $\phi_n(\cos\left(\theta\right))$ depends on the angular cosine $\cos\left(\theta\right)$. The functions ϕ_n are determined by the Legendre polynomials P_n according to [141, 182]

$$\phi_n(\cos\left(\theta\right)) = \frac{2}{n\left(n+1\right)} \sin\left(\theta\right) P_n'(\cos\left(\theta\right)), \tag{2.19}$$

where θ is the polar angle of the particle, see Fig. 2.2. The resulting particle velocity as given by Saintillan and Shelley [182] is $v = \frac{2B_1}{3}$.

Propulsion mechanisms such as cilia or flagella do not directly generate a velocity, but rather exert a force on the surrounding fluid. Hence, instead of prescribing an active velocity, a mechanical stress with the magnitude f^{ac} is imposed at the particle surface, see Fig. 2.1d. In the case of a real active particle the magnitude f^{ac} would be time-dependent, because it might change during the cycle of a flagellum or the stroke of a cilium. However, in the model it is assumed to be constant, effectively being the average of the stress exerted by the real active particle during one cycle of the propulsion mechanism [181]. The active stress permits a fluid slip velocity at the surface, which in return induces a particle velocity. Kanevsky et al. [116]

define the boundary conditions for a stress-driven particle as follows. The particle exerts a certain active stress on the surrounding fluid given by $f_i^{ac} = f^{ac} t_i$ and

$$t_i = \epsilon_{ijk} \left(\epsilon_{jlm} e_l^p n_m \right) n_k = \left(e_j^p n_j \right) n_i - e_i^p, \tag{2.20}$$

where t_i is the tangential vector at the surface, n_i is the outward pointing normal vector at the surface and e_i^p is the orientation vector of a specific particle p. Due to the inner product

$$e_i^p t_i = \left(e_i^p n_i \right)^2 - \left(e_i^p e_i^p \right) \leq 0, \tag{2.21}$$

the tangential vector faces in the backwards direction of the particle, i.e opposing the orientation vector. Hence, the boundary condition for the stress f_i at the particle surface defined by the tangential stress f_i^{ac} is given by

$$\left(\delta_{ij} - n_i n_j \right) \left(\delta_{jk} - t_j^\perp t_k^\perp \right) f_k = f^{ac} t_i, \quad t_i^\perp = \epsilon_{ijk} e_j^p n_k, \tag{2.22}$$

with the unit tensor δ_{ij}, see Fig. 2.1d. The vector $t_i^\perp$ is tangential to the particle surface and perpendicular to the normal vector n_i, the orientation vector e_i^p and the tangential vector t_i. The boundary conditions are defined with respect to the body reference frame, hence, all velocity components beside $u^t = u_i t_i$ vanish at the particle surface, implying

$$u^n = u_i n_i = 0, \quad u^\perp = u_i e_i^\perp = 0. \tag{2.23}$$

The complete set of boundary condition is, thus, formed by the active stress condition (2.22) and the conditions in (2.23). Furthermore, the particle is considered to be force and torque free

$$F_i = \int_{\Gamma_p} f_i \, \mathrm{d}s = 0, \qquad T_i = \int_{\Gamma_p} \epsilon_{ijk} r_j f_k = 0, \tag{2.24}$$

which is a necessary condition to close the model. Forces and torques are obtained by a surface integration of the stress f_i, exerted by the fluid on the particle, where Γ_p is the particle surface, $r_i = x_i - \chi_i^p, \quad \forall \boldsymbol{x} \in \Gamma_p$ is the radial vector and χ_i^p is the centre of mass of the specific particle p. For more details see Kanevsky et al. [116].

2.3. Janus particle model

The model used throughout this work is closely related to the squirmer model presented by Kanevsky et al. [116]. However, for many active particles, only a part of the body is responsible for propulsion. In the case of *E. coli*, which is a pusher particle, multiple flagella are situated at the back of the bacterium, whereas the propulsion mechanism of a puller particle, e.g. *C. reinhardtii*, is mounted at the front of the particle body, see Fig. 1.3. Thus, instead of prescribing the active stress at the entire surface Γ_p, the particle surface is split into two halves. One half Γ_p^{ac} is active and has a prescribed active stress, whereas on the other half a no-slip boundary condition is used without an additional stress, i.e. it is a passive surface Γ_p^{pa}. Hence, the model resembles a Janus particle as presented in Fig. 2.1e. For a rod-like particle this idea was examined by Saintillan and Shelley [182]. Building on the two publications mentioned before [116, 182], a Janus particle model for ellipse-shaped two-dimensional and ellipsoidal three-dimensional particles is used throughout the present work. The suspension

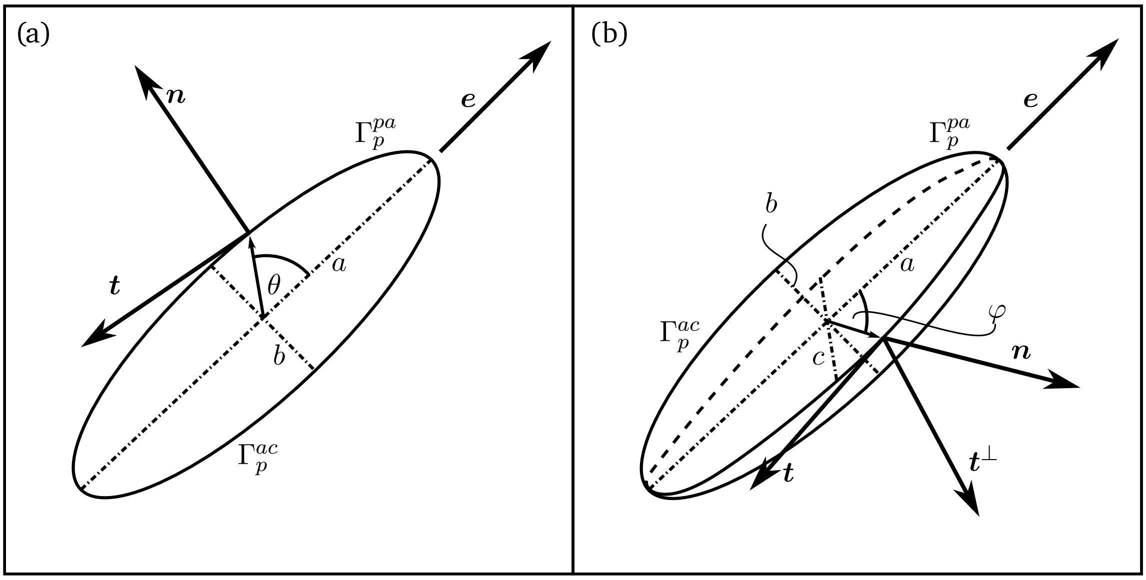

Fig. 2.2.: (a) Depiction of a two-dimensional particle: The particle geometry is defined by the two axes a and b and the orientation vector $e_i = e_{ip}\gamma_p$, where γ_p is the particle indicator function. The normal vector n_i and the tangential vector t_i at a point of the particle surface are both functions of the polar angle θ. The surface of the particle Γ_p is split by the axis b into a passive part Γ_p^{pa} at the front and an active part at the rear Γ_p^{ac}. (b) Depiction of a three-dimensional particle: The particle geometry is defined by the three axes a, b and c and the orientation vector $e_i = e_{ip}\gamma_p$. The polar angle θ and the azimuth angle φ define the position of the normal vector system on a surface point consisting of the normal vector n_i, the tangential vector t_i and the perpendicular tangential vector $t_i^{\perp}$. Analogous to the two-dimensional case , the particle surface is split by the axes b and c into a passive part Γ_p^{pa} at the front and an active part at the rear Γ_p^{ac}. For better readability $\theta = 0$ was chosen in this sketch.

is considered to consists of N identical Janus particles in a Newtonian fluid. For the geometric description of the particles, it applies that a two-dimensional particle is defined by its two axes a and b, see Fig. 2.2a. This leads to the definition of the aspect ratio

$$\varepsilon = \frac{a}{b}. \tag{2.25}$$

A three-dimensional ellipsoid on the other hand contains an additional axis c, see Fig. 2.2b. However, it is assumed that $b = c$, hence, the definition of the aspect ratio (2.25) is still valid. The particles are considered to be rigid and it is required that two particles do not overlap, giving rise to the relation

$$\Omega_p \cap \Omega_q = \varnothing, \quad p \neq q, \tag{2.26}$$

where Ω_p is the domain occupied by a rigid particle. Accordingly, the union of all N particle domains is the solid phase domain

$$\Omega^S = \bigcup_{p=1}^{N} \Omega_p, \tag{2.27}$$

which, together with the fluid domain Ω^F, forms the global domain Ω. It is required that Ω^S and Ω^F do not intersect, leading to

$$\Omega^S \cup \Omega^F = \Omega, \quad \Omega^S \cap \Omega^F = \varnothing. \tag{2.28}$$

Thus, at any space-time point $(\boldsymbol{x}, t)$ only a single particle or the fluid is present. Furthermore, the subset $\Omega^F \in \Omega$ is a closed set

$$\Omega^F = \operatorname{cl} \Omega^F, \tag{2.29}$$

i.e. it contains its own boundary. To distinguish between the two domains a phase indicator function $\gamma^{\mathfrak{P}}$ is introduced, reading

$$\gamma^{\mathfrak{P}} = \begin{cases} 1 & \text{in } \Omega^{\mathfrak{P}} \\ 0 & \text{in } \Omega \setminus \Omega^{\mathfrak{P}} \end{cases} \qquad \forall \mathfrak{P} \in \{F, S\}\,. \tag{2.30}$$

Single particles are identified by a particle indicator function

$$\gamma_p = \begin{cases} 1 & \text{in } \Omega_p \\ 0 & \text{in } \Omega \setminus \Omega_p \end{cases}. \tag{2.31}$$

The indicator functions of all particles form a vector $\boldsymbol{\gamma} = [\gamma_1, ..., \gamma_p, ..., \gamma_N]$, i.e. the function γ_p is an element of the particle indicator vector $\boldsymbol{\gamma}$. The absolute value of $\boldsymbol{\gamma}$ gives the solid phase indicator function

$$\gamma^S = |\boldsymbol{\gamma}|\,. \tag{2.32}$$

It should be noted that due to the non-overlapping nature of the particles only one element of the vector $\boldsymbol{\gamma}$ can be non-zero at any space-time point $(\boldsymbol{x}, t)$. Hence, all possible vector norms deliver the same result for γ^S. Due to the condition that both phases do not intersect, see (2.28), the fluid phase indicator function is

$$\gamma^F = 1 - \gamma^S, \tag{2.33}$$

which is known as saturation condition.

The surface of a particle p is denoted by Γ_p. The union of all particle surfaces delivers the interface Γ^S between the two phases

$$\Gamma^S = \bigcup_{p=1}^{N} \Gamma_p, \quad \Gamma_p \cap \Gamma_q = \varnothing \quad \forall p \neq q, \tag{2.34}$$

where the condition $\Gamma_p \cap \Gamma_q = \varnothing$ is enforced by the non-overlapping condition for the particles (2.26). The orientation vector of the particles is necessary to define the normal vector system depicted in Fig. 2.2. The orientation vectors of all particles form a tensor

$$\boldsymbol{e} = [\boldsymbol{e}_1, ..., \boldsymbol{e}_p, ..., \boldsymbol{e}_N] = \begin{bmatrix} e_{11}, & ..., & e_{1p}, & ..., & e_{1N} \\ e_{21}, & ..., & e_{2p}, & ..., & e_{2N} \\ e_{31}, & ..., & e_{3p}, & ..., & e_{3N} \end{bmatrix}. \tag{2.35}$$

The inner product $e_{ip}\gamma_p\,(\boldsymbol{x}, t)$ of this tensor with the particle indicator function delivers the orientation vector of the particle at the space-time point $(\boldsymbol{x}, t)$, i.e. an individual column vector

$e_i = e_{ip}\gamma_p$ of the tensor (2.35). At each point of the surface Γ_p an outward pointing normal vector n_i is defined, see Fig. 2.2. The perpendicular tangential vector $t_i^{\perp}$ is defined by the cross product of the normal vector and the orientation vector

$$t_i^{\perp} = \epsilon_{ijk} e_{jp} \gamma_p n_k, \tag{2.36}$$

which is the vector perpendicular to the Euclidean plane in the case of two spatial dimensions. The cross product of the normal vector n_i and the perpendicular tangential vector $t_i^{\perp}$ yields the tangential vector t_i, meaning

$$t_i = \epsilon_{ijk} t_j^{\perp} n_k = \gamma_p \left(n_i n_j e_{jp} - e_{ip} \right). \tag{2.37}$$

Due to the definition (2.37), the tangential vector t_i always points in the opposite direction of the particle orientation, i.e. the sign of the scalar product of the orientation vector and the tangential vector is always negative

$$t_i e_{ip} \gamma_p = \left(n_i e_{ip} \gamma_p \right)^2 - e_{ip} \gamma_p e_{iq} \gamma_q \leq 0, \tag{2.38}$$

a property which is used later to define the active stress at the particle boundary. Note that, due to the non-overlap condition (2.26), the second term on the right hand side of (2.38) is non-zero only if γ_p and γ_q refer to the same particle, because only one element of the indicator function vector is non-zero at a specific point x_i. The different indices solely ensure the correct employment of the summation convention.

Due to the nature of a Janus particle, each particle has a passive surface Γ_p^{pa} and an active surface Γ_p^{ac} (Fig. 2.2), separated by the half axes b and c. Together, Γ_p^{ac} and Γ_p^{pa} form the entire particle surface and do not overlap

$$\Gamma_p = \Gamma_p^{ac} \cup \Gamma_p^{pa}, \quad \Gamma_p^{ac} \cap \Gamma_p^{pa} = \varnothing, \quad \Gamma^{ac} = \bigcup_{p=1}^{N} \Gamma_p^{ac}, \quad \Gamma^{pa} = \bigcup_{p=1}^{N} \Gamma_p^{pa}. \tag{2.39}$$

Since there is no slip velocity permitted on the passive surface Γ_p^{pa}, the local particle velocity u_i^S, which is defined in the next section in (2.51), and the fluid velocity u_i^F must be equal

$$u_i^F = u_i^S \quad \forall \boldsymbol{x} \in \Gamma^{pa}. \tag{2.40}$$

At the active part of the surface Γ^{ac} this relation only holds in normal direction, because the surface is considered to be impermeable and a slip velocity is permitted in the tangential diraction, meaning

$$u_i^F n_i = u_i^S n_i \quad \forall \boldsymbol{x} \in \Gamma^{ac}. \tag{2.41}$$

Following Kanevsky et al. [116], the active stress at Γ^{ac} is defined by

$$f_i^{ac} = f^{ac} t_i \quad \forall \boldsymbol{x} \in \Gamma^{ac}, \tag{2.42}$$

which depending on the sign of f^{ac}, opposes the direction of the orientation vector e_{ip} (f^{ac} positive) or points in the same direction (f^{ac} negative), as follows from the definition of the tangential vector (2.37). The sign of the active stress magnitude f^{ac} defines whether the particle is a pusher or puller particle. In correspondence to the solution for the Stokes dipole, (1.3) in three dimension and (1.5) in the two-dimensional case, a positive sign leads to a pusher particle, whereas a negative sign produces a puller particle. Using the fluid density ρ^F and a characteristic particle velocity and length, delivers the dimensionless active stress magnitude

$$A^c = \frac{f^{ac}}{\rho^F \left(U^c \right)^2}. \tag{2.43}$$

2.3.1. Solid particle phase

All N particles together form the solid phase of the active suspension. As each particle occupies an exclusive space of the domain Ω, see (2.26), they are clearly identifiable by their position $\boldsymbol{\chi}_p = \boldsymbol{\chi}_p\left(t\right)$ and orientation angle $\boldsymbol{\beta}_p = \boldsymbol{\beta}_p\left(t\right)$, which are both solely functions of the time t. The positions of all particles form a tensor, as established in (2.1)

$$\boldsymbol{\chi} = \left[\boldsymbol{\chi}_1,\, ...,\, \boldsymbol{\chi}_p,\, ...,\, \boldsymbol{\chi}_N\right] = \begin{bmatrix} \chi_{11},\, ...,\, \chi_{1p},\, ...,\, \chi_{1N} \\ \chi_{21},\, ...,\, \chi_{2p},\, ...,\, \chi_{2N} \\ \chi_{31},\, ...,\, \chi_{3p},\, ...,\, \chi_{3N} \end{bmatrix}.$$

In three dimensions the orientation angles also form a $3 \times N$ tensor

$$\boldsymbol{\beta} = \left[\boldsymbol{\beta}_1,\, ...,\, \boldsymbol{\beta}_p,\, ...,\, \boldsymbol{\beta}_N\right] = \begin{bmatrix} \beta_{11},\, ...,\, \beta_{1p},\, ...,\, \beta_{1N} \\ \beta_{21},\, ...,\, \beta_{2p},\, ...,\, \beta_{2N} \\ \beta_{31},\, ...,\, \beta_{3p},\, ...,\, \beta_{3N} \end{bmatrix}, \tag{2.44}$$

where each element is defined by its cosine and the scalar product of the basis vectors e_i^j, $j = 1, 2, 3$ of the coordinate space and the orientation vector

$$\cos\left(\beta_{jp}\right) = e_i^j e_{ip}, \qquad \forall j \in \{1, 2, 3\}\,. \tag{2.45}$$

Due to (2.45) both formulations (2.44) and the tensor of orientation vectors (2.35) can be used equivalent. However, in three dimensions the usage of the orientation vector is advantageous, whereas in two dimensions the tensor (2.44) is reduced to a $1 \times N$ vector β_p, because a single cosine is sufficient to describe the direction of the orientation vector. Thus, the orientation angle β_p delivers a more simple description.

The temporal derivative of the particle position delivers the translational velocity

$$\frac{\mathrm{d}\chi_{ip}}{\mathrm{d}t} = v_{ip}. \tag{2.46}$$

The rotational velocity is obtained by

$$\frac{\mathrm{d}\beta_{ip}}{\mathrm{d}t} = \omega_{ip}. \tag{2.47}$$

where in the case of two dimensions the second order tensors are reduced to vectors. Thus, in the case of a single particle, (2.47) becomes a scalar equation. The temporal derivative of the orientation vector (2.35) is

$$\gamma_p \frac{\mathrm{d}e_{ip}}{\mathrm{d}t} = \epsilon_{ijk}\omega_{jp}\gamma_p e_{kq}\gamma_q, \tag{2.48}$$

where the indicator function γ_p was used to select the correct particle. Again, the right hand side is non-zero only if the indicator functions γ_p and γ_q refer to the same particle, because of the non-overlapping condition (2.26). The different indices p and q ensure the correct application of the summation convention.

The density ρ^S is constant for all particles. Thus, the material derivative $\mathrm{d}\rho^S/\,\mathrm{d}t = 0$ vanishes and the mass balance

$$\frac{\partial \rho^S}{\partial t} + \frac{\partial \rho^S u_i^S}{\partial x_i} = \frac{\mathrm{d}\rho^S}{\mathrm{d}t} + \rho^S \frac{\partial u_i^S}{\partial x_i} = 0 \tag{2.49}$$

is reduced to

$$\frac{\partial u_i^S}{\partial x_i} = 0. \tag{2.50}$$

The local velocity u_i^S of any point within the solid phase domain is

$$u_i^S\left(\boldsymbol{x},t\right) = \gamma_p\left(\boldsymbol{x},t\right)\left[v_{ip}\left(t\right) + \epsilon_{ijk}\omega_{jp}\left(t\right)r_k\left(\boldsymbol{x},t\right)\right], \tag{2.51}$$

where u_i^S is a function of space and time in contrast to the translational and rotational velocities, which only depend on time. Here, we introduce the radial vector

$$r_i\left(\boldsymbol{x},t\right) = x_i - \chi_{ip}\left(t\right)\gamma_p\left(\boldsymbol{x},t\right) \tag{2.52}$$

to refer to points within the particle domain relative to the position χ_{ip} of the particles. Forming the material derivative yields the acceleration of the solid phase

$$\frac{\mathrm{d}u_i^S}{\mathrm{d}t} = \frac{\partial u_i^S}{\partial t} + u_j^S\frac{\partial u_i^S}{\partial x_j} = \gamma_p\left[\frac{\mathrm{d}v_{ip}}{\mathrm{d}t} + \epsilon_{ijk}\frac{\mathrm{d}\omega_{jp}}{\mathrm{d}t}r_k\right] - \left(\omega_{jp}\gamma_p\right)^2 r_i, \tag{2.53}$$

where the derivatives $\frac{\mathrm{d}v_{ip}}{\mathrm{d}t}$ and $\frac{\mathrm{d}\omega_{jp}}{\mathrm{d}t}$ are defined by the Newton-Euler equations

$$V^P\mathfrak{D}\frac{\mathrm{d}v_{ip}}{\mathrm{d}t} = \int_{\Gamma_p}\tau_{ij}^F n_{jp}\,\mathrm{d}s \tag{2.54}$$

and

$$\Theta_{ij}^S\frac{\mathrm{d}\omega_{jp}}{\mathrm{d}t} + \epsilon_{ijk}\Theta_{kl}^S\omega_{jp}\omega_{lq}\gamma_q = \int_{\Gamma_p}\epsilon_{ijk}r_j\tau_{kl}^F n_{lp}\,\mathrm{d}s. \tag{2.55}$$

Note that not only the particle velocities v_{ip} and ω_{ip} are second order tensors, but also n_{ip}. The column vectors of the latter tensor $n_i = n_{ip}\gamma_p$ are the normal vectors at a specific point at the surface of a specific particle p. Both, the normal vector n_i and the normal vector tensor n_{ip} are derived in Sec. 2.3.3. Furthermore, the definition of Ω^F as a closed set, see (2.29), was used. The fluid stress tensor τ_{ij}^F is only defined on Ω^F, which does contain its own boundary, including the particle surface Γ_p, allowing the integration as presented in (2.54) and (2.55). The non-dimensional mass $m = V^P\mathfrak{D}$ of each particle is formed with the density ratio $\mathfrak{D} = \rho^S/\rho^F$ and the non-dimensional particle volume

$$V^P = \int_{\Omega_p} 1\,\mathrm{d}\boldsymbol{x}, \tag{2.56}$$

which is the volume enclosed by the particle domain Ω_p. It is assumed that all N particles are identical. Hence, while each particle occupies an individual domain Ω_p, the volume V^P is identical for all particles.

The non-dimensional moment of inertia Θ_{ij}^S is a second order tensor in three dimensions and defined by

$$\Theta_{ij}^S = \mathfrak{D}\int_{\Omega_p}\left(r_k r_k\delta_{ij} - r_i r_j\right)\mathrm{d}\boldsymbol{x}. \tag{2.57}$$

The rotational Newton-Euler equation (2.55) is given in a rotating body reference frame. It is assumed that the axes of the coordinate frame align with the principle axis of inertia, thus, the tensor Θ_{ij}^S is diagonal. Furthermore, because all particles are identical, Θ_{ij}^S is the same for all particles. In the two-dimensional case, (2.55) is reduced to a vector equation

$$\Theta^S \frac{\mathrm{d}\omega_p}{\mathrm{d}t} = \int_{\Gamma_p} \epsilon_{3ij} r_i \tau_{jk}^F n_{kp} \, \mathrm{d}s, \tag{2.58}$$

where $\Theta^S = \Theta_{33}^S$. Again, because all particles are identical, each particle is described by the same moment of inertia Θ^S. The notation ϵ_{3ij} of the Levi-Civita symbol refers to the two-dimensional cross-product, where the result is a scalar, which would be the vector perpendicular to the $\mathbb{R}^2$-plane in three dimensions. The second term on the left hand side of (2.55) vanishes in (2.58) due to the occurrence of the Levi-Civita symbol with two identical subscripts $\epsilon_{i33}\Theta_{33}^S\omega_{3p}\omega_{3q}\gamma_q = 0$.

Due to the small size of the considered particles, they have to be assumed to be Brownian particles. By the latter term a particle is meant where Brownian motion [67, 188] has a significant effect, i.e. the particle shows a random motion based on collisions with fluid molecules. However, throughout the present work it is assumed that the effects of the active stress are significantly larger than the diffusive transport of the Brownian motion. Consider the Péclet number as defined by Bechinger et al. [18]

$$\mathrm{Pe} = \frac{v^{ac}}{\sqrt{D^T D^R}}, \tag{2.59}$$

where v^{ac} is the speed of the particle due to the active motion and D^T and D^R are the translational and rotational diffusion coefficient due to Brownian motion. Throughout the present work it is assumed that the Péclet number is large $\mathrm{Pe} > 1$ and Brownian motion can be neglected. In the reversed case, i.e. the active transport has diminishing effects on the particle and diffusive transport dominates, stochastic terms would have to be considered in the particle equations of motion, see Bechinger et al. [18].

2.3.2. Fluid phase

Momentum conservation in any continuum, i.e. also in a fluid, is described by the Cauchy momentum equation [194]

$$\frac{\partial \rho^F u_i^F}{\partial t} + \frac{\partial \rho^F u_i^F u_j^F}{\partial x_j} = \frac{\partial \tau_{ij}^F}{\partial x_j}, \tag{2.60}$$

where u_i^F is the fluid velocity, ρ^F the mass density of the fluid and τ_{ij}^F the stress tensor. External forces such as gravity are neglected. The conservation of angular momentum [194]

$$\frac{\partial \rho^F \epsilon_{ijk} x_j u_k}{\partial t} + \frac{\partial \rho^F \epsilon_{ijk} x_j u_k u_l}{\partial x_l} = \frac{\partial \epsilon_{ijk} x_j \tau_{kl}^F}{\partial x_l} \quad \Rightarrow \quad \epsilon_{ijk}\tau_{kj}^F = 0 \tag{2.61}$$

delivers the symmetry of the stress tensor $\tau_{ij}^F = \tau_{ji}^F$, which has to be further defined by a material law. Throughout this work we will assume the fluid phase to be Newtonian, hence, the stress tensor of the fluid phase is defined by

$$\tau_{ij}^F = -p^F \delta_{ij} + \mu^F \left[\frac{\partial u_i^F}{\partial x_j} + \frac{\partial u_j^F}{\partial x_i} \right], \tag{2.62}$$

where μ^F is the constant fluid viscosity.

Conservation of mass is described by

$$\frac{\partial \rho^F}{\partial t} + \frac{\partial \rho^F u_i^F}{\partial x_i} = \frac{\mathrm{d}\rho^F}{\mathrm{d}t} + \rho^F \frac{\partial u_i^F}{\partial x_i} = 0, \tag{2.63}$$

where

$$\frac{\mathrm{d}\rho^F}{\mathrm{d}t} = \frac{\partial \rho^F}{\partial t} + u_i^F \frac{\partial \rho^F}{\partial x_i} \tag{2.64}$$

is the material derivative of the mass density ρ^F. Assuming incompressibility $\mathrm{d}\rho^F / \mathrm{d}t = 0$, i.e. the mass density of the observed fluid element does not change along its path [194], yields the continuity equation

$$\frac{\partial u_i^F}{\partial x_i} = 0. \tag{2.65}$$

Using (2.60) and (2.62) together with (2.65) delivers the Navier-Stokes equation for an incompressible Newtonian fluid

$$\rho^F \frac{\mathrm{d}u_i^F}{\mathrm{d}t} = \rho^F \left(\frac{\partial u_i}{\partial t} + u_j^F \frac{\partial u_i^F}{\partial x_j} \right) = -\frac{\partial p^F}{\partial x_i} + \mu^F \frac{\partial^2 u_i^F}{\partial x_j^2}. \tag{2.66}$$

Non-dimensionalisation of (2.66) yields

$$\frac{\partial u_i^F}{\partial t} + u_j^F \frac{\partial u_i^F}{\partial x_j} = -\frac{\partial p^F}{\partial x_i} + \frac{1}{\mathrm{Re}} \frac{\partial^2 u_i^F}{\partial x_j^2}, \tag{2.67}$$

with the Reynolds number (1.1)

$$\mathrm{Re} = \frac{\rho^F U^c L^c}{\mu^F}.$$

If the characteristic length scale L^c and velocity U^c of the problem are small or alternatively the viscosity μ^F is large, the Reynolds number becomes small. Applying $\mathrm{Re} \ll 1$ to (2.67) delivers the Stokes equation (2.17)

$$0 = -\frac{\partial p^F}{\partial x_i} + \frac{1}{\mathrm{Re}} \frac{\partial^2 u_i^F}{\partial x_j^2}.$$

Due to the motion of the particles, the particle surface and, thus, the boundary conditions at the surface are time-dependent in the present problem. Hence, it might be useful to still consider the temporal derivative, leading to the unsteady Stokes equation

$$\frac{\partial u_i^F}{\partial t} = -\frac{\partial p^F}{\partial x_i} + \frac{1}{\mathrm{Re}} \frac{\partial^2 u_i^F}{\partial x_j^2}. \tag{2.68}$$

It is implied throughout this work, that, whenever a solution of the Stokes or Navier-Stokes equation is mentioned, it also solves the continuity equation. At the external surface $\Gamma^F = \partial\Omega^F \cap \partial\Omega$ of the fluid domain Ω^F boundary conditions need to be applied. The boundary conditions are either of Dirichlet- or Neumann-type, where a boundary with a Dirichlet conditions is notated as Γ^D and Γ^N refers to a boundary with a Neumann condition. A Dirichlet boundary is defined by

$$u_i^F = u_i^D \quad \forall \boldsymbol{x} \in \Gamma^D \tag{2.69}$$

and a Neumann boundary is defined by

$$-p^F n_i + \frac{1}{\mathrm{Re}}\left(\frac{\partial u_i^F}{\partial x_j} + \frac{\partial u_j^F}{\partial x_i}\right) n_j = -p^N n_i \quad \forall \boldsymbol{x} \in \Gamma^N, \tag{2.70}$$

where u_i^D and p^N are prescribed functions, see for example Smuda [189]. It should be noted that in the case of the Neumann condition the pressure is prescribed, i.e. defined by a Dirichlet condition.

Either the Navier-Stokes equation (2.67) or the unsteady Stokes equation (2.68) together with the continuity equation (2.65) and the particle equations (2.46), (2.47) (2.54) and (2.55) form a complete model for an active suspension, where both phases are coupled by the hydrodynamic forces and torques occurring as integral terms in the Newton-Euler equations (2.54), (2.55) and the passive (2.40) and the active (2.41), (2.42) boundary conditions.

2.3.3. Level-Set method

In both, numerical simulations and theoretical considerations, the level-set method is used to represent the surface of the particles. The level-set method allows to represent a sharp interface between solid and liquid [163]. This exact approach makes it superior to other methods, such as the volume of fluid method [96] or the phase-field approach [129].

The particle surface Γ_p is represented by the zero level set $\phi_p = 0$ of the function $\phi_p = \phi_p\left(\boldsymbol{x}; \boldsymbol{\chi}_p(t), \boldsymbol{\beta}_p(t)\right)$. The particles are considered to be rigid, hence, their shape does not change and subsequently ϕ_p does not depend directly on the time t. Instead it is a function of the Eulerian spatial coordinate $\boldsymbol{x}$, the centre of mass $\boldsymbol{\chi}_p$ and the orientation angles $\boldsymbol{\beta}_p$ of the particles. The two latter variables are solely functions of the time t, thus, ϕ_p depends implicitly on time. A vector is used to represent all functions of all particles

$$\boldsymbol{\phi} = \left[\phi_1, ..., \phi_p, ..., \phi_N\right], \tag{2.71}$$

which are defined by

$$\phi_p \begin{cases} < 0 & \text{in } \Omega_p \\ = 0 & \text{on } \Gamma_p \\ > 0 & \text{elsewhere.} \end{cases} \tag{2.72}$$

The normal vector at the surface of p is defined by the gradient of ϕ_p, leading to a second order tensor, where each column vector is a normal vector related to a specific element of the vector ϕ_p

$$n_{ip} = \frac{\partial \phi_p}{\partial x_i} \left|\nabla \phi_p\right|^{-1}. \tag{2.73}$$

Here, the normal vector at the surface of the particle p is normalised instead of a normalisation of the entire tensor n_{ip}.

Instead of using the single-particle function ϕ_p and the tensor n_{ip}, it is advantageous to define a global function ϕ by the infimum

$$\phi = \inf(\Phi), \tag{2.74}$$

where

$$\Phi\left(\boldsymbol{x},t\right)=\left\{\phi_1\left(\boldsymbol{x},t\right),\phi_2\left(\boldsymbol{x},t\right),...,\phi_p\left(\boldsymbol{x},t\right),...,\phi_N\left(\boldsymbol{x},t\right)\right\} \tag{2.75}$$

is the set of all particle distance functions [51]. The normalised gradient of ϕ is the general normal vector at the interface

$$n_i=\frac{\partial\phi}{\partial x_i}\left|\nabla\phi\right|^{-1}, \tag{2.76}$$

see Fig. 2.2. The normal vector n_i and the column vectors of n_{ip} are equivalent for a specific particle p and related by (2.74).

By introducing the Heaviside function $\mathcal{H}$ one obtains a relation between ϕ_p and the particle indicator function γ_p

$$\gamma_p=\mathcal{H}(-\phi_p)=\begin{cases}1 & \text{if } \phi_p<0\\ 0 & \text{if } \phi_p\geq 0\end{cases}. \tag{2.77}$$

The functions ϕ_p and ϕ and the indicator functions γ_p, γ^S and γ^F are material constants, hence, their material derivatives vanish

$$\frac{\mathrm{d}\phi_p}{\mathrm{d}t}=\frac{\partial\phi_p}{\partial t}+U_i\frac{\partial\phi_p}{\partial x_i}=0,\qquad \frac{\mathrm{d}\gamma_p}{\mathrm{d}t}=\frac{\partial\gamma_p}{\partial t}+U_i\frac{\partial\gamma_p}{\partial x_i}=\delta\left(\phi_p\right)\frac{\mathrm{d}\phi_p}{\mathrm{d}t}=0, \tag{2.78}$$

where $\delta\left(\cdot\right)$ indicates the Dirac delta function and U_i is the combined velocity of both phases, which will be introduced in detail in Sec. 2.3.4. While (2.78) is given for the single-particle functions ϕ_p and γ_p, analogous statements can be made for the remaining functions ϕ, γ^S and γ^F.

The function ϕ and the level-set method allows to rewrite surface integrals, occurring e.g. in the Newton-Euler equation (2.54) and (2.55), into volume integrals, where the following derivation is based on Chang et al. [40]. A second function ψ is introduced, tangentially to ϕ

$$\frac{\partial\phi}{\partial x_i}\frac{\partial\psi}{\partial x_i}=0,\qquad \frac{\partial\psi}{\partial x_i}\neq 0. \tag{2.79}$$

Both functions ϕ and ψ allow the introduction of the new coordinates [40]

$$x'=\psi\left(\boldsymbol{x},t\right),\qquad y'=\phi\left(\boldsymbol{x},t\right), \tag{2.80}$$

whose transformation to the Cartesian coordinate system is well defined since

$$\det\left[\frac{\partial\left(x',y'\right)}{\partial\left(x,y\right)}\right]=\left|\nabla\psi\right|\left|\nabla\phi\right|\neq 0. \tag{2.81}$$

Let s be an arc length variable along the interface Γ^S. The derivative of the new coordinate x' with respect to s along Γ^S is

$$\frac{\mathrm{d}x'}{\mathrm{d}s}=\frac{\mathrm{d}\psi}{\mathrm{d}s}=\frac{\partial\psi}{\partial x_i}\frac{\partial x_i}{\partial s}=\left|\nabla\psi\right|. \tag{2.82}$$

Here, the derivative $\partial x_i/\partial s$ is the unit tangent vector [40]. The vector $\partial\psi/\partial x_i$ is by definition (2.79) parallel to the unit tangent vector, hence, the result of (2.82) is the length of the gradient of ψ. The surface integral of an arbitrary function f_i is, thus, transformed into a volume integral

$$\begin{aligned}\int_{\Gamma^S} f_i n_i \,\mathrm{d}s &= \int_{\phi=0} f_i n_i \left|\nabla\psi\right|^{-1} \mathrm{d}x' \\ &= \int_\Omega \delta\left(\phi\right) f_i \frac{\partial \phi}{\partial x_i} \left(\left|\nabla\psi\right| \left|\nabla\phi\right|\right)^{-1} \mathrm{d}x' \,\mathrm{d}y', \\ &= \int_\Omega \delta\left(\phi\right) f_i \frac{\partial \phi}{\partial x_i} \,\mathrm{d}\boldsymbol{x} = -\int_\Omega f_i \frac{\partial \gamma^S}{\partial x_i} \,\mathrm{d}\boldsymbol{x}, \end{aligned} \tag{2.83}$$

where the definition of the normal vector (2.76), the determinant (2.81) and equation (2.82) are used. Due to the non-overlapping condition (2.26) and the definition of ϕ in (2.74), the function ϕ and the specific element ϕ_p of the $\boldsymbol{\phi}$ vector are equivalent at a particle p. Thus, the transformation derived in (2.83) can be applied to surface integrals of the following form

$$\int_{\Gamma_p} f_i n_{ip} \,\mathrm{d}s = \int_\Omega \delta\left(\phi_p\right) f_i \frac{\partial \phi_p}{\partial x_i} = -\int_\Omega f_i \frac{\partial \gamma_p}{\partial x_i} \,\mathrm{d}\boldsymbol{x} \tag{2.84}$$

for the individual particles. Thus, it is possible to apply the level-set method to the Newton-Euler equations. The translational equation (2.54) with transformed integrals is

$$V^P \mathfrak{D} \frac{\mathrm{d}v_{ip}}{\mathrm{d}t} = -\int \tau^F_{ij} \frac{\partial \gamma_p}{\partial x_j} \,\mathrm{d}\boldsymbol{x}, \tag{2.85}$$

and the rotational equation (2.55) becomes in three dimensions

$$\Theta^S_{ij} \frac{\mathrm{d}\omega_{jp}}{\mathrm{d}t} + \epsilon_{ijk} \Theta^S_{kl} \omega_{jp} \omega_{lq} \gamma_q = -\int \epsilon_{ijk} \left(x_j - \chi_{jq}\gamma_q\right) \tau^F_{kl} \frac{\partial \gamma_p}{\partial x_l} \,\mathrm{d}\boldsymbol{x}. \tag{2.86}$$

The rotational Newton-Euler equation in the two-dimensional case reads

$$\Theta^S \frac{\mathrm{d}\omega_p}{\mathrm{d}t} = -\int \epsilon_{3ij} \left(x_i - \chi_{iq}\gamma_q\right) \tau^F_{jk} \frac{\partial \gamma_p}{\partial x_k} \,\mathrm{d}\boldsymbol{x}. \tag{2.87}$$

2.3.4. Single field velocity description

The indicator functions for the solid phase (2.32) and the fluid phase (2.33) can be used to define a global single-field velocity in two dimensions

$$U_i = \gamma^F u^F_i + \gamma^S u^S_i = \gamma^F u^F_i + \gamma_p \left(v_{ip} + \epsilon_{i3k} \omega_p \left(x_k - \chi_{kq}\gamma_q\right)\right), \tag{2.88}$$

where u^F_i and u^S_i (Eq. (2.51)) are the local fluid and solid phase velocities. The ansatz has been introduced by Deußen et al. [51], a publication which will be followed closely in this section. The following derivation is done for two spatial dimensions, hence, the rotational velocity ω_p and the orientation angle β_p are vector variables. In case of three dimensions it is necessary to extend the rotational velocity to a vector for a single particle and a second order tensor ω_{ip} for the combined particle phase. Due to the non-overlap condition (2.26) of the particles, both γ_p and γ_q in (2.88) refer to the same particle despite different indices, which are necessary to fulfil Einstein's summation convention. The material derivative of (2.88) is

$$\begin{aligned}\frac{\mathrm{d}U_i}{\mathrm{d}t} &= \gamma^F \frac{\mathrm{d}u_i^F}{\mathrm{d}t} + u_i^F \frac{\mathrm{d}\gamma^F}{\mathrm{d}t} + \gamma^S \frac{\mathrm{d}u_i^S}{\mathrm{d}t} + u_i^S \frac{\mathrm{d}\gamma^S}{\mathrm{d}t} \\ &= \gamma^F \frac{\mathrm{d}u_i^F}{\mathrm{d}t} + \gamma_p \left(\frac{\mathrm{d}v_{ip}}{\mathrm{d}t} + \epsilon_{i3j} \frac{\mathrm{d}\omega_p}{\mathrm{d}t} \left(x_j - \chi_{jq}\gamma_q\right) \right) - \left(\gamma_p \omega_p\right)^2 \left(x_i - \chi_{iq}\gamma_q\right), \end{aligned} \tag{2.89}$$

where (2.78) was used to eliminate the derivatives of the indicator functions $\mathrm{d}\gamma^F/\,\mathrm{d}t$ and $\mathrm{d}\gamma^S/\,\mathrm{d}t$. The goal of the following considerations is to express each term in (2.89) in terms of the single field velocity U_i. The material derivatives $\mathrm{d}u_i^F/\,\mathrm{d}t$, $\mathrm{d}v_{ip}/\,\mathrm{d}t$ and $\mathrm{d}\omega_p/\,\mathrm{d}t$ can be expressed via the Navier Stokes equation (2.67) or unsteady Stokes equation (2.68) and Newton-Euler equations (2.54), (2.55) respectively. However, in (2.89) the rotational velocity ω_p occurs directly, which cannot expressed by any of the aforementioned equations. Consider ${}_1x_i$ to be an arbitrary point within a particle p, then the velocity of the same particle at the centre of mass is

$${}_1v_i{}^S = \lim_{{}_2\boldsymbol{x} \to \boldsymbol{\chi} \cdot {}_1\boldsymbol{\gamma}} {}_2U_i = \int \delta\left({}_2\boldsymbol{x} - \boldsymbol{\chi} \cdot {}_1\boldsymbol{\gamma}\right) {}_2U_i \,\mathrm{d}\,{}_2\boldsymbol{x}, \tag{2.90}$$

i.e. the translational velocity of the particle. Subsequently, the rotational velocity ${}_1\omega_p$ of the particle at ${}_1x_i$ is

$$\begin{aligned}{}_1\omega_p &= {}_1\gamma_p \frac{\epsilon_{3ij} r_i}{|\boldsymbol{r}|^2} \left({}_1U_j - {}_1v_i^S\right) \\ &= {}_1\gamma_p \frac{\epsilon_{3ij}\left({}_1x_i - \chi_{iq}\,{}_1\gamma_q\right)}{\left|{}_1\boldsymbol{x} - \boldsymbol{\chi} \cdot {}_1\boldsymbol{\gamma}\right|^2} \left({}_1U_j - {}_1v_i{}^S\right) \\ &= {}_1\gamma_p \frac{\epsilon_{3ij}\left({}_1x_i - \chi_{iq}\,{}_1\gamma_q\right)}{\left|{}_1\boldsymbol{x} - \boldsymbol{\chi} \cdot {}_1\boldsymbol{\gamma}\right|^2} \left({}_1U_j - \int \delta\left({}_2\boldsymbol{x} - \boldsymbol{\chi} \cdot {}_1\boldsymbol{\gamma}\right) {}_2U_j \,\mathrm{d}\,{}_2\boldsymbol{x}\right). \end{aligned} \tag{2.91}$$

The single field velocity U_i is defined for the entire domain Ω, thus, the boundary conditions defined at the particle surface for the fluid domain Ω^F are positioned inside Ω and take the form of continuity and jump conditions. The passive particle boundary is a no-slip wall (2.40) hence, the single field velocity U_i is continuous at the interface

$${}_1U_i = \lim_{{}_2\boldsymbol{x} \to {}_1\boldsymbol{x}} {}_2U_i \quad \forall\, {}_1\boldsymbol{x} \in \Gamma^{pa}. \tag{2.92}$$

Similarly for the condition of an impermeable active surface (2.41) one obtains

$${}_1U_i\,{}_1n_i = \lim_{{}_2\boldsymbol{x} \to {}_1\boldsymbol{x}} {}_2U_i\,{}_2n_i \quad \forall\, {}_1\boldsymbol{x} \in \Gamma^{ac}. \tag{2.93}$$

While the velocity in normal direction is continuous, a slip velocity exists in tangential direction, permitted by the active stress. The active stress acts as a source of momentum for the fluid phase, subsequently, we define the active source term by using the level-set approach outlined in Sec. 2.3.3. The non-dimensional active force $\mathfrak{A}_i^c$ exerted by the particle on the fluid is obtained by a surface integration

$$\mathfrak{A}_i^c = \mathfrak{A}^c e_{ip}\gamma_p = \int_{\Gamma^{ac}} A^c t_i \,\mathrm{d}s = \int \delta\left(\boldsymbol{x} - \Gamma^{ac}\right) A^c t_i \,\mathrm{d}\boldsymbol{x}, \tag{2.94}$$

where $\mathfrak{A}^c$ is the magnitude of the active force, defined by

$$\mathfrak{A}^c = \frac{2aA^c}{\varepsilon} \int_{\frac{\pi}{2}}^{\pi} \sin(\theta) \sqrt{\varepsilon^2 \sin^2(\theta) + \cos^2(\theta)} \, \mathrm{d}\theta \tag{2.95}$$

in two dimensions. Here, the elliptical integral is carried out with respect to the polar angle θ (Fig. 2.2) within the interval $[\pi/2, \pi]$, which includes the entire active surface of the particle. By adding (2.94) as a source to the integral form of the Navier-Stokes equation one obtains

$$\int_{\Omega^F} \frac{\mathrm{d}u_i^F}{\mathrm{d}t} - \frac{\partial \tau_{ij}^F}{\partial x_j} - \delta\left(\boldsymbol{x} - \Gamma^{ac}\right) A^c t_i \gamma_p \, \mathrm{d}\boldsymbol{x} = 0. \tag{2.96}$$

For a valid choice for the source term, Γ^{ac} is defined on all points at the active interface within the fluid domain, where the fact was used that Ω^F is a closed set, see (2.29). Eq. (2.96) together with the Newtonian stress tensor (2.62) and the Reynolds number (1.1) yields the differential form

$$\frac{\mathrm{d}u_i^F}{\mathrm{d}t} = \frac{\partial \tau_{ij}^F}{\partial x_j} + \delta\left(\boldsymbol{x} - \Gamma^{ac}\right) A^c t_i = -\frac{\partial p^F}{\partial x_i} + \frac{1}{\mathrm{Re}} \frac{\partial^2 u_i^F}{\partial x_j^2} + A_i, \tag{2.97}$$

which will be call active Navier-Stokes equation with the active source term

$$A_i = \delta\left(\boldsymbol{x} - \Gamma^{ac}\right) A^c t_i. \tag{2.98}$$

Again by neglecting the convective term, one obtains the active unsteady Stokes equation

$$\frac{\partial u_i^F}{\partial t} = -\frac{\partial p^F}{\partial x_i} + \frac{1}{\mathrm{Re}} \frac{\partial^2 u_i^F}{\partial x_j^2} + A_i, \tag{2.99}$$

which, in the steady case, becomes

$$0 = -\frac{\partial p^F}{\partial x_i} + \frac{1}{\mathrm{Re}} \frac{\partial^2 u_i^F}{\partial x_j^2} + A_i, \tag{2.100}$$

Using the active Navier-Stokes equation (2.97) and the Newton-Euler equations (2.54) and (2.55) to express the temporal derivatives in (2.89) delivers the momentum balance for the entire suspension

$$\begin{aligned}
\frac{\mathrm{d}\,{}_1U_i}{\mathrm{d}t} = {}_1\gamma^F \left(\frac{\partial\,{}_1\tau_{ij}}{\partial\,{}_1x_j} {}_1x_j + \delta\left({}_1\boldsymbol{x} - \Gamma^{ac}\right) A^c \left(n_i n_j e_{jp} - e_{ip}\right) \gamma_p \right) - {}_1\gamma_p \Bigg[\frac{1}{V^P \mathfrak{D}} \int {}_2\tau_{ij} \frac{\partial\,{}_2\gamma_p}{\partial\,{}_2x_j} \, \mathrm{d}\,{}_2\boldsymbol{x} \\
+ \epsilon_{i3k} \frac{\left({}_1x_k - \chi_{kr}\,{}_1\gamma_r\right)}{\Theta^S} \int \epsilon_{3ij} \left({}_2x_i - \chi_{iq}\,{}_2\gamma_q\right) {}_2\tau_{jk} \frac{\partial\,{}_2\gamma_p}{\partial x_j} {}_2x_k \, \mathrm{d}\,{}_2\boldsymbol{x} \\
+ \left({}_1\gamma_p \frac{\epsilon_{3jk}\left({}_1x_j - \chi_{jq}\,{}_1\gamma_q\right)}{\left|{}_1\boldsymbol{x} - \boldsymbol{\chi} \cdot {}_1\boldsymbol{\gamma}\right|^2} \left({}_1U_k - \int \delta\left({}_2\boldsymbol{x} - \boldsymbol{\chi} \cdot {}_1\boldsymbol{\gamma}\right) {}_2U_k \, \mathrm{d}\,{}_2\boldsymbol{x} \right) \right)^2 \left({}_1x_i - \chi_{ir}\,{}_1\gamma_r\right) \Bigg],
\end{aligned} \tag{2.101}$$

which contains the single-field velocity U_i and the particle position tensor χ_{ip} as unknown variables. Additionally, the orientation β_p enters (2.101) via Γ^{ac} and e_{ip}. The equation is closed by the equations for the evolution of the particle position (2.46) and orientation (2.47).

To obtain a relation for the conservation of mass the divergence of the single field velocity is formed, leading to

$$\begin{aligned}\frac{\partial U_i}{\partial x_i} &= \frac{\partial \gamma^F u_i^F}{\partial x_i} + \frac{\partial \gamma_p u_{ip}}{\partial x_i} \\ &= \gamma^F \frac{\partial u_i^F}{\partial x_i} + \gamma_p \frac{\partial u_{ip}}{\partial x_i} + u_i^F \frac{\partial \gamma^F}{\partial x_i} + u_{ip} \frac{\partial \gamma_p}{\partial x_i} \\ &= \gamma^F \frac{\partial u_i^F}{\partial x_i} + \gamma_p \frac{\partial u_{ip}}{\partial x_i} + u_i^F \sum_{p=1}^{N} \delta\left(\phi_p\right) \frac{\partial \phi_p}{\partial x_i} - u_{ip} \delta\left(\phi_p\right) \frac{\partial \phi_p}{\partial x_i} \\ &= \gamma^F \frac{\partial u_i^F}{\partial x_i} + \gamma_p \frac{\partial u_{ip}}{\partial x_i} + [\![U_i n_i]\!] \, \delta\left(\phi\right) = 0, \end{aligned} \tag{2.102}$$

where the continuity equations for the fluid phase (2.65) and the solid phase (2.50) and the impermeability of the particle surface

$$u_i^F n_i = u_i^S n_i \quad \Rightarrow \quad [\![U_i n_i]\!] = 0 \tag{2.103}$$

are used. The brackets $[\![\mathfrak{u}]\!] = \mathfrak{u}^F - \mathfrak{u}^S$ indicate a jump of the enclosed variable $\mathfrak{u}$.

3. Lie symmetry analysis in the physical and sample space

In this section the theoretical foundation for the examination of the classical and statistical symmetries in the context of an active suspension is established. Sophus Lie first applied the concept of a symmetry transformation to differential equations, which is employed here to generate insights about the behaviour of an active suspension [137, 138, 139]. Basic definitions and transformation rules for a symmetry transformation are introduced in Sec. 3.1, including the introduction of invariant solutions in Sec. 3.1.2.

The physical behaviour of an active suspension is described by the balance equations introduced in the previous section. The equations describing the fluid are examined based on their symmetries in Sec. 3.2. The fluid is either described by the Navier-Stokes equation (2.67) or the Stokes equation, where one might choose the steady (2.17) or unsteady (2.68) version. To describe the motion of the rigid particles, the Newton-Euler equations (2.54) and (2.55) are sufficient. The symmetries of the full system are subsequently discussed in Sec. 3.3.

The aforementioned equations describe the Euclidean physical space, i.e. the outcome of an individual experiment. The sample space on the other hand contains all outcomes of an ensemble of experiments in the form of probabilities. A description of an active suspension in the sample space based on PDFs is established in Sec. 3.4. The symmetries of the resulting hierarchy of transport equations are presented in Sec. 3.5. The set comprises new statistical symmetries, which are not present in the physical description of the suspension, see Sec. 3.6. Nevertheless, they describe important patterns of behaviour, visible in the physical space. Both statistical and classical symmetries are later used to analyse data obtained by simulations, see Sec. 6.

3.1. Lie-Symmetries

A symmetry is, generally speaking, an operation to map a certain object onto itself. The nature of this object is not specified, most commonly the term is applied to geometric objects. For example the rotation of a cylinder around its centreline is a symmetry transformation because the result is a cylinder with the exact same properties. An equivalent concept can be applied to mathematical expressions, especially but not exclusively to differential equations. Let

$$F_k\left(\boldsymbol{x}, \boldsymbol{y}, \boldsymbol{y}_1, \boldsymbol{y}_2, ..., , \boldsymbol{y}_N\right) = 0, \quad k = 1, 2, ..., K \tag{3.1}$$

be as system of K differential equations with the independent variables $\boldsymbol{x}$, the dependent variables $\boldsymbol{y}$ and the derivatives $\boldsymbol{y}_n$ up to Nth order

$$\begin{aligned}\boldsymbol{y}_1 &= \left[\frac{\partial y_1}{\partial x_1}, \frac{\partial y_1}{\partial x_2}, \ldots, \frac{\partial y_i}{\partial x_j}, \ldots\right], \\ \boldsymbol{y}_2 &= \left[\frac{\partial^2 y_1}{\partial x_1^2}, \frac{\partial y_1}{\partial x_1 \partial x_2}, \ldots, \frac{\partial^2 y_i}{\partial x_j \partial x_k}, \ldots\right] \\ \ldots.\end{aligned} \tag{3.2}$$

A transformation

$$T_\alpha : \quad x_i^* = \Phi_i\left(\boldsymbol{x}, \boldsymbol{y}, \alpha\right), \quad y_i^* = \Psi_i\left(\boldsymbol{x}, \boldsymbol{y}, \alpha\right) \tag{3.3}$$

is called a symmetry acting on $[\boldsymbol{x}, \boldsymbol{y}]$ if the resulting system of equations

$$F_k\left(\boldsymbol{x}^*, \boldsymbol{y}^*, \boldsymbol{y}_1^*, \boldsymbol{y}_2^*, \ldots, , \boldsymbol{y}_N^*\right) = 0 \quad \Leftrightarrow \quad F_k\left(\boldsymbol{x}, \boldsymbol{y}, \boldsymbol{y}_1, \boldsymbol{y}_2, \ldots, , \boldsymbol{y}_N\right) = 0 \tag{3.4}$$

has the same form as (3.1), i.e. (3.1) is form invariant under the transformation (3.3). A group G is a set of elements α, β, $\gamma, \ldots$ together with a binary operation $(*)$ [28]. The construct G needs to satisfy a number of conditions in order to be called a group [28, 89]:

- the result of the operation $(*)$ applied to two elements of the group is another element of the group $\alpha * \beta = \gamma$,
- the operation $(*)$ is associative, i.e. $\alpha * (\beta * \gamma) = (\alpha * \beta) * \gamma$,
- the group G contains a unique identity element I which maps any element of G onto itself $\alpha \, * \, I = I \, * \alpha = \alpha$,
- the group G contains for any element α a unique inverse element α^{-1} such that $\alpha * \alpha^{-1} = \alpha^{-1} * \alpha = I$.

Let the variables $[\boldsymbol{x}, \boldsymbol{y}]$ of F_k lie within a region $D \subset \mathbb{R}^n$. The set of transformations (3.3) with the parameter $\alpha \in S \subset \mathbb{R}$ and the operation $(*)$ form a one-parameter Lie group if [28, 106, 159]

- the set S and the operation $(*)$ form a group G,
- the transformations (3.3) map $[\boldsymbol{x}, \boldsymbol{y}] \in D$ onto $[\boldsymbol{x}^*, \boldsymbol{y}^*]$, where the transformed variables also lie within D,
- the parameter $\alpha \in S$ is continuos, i.e. S is an interval on $\mathbb{R}$,
- the successive application of the transformations

  $$\begin{aligned}T_\alpha : &\quad x_i^* = \Phi_i\left(\boldsymbol{x}, \boldsymbol{y}, \alpha\right), \quad y_i^* = \Psi_i\left(\boldsymbol{x}, \boldsymbol{y}, \alpha\right), \\ T_\beta : &\quad x_i^{**} = \Phi_i\left(\boldsymbol{x}^*, \boldsymbol{y}^*, \beta\right), \quad y_i^{**} = \Psi_i\left(\boldsymbol{x}^*, \boldsymbol{y}^*, \beta\right)\end{aligned}$$

  yields $\quad T_\gamma : \quad x_i^{**} = \Phi_i\left(\boldsymbol{x}, \boldsymbol{y}, \gamma = \alpha * \beta\right), \quad y_i^{**} = \Psi_i\left(\boldsymbol{x}, \boldsymbol{y}, \gamma = \alpha * \beta\right)$,
- $\gamma = \alpha * \beta$ is an analytical function of $\alpha \in S$ and $\beta \in S$,
- Φ_i and Ψ_i are infinitely differentiable with respect to $[\boldsymbol{x}, \boldsymbol{y}]$ in a region D and analytical functions of the group parameter α.

Without loss of generality $\alpha = 0$ corresponds to the identity element. A Taylor expansion of (3.3) with respect to the group parameter α yields

$$x_i^* = \Phi_i\left(\boldsymbol{x}, \boldsymbol{y}, \alpha = 0\right) + \alpha \left.\frac{\partial \Phi_i\left(\boldsymbol{x}, \boldsymbol{y}, \alpha\right)}{\partial \alpha}\right|_{\alpha=0} + \mathcal{O}\left(\alpha^2\right), \tag{3.5}$$

$$y_i^* = \Psi_i\left(\boldsymbol{x}, \boldsymbol{y}, \alpha = 0\right) + \alpha \left.\frac{\partial \Psi_i\left(\boldsymbol{x}, \boldsymbol{y}, \alpha\right)}{\partial \alpha}\right|_{\alpha=0} + \mathcal{O}\left(\alpha^2\right). \tag{3.6}$$

Due to the identity element $\alpha = 0$, one obtains the identity transformations [159]

$$\Phi_i\left(\boldsymbol{x}, \boldsymbol{y}, \alpha = 0\right) = x_i \quad \text{and} \quad \Psi_i\left(\boldsymbol{x}, \boldsymbol{y}, \alpha = 0\right) = y_i. \tag{3.7}$$

Furthermore, the infinitesimals

$$\xi_i\left(\boldsymbol{x}, \boldsymbol{y}\right) = \left.\frac{\partial \Phi_i\left(\boldsymbol{x}, \boldsymbol{y}, \alpha\right)}{\partial \alpha}\right|_{\alpha=0}, \quad \eta_i\left(\boldsymbol{x}, \boldsymbol{y}\right) = \left.\frac{\partial \Psi_i\left(\boldsymbol{x}, \boldsymbol{y}, \alpha\right)}{\partial \alpha}\right|_{\alpha=0} \tag{3.8}$$

are introduced. Following Lie's first theorem, the infinitesimals uniquely define the global form (3.3) of the symmetry transformation [159]. Eqs. (3.5) and (3.6) can be reformulated

$$x_i^* = x_i + \alpha \xi_i + \mathcal{O}\left(\alpha^2\right), \quad y_i^* = y_i + \alpha \eta_i + \mathcal{O}\left(\alpha^2\right). \tag{3.9}$$

Eq. (3.8) together with the definition of the transformation (3.3) leads to [159]

$$\left.\frac{\partial x_i^*}{\partial \alpha}\right|_{\alpha=0} = \xi_i\left(\boldsymbol{x}^*, \boldsymbol{y}^*\right), \quad \left.\frac{\partial y_i^*}{\partial \alpha}\right|_{\alpha=0} = \eta_i\left(\boldsymbol{x}^*, \boldsymbol{y}^*\right). \tag{3.10}$$

In a geometrical interpretation, the vector formed by the infinitesimals $[\xi_i, \eta_i]$ is tangential to the differentiable curve defined by Φ_i and Ψ_i in a C^∞ manifold. Any tangential vector field can be expressed by the directional derivative [106]

$$\mathfrak{X} = \xi_i\left(\boldsymbol{x}, \boldsymbol{y}\right) \frac{\partial}{\partial x_i} + \eta_i\left(\boldsymbol{x}, \boldsymbol{y}\right) \frac{\partial}{\partial y_i}, \tag{3.11}$$

called infinitesimal generator or Lie operator. The system F_k is, hence, invariant under the transformation (3.3) if the directional derivative of F_k vanishes [106]

$$\mathfrak{X} F_k|_{F_k=0} = 0. \tag{3.12}$$

A proof for the equivalence of (3.4) and (3.12) can be found in Appendix A.1. The operator (3.11) only considers the independent and dependent variables, however, the action of the transformation on the derivatives of the dependent variables is yet unknown. In the next section the transformation of the derivatives is introduced and the definition of the operator is extended to account for said derivatives.

3.1.1. Prolonged operator

The total differential operator is defined as [28]

$$\frac{D}{Dx_i} = \frac{\partial}{\partial x_i} + y_{j,x_i} \frac{\partial}{\partial y_j} + y_{j,x_i,x_k} \frac{\partial}{\partial y_{j,x_k}} + \ldots . \tag{3.13}$$

Here, the notation

$$y_{j,x_i} = \frac{\partial y_j}{\partial x_i}, \quad y_{j,x_i,x_k} = \frac{\partial^2 y_j}{\partial x_i \partial x_k}, \dots \tag{3.14}$$

for the derivatives is introduced, i.e. the derivatives are treated as variables similar to y_i. Such an extension of the space of independent and dependent variables $[\boldsymbol{x}, \boldsymbol{y}]$ to also include the derivatives $[\boldsymbol{x}, \boldsymbol{y}, \boldsymbol{y}_1, \dots, \boldsymbol{y}_N]$ up to a finite order N, is called jet space [28]. Analogously to (3.13), the transformed total operator is defined as

$$\frac{D}{Dx_i^*} = \frac{\partial}{\partial x_i^*} + y_{j,x_i}^* \frac{\partial}{\partial y_j^*} + y_{j,x_i,x_k}^* \frac{\partial}{\partial y_{j,x_k}^*} + \dots . \tag{3.15}$$

Both operators are connected by the chain rule

$$\frac{D}{Dx_i} = J_{ji} \frac{D}{Dx_j^*} \tag{3.16}$$

where $J_{ji} = D\Phi_j / Dx_i$ is the Jacobian matrix of Φ_i. Applying (3.16) to the transformed variable $y_i^* = \Psi_i$ delivers the transformed first order derivative

$$y_{i,x_j}^* = \Psi_{i,x_j} = J_{kj}^{-1} \frac{D\Psi_i}{Dx_k}. \tag{3.17}$$

Higher order derivatives are obtained by applying (3.17) recursively [28],

$$y_{i,x_{k_1},\dots,x_{k_N}}^* = \Psi_{i,x_{k_1},\dots,x_{k_N}} = J_{ji}^{-1} \frac{D\Psi_{i,x_{k_1},\dots,x_{k_{N-1}}}}{Dx_{k_N}}. \tag{3.18}$$

Instead of the application of a matrix it is favourable to directly transform the derivatives analogously to the independent and dependent variables, see (3.5) and (3.6). The infinitesimals of the derivatives of $\boldsymbol{y}$ are

$$\begin{aligned} y_{i,x_j}^* &= \Psi_{i,x_j}\left(\boldsymbol{x}, \boldsymbol{y}, \boldsymbol{y}_1, \alpha = 0\right) + \alpha \left.\frac{\partial \Psi_{i,x_j}\left(\boldsymbol{x}, \boldsymbol{y}, \boldsymbol{y}_1, \alpha\right)}{\partial \alpha}\right|_{\alpha=0} + \mathcal{O}\left(\alpha^2\right) \\ &= y_{i,x_j} + \alpha \eta_{i,j} + \mathcal{O}\left(\alpha^2\right), && (3.19) \\ y_{i,x_j,x_k}^* &= \Psi_{i,x_j,x_k}\left(\boldsymbol{x}, \boldsymbol{y}, \boldsymbol{y}_1, \boldsymbol{y}_2, \alpha = 0\right) + \alpha \left.\frac{\partial \Psi_{i,x_j,x_k}\left(\boldsymbol{x}, \boldsymbol{y}, \boldsymbol{y}_1, \boldsymbol{y}_2, \alpha\right)}{\partial \alpha}\right|_{\alpha=0} + \mathcal{O}\left(\alpha^2\right) \\ &= y_{i,x_j,x_k} + \alpha \eta_{i,j,k} + \mathcal{O}\left(\alpha^2\right) && (3.20) \\ &\dots . \end{aligned}$$

Any infinitesimal $\eta_{i,k_1,k_2,\dots,k_N}$ related to the Nth order derivative $y_{i,x_{k_1},x_{k_2},\dots,x_{k_N}}$ can be calculated by

$$\eta_{i,k_1,k_2,\dots,k_N} = \frac{D\eta_{i,x_{k_1},x_{k_2},\dots,x_{k_{N-1}}}}{Dx_{k_N}} - y_{i,x_{k_1},x_{k_2},\dots,x_j} \frac{D\xi_j}{Dx_{k_N}}, \tag{3.21}$$

which is derived in the appendix (App. A.1.2). The new infinitesimals can be used to construct a prolonged operator

$$\mathfrak{X}_N = \xi_i \frac{\partial}{x_i} + \eta_i \frac{\partial}{\partial y_i} + \eta_{i,x_j} \frac{\partial}{\partial y_{i,x_j}} + \dots + \eta_{i,k_1,k_2,\dots,k_N} \frac{\partial}{\partial y_{i,x_{k_1},x_{k_2},\dots,x_{k_N}}}, \tag{3.22}$$

which again describes the tangent space at any point $[\boldsymbol{x}, \boldsymbol{y}, \boldsymbol{y}_1, ..., \boldsymbol{y}_N]$. A Lie-transformation group G exists if the system $\boldsymbol{F}\left(\boldsymbol{x}, \boldsymbol{y}, \boldsymbol{y}_1, \boldsymbol{y}_2, ..., , \boldsymbol{y}_N\right) = 0$ is invariant under the action of the prolonged operator $\mathfrak{X}_N$, see for reference Def. 1.4 in Ibragimov [106]. Hence, to obtain the infinitesimals it is necessary to solve

$$\mathfrak{X}_N \left. F_k\right|_{F_k=0} = 0, \quad k = 1, 2, ..., K, \tag{3.23}$$

in analogy to (3.12), which in practice is often delegated to a computer algebra system. It is important to note that all variables in the jet space, including the derivatives $\boldsymbol{y}_1, \boldsymbol{y}_2, ..., , \boldsymbol{y}_N$, need to be treated as independent variables when applying the prolonged operator [159]. Once (3.23) is solved, the resulting infinitesimals ξ_i and η_i can be used to determine the global form of the symmetry transformation by applying (3.10). In conclusion, (3.23) can be viewed as a determining equation allowing one to obtain the symmetries of the differential equation system F_k.

In the following example the process of obtaining a symmetry transformation is reversed. A known transformation is chosen and it is shown that it fulfils (3.23). Applying the rotational operator $\nabla\times$ to the unsteady Stokes equation (2.68) delivers the vorticity equation. In two dimensions this is a scalar equation

$$F\left(\boldsymbol{x}, t, \omega^F, \omega^F_t, \omega^F_{x_j,x_j}\right) = \omega^F_t - \frac{1}{\mathrm{Re}}\omega^F_{x_j,x_j} = 0, \tag{3.24}$$

which is equivalent to the heat equation. The occurring variables are the vorticity ω^F and its derivatives ω^F_t and $\omega^F_{x_i,x_j}$ according to the previously introduced notation. The scaling

$$T_{\mathrm{Sc4}}: \quad t^* = e^{2c_{\mathrm{Sc4}}}t, \quad x_i^* = e^{c_{\mathrm{Sc4}}}x_i, \quad \omega^{F*} = e^{-c_{\mathrm{Sc4}}}\omega^F \tag{3.25}$$

is a symmetry of (3.24), see Ibragimov [106]. Here, c_{Sc4} is the group parameter. The infinitesimals are calculated by

$$\xi_t = \left.\frac{\partial t^*}{\partial c_{\mathrm{Sc4}}}\right|_{c_{\mathrm{Sc4}}=0} = 2t, \quad \xi_{x_i} = \left.\frac{\partial x_i^*}{\partial c_{\mathrm{Sc4}}}\right|_{c_{\mathrm{Sc4}}=0} = x_i, \quad \eta_\omega = \left.\frac{\partial \omega^{F*}}{\partial c_{\mathrm{Sc4}}}\right|_{c_{\mathrm{Sc4}}=0} = -\omega^F. \tag{3.26}$$

The infinitesimals of the derivatives are obtained using (3.21) and read

$$\eta_{\omega,t} = -3\omega^F_t, \quad \eta_{\omega,x_i,x_i} = -3\omega^F_{x_i,x_i}, \tag{3.27}$$

leading to the prolonged operator

$$\mathfrak{X} = 2t\frac{\partial}{\partial t} + x_i\frac{\partial}{\partial x_i} - \omega^F\frac{\partial}{\partial \omega^F} - 3\omega^F_t\frac{\partial}{\partial \omega^F_t} - 3\omega^F_{x_i,x_i}\frac{\partial}{\partial \omega^F_{x_i,x_i}}. \tag{3.28}$$

Using (3.12) together with (3.28) and (3.24) yields

$$\mathfrak{X}F\left.\left(\boldsymbol{x}, t, \omega^F, \omega^F_t, \omega^F_{x_j,x_j}\right)\right|_{F=0} = 3\left[-\omega^F_t + \frac{1}{\mathrm{Re}}\omega^F_{x_i,x_i}\right]_{\left(\omega^F_t - \frac{1}{\mathrm{Re}}\omega^F_{x_i,x_i}\right)=0} = 0, \tag{3.29}$$

hence, the transformation (3.25) is indeed a symmetry of the vorticity equation (3.24).

3.1.2. Invariant solutions

The symmetries obtained from (3.23) can be used to construct similarity or invariant solutions $Y_k = y_k\left(\boldsymbol{x}\right)$. An expression Y_k is an invariant solution if the auxiliary function $H_k = Y_k - y_k\left(\boldsymbol{x}\right)$ is invariant under the action of the prolonged operator X_N and if Y_k solves F_k [28]. Thus, the equation

$$\mathfrak{X}_N H_k|_{H_k=0} = 0. \tag{3.30}$$

yields possible invariant solutions of the system of differential equations F_k. Invariant solutions obtained from the symmetries presented in the following sections are used to analyse data obtained from simulations as presented in Sec. 6.

3.2. Symmetries of the Navier-Stokes equation and the Stokes equation

The symmetries of the Navier-Stokes equations were first derived by Bytev [37]. The transformation group in the form given by Bytev [37] and Klingenberg et al. [119] for the single-phase problem are

$$\begin{aligned}
T_t: &\quad t^* = t + c_t, \quad x_i^* = x_i, \quad u_i^{F*} = u_i^F, \quad p^{F*} = p^F, && (3.31a)\\
T_{\text{Rot}}: &\quad t^* = t, \quad x_i^* = Q_{ij}x_j, \quad u_i^{F*} = Q_{ij}u_i^F, \quad p^{F*} = p^F, && (3.31b)\\
T_{\text{G}}: &\quad t^* = t, \quad x_i^* = x_i + f_{\text{G},i}\left(t\right), \quad u_i^{F*} = u_i^F + f'_{\text{G},i}\left(t\right), \quad p^{F*} = p^F - x_i f''_{\text{G},i}\left(t\right), && (3.31c)\\
T_p: &\quad t^* = t, \quad x_i^* = x_i, \quad u_i^{F*} = u_i^F, \quad p^{F*} = p^F + f_p(t), && (3.31d)\\
T_{\text{Sc1}}: &\quad t^* = te^{2c_{\text{Sc1}}}, \quad x_i^* = x_i e^{c_{\text{Sc1}}}, \quad u_i^{F*} = u_i^F e^{-c_{\text{Sc1}}}, \quad p^{F*} = p^F e^{-2c_{\text{Sc1}}}, && (3.31e)
\end{aligned}$$

where the c_i denote group parameters and the f_i are free time-dependent functions. Each symmetry transformation is related to certain physical properties of the Navier-Stokes equation. The transformation T_t describes the invariance of the Navier-Stokes equation under a time shift. Hence, the outcome of an experiment is independent of the start time t_0. The rotation matrix in the symmetry T_{Rot}, which, in the two-dimensional case, reads

$$Q_{ij} = \begin{bmatrix} \cos\left(\varphi\right) & \sin\left(\varphi\right) \\ -\sin\left(\varphi\right) & \cos\left(\varphi\right) \end{bmatrix}, \tag{3.32}$$

is applied to the reference frame in case of T_{rot}. The entire coordinate system is rotated by the angle φ, where φ can be interpreted as group parameter. The generalised Galilean symmetry T_{G} transforms the spatial coordinate, the velocity and the pressure by applying a free function $f_{\text{G},i}\left(t\right)$, which might be time-dependent. Hence, the entire coordinate system moves with a velocity $f'_{\text{G},i}\left(t\right)$. As a special case it contains the spatial shift $f_{\text{G},i} = c_{\text{G},i}$. A second free function $f_p\left(t\right)$ is applied to the pressure in T_p. This transformation is related to the fact that the absolute value of the pressure can be chosen arbitrarily in an incompressible fluid. The last transformation T_{Sc1} is a scaling of the entire experiment. This is often exploited in order to simplify wind-tunnel experiments, because it makes possible a downsizing of the model under investigation. Furthermore, this scaling symmetry is equivalent to the principle of free choice of the system of units as well as the transformation of results between different systems. The Lie operators related to the symmetry transformations (3.31) are [107]

$$\mathfrak{X}_t = \frac{\partial}{\partial t}, \tag{3.33a}$$

$$\mathfrak{X}_{i,\mathrm{Rot}} = \epsilon_{jki} x_j \frac{\partial}{\partial x_k} + \epsilon_{jki} u_j^F \frac{\partial}{\partial u_k^F}, \tag{3.33b}$$

$$\mathfrak{X}_{\mathrm{G},i} = f_{\mathrm{G},i}\left(t\right) \frac{\partial}{\partial x_i} + f'_{\mathrm{G},i}\left(t\right) \frac{\partial}{\partial u_i^F} - x_i f''_{\mathrm{G},i}\left(t\right) \frac{\partial}{\partial p^F}, \tag{3.33c}$$

$$\mathfrak{X}_p = f_p\left(t\right) \frac{\partial}{\partial p^F}, \tag{3.33d}$$

$$\mathfrak{X}_{\mathrm{Sc1}} = 2t \frac{\partial}{\partial t} + x_i \frac{\partial}{\partial x_i} - u_i^F \frac{\partial}{\partial u_i^F} - 2p^F \frac{\partial}{\partial p^F}. \tag{3.33e}$$

The simplifications leading to the steady (2.17) and unsteady (2.68) Stokes equation also affect the symmetries. The partial time derivative is not Galilean invariant, hence, the general transformation T_G is not applicable to the unsteady Stokes equation because an additional term arises, i.e.

$$\frac{\partial u_i^F}{\partial t} = -\frac{\partial p^F}{\partial x_i} + \frac{1}{\mathrm{Re}} \frac{\partial^2 u_i^F}{\partial x_j^2} \Rightarrow \frac{\partial u_i^{F*}}{\partial t^*} + f'_{G,j}\left(t^*\right) \frac{\partial u_i^{F*}}{\partial x_j^*} = -\frac{\partial p^{F*}}{\partial x_i^*} + \frac{1}{\mathrm{Re}} \frac{\partial^2 u_i^{F*}}{\partial x_j^* \partial x_j^*}, \tag{3.34}$$

where (3.16) was used to obtain the transformation of the temporal derivative $\partial u_i^*/\partial t = \partial u_i^*/\partial t^* + f'_{G,j}\left(t\right) \partial u_i^*/\partial x_j^*$. In the case of the Navier-Stokes equation this additional term would vanish due to the convective term. Subsequently, the first derivative of $f_{\mathrm{G},i}$ needs to vanish, hence, T_G is a symmetry of the unsteady Stokes equation, only if $f_{\mathrm{G},i} = c_{\mathrm{G},i}$ is a constant. Interestingly, one obtains from (3.34), by assuming a steady system $\partial u_i^*/\partial t^* = 0$ with a single particle moving with the constant velocity $f'_{\mathrm{G},i} = \tilde{v}_i$, the Oseen equation [162]

$$\tilde{v}_j \frac{\partial u_i^F}{\partial x_j} = -\frac{\partial p^F}{\partial x_i} + \frac{1}{\mathrm{Re}} \frac{\partial^2 u_i^F}{\partial x_j^2}, \tag{3.35}$$

where the asterisk was omitted.

For the unsteady Stokes equation, while the generalised Galilean symmetry reduces to a constant spatial shift, additional symmetries arise due to the linearity of the equation. The full transformation group is

$$T_t: \quad t^* = t + c_t, \quad x_i^* = x_i, \quad u_i^{F*} = u_i^F, \quad p^{F*} = p^F, \tag{3.36a}$$

$$T_\mathrm{Rot}: \quad t^* = t, \quad x_i^* = Q_{ij} x_j, \quad u_i^{F*} = Q_{ij} u_i^F, \quad p^{F*} = p^F, \tag{3.36b}$$

$$T_\mathrm{G}: \quad t^* = t, \quad x_i^* = x_i + c_{\mathrm{G},i}, \quad u_i^{F*} = u_i^F, \quad p^{F*} = p^F, \tag{3.36c}$$

$$T_p: \quad t^* = t, \quad x_i^* = x_i, \quad u_i^{F*} = u_i^F, \quad p^{F*} = p^F + f_p(t), \tag{3.36d}$$

$$T_\mathrm{Sc2}: \quad t^* = t, \quad x_i^* = x_i, \quad u_i^{F*} = u_i^F e^{c_\mathrm{Sc2}}, \quad p^{F*} = p^F e^{c_\mathrm{Sc2}}, \tag{3.36e}$$

$$T_\mathrm{Sc3}: \quad t^* = t e^{2c_\mathrm{Sc3}}, \quad x_i^* = x_i e^{c_\mathrm{Sc3}}, \quad u_i^{F*} = u_i^F e^{c_\mathrm{Sc3}}, \quad p^{F*} = p^F, \tag{3.36f}$$

$$T_\mathrm{lin}: \quad t^* = t, \quad x_i^* = x_i, \quad u_i^{F*} = u_i^F + f_{i,u}\left(\boldsymbol{x}, t\right), \quad p^{F*} = p^F + f_p\left(\boldsymbol{x}, t\right). \tag{3.36g}$$

The transformations T_t, T_Rot, and T_p are the same as for the Navier-Stokes equation. The Galilean invariance T_G is reduced to a constant spatial shift $c_{\mathrm{G},i}$ due to (3.34) and explained in the latter. Furthermore, two additional scaling symmetries arise, where a combination of T_{Sc2} and T_{Sc3} delivers the classical scaling symmetry of the Navier-Stokes equation

$$\mathfrak{X}_{\text{Sc1}} = -2\mathfrak{X}_{\text{Sc2}} + \mathfrak{X}_{\text{Sc3}}, \tag{3.37}$$

where the operators $\mathfrak{X}_{\text{Sc2}}$ and $\mathfrak{X}_{\text{Sc3}}$ are given below in (3.38). The free functions $f_{i,u}(\boldsymbol{x},t)$ and $f_p(\boldsymbol{x},t)$ in the last transformation T_{lin} are solutions of the unsteady Stokes equation (2.68). Such symmetries occur in any linear equation and allow to construct solutions by a linear combination of other solutions, which is known as superposition principle. The Lie operators corresponding to the transformations (3.36) are

$$\mathfrak{X}_t = \frac{\partial}{\partial t}, \tag{3.38a}$$

$$\mathfrak{X}_{i,\text{Rot}} = \epsilon_{jki} x_j \frac{\partial}{\partial x_k} + \epsilon_{jki} u_j^F \frac{\partial}{\partial u_k^F}, \tag{3.38b}$$

$$\mathfrak{X}_{\text{G},i} = \frac{\partial}{\partial x_i}, \tag{3.38c}$$

$$\mathfrak{X}_p = f_p(t) \frac{\partial}{\partial p^F}, \tag{3.38d}$$

$$\mathfrak{X}_{\text{Sc2}} = u_i^F \frac{\partial}{\partial u_i^F} + p^F \frac{\partial}{\partial p^F}, \tag{3.38e}$$

$$\mathfrak{X}_{\text{Sc3}} = 2t\frac{\partial}{\partial t} + x_i \frac{\partial}{\partial x_i} + u_i^F \frac{\partial}{\partial u_i^F}, \tag{3.38f}$$

$$\mathfrak{X}_{\text{lin}} = f_{i,u}(\boldsymbol{x},t) \frac{\partial}{\partial u_i^F} + f_p(\boldsymbol{x},t) \frac{\partial}{\partial p^F}. \tag{3.38g}$$

The steady Stokes equation contains a set of symmetries similar to the symmetries of the unsteady Stokes equation (3.36). The time-dependent function of the generalised Galilean symmetry might depend linearly on time $f_{\text{G},i} = c_{\text{G},i} t$, because the derivative $\partial u_i^F / \partial t = 0$ needs to vanish for a steady problem. Subsequently, the transformation for T_{G} in the case of the steady Stokes equation reads

$$T_{\text{G}}: \quad t^* = t, \quad x_i^* = x_i + c_{\text{G},i} t, \quad U_i^* = U_i + c_{\text{G},i}, \quad p^{F*} = p^F, \tag{3.39}$$

while the other symmetries are identical to (3.36).

3.2.1. Symmetries of the vorticity equation

Applying the rotation operator $\nabla\times$ to the unsteady Stokes equation (2.68) delivers an equation for the vorticity of the fluid field

$$\frac{\partial \omega^F}{\partial t} = \frac{1}{\text{Re}} \frac{\partial^2 \omega^F}{\partial x_i^2}, \tag{3.40}$$

which is a scalar equation for two dimensional Stokes flows. As mentioned in example (3.24) the vorticity equation is equivalent to the linear heat equation whose symmetries are known, see Ibragimov [106]. The symmetries in two dimensions are

$$T_t: \quad t^* = t + c_t, \quad x_i^* = x_i, \quad \omega^{F*} = \omega^F, \tag{3.41a}$$

$$T_x: \quad t^* = t, \quad x_i^* = x_i + c_{x,i}, \quad \omega^{F*} = \omega^F, \tag{3.41b}$$

$$T_{\text{Rot}}: \quad t^* = t, \quad x_i^* = Q_{ij} x_j, \quad \omega^{F*} = \omega^F, \tag{3.41c}$$

$$T_{\text{G}}: \quad t^* = t, \quad x_i^* = x_i + 2tc_{\text{G},i} \quad \omega^{F*} = \omega^F e^{-(x_i + c_{\text{G},i} t) c_{\text{G},i}}, \tag{3.41d}$$

$$T_{\text{Sc}\omega}: \quad t^* = t, \quad x_i^* = x_i, \quad \omega^{F*} = \omega^F e^{c_\omega}, \tag{3.41e}$$

$$T_{\text{Sc4}}: \quad t^* = te^{2c_{\text{Sc4}}}, \quad x_i^* = x_i e^{c_{\text{Sc4}}}, \quad \omega^{F*} = \omega^F, \tag{3.41f}$$

$$T_\mu: \quad t^* = \frac{t}{1 - 4c_\mu t}, \quad x_i^* = \frac{x_i}{1 - 4c_\mu t}, \quad \omega^{F*} = \omega^F \left(1 - 4c_\mu t\right) e^{\frac{-c_\mu \left(x_1^2 + x_2^2\right)}{4t - 16c_\mu t^2}}, \tag{3.41g}$$

$$T_{\text{lin}}: \quad t^* = t, \quad x_i^* = x_i \quad \omega^{F*} = \omega^F + f_\omega\left(\boldsymbol{x}, t\right). \tag{3.41h}$$

The spatial coordinates x_1, x_2 are transformed independently of each other in any symmetry transformation given by (3.41). The first four symmetries are already known in primitive variables, i.e. a time shift T_t, a spatial shift T_x, a rotation T_{Rot} and a variant of the Galilean invariance T_{G}. It is especially interesting that the transformation for the spatial coordinate x_i in T_{G} depends linearly on time, whereas the counterpart in the case of the unsteady Stokes equation is not a function of the time. Both spatial coordinates in T_{G} are transformed independently from each other, i.e. the symmetry transformation for an individual component is equivalent to the one-dimensional transformation given by Ibragimov [106]. The invariant solution obtained with T_{G} in the one-dimensional case is [106]

$$\omega^F_{T_{\text{G}}} = \frac{C}{\sqrt{t}} e^{-\frac{x^2}{4t}}, \quad t > 0, \tag{3.42}$$

which differs from the fundamental solution of the heat equation only by a constant factor. $T_{\text{Sc}\omega}$ is a scaling symmetry for the vorticity and T_{Sc4} a scaling symmetry for the independent variables. The symmetry transformation T_μ differs from the equivalent transformation in the one-dimensional case given by Ibragimov [106]. Considering only a single spatial dimension yields

$$T_\mu: \quad t^* = \frac{t}{1 - 4c_\mu t}, \quad x_i^* = \frac{x_i}{1 - 4c_\mu t}, \quad \omega^{F*} = \omega^F \sqrt{1 - 4c_\mu t}\, e^{\frac{-c_\mu x_1^2}{1 - 4\mu t}}. \tag{3.43}$$

The symmetry describes dissipation and decay of the vorticity, which is revealed by the general invariant solution obtained form T_μ in the one-dimensional case [106]

$$\omega^F_{T_\mu} = t^{-\frac{1}{2}} e^{-\frac{x^2}{4t}} f\left(\frac{x}{t}\right). \tag{3.44}$$

The symmetry T_μ contains a singularity at $t = (4c_\mu)^{-1}$, which must be taken into account if invariant solutions are to be generated. The last transformation in (3.41) T_{lin} is again the general linear transformation, revealing the superposition principle, where $f_\omega\left(\boldsymbol{x}, t\right)$ is a solution of (3.40).

3.3. Lie symmetries for an active suspension

The system of equations describing an active suspension consists of the equations for the fluid and for the solid particle phase. The fluid is either described by the active Navier-Stokes equation (2.97) or the active unsteady (2.99) or steady (2.100) Stokes equation. In each of the aforementioned equations an additional term occurs to account for the source of momentum due to the active stress at the particle surface. Additionally the continuity equation (2.65) needs to be upheld. The particle phase is governed by the evolution equations for the particle position (2.46) and orientation (2.47) and the Newton-Euler equations (2.54) and (2.55), which describe the translational and rotational particle velocity. The fluid velocity u_i^F and the particle velocity u_i^S always transform in the same way in order not to violate the boundary conditions at the particle surface (2.40) and (2.41). Hence, the single-field velocity U_i, which combines the velocities of both phases, see (2.88), is used in the subsequent symmetries. Due to the occurrence of the radial vector $r_i = (x_i - \chi_{ip}\gamma_p)$ in the definition of the particle velocity (2.51) and in the rotational Newton-Euler equation (2.55), it is necessary that the spatial coordinate x_i and the particle position χ_{ip} obey identical transformations.

3.3.1. Navier-Stokes equation

In the case of an active suspension, the set of symmetry transformations of the Navier-Stokes equation (3.31) is extended to

$$\begin{aligned} T_t: \quad & t^* = t + c_t, \quad x_i^* = x_i, \quad U_i^* = U_i, \quad p^{F*} = p^F, \\ & \chi_{ip}^* = \chi_{ip}, \quad \beta_p^* = \beta_p, \quad A_i^* = A_i, \end{aligned} \tag{3.45a}$$

$$\begin{aligned} T_{\text{Rot}}: \quad & t^* = t, \quad x_i^* = Q_{ij}x_j, \quad U_i^* = Q_{ij}U_i, \quad p^{F*} = p^F, \\ & \chi_{ip}^* = Q_{ij}\chi_{jp}, \quad \beta_p^* = \beta_p - \varphi, \quad A_i^* = A_i, \end{aligned} \tag{3.45b}$$

$$\begin{aligned} T_{\text{G}}: \quad & t^* = t, \quad x_i^* = x_i + f_{\text{G},i}(t), \quad U_i^* = U_i + f'_{\text{G},i}(t), \quad p^{F*} = p^F - x_i f''_{\text{G},i}(t), \\ & \chi_{ip}^* = \chi_{ip} + f_{\text{G},i}(t)\gamma_p, \quad \beta_p^* = \beta_p, \quad A_i^* = A_i, \end{aligned} \tag{3.45c}$$

$$\begin{aligned} T_p: \quad & t^* = t, \quad x_i^* = x_i, \quad U_i^* = U_i, \quad p^{F*} = p^F + f_p(t), \\ & \chi_{ip}^* = \chi_{ip}, \quad \beta_p^* = \beta_p, \quad A_i^* = A_i, \end{aligned} \tag{3.45d}$$

$$\begin{aligned} T_{\text{Sc1}}: \quad & t^* = te^{2c_{\text{Sc1}}}, \quad x_i^* = x_i e^{c_{\text{Sc1}}}, \quad U_i^* = U_i e^{-c_{\text{Sc1}}}, \quad p^{F*} = p^F e^{-2c_{\text{Sc1}}}, \\ & \chi_{ip}^* = \chi_{ip} e^{c_{\text{Sc1}}}, \quad \beta_p^* = \beta_p, \quad A_i^* = A_i e^{-3c_{\text{Sc1}}}. \end{aligned} \tag{3.45e}$$

Two additional symmetries exist

$$\begin{aligned} T_\beta: \quad & t^* = t, \quad x_i^* = x_i, \quad U_i^* = U_i, \quad p^{F*} = p^F, \\ & \chi_{ip}^* = \chi_{ip}, \quad \beta_p^* = \beta_p + c_\beta, \quad A_i^* = A_i, \end{aligned} \tag{3.45f}$$

$$\begin{aligned} T_{\text{Ac}}: \quad & t^* = t, \quad x_i^* = x_i, \quad U_i^* = U_i + f_i^U(t)\,\delta(\boldsymbol{x} - \Gamma^{ac}), \quad p^{F*} = p^F, \\ & \chi_{ip}^* = \chi_{ip}, \quad \beta_p^* = \beta_p, \quad A_i^* = A_i + f_i^A(t)\,\delta(\boldsymbol{x} - \Gamma^{ac}), \end{aligned} \tag{3.45g}$$

where the free functions f_i^U and f_i^A have to fulfil the condition

$$\frac{\partial f_i^U(t)}{\partial t} + f_j^U(t)\frac{\partial U_i}{\partial x_j} = f_i^A(t) \qquad \forall \boldsymbol{x} \in \Gamma^{ac}. \tag{3.46}$$

Consequently, the transformation T_{Ac} provides a way to determine the slip velocity caused by the active stress by solving (3.46) for a known velocity field U_i and active stress modification f_i^A. The additional Lie operators are

$$\mathfrak{X}_{p,\beta} = \frac{\partial}{\partial \beta_p}, \quad \mathfrak{X}_{\text{Ac}} = f_i^U(t)\,\delta(\boldsymbol{x} - \Gamma^{ac})\frac{\partial}{\partial U_i} + f_i^A(t)\,\delta(\boldsymbol{x} - \Gamma^{ac})\frac{\partial}{\partial A_i} \tag{3.47}$$

The new transformation T_β, which affects only the orientation of the particles, is universally applicable in a passive suspension with disk-shaped two-dimensional or spherical three-dimensional particles in an infinite domain. In fact, it might even be time-dependent. In the case of arbitrarily shaped active particles T_β is no longer a Lie symmetry, because additional discrete symmetries are necessary. Hence, the Lie-operator (3.11) is not defined, because it is derived with a Taylor expansion (3.6). Each particle needs to possess at least one geometrical symmetry where $\gamma_p\left(\beta_p^*\right) = \gamma_p\left(\beta_p\right)$. Otherwise, the fluid and particle domains would change, leading to a change in the single-field velocity U_i. Furthermore, the active stress term must be invariant $A_i\left(\beta_p^*\right) = A_i\left(\beta_p\right)$, which ensures that the active Navier-Stokes equation (2.97) is form invariant at each point $\boldsymbol{x} \in \Omega$. For elliptical active particles the aforementioned conditions are fulfilled for the transformation $\beta^* = \beta \pm \pi$, where additionally the sign of the active stress magnitude is reversed $A^{c*} = -A^c$. In other words, the orientation of the particles is reversed and pusher particles are replaced with puller particles and vice versa. Despite the fact that T_β is not a Lie-symmetry in the case of an active suspension, invariant solutions for T_β in the case of a passive suspension with disk-shaped particles can be used to describe limiting cases of an active suspension, which is done in Sec. 6.2.3.

The scaling transformation (3.45e) implies additionally the transformation of the particle quantities ω_p, V^P and Θ_{ij}^S. Due to the scaling of time and velocity, the particle rotational velocity becomes $\omega_p^* = \omega_p e^{-2c_{\mathrm{Sc1}}}$, whereas the translational particle velocity $v_{ip}^* = v_{ip}e^{-c_{\mathrm{Sc1}}}$ has the same scaling factor as the single-field velocity U_i. The particle volume is obtained by the integration $\int_{\Omega_p} 1\,\mathrm{d}\boldsymbol{x}$. Therefore, the resulting scaling is $V^{P*} = V^P e^{dc_{\mathrm{Sc1}}}$, where d is the spatial dimension. Analogously, the scaling for the moment of inertia tensor $\Theta_{ij}^{S*} = \Theta_{ij}^S e^{(2+d)c_{\mathrm{Sc1}}}$ is obtained, which reduces to a scalar $\Theta^{S*} = \Theta^S e^{(4)c_{\mathrm{Sc1}}}$ in two dimensions.

The generalised Galilean symmetry (3.45c) is only valid for suspensions with equal mass densities of the separate phases, i.e. $\mathfrak{D} = 1$. Otherwise, the application of (3.45c) to the equation for the translational particle velocity delivers

$$\mathfrak{D}V^P\frac{\mathrm{d}^2\chi_{ip}}{\mathrm{d}t} - \mathfrak{D}V^P f''_{\mathrm{G},i}\left(t\right)\gamma_p = -\int \tau_{ij}^F\frac{\partial\gamma_p}{\partial x_j}\,\mathrm{d}\boldsymbol{x} - f''_{\mathrm{G},i}\left(t\right)\gamma_p V^P, \tag{3.48}$$

where the asterisks are omitted for better readability. The additional terms on the right and left side of the equation vanish either if $\mathfrak{D} = 1$ or if the second derivative $f''_{\mathrm{G},i}\left(t\right) = 0$ is zero. For $\mathfrak{D} \neq 1$ the function $f_{\mathrm{G},i}$ in (3.45c) is reduced to the linear function

$$f_{\mathrm{G},i}\left(t\right) = c_{\mathrm{G},i}t, \quad f'_{\mathrm{G},i}\left(t\right) = c_{\mathrm{G},i}, \tag{3.49}$$

where $c_{\mathrm{G},i}$ is a constant. If $f''_{\mathrm{G},i}\left(t\right) \neq 0$ the entire system would be accelerated. Due to different mass densities $\mathfrak{D} \neq 1$ the resulting forces and momentum on the two phases would be different, hence, the invariance is violated.

3.3.2. Unsteady Stokes equation

The symmetries for a suspension, where the fluid is governed by the active unsteady Stokes equation (2.99), are

$$\begin{aligned} T_t:\quad & t^* = t + c_t, \quad x_i^* = x_i, \quad U_i^* = U_i, \quad p^{F*} = p^F, \\ & \chi_{ip}^* = \chi_{ip}, \quad \beta_p^* = \beta_p, \quad A_i^* = A_i, \end{aligned} \tag{3.50a}$$

$$\begin{aligned} T_{\mathrm{Rot}}:\quad & t^* = t, \quad x_i^* = Q_{ij}x_j, \quad U_i^* = Q_{ij}U_i, \quad p^{F*} = p^F, \\ & \chi_{ip}^* = Q_{ij}\chi_{jp}, \quad \beta_p^* = \beta_p - \varphi, \quad A_i^* = A_i, \end{aligned} \tag{3.50b}$$

$$\begin{aligned} T_{\mathrm{G}}:\quad & t^* = t, \quad x_i^* = x_i + c_{\mathrm{G},i}, \quad U_i^* = U_i, \quad p^{F*} = p^F, \\ & \chi_{ip}^* = \chi_{ip} + c_{\mathrm{G},i}\gamma_p, \quad \beta_p^* = \beta_p, \quad A_i^* = A_i, \end{aligned} \tag{3.50c}$$

$$\begin{aligned} T_p:\quad & t^* = t, \quad x_i^* = x_i, \quad U_i^* = U_i, \quad p^{F*} = p^F + f_p(t), \\ & \chi_{ip}^* = \chi_{ip}, \quad \beta_p^* = \beta_p, \quad A_i^* = A_i, \end{aligned} \tag{3.50d}$$

$$\begin{aligned} T_{\mathrm{Sc1}}:\quad & t^* = te^{2c_{\mathrm{Sc1}}}, \quad x_i^* = x_i e^{c_{\mathrm{Sc1}}}, \quad U_i^* = U_i e^{-c_{\mathrm{Sc1}}}, \quad p^{F*} = p^F e^{-2c_{\mathrm{Sc1}}}, \\ & \chi_{ip}^* = \chi_{ip} e^{c_{\mathrm{Sc1}}}, \quad \beta_p^* = \beta_p, \quad A_i^* = A_i e^{-3c_{\mathrm{Sc1}}}. \end{aligned} \tag{3.50e}$$

$$\begin{aligned} T_\beta:\quad & t^* = t, \quad x_i^* = x_i, \quad U_i^* = U_i, \quad p^{F*} = p^F, \\ & \chi_{ip}^* = \chi_{ip}, \quad \beta_p^* = \beta_p + c_\beta, \quad A_i^* = A_i, \end{aligned} \tag{3.50f}$$

$$\begin{aligned} T_{\mathrm{Ac}}:\quad & t^* = t, \quad x_i^* = x_i, \quad U_i^* = U_i + f_i^U(t)\,\delta\left(\boldsymbol{x} - \Gamma^{Ac}\right), \quad p^{F*} = p^F, \\ & \chi_{ip}^* = \chi_{ip}, \quad \beta_p^* = \beta_p, \quad A_i^* = A_i + f_i^A(t)\,\delta\left(\boldsymbol{x} - \Gamma^{Ac}\right). \end{aligned} \tag{3.50g}$$

The unsteady Stokes equation for a single-phase flow contains additional symmetries compared to the single-phase Navier-Stokes equation. The additional symmetries in the single-phase low-Reynolds system (3.36e)-(3.36g) do not occur in the system of equations describing a low-Reynolds active suspension. This can easily be seen by applying (3.36e)-(3.36g) to the equation for the particle position (2.46). Considering the fact that the particle position χ_{ip} needs to be transformed the same way as the spatial coordinate x_i, as explained in Sec. 3.3, and the transformation for the translational particle velocity is equivalent to the transformation of the local velocity U_i, $\mathrm{d}\chi_{ip}/\,\mathrm{d}t = v_{ip}$ is not invariant under the given transformations. The slip velocity equation (3.46) simplifies to

$$\frac{\partial f_i^U(t)}{\partial t} = f_i^A(t)\,, \tag{3.51}$$

i.e. due to the assumption of a Stokes flow, the equation (3.51) for the slip velocity is accordingly also linear. Furthermore, while the vorticity and the rotational velocity of the particles are related by

$$\epsilon_{ijk}\frac{\partial u_k^S}{\partial x_j} = 2\omega_i^S\,, \tag{3.52}$$

the additional symmetries of the vorticity equation, transforming the vorticity itself, are not generally applicable to a two-phase system. Due to their time-dependency, (3.41d), (3.41g) and (3.41h) are broken by (2.47). The time-dependent transformations of the vorticity are closely related to the particle rotational symmetry T_β, as the vorticity clearly influences the orientation of the particles via (3.52) and (2.47). Similar to T_β, (3.41d), (3.41g) and (3.41h) are universally applicable in a passive suspension of rotationally symmetric particles, such as disks in two dimensions and spheres in three dimensions.

3.3.3. Steady Stokes equation

A steady state in an active suspension is only reached if all particles are uncorrelated. This requires sufficiently large distances between individual particles, i.e. a dilute suspension. Thus, each particle can be observed separately. The particle motion is steady if the translational velocity becomes a constant $\tilde{v}_i$ and the rotational velocity vanishes. The latter requirement is necessary, because a changing orientation β_p would lead to a change in the particle translational velocity v_{ip} due to the active stress. Subsequently, all particle equations except for the position equation (2.46) deliver trivial identities. The generalised Galilean transformation is less restricted in case of the steady Stokes equation and the linear form $f_{\mathrm{G},i} = c_{\mathrm{G},i}t$ is allowed. Using $f_{\mathrm{G},i} = \tilde{v}_i t$ to describe a moving reference frame allows to set the origin at the particle position. Thus,the solution of the particle position equation (2.46) also becomes trivial. In contrast to the unsteady case, no symmetries are broken because of the triviality of the particle equations. Hence, the transformation group for the steady state contains all symmetries of the Stokes equation and the particle rotational transformation

$$
\begin{aligned}
T_{\mathrm{Rot}}: \quad & t^* = t, \quad x_i^* = Q_{ij}x_j, \quad U_i^* = Q_{ij}U_i, \quad p^{F*} = p^F, \\
& \chi_{ip}^* = Q_{ij}\chi_{jp}, \quad \beta_p^* = \beta_p - \varphi, \quad A_i^* = A_i, && \text{(3.53a)} \\
T_{\mathrm{G}}: \quad & t^* = t, \quad x_i^* = x_i + c_{\mathrm{G},i}t, \quad U_i^* = U_i + c_{\mathrm{G},i}, \quad p^{F*} = p^F, \\
& \chi_{ip}^* = \chi_{ip} + c_{\mathrm{G},i}t\gamma_p, \quad \beta_p^* = \beta_p, \quad A_i^* = A_i, && \text{(3.53b)} \\
T_p: \quad & t^* = t, \quad x_i^* = x_i, \quad U_i^* = U_i, \quad p^{F*} = p^F + f_p\left(t\right), \\
& \chi_{ip}^* = \chi_{ip}, \quad \beta_p^* = \beta_p, \quad A_i^* = A_i, && \text{(3.53c)} \\
T_{\mathrm{Sc2}}: \quad & t^* = t, \quad x_i^* = x_i, \quad U_i^* = U_i e^{c_{\mathrm{Sc2}}}, \quad p^{F*} = p^F e^{c_{\mathrm{Sc2}}}, \\
& \chi_{ip}^* = \chi_{ip}, \quad \beta_p^* = \beta_p, \quad A_i^* = A_i e^{c_{\mathrm{Sc2}}} && \text{(3.53d)} \\
T_{\mathrm{Sc3}}: \quad & t^* = t, \quad x_i^* = x_i e^{c_{\mathrm{Sc3}}}, \quad U_i^* = U_i e^{c_{\mathrm{Sc3}}}, \quad p^{F*} = p^F, \\
& \chi_{ip}^* = \chi_{ip} e^{c_{\mathrm{Sc3}}}, \quad \beta_p^* = \beta_p, \quad A_i^* = A_i e^{-c_{\mathrm{Sc2}}} && \text{(3.53e)} \\
T_{\mathrm{lin}}: \quad & t^* = t, \quad x_i^* = x_i, \quad U_i^* = U_i + f_{i,U}\left(\boldsymbol{x}\right), \quad p^{F*} = p^F + f_p\left(\boldsymbol{x}\right), \\
& \chi_{ip}^* = \chi_{ip}, \quad \beta_p^* = \beta_p, \quad A_i^* = A_i, && \text{(3.53f)} \\
T_{\beta}: \quad & t^* = t, \quad x_i^* = x_i, \quad U_i^* = U_i, \quad p^{F*} = p^F, \\
& \chi_{ip}^* = \chi_{ip}, \quad \beta_p^* = \beta_p + c_\beta, \quad A_i^* = A_i. && \text{(3.53g)}
\end{aligned}
$$

The time shift transformation vanishes due to the steadiness of the problem, however, it is still applicable per definition of the terminology steady. The scaling symmetry T_{Sc1} can be obtained by employing (3.37). As a direct consequence of the constant particle velocity, the active symmetry T_{Ac} is no longer a symmetry of the system, since a changing active force results in a change of velocity. Furthermore, it should be emphasised that the linear symmetry T_{lin} is still valid in the steady case of an active suspension, in contrast to the unsteady case discussed in the previous section.

3.4. Probability density functions

In the study of hydrodynamic turbulence a statistical approach based on PDFs was introduced. Lundgren, Monin and Novikov (LMN) derived a statistical framework known as LMN hierarchy based on first principles [142, 153, 157]. An infinite set of equations of motion for the multi-point velocity PDF forms the LMN hierarchy. The PDF contains information about all statistical moments, subsequently, the Reynolds-Averaged Navier-Stokes (RANS) equation and other statistical models can be directly derived from the LMN hierarchy. Furthermore, it reveals, in combination with the Lie-symmetry approach, further information about the structure of the flow. The application of the PDF approach is not restricted to single-phase turbulent flows. It has been extended to magneto-hydrodynamics [79], to reactive flows and combustion [168] and to compressible turbulence [170]. In this section a PDF hierarchy for an active suspension is derived. The results were published in Deußen et al. [51], which forms the basis for this section.

The starting point for the derivation are the Newton-Euler equations (2.54), (2.55) and the active Navier-Stokes equation (2.97), describing the solid and fluid phase, respectively. The separate equations of motion are combined into a single-field velocity description using the level-set method and the phase indicator function γ^S and γ^F, see equation (2.101). This single-field system is then transferred from the physical space into the sample space by employing ensemble averages. In the derivation of the PDF hierarchy of equations only two spatial dimensions are considered. The main difference compared to a three-dimensional system is the scalar nature of the rotational velocity of the particles.

3.4.1. General properties of a PDF

A PDF describes the statistical behaviour of a system. Instead of observing a single experiment and describing its outcome with physical equations as for example the Navier-Stokes equation (2.67), an ensemble of experiments is observed. An ensemble is an infinite number of experiments with the same physical properties, i.e. the same number of active particles in the same domain with the same fluid viscosity and mass densities. The initial conditions might vary in each experiment and perturbations exist, hence, the outcome of each experiment is different. The PDF is used to describe the statistical behaviour of the entire ensemble and contains information about all statistical moments and outcomes of each experiment of the ensemble.

A single manifestation of the ensemble, i.e. a single experiment, is described by the fine-grained PDF

$$\widehat{f}(\mathfrak{U}) = \delta\left(\mathfrak{U} - \mathfrak{u}(\boldsymbol{x}, t)\right), \tag{3.54}$$

where $\mathfrak{u}(\boldsymbol{x}, t)$ is a physical variable dependent on the space-time point $(\boldsymbol{x}, t)$ and $\mathfrak{U}$ the corresponding independent variable in the sample space. Subsequently, the probability for an event

$$E_1 \equiv \{\mathfrak{u} < \mathfrak{U}^a\} \tag{3.55}$$

is obtained with the integral

$$\widehat{P}_1 = \int_{-\infty}^{\mathfrak{U}^a} \delta\left(\mathfrak{U} - \mathfrak{u}(\boldsymbol{x}, t)\right) \mathrm{d}\mathfrak{U} \tag{3.56}$$

whose result is either zero if $\mathfrak{U}^a < \mathfrak{u}(\boldsymbol{x}, t)$ or unity if $\mathfrak{U}^a > \mathfrak{u}(\boldsymbol{x}, t)$. Hence, the event is either impossible or certain as the outcome of the single experiment is deterministic.

The PDF is obtained by forming the ensemble average, indicated by the brackets $\langle \cdot \rangle$, of (3.54) [169]

$$f(\mathfrak{U}) = \left\langle \widehat{f}(\mathfrak{U}) \right\rangle = \langle \delta\left(\mathfrak{U} - \mathfrak{u}(\boldsymbol{x}, t)\right)\rangle . \tag{3.57}$$

The probability for the event E_1 in the case of the ensemble-PDF is obtained by

$$P_1 = \int_{-\infty}^{\mathfrak{U}^a} \langle \delta\left(\mathfrak{U} - \mathfrak{u}(\boldsymbol{x}, t)\right)\rangle \, \mathrm{d}\mathfrak{U}, \tag{3.58}$$

whose result is a value between zero and unity $0 \leq P_1 \leq 1$, i.e. the outcome is stochastic. The probability of a second event

$$E_2 \equiv \left\{\mathfrak{U}^b < \mathfrak{u} < \mathfrak{U}^a\right\} \tag{3.59}$$

is determined by

$$P_2 = \int_{\mathfrak{U}^b}^{\mathfrak{U}^a} \langle \delta\left(\mathfrak{U} - \mathfrak{u}(\boldsymbol{x}, t)\right)\rangle \, \mathrm{d}\mathfrak{U}, \tag{3.60}$$

again resulting in a value between zero and unity. Already implied in the given intervals for the exemplary calculation of the probabilities, i.e. $0 \leq P_1 \leq 1$, are important properties of any PDF. The integral over the entire sample space yields unity

$$\int_{-\infty}^{\infty} f(\mathfrak{U}) \, \mathrm{d}\mathfrak{U} = 1, \tag{3.61}$$

and in the limiting case

$$\lim_{\mathfrak{U} \to \infty} f(\mathfrak{U}) = 0, \qquad \lim_{\mathfrak{U} \to -\infty} f(\mathfrak{U}) = 0 \tag{3.62}$$

the PDF vanishes. Furthermore, the PDF is always non-negative for all values of $\mathfrak{U}$

$$f\left(\mathfrak{U}\right) \geq 0 \quad \forall \mathfrak{U}. \tag{3.63}$$

So far the PDF was only considered at a single point ${}_1x_i$ within Ω. Correlating multiple points delivers multi-point PDFs. The correlation of the variable $\mathfrak{U}$ at two points ${}_1x_i$ and ${}_2x_i$ delivers the two-point PDF

$${}_2f({}_1\mathfrak{U}, {}_2\mathfrak{U}) = \langle \delta\left({}_1\mathfrak{U} - {}_1\mathfrak{u}\right) \delta\left({}_2\mathfrak{U} - {}_2\mathfrak{u}\right)\rangle , \tag{3.64}$$

where the dependency of the physical variables ${}_1\mathfrak{u} = \mathfrak{u}\left({}_1\boldsymbol{x}, t\right)$ and ${}_2\mathfrak{u} = \mathfrak{u}\left({}_2\boldsymbol{x}, t\right)$ on space and time was omitted for better readability. The preceding subscript of the PDF ${}_2f$ describes the number of points correlated. Extending (3.64) leads to the K-point PDF

$${}_Kf({}_1\mathfrak{U}, ..., {}_K\mathfrak{U}) = \left\langle \prod_{k=1}^{K} \delta\left({}_k\mathfrak{U} - {}_k\mathfrak{u}\right) \right\rangle . \tag{3.65}$$

Applying (3.61) to the multi-point PDF delivers the reduction property

$$\int_{-\infty}^{\infty} {}_Kf({}_1\mathfrak{U}, ..., {}_K\mathfrak{U}) \, \mathrm{d}\, {}_K\mathfrak{U} = {}_{K-1}f\left({}_1\mathfrak{U}, ..., {}_{K-1}\mathfrak{U}\right), \tag{3.66}$$

i.e. each integration with respect to a single sample space variable ${}_K\mathfrak{U}$ reduces the order of the PDF by one. The order of the points ${}_1\boldsymbol{x}$ to ${}_K\boldsymbol{x}$ is arbitrary, i.e. any point in the domain Ω can be marked by K. Hence, the integration can be carried out with respect to the sample space variable related to any point $\boldsymbol{x} \in \Omega$.

Two physical variables at two points at infinite distance are assumed to be statistically independent [142]

$$\lim_{|{}_1\boldsymbol{x} - {}_2\boldsymbol{x}| \to \infty} {}_2f\left({}_1\mathfrak{U}, {}_2\mathfrak{U}\right) = {}_1f\left({}_1\mathfrak{U}\right) {}_1f\left({}_2\mathfrak{U}\right), \tag{3.67}$$

which is the separation property of the PDF. Hence, for the K-point PDF one obtains

$$\lim_{|{}_k\boldsymbol{x} - {}_K\boldsymbol{x}| \to \infty} {}_Kf\left({}_1\mathfrak{U}, ..., {}_K\mathfrak{U}\right) = {}_{K-1}f\left({}_1\mathfrak{U}, ..., {}_{K-1}\mathfrak{U}\right) {}_1f\left({}_K\mathfrak{U}\right) \quad \forall k = \{1, ..., K-1\}, \tag{3.68}$$

where the order of the points is irrelevant and thus any point could be marked by the index K. Again, the index preceding the PDF refers to the number of points correlated, i.e. ${}_1f\left({}_K\mathfrak{U}\right)$ is a single-point PDF at the Kth point. The separation property is the only occurrence in the present work of a PDF ${}_1f\left({}_K\mathfrak{U}\right)$, i.e. a PDF where the highest index of the sample space variable K is unequal to the order of the PDF. In the following derivations the separation property is, however, not used directly. Hence, the order of the PDF is always equal to the highest index of the sample space variable, which allows to introduce the shorthand notation

$${}_Kf^{\mathfrak{U}} = {}_Kf({}_1\mathfrak{U}, ..., {}_K\mathfrak{U}). \tag{3.69}$$

A direct consequence of the reduction property (3.66) is the coincidence property [142]

$$\lim_{|{}_1\boldsymbol{x} - {}_2\boldsymbol{x}| \to 0} {}_2f^{\mathfrak{U}} = {}_1f^{\mathfrak{U}} \delta\left({}_2\mathfrak{U} - {}_1\mathfrak{U}\right), \tag{3.70}$$

which refers to the fact that the physical variables at a single point are identical and, subsequently, the probabilities and sample space variables need to be identical. Similarly, one obtains for the K-point PDF

$$\lim_{|{}_k\boldsymbol{x} - {}_K\boldsymbol{x}| \to 0} {}_Kf^{\mathfrak{U}} = {}_{K-1}f^{\mathfrak{U}} \delta\left({}_K\mathfrak{U} - {}_k\mathfrak{U}\right), \quad k \in \{1, ..., K-1\}. \tag{3.71}$$

Derivatives of the PDF

In general, the multi-point PDF ${}_Kf^{\mathfrak{U}} = {}_Kf({}_1\mathfrak{U}, ..., {}_K\mathfrak{U}; {}_1\boldsymbol{x}, ..., {}_K\boldsymbol{x}, t)$ is a function of space and time. Derivatives with respect to both independent variables are formed with the chain rule. The temporal derivative of the multi-point PDF is

$$\frac{\partial\, {}_Kf^{\mathfrak{U}}}{\partial t} = -\left\langle \sum_{k=1}^{K} \frac{\partial\, {}_k\mathfrak{u}}{\partial t} \frac{\partial\, {}_K\widehat{f}^{\mathfrak{U}}}{\partial\, {}_k\mathfrak{U}} \right\rangle = -\sum_{k=1}^{K} \frac{\partial}{\partial\, {}_k\mathfrak{U}} \left\langle \frac{\partial\, {}_k\mathfrak{u}}{\partial t}\, {}_K\widehat{f}^{\mathfrak{U}} \right\rangle. \tag{3.72}$$

The gradient of the multi-point PDF with respect to the kth point is

$$\begin{aligned}\frac{\partial\, {}_K f^{\mathfrak{U}}}{\partial\, {}_k x_i} &= -\left\langle \frac{\partial\, {}_k \mathfrak{u}}{\partial\, {}_k x_i} \frac{\partial\, {}_K \widehat{f}^{\mathfrak{U}}}{\partial\, {}_k \mathfrak{U}} \right\rangle = -\frac{\partial}{\partial\, {}_k \mathfrak{U}} \left\langle \frac{\partial\, {}_k \mathfrak{u}}{\partial\, {}_k x_i}\, {}_K \widehat{f}^{\mathfrak{U}} \right\rangle \\ &= -\frac{\partial}{\partial\, {}_k \mathfrak{U}} \left\langle \int \delta\left({}_{K+1}\boldsymbol{x} - {}_k\boldsymbol{x}\right) \frac{\partial\, {}_{K+1}\mathfrak{u}}{\partial\, {}_{K+1} x_i}\, {}_K \widehat{f}^{\mathfrak{U}}\, \mathrm{d}\, {}_{K+1}\boldsymbol{x} \right\rangle \\ &= -\frac{\partial}{\partial\, {}_k \mathfrak{U}} \int \delta\left({}_{K+1}\boldsymbol{x} - {}_k\boldsymbol{x}\right) \frac{\partial}{\partial\, {}_{K+1} x_i}\, {}_{K+1} f^{\mathfrak{U}}\, {}_{K+1}\mathfrak{U}\, \mathrm{d}\, {}_{K+1}\mathfrak{U}\, \mathrm{d}\, {}_{K+1}\boldsymbol{x}, \end{aligned} \tag{3.73}$$

which was mentioned in Ulinich and Lyubimov [199] as consistency condition. Here, the Dirac distribution was used as an expression for the limit

$$\lim_{{}_{K+1}\boldsymbol{x} \to {}_k\boldsymbol{x}} {}_{K+1}\mathfrak{u} = \int \delta\left({}_{K+1}\boldsymbol{x} - {}_k\boldsymbol{x}\right) {}_{K+1}\mathfrak{u}\, \mathrm{d}\, {}_{K+1}\boldsymbol{x}. \tag{3.74}$$

3.4.2. Marginal PDF

Three multi-dimensional physical variables are sufficient to describe the entire active suspension. These variables are the unified single-field velocity U_i, the position of the particles χ_{ip} and the orientation angle of the particles β_p. While χ_{ip} is a tensor of second order, the orientation angles of all particles are organised in a vector. Accordingly, three multi-dimensional sample space variables exist to describe the statistical behaviour of an active suspension. Corresponding to the single-field velocity U_i is the sample space variable V_i. The particle variables translate to X_{ip} and b_p for the position and angle, respectively. Marginal PDFs for the individual variables only describe the probabilities of said variable without referencing the entire set of sample space variables

$$\begin{gathered} {}_1 f^V = \left\langle {}_1 \widehat{f}^V \right\rangle = \left\langle \delta\left({}_1\boldsymbol{V} - {}_1\boldsymbol{U}\right) \right\rangle, \quad f^X = \left\langle \widehat{f}^X \right\rangle = \left\langle \delta\left(\boldsymbol{X} - \boldsymbol{\chi}\right) \right\rangle, \\ f^b = \left\langle \widehat{f}^b \right\rangle = \left\langle \delta\left(\boldsymbol{b} - \boldsymbol{\beta}\right) \right\rangle, \end{gathered} \tag{3.75}$$

where ${}_1\widehat{f}^V$, $\widehat{f}^X$ and $\widehat{f}^b$ are the fine-grained PDFs. It will become visible in the transport equations for the marginal PDFs that they are not sufficient to fully describe the system. Instead, each equation for the marginal PDFs depends on a joint PDF containing information about all three variables. The velocity U_i, the particle position χ_{ip} and the particle orientation angle β_p are, hence, statistical dependent. The multi-point joint PDF is

$${}_K f = \left\langle \prod_{k=1}^{K} \delta\left({}_k\boldsymbol{V} - {}_k\boldsymbol{U}\right) \delta\left(\boldsymbol{X} - \boldsymbol{\chi}\right) \delta\left(\boldsymbol{b} - \boldsymbol{\beta}\right) \right\rangle, \tag{3.76}$$

whose equations of motion will be derived based on the equations of the marginal PDFs, see Sec. 3.4.3.

Velocity marginal PDF

The single-point velocity marginal PDF ${}_1f^V$ describes the statistical behaviour of the single-field velocity U_i at a single point ${}_1x_i$. The material derivative of ${}_1f^V\left({}_1V;{}_1\boldsymbol{x},t\right)$ is [142]

$$\begin{aligned}
\frac{\mathrm{d}\,{}_1f^V}{\mathrm{d}t} &= -\left\langle \frac{\mathrm{d}\,{}_1U_i}{\mathrm{d}t}\frac{\partial\,{}_1\hat{f}^V}{\partial\,{}_1V_i}\right\rangle = -\frac{\partial}{\partial\,{}_1V_i}\left\langle \frac{\mathrm{d}\,{}_1U_i}{\mathrm{d}t}\,{}_1\hat{f}^{(V)}\right\rangle \\
&= -\frac{\partial}{\partial\,{}_1V_i}\left\langle \frac{\partial\,{}_1U_i}{\partial t}\,{}_1\hat{f}^V\right\rangle - \frac{\partial}{\partial\,{}_1V_i}\left\langle {}_1U_j\frac{\partial\,{}_1U_i}{\partial\,{}_1x_j}\,{}_1\hat{f}^V\right\rangle \\
&= -\frac{\partial}{\partial\,{}_1V_i}\left\langle \frac{\partial\,{}_1U_i}{\partial t}\,{}_1\hat{f}^V\right\rangle + {}_1V_i\left\langle \frac{\partial\,{}_1\hat{f}^V}{\partial\,{}_1x_i}\right\rangle \\
&= \frac{\partial\,{}_1f^V}{\partial t} + {}_1V_i\frac{\partial\,{}_1f^V}{\partial x_i},
\end{aligned} \tag{3.77}$$

where (3.72) and (3.73) where used. The structure of the physical material derivative, consisting of a term describing the local change and a convective term, is preserved in the sample space.

The equation of motion for ${}_1f^V$ is obtained by using the single-field velocity momentum balance (2.101) together with (3.77). The individual terms of (2.101) are multiplied with the fine-grained velocity PDF ${}_1\widehat{f}^V$, furthermore, the ensemble average and the derivative with respect to the sample space variable ${}_1V_i$ are taken according to (3.72). In the following paragraphs each term of (2.101) is transformed into the sample space individually. The stress tensor ${}_1\tau_{ij} = -{}_1p\delta_{ij} + 1/\mathrm{Re}\left(\partial U_i/\partial x_j + \partial U_j/\partial x_i\right)$ consists of a pressure term and a viscous term. Using Green's function, the pressure can be expressed in terms of the velocity

$${}_1p = \frac{1}{4\pi}\int \frac{1}{\left|{}_2\boldsymbol{x} - {}_1\boldsymbol{x}\right|}\frac{\partial\,{}_2U_i}{\partial\,{}_2x_j}\frac{\partial\,{}_2U_j}{\partial\,{}_2x_i}\,\mathrm{d}\,{}_2\boldsymbol{x}. \tag{3.78}$$

Subsequently, the pressure term in the sample space becomes

$$\begin{aligned}
\frac{\partial}{\partial\,{}_1V_i}\left\langle \frac{\partial\,{}_1p}{\partial\,{}_1x_i}\,{}_1\hat{f}^V\right\rangle &= -\frac{1}{4\pi}\frac{\partial}{\partial\,{}_1V_i}\left\langle {}_1\gamma^F\frac{\partial}{\partial\,{}_1x_i}\int \frac{1}{\left|{}_2\boldsymbol{x} - {}_1\boldsymbol{x}\right|}\frac{\partial\,{}_2U_i}{\partial\,{}_2x_j}\frac{\partial\,{}_2U_j}{\partial\,{}_2x_i}\,\mathrm{d}\,{}_2\boldsymbol{x}\,{}_1\hat{f}^V\right\rangle \\
&= \frac{1}{4\pi}\frac{\partial}{\partial\,{}_1V_i}\int {}_1g^F\frac{\partial}{\partial\,{}_1x_i}\frac{1}{\left|{}_2\boldsymbol{x} - {}_1\boldsymbol{x}\right|}\left({}_2V_i\frac{\partial}{\partial\,{}_2x_i}\right)^2{}_2f\,\mathrm{d}\,{}_2\boldsymbol{x}\,\mathrm{d}\,{}_2\boldsymbol{V}\,\mathrm{d}\boldsymbol{X}\,\mathrm{d}\boldsymbol{b}.
\end{aligned} \tag{3.79}$$

Due to the non-locality of the pressure, see (3.78), two points are correlated in (3.79). Furthermore, due to the presence of the indicator function ${}_1\gamma^F$, which is a function of the position and orientation of the particles, the velocity marginal PDF depends on the two-point joint PDF ${}_2f$ of all three variables. The function ${}_1g^F = {}_1g^F\left(\boldsymbol{X}_p, b_p\right)$ is the sample space version of the indicator function

$$\left\langle {}_1\gamma^F\widehat{f}^X\widehat{f}^b\right\rangle = {}_1g^F f^X f^b, \tag{3.80}$$

which is the reason for the integration with respect to $\boldsymbol{X}$ and $\boldsymbol{b}$ in (3.79). The sample space version of the viscous term is

$$
\begin{aligned}
-\frac{1}{\mathrm{Re}}\frac{\partial}{\partial\,{}_1V_i}\left\langle {}_1\gamma^F\frac{\partial^2\,{}_1U_i}{\partial\,{}_1x_j{}^2}\,{}_1\widehat{f}^V\right\rangle &= -\frac{1}{\mathrm{Re}}\frac{\partial}{\partial\,{}_1V_i}\left\langle\int\delta\left({}_2\boldsymbol{x}-{}_1\boldsymbol{x}\right){}_1\gamma^F\frac{\partial^2\,{}_2U_i}{\partial\,{}_2x_j{}^2}\,{}_2\widehat{f}\,\mathrm{d}\,{}_2\boldsymbol{x}\,\mathrm{d}\,{}_2\boldsymbol{V}\,\mathrm{d}\boldsymbol{X}\,\mathrm{d}\boldsymbol{b}\right\rangle \\
&= -\frac{1}{\mathrm{Re}}\frac{\partial}{\partial\,{}_1V_i}\int\delta\left({}_2\boldsymbol{x}-{}_1\boldsymbol{x}\right){}_1g^F\,{}_2V_i\frac{\partial^2\,{}_2f}{\partial\,{}_2x_j{}^2}\,\mathrm{d}\,{}_2\boldsymbol{x}\,\mathrm{d}\,{}_2\boldsymbol{V}\,\mathrm{d}\boldsymbol{X}\,\mathrm{d}\boldsymbol{b},
\end{aligned}
\tag{3.81}
$$

which also depends on the two-point joint PDF. Apart from the reference to the sample space fluid indicator function ${}_1g^F$, both terms (3.79) and (3.81) are equivalent to the pressure and viscous terms given by Lundgren [142] for the single phase velocity PDF.

Four new sample space functions are necessary to describe the active stress. The particle indicator function γ_p and the function ϕ_p are transformed into the sample space by

$$
\left\langle {}_1\gamma_p\widehat{f}^X\widehat{f}^b\right\rangle = {}_1g_pf^Xf^b, \quad \left\langle {}_1\phi\widehat{f}^X\widehat{f}^b\right\rangle = {}_1hf^Xf^b \tag{3.82}
$$

and the set of all points at the active and passive surfaces becomes

$$
\left\langle \Gamma^{ac}\widehat{f}^X\widehat{f}^b\right\rangle = \widehat{\Gamma}^{ac}f^b, \quad \left\langle \Gamma^{pa}\widehat{f}^{(X)}\widehat{f}^b\right\rangle = \widehat{\Gamma}^{pa}f^b. \tag{3.83}
$$

The orientation vector, necessary to define the direction of the active stress at the boundary retains its structure and is defined by $\widehat{e}_{ip} = [\cos(b_p)\sin(b_p)]$. The active stress term in the sample space is

$$
\begin{aligned}
&-\frac{\partial}{\partial\,{}_1V_i}\left\langle\delta\left({}_1\boldsymbol{x}-\Gamma^{ac}\right)A^c\left(n_in_je_{jp}-e_{ip}\right)\gamma_p\,{}_1\widehat{f}^V\right\rangle \\
&= -A^c\frac{\partial}{\partial\,{}_1V_i}\left\langle\int\delta\left({}_1\boldsymbol{x}-\Gamma^{ac}\right)\left(\frac{\partial\,{}_1\phi}{\partial\,{}_1x_i}\frac{\partial\,{}_1\phi}{\partial\,{}_1x_j}e_{jp}-e_{ip}\right)\gamma_p\,{}_1\widehat{f}\,\mathrm{d}\boldsymbol{X}\,\mathrm{d}\boldsymbol{b}\right\rangle \\
&= -A^c\frac{\partial}{\partial\,{}_1V_i}\int\delta\left({}_1\boldsymbol{x}-\widehat{\Gamma}^{ac}\right)\left(\frac{\partial\,{}_1h}{\partial\,{}_1x_i}\frac{\partial\,{}_1h}{\partial\,{}_1x_j}\widehat{e}_{jp}-\widehat{e}_{ip}\right)g_p\,{}_1f\,\mathrm{d}\boldsymbol{X}\,\mathrm{d}\boldsymbol{b}
\end{aligned}
\tag{3.84}
$$

and depends only on the single-point joint PDF of all three sample space variables. To define the normal vector n_i in the sample space, it was assumed that $|\nabla\phi| = 1$ holds at the entire particle surface. Thus, the normalisation with $|\nabla\phi|^{-1}$ was omitted in (3.84) for better readability.

The particle translational velocity term in (2.101) already contains a second point ${}_2x_i$. Hence, the sample space version depends on the three-point joint PDF

$$
\begin{aligned}
&-\frac{\partial}{\partial\,{}_1V_i}\left\langle\frac{1}{V^P\mathfrak{D}}\,{}_1\gamma_p\int{}_2\tau_{ij}\frac{\partial\,{}_2\gamma_p}{\partial\,{}_2x_j}\,\mathrm{d}\,{}_2\boldsymbol{x}\,{}_1\widehat{f}^V\right\rangle\\
=&\frac{\partial}{\partial\,{}_1V_i}\left\langle\frac{1}{V^P\mathfrak{D}}\,{}_1\gamma_p\int\left({}_2p\delta_{ij}-\frac{1}{\mathrm{Re}}\left(\frac{\partial\,{}_2U_i}{\partial\,{}_2x_j}+\frac{\partial\,{}_2U_j}{\partial\,{}_2x_i}\right)\right)\frac{\partial\,{}_2\gamma_p}{\partial\,{}_2x_j}\,\mathrm{d}\,{}_2\boldsymbol{x}\,{}_1\widehat{f}^V\right\rangle\\
=&\frac{\partial}{\partial\,{}_1V_i}\left\langle\frac{1}{4\pi V^P\mathfrak{D}}\,{}_1\gamma_p\int\frac{1}{|{}_3\boldsymbol{x}-{}_2\boldsymbol{x}|}\frac{\partial\,{}_3U_j}{\partial\,{}_3x_k}\frac{\partial\,{}_3U_k}{\partial\,{}_3x_j}\frac{\partial\,{}_2\gamma_p}{\partial\,{}_2x_i}\,{}_1\widehat{f}^V\,\mathrm{d}\,{}_3\boldsymbol{x}\,\mathrm{d}\,{}_2\boldsymbol{x}\right\rangle\\
&-\frac{1}{\mathrm{Re}\,V^P\mathfrak{D}}\frac{\partial}{\partial\,{}_1V_i}\left\langle{}_1\gamma_p\int\delta\left({}_3\boldsymbol{x}-{}_2\boldsymbol{x}\right)\left(\frac{\partial\,{}_3U_i}{\partial\,{}_3x_j}+\frac{\partial\,{}_3U_j}{\partial\,{}_3x_i}\right)\frac{\partial\,{}_2\gamma_p}{\partial\,{}_2x_j}\,{}_1\widehat{f}^V\,\mathrm{d}\,{}_3\boldsymbol{x}\,\mathrm{d}\,{}_2\boldsymbol{x}\right\rangle\\
=&\frac{1}{4\pi V^P\mathfrak{D}}\frac{\partial}{\partial\,{}_1V_i}\int{}_1g_p\frac{1}{|{}_3\boldsymbol{x}-{}_2\boldsymbol{x}|}\frac{\partial\,{}_2g_p}{\partial\,{}_2x_i}\left({}_3V_j\frac{\partial}{\partial\,{}_3x_j}\right)^2{}_3f\,\mathrm{d}\,{}_3\boldsymbol{x}\,\mathrm{d}\,{}_2\boldsymbol{x}\,\mathrm{d}\,{}_3\boldsymbol{V}\,\mathrm{d}\,{}_2\boldsymbol{V}\,\mathrm{d}\boldsymbol{X}\,\mathrm{d}\boldsymbol{b}\\
&-\frac{1}{\mathrm{Re}\,V^P\mathfrak{D}}\frac{\partial}{\partial\,{}_1V_i}\int{}_1g_p\delta\left({}_3\boldsymbol{x}-{}_2\boldsymbol{x}\right)\frac{\partial\,{}_2g_p}{\partial\,{}_2x_j}\left({}_3V_i\frac{\partial\,{}_3f}{\partial\,{}_3x_j}+{}_3V_j\frac{\partial\,{}_3f}{\partial\,{}_3x_i}\right)\mathrm{d}\,{}_3\boldsymbol{x}\,\mathrm{d}\,{}_2\boldsymbol{x}\,\mathrm{d}\,{}_3\boldsymbol{V}\,\mathrm{d}\,{}_2\boldsymbol{V}\,\mathrm{d}\boldsymbol{X}\,\mathrm{d}\boldsymbol{b}.
\end{aligned}
\tag{3.85}
$$

Analogously, one obtains the sample space version of the particle rotational velocity term, depending on the three-point joint PDF

$$
\begin{aligned}
&-\frac{\partial}{\partial\,{}_1V_i}\left\langle\gamma_p\epsilon_{i3j}\frac{\left({}_1x_j-\chi_{jq}\,{}_1\gamma_q\right)}{\Theta^S}\int\epsilon_{3kl}\left({}_2x_k-\chi_{kr}\,{}_2\gamma_r\right){}_2\tau_{lm}\frac{\partial\,{}_2\gamma_p}{\partial\,{}_2x_m}\,\mathrm{d}\,{}_2\boldsymbol{x}\right\rangle\\
=&\frac{\epsilon_{i3j}\epsilon_{3kl}}{4\pi\Theta^S}\frac{\partial}{\partial\,{}_1V_i}\int{}_1g_p\frac{\left({}_1x_j-X_{jq}\,{}_1g_q\right)\left({}_2x_k-X_{kr}\,{}_2g_r\right)}{|{}_3\boldsymbol{x}-{}_2\boldsymbol{x}|}\frac{\partial\,{}_2g_p}{\partial\,{}_2x_l}\left({}_3V_m\frac{\partial}{\partial\,{}_3x_m}\right)^2{}_3f\times\\
&\qquad\times\mathrm{d}\,{}_3\boldsymbol{x}\,\mathrm{d}\,{}_2\boldsymbol{x}\,\mathrm{d}\,{}_3\boldsymbol{V}\,\mathrm{d}\,{}_2\boldsymbol{V}\,\mathrm{d}\boldsymbol{X}\,\mathrm{d}\boldsymbol{b}\\
&-\frac{\epsilon_{i3j}\epsilon_{3kl}}{\mathrm{Re}\,\Theta^S}\frac{\partial}{\partial\,{}_1V_i}\int{}_1g_p\left({}_1x_j-X_{jq}\,{}_1g_q\right)\left({}_2x_k-X_{kr}\,{}_2g_r\right)\delta\left({}_3\boldsymbol{x}-{}_2\boldsymbol{x}\right)\frac{\partial\,{}_2g_p}{\partial\,{}_2x_j}\times\\
&\qquad\times\left({}_3V_i\frac{\partial\,{}_3f}{\partial\,{}_3x_j}+{}_3V_j\frac{\partial\,{}_3f}{\partial\,{}_3x_i}\right)\mathrm{d}\,{}_3\boldsymbol{x}\,\mathrm{d}\,{}_2\boldsymbol{x}\,\mathrm{d}\,{}_3\boldsymbol{V}\,\mathrm{d}\,{}_2\boldsymbol{V}\,\mathrm{d}\boldsymbol{X}\,\mathrm{d}\boldsymbol{b}.
\end{aligned}
\tag{3.86}
$$

The second particle rotational velocity term in (2.101) becomes

$$
\begin{aligned}
&\frac{\partial}{\partial\,{}_1V_i}\left\langle\left({}_1\gamma_p\frac{\epsilon_{3jk}\left({}_1x_j-\chi_{jq}\,{}_1\gamma_q\right)}{\left|{}_1\boldsymbol{x}-\boldsymbol{\chi}\cdot{}_1\boldsymbol{\gamma}\right|^2}\left({}_1U_k-\int\delta\left({}_2\boldsymbol{x}-\boldsymbol{\chi}\cdot{}_1\boldsymbol{\gamma}\right){}_2U_k\,\mathrm{d}\,{}_2\boldsymbol{x}\right)\right)^2\times\left({}_1x_i-\chi_{ir}\,{}_1\gamma_r\right)\right\rangle\\
=&\frac{\partial}{\partial\,{}_1V_i}\int\left({}_1g_p\frac{\epsilon_{3jk}\left({}_1x_j-X_{jq}\,{}_1g_q\right)}{\left|{}_1\boldsymbol{x}-\boldsymbol{X}\cdot{}_1\boldsymbol{g}\right|^2}\left({}_1V_k-\int\delta\left({}_2\boldsymbol{x}-\boldsymbol{X}\cdot{}_1\boldsymbol{g}\right){}_2V_k\,\mathrm{d}\,{}_2\boldsymbol{x}\right)\right)^2\times\\
&\qquad\times\left({}_1x_i-X_{ir}\,{}_1g_r\right)\mathrm{d}\,{}_2\boldsymbol{V}\,\mathrm{d}\boldsymbol{X}\,\mathrm{d}\boldsymbol{b}
\end{aligned}
\tag{3.87}
$$

in the sample space. As it does not contain gradients or references to the fluid pressure it only depends on the two-point joint PDF.

Combining the different sample space terms (3.79)-(3.87) delivers the transport equation for the velocity marginal PDF

$$
\begin{aligned}
\frac{\mathrm{d}\,{}_1f^V}{\mathrm{d}t} &= \frac{\partial\,{}_1f^V}{\partial t} + {}_1V_i \frac{\partial\,{}_1f^V}{\partial\,{}_1x_i} \\
&= \frac{1}{4\pi}\frac{\partial}{\partial\,{}_1V_i} \int {}_1g^F \frac{\partial}{\partial\,{}_1x_i} \frac{1}{\left|{}_2\boldsymbol{x} - {}_1\boldsymbol{x}\right|} \left({}_2V_i \frac{\partial}{\partial\,{}_2x_i}\right)^2 {}_2f \,\mathrm{d}\,{}_2\boldsymbol{x} \,\mathrm{d}\,{}_2\boldsymbol{V} \,\mathrm{d}\boldsymbol{X} \,\mathrm{d}\boldsymbol{b} \\
&- \frac{1}{\mathrm{Re}}\frac{\partial}{\partial\,{}_1V_i} \int \delta\left({}_2\boldsymbol{x} - {}_1\boldsymbol{x}\right) {}_1g^F \,{}_2V_i \frac{\partial^2\,{}_2f}{\partial\,{}_2{x_j}^2} \,\mathrm{d}\,{}_2\boldsymbol{x} \,\mathrm{d}\,{}_2\boldsymbol{V} \,\mathrm{d}\boldsymbol{X} \,\mathrm{d}\boldsymbol{b} \\
&- A^c \frac{\partial}{\partial\,{}_1V_i} \int \delta\left({}_1\boldsymbol{x} - \widehat{\Gamma}^{ac}\right) \left(\frac{\partial\,{}_1h}{\partial\,{}_1x_i}\frac{\partial\,{}_1h}{\partial\,{}_1x_j}\widehat{e}_{jp} - \widehat{e}_{ip}\right) g_p\,{}_1f \,\mathrm{d}\boldsymbol{X} \,\mathrm{d}\boldsymbol{b} \\
&- \frac{1}{4\pi V^P \mathfrak{D}} \frac{\partial}{\partial\,{}_1V_i} \int {}_1g_p \frac{1}{\left|{}_3\boldsymbol{x} - {}_2\boldsymbol{x}\right|} \frac{\partial\,{}_2g_p}{\partial\,{}_2x_i} \left({}_3V_j \frac{\partial}{\partial\,{}_3x_j}\right)^2 {}_3f \,\mathrm{d}\,{}_3\boldsymbol{x} \,\mathrm{d}\,{}_2\boldsymbol{x} \,\mathrm{d}\,{}_3\boldsymbol{V} \,\mathrm{d}\,{}_2\boldsymbol{V} \,\mathrm{d}\boldsymbol{X} \,\mathrm{d}\boldsymbol{b} \\
&+ \frac{1}{\mathrm{Re}\,V^P \mathfrak{D}} \frac{\partial}{\partial\,{}_1V_i} \int {}_1g_p \delta\left({}_3\boldsymbol{x} - {}_2\boldsymbol{x}\right) \frac{\partial\,{}_2g_p}{\partial\,{}_2x_j} \left({}_3V_i \frac{\partial\,{}_3f}{\partial\,{}_3x_j} + {}_3V_j \frac{\partial\,{}_3f}{\partial\,{}_3x_i}\right) \times \\
&\qquad \times \mathrm{d}\,{}_3\boldsymbol{x} \,\mathrm{d}\,{}_2\boldsymbol{x} \,\mathrm{d}\,{}_3\boldsymbol{V} \,\mathrm{d}\,{}_2\boldsymbol{V} \,\mathrm{d}\boldsymbol{X} \,\mathrm{d}\boldsymbol{b} \\
&- \frac{\epsilon_{i3j}\epsilon_{3kl}}{4\pi\Theta^S} \frac{\partial}{\partial\,{}_1V_i} \int {}_1g_p \frac{\left({}_1x_j - X_{jq}\,{}_1g_q\right)\left({}_2x_k - X_{kr}\,{}_2g_r\right)}{\left|{}_3\boldsymbol{x} - {}_2\boldsymbol{x}\right|} \frac{\partial\,{}_2g_p}{\partial\,{}_2x_l} \left({}_3V_m \frac{\partial}{\partial\,{}_3x_m}\right)^2 {}_3f \times \\
&\qquad \times \mathrm{d}\,{}_3\boldsymbol{x} \,\mathrm{d}\,{}_2\boldsymbol{x} \,\mathrm{d}\,{}_3\boldsymbol{V} \,\mathrm{d}\,{}_2\boldsymbol{V} \,\mathrm{d}\boldsymbol{X} \,\mathrm{d}\boldsymbol{b} \\
&+ \frac{\epsilon_{i3j}\epsilon_{3kl}}{\mathrm{Re}\,\Theta^S} \frac{\partial}{\partial\,{}_1V_i} \int {}_1g_p \left({}_1x_j - X_{jq}\,{}_1g_q\right)\left({}_2x_k - X_{kr}\,{}_2g_r\right) \delta\left({}_3\boldsymbol{x} - {}_2\boldsymbol{x}\right) \frac{\partial\,{}_2g_p}{\partial\,{}_2x_j} \times \\
&\qquad \times \left({}_3V_i \frac{\partial\,{}_3f}{\partial\,{}_3x_j} + {}_3V_j \frac{\partial\,{}_3f}{\partial\,{}_3x_i}\right) \mathrm{d}\,{}_3\boldsymbol{x} \,\mathrm{d}\,{}_2\boldsymbol{x} \,\mathrm{d}\,{}_3\boldsymbol{V} \,\mathrm{d}\,{}_2\boldsymbol{V} \,\mathrm{d}\boldsymbol{X} \,\mathrm{d}\boldsymbol{b} \\
&+ \frac{\partial}{\partial\,{}_1V_i} \int \left({}_1g_p \frac{\epsilon_{3jk}\left({}_1x_j - X_{jq}\,{}_1g_q\right)}{\left|{}_1\boldsymbol{x} - \boldsymbol{X}\cdot{}_1\boldsymbol{g}\right|^2} \left({}_1V_k - \int \delta\left({}_2\boldsymbol{x} - \boldsymbol{X}\cdot{}_1\boldsymbol{g}\right) {}_2V_k \,\mathrm{d}\,{}_2\boldsymbol{x}\right)\right)^2 \times \\
&\qquad \times \left({}_1x_i - X_{ir}\,{}_1g_r\right) \mathrm{d}\,{}_2\boldsymbol{V} \,\mathrm{d}\boldsymbol{X} \,\mathrm{d}\boldsymbol{b}.
\end{aligned}
\tag{3.88}
$$

As expected, the marginal velocity PDF is not solely sufficient to describe the system, it depends on different multi-point joint PDFs, ranging from the single point PDF in the active stress term to the three point PDFs in the particle translational and rotational velocity terms.

Particle position marginal PDF

The material derivative of the particle position marginal PDF is

$$
\begin{aligned}
\frac{\mathrm{d}f^X}{\mathrm{d}t} &= -\frac{\partial}{\partial X_{ip}} \left\langle \frac{\mathrm{d}\chi_{ip}}{\mathrm{d}t} \widehat{f}^X \right\rangle = -\frac{\partial}{\partial X_{ip}} \left\langle v_{ip} \widehat{f}^X \right\rangle \\
&= -\frac{\partial}{\partial X_{ip}} \left\langle \int \delta\left({}_1\boldsymbol{x} - \boldsymbol{\chi}\cdot{}_1\gamma\right) {}_1U_i\,{}_1\gamma_p \widehat{f}^X \,\mathrm{d}\,{}_1\boldsymbol{x} \right\rangle \\
&= -\frac{\partial}{\partial X_{ip}} \int \delta\left({}_1\boldsymbol{x} - \boldsymbol{X}\cdot{}_1\boldsymbol{g}\right) {}_1V_i\,{}_1g_p\,{}_1f \,\mathrm{d}\,{}_1\boldsymbol{x} \,\mathrm{d}\,{}_1\boldsymbol{V} \,\mathrm{d}\boldsymbol{b}
\end{aligned}
\tag{3.89}
$$

Note that the PDF f^X is not a function of the Eulerian coordinate x_i. Hence, it is necessary to introduce the integration with respect to ${}_1x_i$ in order to introduce the single point joint PDF.

Similarly to the velocity marginal PDF, the particle position marginal PDF depends on the joint PDF of the velocity, particle position and particle orientation. Due to the Lagrangian nature of the particle position, only the single-point joint PDF appears in (3.89).

Particle orientation marginal PDF

The material derivative of the particle orientation marginal PDF leads to the following equation of motion

$$\begin{aligned}\frac{\mathrm{d}f^b}{\mathrm{d}t} &= -\frac{\partial}{\partial b_p}\left\langle \frac{\mathrm{d}\beta_p}{\mathrm{d}t}\widehat{f}^b \right\rangle = -\frac{\partial}{\partial b_p}\left\langle \omega_p \widehat{f}^b \right\rangle \\ &= -\frac{\partial}{\partial b_p}\left\langle {}_1\gamma_p \frac{\epsilon_{3ij}\left({}_1x_i - \chi_{ip}\,{}_1\gamma_p\right)}{\left|{}_1\boldsymbol{x} - \boldsymbol{\chi}\cdot{}_1\boldsymbol{\gamma}\right|^2}\left({}_1U_j - \int \delta\left({}_2\boldsymbol{x} - \boldsymbol{\chi}\cdot{}_1\boldsymbol{\gamma}\right){}_2U_j \,\mathrm{d}\,{}_2\boldsymbol{x}\right)\widehat{f}^b \right\rangle \\ &= -\frac{\partial}{\partial b_p}\int {}_1g_p \frac{\epsilon_{3ij}\left({}_1x_i - X_{ip}\,{}_1g_p\right)}{\left|{}_1\boldsymbol{x} - \boldsymbol{X}\cdot{}_1\boldsymbol{g}\right|^2}\left({}_1V_j - \delta\left({}_2\boldsymbol{x} - \boldsymbol{X}\cdot{}_1\boldsymbol{g}\right){}_2V_j\right){}_2f \,\mathrm{d}\,{}_2\boldsymbol{x}\,\mathrm{d}\,{}_1\boldsymbol{x}\,\mathrm{d}\,{}_2\boldsymbol{V}\,\mathrm{d}\,{}_1\boldsymbol{V}\,\mathrm{d}\boldsymbol{X},\end{aligned} \tag{3.90}$$

where (2.91) is used to express the rotational velocity of the particle in terms of the single-field velocity. Due to the dependency of the rotational velocity $\omega_p = \epsilon_{3ij} r_i U_j / \left|\boldsymbol{r}\right|$ on the radial vector $r_i = {}_1x_i - \chi_{ip}\,{}_1\gamma_p$ the two-point joint PDF occurs in (3.90). Nevertheless, the PDF f^b itself does not depend on the Eulerian coordinates of the domain.

3.4.3. Multi-point joint PDF

The equations of motion for the marginal PDFs (3.88), (3.89) and (3.90) all depend on multi-point joint PDFs ${}_K f$, which are necessary to fully describe the statistical behaviour of an active suspension. The single-point joint PDF is

$$ {}_1 f\left({}_1\boldsymbol{V}, \boldsymbol{X}, \boldsymbol{b}\right) = \left\langle \delta\left({}_1\boldsymbol{V} - {}_1\boldsymbol{U}\right) \delta\left(\boldsymbol{X} - \boldsymbol{\chi}\right) \delta\left(\boldsymbol{b} - \boldsymbol{\beta}\right) \right\rangle . \tag{3.91} $$

It should be noted that the joint PDF is not the product of the marginal PDFs, i.e.

$$ {}_1 f\left({}_1\boldsymbol{V}, \boldsymbol{X}, \boldsymbol{b}\right) \neq {}_1 f^V f^X f^b, \tag{3.92} $$

but instead the averaged product of the marginal fine-grained PDF

$$ {}_1 f\left({}_1\boldsymbol{V}, \boldsymbol{X}, \boldsymbol{b}\right) = \left\langle {}_1\widehat{f}^V \widehat{f}^X \widehat{f}^b \right\rangle , \tag{3.93} $$

because the three variables are statistically dependent. The K-point PDF is

$$ {}_K f\left({}_1\boldsymbol{V}, \ldots, {}_K\boldsymbol{V}, \boldsymbol{X}, \boldsymbol{b}\right) = \left\langle \delta\left(\prod_{k=1}^{K} {}_k\boldsymbol{V} - {}_1\boldsymbol{U}\right) \delta\left(\boldsymbol{X} - \boldsymbol{\chi}\right) \delta\left(\boldsymbol{b} - \boldsymbol{\beta}\right) \right\rangle . \tag{3.94} $$

Subsequently, the material derivative of ${}_K f$ is obtained with the product rule

$$ \begin{aligned} \frac{\mathrm{d}\,{}_K f}{\mathrm{d}t} =& \left\langle \prod_{k=1}^{K} \delta\left({}_k\boldsymbol{V} - {}_k\boldsymbol{U}\right) \frac{\mathrm{d}\delta\left(\boldsymbol{X} - \boldsymbol{\chi}\right)}{\mathrm{d}t} \delta\left(\boldsymbol{b} - \boldsymbol{\beta}\right) \right\rangle \\ & + \left\langle \prod_{k=1}^{K} \delta\left({}_k\boldsymbol{V} - {}_k\boldsymbol{U}\right) \delta\left(\boldsymbol{X} - \boldsymbol{\chi}\right) \frac{\mathrm{d}\delta\left(\boldsymbol{b} - \boldsymbol{\beta}\right)}{\mathrm{d}t} \right\rangle \\ & + \sum_{k=1}^{K} \left\langle \prod_{i=1}^{k-1} \delta\left({}_i\boldsymbol{V} - {}_i\boldsymbol{U}\right) \frac{\mathrm{d}\delta\left({}_k\boldsymbol{V} - {}_k\boldsymbol{U}\right)}{\mathrm{d}t} \prod_{j=k+1}^{K} \delta\left({}_j\boldsymbol{V} - {}_j\boldsymbol{U}\right) \delta\left(\boldsymbol{X} - \boldsymbol{\chi}\right) \delta\left(\boldsymbol{b} - \boldsymbol{\beta}\right) \right\rangle . \\ =& \frac{\partial}{\partial X_{ip}} \left\langle \frac{\mathrm{d}\chi_{ip}}{\mathrm{d}t} {}_K\widehat{f}^V \widehat{f}^X \widehat{f}^b \right\rangle + \frac{\partial}{\partial b_p} \left\langle \frac{\mathrm{d}\beta_p}{\mathrm{d}t} {}_K\widehat{f}^V \widehat{f}^X \widehat{f}^b \right\rangle + \sum_{k=1}^{K} \frac{\partial}{\partial\,{}_k V_i} \left\langle \frac{\mathrm{d}\,{}_k U_i}{\mathrm{d}t} {}_K\widehat{f}^V \widehat{f}^X \widehat{f}^b \right\rangle \end{aligned} \tag{3.95} $$

Hence, it is possible to construct the multi-point joint PDF for all three sample space variables from the marginal PDFs for the individual variables. The hierarchy of equations of motion for the K-point PDF is

$$
\begin{aligned}
&\frac{\mathrm{d}\,{}_{K}f}{\mathrm{d}t} = \frac{\partial\,{}_{K}f}{\partial t} + \sum_{k=1}^{K} {}_{k}V_i \frac{\partial\,{}_{K}f}{\partial\,{}_{k}x_i} = -\frac{\partial}{\partial X_{ip}} \delta\left({}_{1}\boldsymbol{x} - \boldsymbol{X} \cdot {}_{1}\boldsymbol{g}\right) {}_{1}V_i\, {}_{1}g_p\, {}_{K}f \\
&- \frac{\partial}{\partial b_p}\, {}_{1}\!\int g_p \frac{\epsilon_{3ij}\left({}_{1}x_i - X_{ip}\, {}_{1}g_p\right)}{\left|{}_{1}\boldsymbol{x} - \boldsymbol{X} \cdot {}_{1}\boldsymbol{g}\right|^2} \left({}_{1}V_j - \delta\left({}_{K+1}\boldsymbol{x} - \boldsymbol{X} \cdot {}_{1}\boldsymbol{g}\right) {}_{K+1}V_j\right) {}_{K+1}f \,\mathrm{d}\,{}_{K+1}\boldsymbol{x} \,\mathrm{d}\,{}_{K+1}\boldsymbol{V} \\
&+ \sum_{k=1}^{K} \frac{1}{4\pi} \frac{\partial}{\partial\,{}_{k}V_i} \int {}_{k}g^F \frac{\partial}{\partial\,{}_{k}x_i} \frac{1}{\left|{}_{K+1}\boldsymbol{x} - {}_{k}\boldsymbol{x}\right|} \left({}_{K+1}V_j \frac{\partial}{\partial\,{}_{K+1}x_j}\right)^2 {}_{K+1}f \,\mathrm{d}\,{}_{K+1}\boldsymbol{x} \,\mathrm{d}\,{}_{K+1}\boldsymbol{V} \\
&- \sum_{k=1}^{K} \frac{1}{\mathrm{Re}} \frac{\partial}{\partial\,{}_{k}V_i} \int \delta\left({}_{K+1}\boldsymbol{x} - {}_{k}\boldsymbol{x}\right) {}_{k}g^F\, {}_{K+1}V_i \frac{\partial^2\, {}_{K+1}f}{\partial\,{}_{K+1}x_j{}^2} \,\mathrm{d}\,{}_{K+1}\boldsymbol{x} \,\mathrm{d}\,{}_{K+1}\boldsymbol{V} \\
&- \sum_{k=1}^{K} A^c \frac{\partial}{\partial\,{}_{k}V_i} \delta\left({}_{k}\boldsymbol{x} - \widehat{\Gamma}^{ac}\right) \left(\frac{\partial\,{}_{k}h}{\partial\,{}_{k}x_i} \frac{\partial\,{}_{k}h}{\partial\,{}_{k}x_j} \widehat{e}_{jp} - \widehat{e}_{ip}\right) {}_{k}g_p\, {}_{K}f \\
&- \sum_{k=1}^{K} \frac{1}{4\pi V^P \mathfrak{D}} \frac{\partial}{\partial\,{}_{k}V_i} \int {}_{k}g_p \frac{1}{\left|{}_{K+2}\boldsymbol{x} - {}_{K+1}\boldsymbol{x}\right|} \frac{\partial\,{}_{K+1}g_p}{\partial\,{}_{K+1}x_i} \left({}_{K+2}V_j \frac{\partial}{\partial\,{}_{K+2}x_j}\right)^2 {}_{K+2}f \times \\
&\quad \times \mathrm{d}\,{}_{K+2}\boldsymbol{x} \,\mathrm{d}\,{}_{K+1}\boldsymbol{x} \,\mathrm{d}\,{}_{K+2}\boldsymbol{V} \,\mathrm{d}\,{}_{K+1}\boldsymbol{V} \\
&+ \sum_{k=1}^{K} \frac{1}{\mathrm{Re}\, V^P \mathfrak{D}} \frac{\partial}{\partial\,{}_{k}V_i} \int {}_{k}g_p \delta\left({}_{K+2}\boldsymbol{x} - {}_{K+1}\boldsymbol{x}\right) \frac{\partial\,{}_{K+1}g_p}{\partial\,{}_{K+1}x_j} \times \\
&\quad \times \left({}_{K+2}V_i \frac{\partial\,{}_{K+2}f}{\partial\,{}_{K+2}x_j} + {}_{K+2}V_j \frac{\partial\,{}_{K+2}f}{\partial\,{}_{K+2}x_i}\right) \mathrm{d}\,{}_{K+2}\boldsymbol{x} \,\mathrm{d}\,{}_{K+1}\boldsymbol{x} \,\mathrm{d}\,{}_{K+2}\boldsymbol{V} \,\mathrm{d}\,{}_{K+1}\boldsymbol{V} \\
&- \sum_{k=1}^{K} \frac{\epsilon_{i3j}\epsilon_{3kl}}{4\pi\Theta^S} \frac{\partial}{\partial\,{}_{k}V_i} \int {}_{k}g_p \frac{\left({}_{k}x_j - X_{jq}\, {}_{k}g_q\right)\left({}_{K+1}x_k - X_{kr}\, {}_{K+1}g_r\right)}{\left|{}_{K+2}\boldsymbol{x} - {}_{K+1}\boldsymbol{x}\right|} \frac{\partial\,{}_{K+1}g_p}{\partial\,{}_{K+1}x_l} \times \\
&\quad \times \left({}_{K+2}V_m \frac{\partial}{\partial\,{}_{K+2}x_m}\right)^2 {}_{K+2}f \,\mathrm{d}\,{}_{K+2}\boldsymbol{x} \,\mathrm{d}\,{}_{K+1}\boldsymbol{x} \,\mathrm{d}\,{}_{K+2}\boldsymbol{V} \,\mathrm{d}\,{}_{K+1}\boldsymbol{V} \\
&+ \sum_{k=1}^{K} \frac{\epsilon_{i3j}\epsilon_{3kl}}{\mathrm{Re}\,\Theta^S} \frac{\partial}{\partial\,{}_{k}V_i} \int {}_{k}g_p \left({}_{k}x_j - X_{jq}\, {}_{k}g_q\right)\left({}_{K+1}x_k - X_{kr}\, {}_{K+1}g_r\right) \delta\left({}_{K+2}\boldsymbol{x} - {}_{K+1}\boldsymbol{x}\right) \times \\
&\quad \times \frac{\partial\,{}_{K+1}g_p}{\partial\,{}_{K+1}x_j} \left({}_{K+2}V_i \frac{\partial\,{}_{K+2}f}{\partial\,{}_{K+2}x_j} + {}_{K+2}V_j \frac{\partial\,{}_{K+2}f}{\partial\,{}_{K+2}x_i}\right) \mathrm{d}\,{}_{K+2}\boldsymbol{x} \,\mathrm{d}\,{}_{K+1}\boldsymbol{x} \,\mathrm{d}\,{}_{K+2}\boldsymbol{V} \,\mathrm{d}\,{}_{K+1}\boldsymbol{V} \\
&+ \sum_{k=1}^{K} \frac{\partial}{\partial\,{}_{k}V_i} \int \left({}_{k}g_p \frac{\epsilon_{3jk}\left({}_{k}x_j - X_{jq}\, {}_{k}g_q\right)}{\left|{}_{k}\boldsymbol{x} - \boldsymbol{X} \cdot {}_{k}\boldsymbol{g}\right|^2} \left({}_{k}V_k \right.\right. \\
&\quad \left.\left. - \int \delta\left({}_{K+1}\boldsymbol{x} - \boldsymbol{X} \cdot {}_{k}\boldsymbol{g}\right) {}_{K+1}V_k \,\mathrm{d}\,{}_{K+1}\boldsymbol{x}\right)\right)^2 \left({}_{k}x_i - X_{ir}\, {}_{k}g_r\right) \mathrm{d}\,{}_{K+1}\boldsymbol{V}. \qquad (3.96)
\end{aligned}
$$

This equation depends on the K-point PDF and the $(K+1)$- and $(K+2)$-point PDF, leading to an infinite hierarchy of equations, similar to the LMN-hierarchy [142, 153, 157]. Thus, similar to the statistical equations of turbulence research, the equations for an active suspension show a closure problem. Furthermore, within each term of the equation, the PDF appears only in a linear form. This is an important property, which will be used to obtain additional statistical symmetries in Sec. 3.6.

3.4.4. Continuity conditions

Continuity conditions are necessary to define in analogy to the side conditions of the LMN hierarchy. The divergence of the single-field velocity is

$$\begin{aligned}
\frac{\partial {}_1U_i}{\partial {}_1x_i} &= {}_1\gamma^F \frac{\partial {}_1u_i^F}{\partial {}_1x_i} + {}_1\gamma^S \frac{\partial {}_1u_i^S}{\partial {}_1x_i} + \left({}_1u_i^S - {}_1u_i^F\right) \frac{\partial {}_1\gamma^S}{\partial {}_1x_i} \\
&= {}_1\gamma^F \frac{\partial {}_1u_i^F}{\partial {}_1x_i} + {}_1\gamma^S \frac{\partial {}_1u_i^S}{\partial {}_1x_i} + \left({}_1u_i^F - {}_1u_i^S\right) \delta\left(\phi\right) \frac{\partial {}_1\phi}{\partial {}_1x_i} \\
&= {}_1\gamma^F \frac{\partial {}_1u_i^F}{\partial {}_1x_i} + {}_1\gamma^S \frac{\partial {}_1u_i^S}{\partial {}_1x_i} + \left({}_1u_i^F - {}_1u_i^S\right) n_i \delta\left(\phi\right),
\end{aligned} \tag{3.97}$$

where in the last step $|\nabla\phi| = 1$ was assumed. The first two terms in (3.97) refer to the single-phase continuity equations for the solid phase (2.50) and the fluid phase (2.65), the last term describes a jump condition of the velocity in normal direction at the particle surface. Due to the no-slip condition (2.92) at the passive surface and the impermeability (2.93) of the active surface the jump $\left({}_1u_i^F - {}_1u_i^S\right) n_i$ vanishes. Both surface continuity conditions can be transformed into the sample space. At the passive boundary the no-slip condition (2.92) turns into

$$\int \delta\left({}_1\boldsymbol{x} - \widehat{\Gamma}^{pa}\right) {}_1V_i\, {}_1f \,\mathrm{d}\,{}_1\boldsymbol{x} = \int \delta\left({}_1\boldsymbol{x} - \widehat{\Gamma}^{pa}\right) \delta\left({}_2\boldsymbol{x} - {}_1\boldsymbol{x}\right) {}_2V_i\, {}_2f \,\mathrm{d}\,{}_2\boldsymbol{x}\,\mathrm{d}\,{}_1\boldsymbol{x}\,\mathrm{d}\,{}_2\boldsymbol{V} \tag{3.98}$$

and the impermeability condition at the active boundary (2.93) is

$$\begin{aligned}
&\int \delta\left({}_1\boldsymbol{x} - \widehat{\Gamma}^{ac}\right) \frac{\partial {}_1h}{\partial {}_1x} {}_1V_i \,\mathrm{d}\,{}_1\boldsymbol{x} \\
&\qquad = \int \delta\left({}_1\boldsymbol{x} - \widehat{\Gamma}^{ac}\right) \delta\left({}_2\boldsymbol{x} - {}_1\boldsymbol{x}\right) \frac{\partial {}_2h}{\partial {}_2x} {}_2V_i\, {}_2f \,\mathrm{d}\,{}_2\boldsymbol{x}\,\mathrm{d}\,{}_1\boldsymbol{x}\,\mathrm{d}\,{}_2\boldsymbol{V}.
\end{aligned} \tag{3.99}$$

Due to the vanishing jump in (3.97), the only remaining terms are the two continuity equations for the fluid and solid phase. Thus, forming the ensemble average delivers the continuity condition

$$\left\langle \frac{\partial {}_1U_i}{\partial {}_1x_i} \right\rangle = \int \left\langle \frac{\partial {}_1U_i}{\partial x_i} {}_1\widehat{f}^V \right\rangle \mathrm{d}\,{}_1\boldsymbol{V} = \frac{\partial}{\partial {}_1x_i} \int {}_1V_i\, {}_1f^V \,\mathrm{d}\,{}_1\boldsymbol{V} = 0. \tag{3.100}$$

As a result of this, the multi-point version of the continuity equation is given by a simple integration with respect to the missing sample space variables

$$\frac{\partial}{\partial {}_kx_i} \int {}_kV_i\, {}_Kf \prod_{j=1}^{K} \mathrm{d}\,{}_j\boldsymbol{V}\,\mathrm{d}\boldsymbol{X}\,\mathrm{d}\boldsymbol{b} = 0 \quad \forall\, {}_k\boldsymbol{x} \in \Omega. \tag{3.101}$$

Both formulations (3.100) and (3.101) are equivalent because of the reduction property (3.66).

3.4.5. Entropy of an active suspension

The statistical information about the probability of a certain event is related to the physical quantity of entropy. The entropy serves as a measure to compare two different random systems and is defined as

$$S = -\int {}_K f \log\left({}_K f\right) \prod_{k=1}^{K} \mathrm{d}\,{}_k\boldsymbol{V}\,\mathrm{d}\boldsymbol{X}\,\mathrm{d}\boldsymbol{b} \tag{3.102}$$

based on Boltzmann's equation [32]. Temporal derivation delivers

$$\frac{dS}{dt} = -\int \frac{d\,{}_K f}{dt}\left(\log\left({}_K f\right) + 1\right) \prod_{k=1}^{K} \mathrm{d}\,{}_k\boldsymbol{V}\,\mathrm{d}\boldsymbol{X}\,\mathrm{d}\boldsymbol{b}. \tag{3.103}$$

Thus, the transport equation (3.96) of the multi-point PDF hierarchy also describes the evolution of the entropy.

Consider two suspensions, one contains active particles and the second one consists of otherwise identical passive particles, i.e. $A^c = 0$. The only difference in (3.96) is the existence of the active stress term in the case of active particles. Thus, the difference between the rate of change of the entropy of an active and a passive suspension is

$$\begin{aligned}\frac{dS^{ac}}{dt} - \frac{dS^{pa}}{dt} = \int \sum_{k=1}^{K} A^c \frac{\partial}{\partial\,{}_k V_i}\delta\left({}_k\boldsymbol{x} - \widehat{\Gamma}^{ac}\right)\left(\frac{\partial\,{}_k h}{\partial\,{}_k x_i}\frac{\partial\,{}_k h}{\partial\,{}_k x_j}\widehat{e}_{jp} - \widehat{e}_{ip}\right){}_k g_p\,{}_K f \times \\ \times \left(\log\left({}_K f\right) + 1\right) \prod_{k=1}^{K} \mathrm{d}\,{}_k\boldsymbol{V}\,\mathrm{d}\boldsymbol{X}\,\mathrm{d}\boldsymbol{b}.\end{aligned} \tag{3.104}$$

The main question arising from this expression and in fact one of the main questions in research on active suspensions is the sign of the integral term in (3.104), or, in other words, whether the active stress causes states which occur unlikely in a passive suspension.

3.5. Classical symmetries of the PDF hierarchy

Classical symmetries, as found in the physical equations, are preserved in the multi-point PDF hierarchy (3.96) with some modifications. The symmetries are [202]

$$\begin{aligned} T_t:\quad & t^* = t + c_t, \quad x_i^* = x_i, \quad V_i^* = V_i, \quad X_{ip}^* = X_{ip}, \\ & b_p^* = b_p, \quad {}_K f^* = {}_K f, \quad A^{c*} = A^c, \end{aligned} \tag{3.105a}$$

$$\begin{aligned} T_{\mathrm{Rot}}:\quad & x_i^* = Q_{ij}x_j, \quad V_i^* = Q_{ij}V_i, \quad p^{F*} = p^F, \quad X_{ip}^* = Q_{ij}X_{jp}, \\ & b_p^* = b_p - \varphi, \quad {}_K f^* = {}_K f, \quad A^{c*} = A^c, \end{aligned} \tag{3.105b}$$

$$\begin{aligned} T_{\mathrm{G}}:\quad & t^* = t, \quad x_i^* = x_i + c_{\mathrm{G},i}, \quad V_i^* = V_i, \quad X_{ip}^* = X_{ip} + c_{\mathrm{G},i}\gamma_p, \\ & b_p^* = b_p, \quad {}_K f^* = {}_K f, \quad A^{c*} = A^c, \end{aligned} \tag{3.105c}$$

$$\begin{aligned} T_{\mathrm{Sc1}}:\quad & t^* = te^{2c_{\mathrm{Sc1}}}, \quad x_i^* = x_i e^{c_{\mathrm{Sc1}}}, \quad V_i^* = V_i e^{-c_{\mathrm{Sc1}}}, \quad X_{ip}^* = X_{ip}e^{c_{\mathrm{Sc1}}}, \\ & b_p^* = b_p, \quad {}_K f^* = {}_K f e^{dK c_{\mathrm{Sc1}}}, \quad A^{c*} = A^c e^{-3c_{\mathrm{Sc1}}}, \end{aligned} \tag{3.105d}$$

$$\begin{aligned} T_{\beta}:\quad & t^* = t, \quad x_i^* = x_i, \quad V_i^* = V_i, \quad X_{ip}^* = X_{ip}, \\ & b_p^* = b_p + c_b, \quad {}_K f^* = {}_K f, \quad A^{c*} = A^c. \end{aligned} \tag{3.105e}$$

The temporal shift transformation (3.105a) and the rotational transformation (3.105b) are identical to the equivalent symmetry transformation of the Navier-Stokes or Stokes equation. The only difference is that the physical variables are replaced by their counterparts in the sample space. The generalised Galilean symmetry can no longer be applied in the form given in (3.45c). As already stated in Wacławczyk et al. [202], the function $f_{\mathrm{G},i} = c_{\mathrm{G},i}t$ to be added to x_i can only depend linearly upon time, because a time-dependent transformation would require the transformation for the pressure

$$p^{F*} = p^F - x_i f''_{\mathrm{G},i}(t) \tag{3.106}$$

in the physical space, see (3.31c). The expression (3.106) is unbounded and, thus, not compatible with the integral representation (3.78) of the pressure introduced in the PDF-hierarchy [202]. Furthermore, the velocity sample space variable occurs explicitly in the first term of the right hand side of (3.96). Therefore, only a constant spatial shift $c_{\mathrm{G},i}$ is possible, see (3.105c); thus, the Galilean symmetry of (3.96) is identical to the Galilean symmetry (3.50c) of the suspension, where the fluid is described by the unsteady Stokes equation.

The scaling symmetry (3.105d) was derived by Wacławczyk et al. [202], where it is especially important for the multi-point PDF to be scaled as well. They wrote the scaling as ${}_Kf^* = {}_Kfe^{3Kc_{\mathrm{Sc1}}}$, however, the exponent depends on the number of spatial dimensions under consideration. Let us assume that the exponent of the scaling exponential function of the multi-point PDF is unknown and denoted by C_k. From the reduction property one obtains

$$\int {}_1f^V \,\mathrm{d}\,{}_1\boldsymbol{V} = \int {}_1f^{V*}e^{-C_1}\,\mathrm{d}\,{}_1\boldsymbol{V}^*e^{dc_{\mathrm{Sc1}}} = 1, \tag{3.107}$$

hence, the scaling exponent of the single-point PDF is $C_1 = dc_{\mathrm{Sc1}}$, where d is the number of spatial dimensions. Due to the restriction to two dimensions we have $d = 2$. For an arbitrary order of the PDF the relation becomes

$$\int {}_{K+1}f^V \,\mathrm{d}\,{}_1\boldsymbol{V} = \int {}_{K+1}f^{V*}e^{-C_{K+1}}\,\mathrm{d}\,{}_{K+1}\boldsymbol{V}^*e^{dc_{\mathrm{Sc1}}} = e^{-C_K}\,{}_Kf^{V*} = {}_Kf^V, \tag{3.108}$$

leading to $C_K = C_{K+1} - dc_{\mathrm{Sc1}}$. Combined with the previous result (3.107) one obtains $C_K = dKc_{\mathrm{Sc1}}$ and $C_{K+1} = d(K+1)c_{\mathrm{Sc1}}$, which, subsequently, leads to the transformation (3.105d).

While ${}_1V_i$ appears directly in (3.96) and cannot be shifted, resulting in the constant spatial shift in T_{G}, the orientation sample space variable does not occur directly in (3.96). Hence, the shift in the orientation is preserved from the physical equations, see (3.105e). However, because b_p dictates the behaviour of ${}_kg$, $\widehat{\Gamma}^{ac}$ and $\widehat{e}_{ip}$ in (3.96), the same restrictions as in the physical system apply, i.e. (3.105e) is only applicable in a passive suspension with disk-shaped particles.

The pressure was expressed in terms of the velocity by Green's function (3.78), thus, the pressure related transformation (3.31d) of the Navier-Stokes equation is not applicable to the PDF hierarchy. For the same reason, the active stress transformation T_{Ac} is not a symmetry of the PDF hierarchy, because the sample space variable ${}_{K+1}V_i$ occurs quadratic in the pressure term.

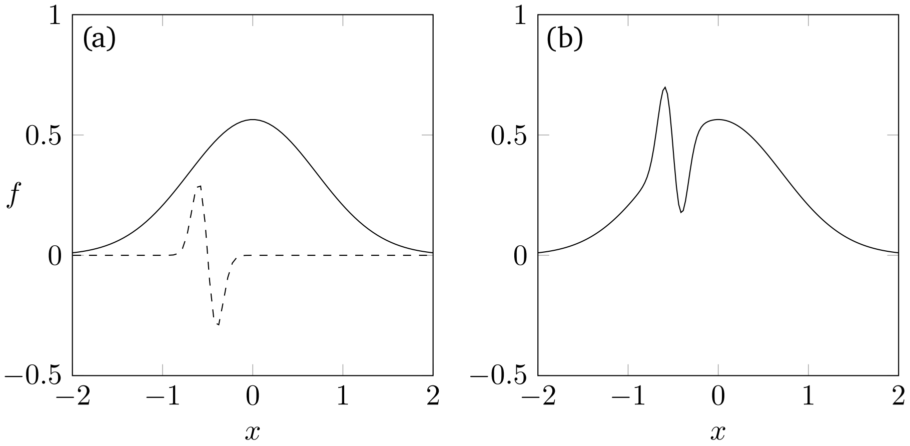

Fig. 3.1.: The two diagrams visualise the action of the free function ψ on an initial PDF. (a) The initial PDF (——) is a normal distribution in this example, the integral of ψ (- - -) over the entire domain vanishes. (b) The transformed PDF $f^* = f + \psi$. Illustration based on Wacławczyk et al. [202].

3.6. Statistical symmetries

Additional symmetries occur in the statistical description of the problem, which are not present in the physical equations. Nevertheless the statistical symmetries carry information about physical properties of the problem. An infinite number of statistical transformation groups of the multi-point correlation equation were discovered by Oberlack and Rosteck [158] and Rosteck and Oberlack [177]. Building on this, Wacławczyk et al. [202] found a symmetry transformation group for the LMN hierarchy, which will serve as a basis for the following examinations: the equations of motion for the multi-point PDF are entirely linear, hence, it is possible to add any solution of the equation hierarchy to the multi-point PDF, similar to the linear symmetry of the Stokes equation (3.36g). However, the properties of the PDF, especially the reduction property, restrict the possible solutions to be added. In order to obey the reduction property either the integral value of the added solution ψ needs to vanish, i.e. $\int_{-\infty}^{\infty} \psi\left(\mathfrak{U}\right) \mathrm{d}\mathfrak{U} = 0$ or, both, the multi-point PDF ${}_K f$ and the added solution needs to be rescaled. Both possibilities were explored by Wacławczyk et al. [202] and are discussed in the following two sections for the case of an active suspension.

3.6.1. Shape symmetry

The first statistical symmetry given by Wacławczyk et al. [202] is the shape symmetry. An exemplary shape symmetry transformation, changing the PDF, is given in Fig. 3.1. Extending the symmetry to the sample space spanned by the sample space variables for the velocity V_i, the position X_{ip} and the orientation b_p delivers

$$T_s : \quad {}_K f^* = {}_K f + \psi\left({}_1\boldsymbol{V}, \boldsymbol{X}_1, b_1\right) \prod_{k=2}^{K} \delta\left({}_k\boldsymbol{V} - {}_1\boldsymbol{V}\right) \prod_{p=2}^{N} \delta\left(\boldsymbol{X}_p - \boldsymbol{X}_1\right) \delta\left(b_p - b_1\right). \tag{3.109}$$

The only known constraint for the free function $\psi\left({}_1\boldsymbol{V}, \boldsymbol{X}_1, b_1\right)$ is

$$\int \psi\left({}_1\boldsymbol{V}, \boldsymbol{X}_1, b_1\right) \mathrm{d}\,{}_1\boldsymbol{V}\, \mathrm{d}\boldsymbol{X}_1\, \mathrm{d}b_1 = 0 \tag{3.110}$$

to ensure that ${}_K f^*$ complies to the reduction property (3.66). Furthermore, (3.66) requires

$$\int \psi\left({}_1\boldsymbol{V}, \boldsymbol{X}_1, b_1\right) \mathrm{d}\,{}_1\boldsymbol{V} = \psi^{Xb}\left(\boldsymbol{X}_1, b_1\right), \quad \int \psi^{Xb}\left(\boldsymbol{X}_1, b_1\right) \mathrm{d}\boldsymbol{X}_1 = \psi^{b}\left(b_1\right), \tag{3.111}$$

where analogous statements result from integration with respect to the other sample space variables. Subsequently, it can be assumed that the free function $\psi\left({}_1\boldsymbol{V}, \boldsymbol{X}_1, b_1\right)$ can be written as a linear combination

$$\psi\left({}_1\boldsymbol{V}, \boldsymbol{X}_1, b_1\right) = \psi^{V}\left({}_1\boldsymbol{V}\right) + \psi^{X}\left(\boldsymbol{X}_1\right) + \psi^{b}\left(b_1\right), \tag{3.112}$$

where the integral on an infinite domain of each of the functions ψ^V, ψ^X and ψ^b vanishes according to (3.110). The Lie operator corresponding to the transformation (3.109) is

$$\mathfrak{X} = \psi\left({}_1\boldsymbol{V}, \boldsymbol{X}_1, b_1\right) \prod_{k=2}^{K} \delta\left({}_k\boldsymbol{V} - {}_1\boldsymbol{V}\right) \prod_{p=2}^{N} \delta\left(\boldsymbol{X}_p - \boldsymbol{X}_1\right) \delta\left(b_p - b_1\right) \frac{\partial}{\partial\, {}_K f}. \tag{3.113}$$

Forming the marginal PDFs by an integration with respect to the different sample space variables delivers the transformations

$${}_K f^{V*} = {}_K f^{V} + \psi^{V}\left({}_1\boldsymbol{V}\right) \prod_{k=2}^{K} \delta\left({}_k\boldsymbol{V} - {}_1\boldsymbol{V}\right), \tag{3.114a}$$

$$f^{X*} = f^{X} + \psi^{X}\left(\boldsymbol{X}_1\right) \prod_{p=2}^{N} \delta\left(\boldsymbol{X}_p - \boldsymbol{X}_1\right), \tag{3.114b}$$

$$f^{b*} = f^{b} + \psi^{b}\left(b_1\right) \prod_{p=2}^{N} \delta\left(b_p - b_1\right). \tag{3.114c}$$

Especially in the case of the particle position and orientation PDF an interesting property of an active suspension directly follows from (3.114b) and (3.114c). The functions ψ^X and ψ^b only depend on the respective sample space variable for the first particle, whereas the transformed PDFs f^{X*} and f^{b*} describe all particles. The choice of the particle described by the sample space variables $\boldsymbol{X}_1$ and b_1 is arbitrary. Hence, the global PDF and the statistical behaviour of any particle only depends on the global state of the suspension and not on the individual state of a single particle.

The function ψ does not depend on space or time. Subsequently, the separation property of a PDF (3.67) is broken, which, however, was not used in the derivation of the PDF equation hierarchy. It follows that, especially in the physical interpretation of the symmetry, it can only be valid in a spatially confined area, since the separation property is a necessary condition of a PDF.

Separation of space and time

A linear combination of the operators of the shape symmetry (3.109) and the temporal shift (3.105a) delivers

$$\mathfrak{X} = \frac{\partial}{\partial t} + \psi\left({}_1\boldsymbol{V}, \boldsymbol{X}_1, b_1\right) \prod_{k=2}^{K} \delta\left({}_k\boldsymbol{V} - {}_1\boldsymbol{V}\right) \prod_{p=2}^{N} \delta\left(\boldsymbol{X}_p - \boldsymbol{X}_1\right) \delta\left(b_p - b_1\right) \frac{\partial}{\partial {}_K f}. \tag{3.115}$$

According to (3.30) the operator needs to be applied to an auxiliary function, which in the present case is defined as

$$H\left(\boldsymbol{x}, t, {}_K\boldsymbol{V}, \boldsymbol{X}, \boldsymbol{b}; {}_K f\right) = {}_K f - {}_K f\left(\boldsymbol{x}, t, {}_K\boldsymbol{V}, \boldsymbol{X}, \boldsymbol{b}\right) = 0. \tag{3.116}$$

Applying the operator (3.115) to H and solving the resulting differential equation $\mathfrak{X}H|_{H=0} = 0$ delivers the invariant solution

$$\begin{aligned} {}_K f &= f_x\left({}_1\boldsymbol{x}, ..., {}_K\boldsymbol{x}, {}_1\boldsymbol{V}, ..., {}_K\boldsymbol{V}, \boldsymbol{X}, \boldsymbol{b}\right) \\ &\quad + t\psi\left({}_1\boldsymbol{V}, \boldsymbol{X}_1, b_1\right) \prod_{k=2}^{K} \delta\left({}_k\boldsymbol{V} - {}_1\boldsymbol{V}\right) \prod_{p=2}^{N} \delta\left(\boldsymbol{X}_p - \boldsymbol{X}_1\right) \delta\left(b_p - b_1\right). \end{aligned} \tag{3.117}$$

The free function $f_x\left({}_1\boldsymbol{x}, ..., {}_K\boldsymbol{x}, {}_1\boldsymbol{V}, ..., {}_K\boldsymbol{V}, \boldsymbol{X}, \boldsymbol{b}\right)$ has to be a PDF, because an integration of ψ with respect to all sample space variables delivers zero, see (3.110), and the solution ${}_K f$ has to fulfil all properties of a PDF. Hence, the dependency of the PDF on space and time has been split between the functions f_x and $t\psi$. The PDF f_x describes the initial state of the ensemble and the product $t\psi$ its development in time. Consider two ensembles, one where the boundaries of the otherwise identical domain are periodic and one where the boundaries a solid walls: given an identical initial distribution f_x, the shape function ψ then describes the different developments of the two ensembles.

3.6.2. Intermittency symmetry

As already mentioned, the second possibility to add a solution of the PDF hierarchy to ${}_K f$, besides adding the shape function ψ, is to rescale both functions accordingly. Hence, the general version of the intermittency symmetry transformation, compliant with the properties of a PDF, is

$${}_K f^* = c_{\text{int}}\, {}_K f + \left(1 - c_{\text{int}}\right) {}_K g, \tag{3.118}$$

where ${}_K g$ is a solution of (3.96) and a multi-point PDF and $0 \leq c_{\text{int}} \leq 1$. In the single point case the general formulation (3.118) and the shape symmetry (3.109) are connected by

$$\psi = \left(1 - c_{\text{int}}\right)\left({}_1 f - {}_1 g\right). \tag{3.119}$$

Considering the two PDFs ${}_K f$ and ${}_K g$, fulfilling the reduction property (3.66), it becomes clear that the integral of ψ necessarily vanishes, see (3.110). Wacławczyk et al. [202] defined ${}_K g$ as a product of Dirac functions

$${}_K f^* = c_{\text{int}}\, {}_K f + \left(1 - c_{\text{int}}\right) \prod_{k=1}^{K} \delta\left({}_k\boldsymbol{V} - {}_k\boldsymbol{U}\right) \delta\left(\boldsymbol{X} - \boldsymbol{\chi}\right) \delta\left(\boldsymbol{b} - \boldsymbol{\beta}\right), \tag{3.120}$$

i.e. the second PDF ${}_K g$ is a deterministic or fine-grained PDF describing a specific solution $[{}_1\boldsymbol{U}, ..., {}_K\boldsymbol{U}, \boldsymbol{\chi}, \boldsymbol{\beta}]$ of the physical system. Necessarily, it is also a solution of the hierarchy of PDF equations (3.96). The choice of ${}_K g$ might reveal interesting behaviour of an active suspension, because the resulting symmetry transformation allows distinguishing between chaotic states and deterministic states, which justifies the formulation of the second symmetry transformation additionally to the shape symmetry. Adopting the terminology of turbulence research, the expression $c_{\text{int}}\, {}_K f$ describes the probability of a turbulent, i.e. chaotic, stochastic, behaviour. The term $(1 - c_{\text{int}}) \prod_{k=1}^{K} \delta\left({}_k\boldsymbol{V} - {}_k\boldsymbol{U}\right) \delta\left(\boldsymbol{X} - \boldsymbol{\chi}\right) \delta\left(\boldsymbol{b} - \boldsymbol{\beta}\right)$, on the other hand, describes laminar, i.e. deterministic, behaviour, because the Dirac functions are equivalent to the fine-grained PDF (3.54). A system which often switches between chaotic and deterministic behaviour is called an intermittent system, which explains the name of the symmetry. A second definition of intermittency is the sudden outburst of an otherwise rare event as mentioned by Li and Meneveau [135] and Wilczek and Friedrich [206]. It will be shown in Sec. 6.2 that the intermittency symmetry can be used to describe heavy-tailed probability distributions, i.e. PDFs where rare events in the tails of the function are more likely than in the case of a comparable normal distribution, thus, complying to the second definition of intermittency.

The Lie operator of the symmetry transformation is

$$\mathfrak{X}_{int} = \left({}_K f - {}_K g\right) \frac{\partial}{\partial\, {}_K f} = \left({}_K f - \prod_{k=1}^{K} \delta\left({}_k\boldsymbol{V} - {}_k\boldsymbol{U}\right) \delta\left(\boldsymbol{X} - \boldsymbol{\chi}\right) \delta\left(\boldsymbol{b} - \boldsymbol{\beta}\right) \right) \frac{\partial}{\partial\, {}_K f}. \tag{3.121}$$

Again by integration with respect to the different sample space variables, marginal PDFs are formed

$${}_K f^{V*} = c_{\text{int}}\, {}_K f + (1 - c_{\text{int}}) \prod_{k=1}^{K} \delta\left({}_k\boldsymbol{V} - {}_k\boldsymbol{U}\right), \tag{3.122a}$$

$$f^{X*} = c_{\text{int}} f^{X} + (1 - c_{\text{int}}) \delta\left(\boldsymbol{X} - \boldsymbol{\chi}\right), \tag{3.122b}$$

$$f^{b*} = c_{\text{int}} f^{b} + (1 - c_{\text{int}}) \delta\left(\boldsymbol{b} - \boldsymbol{\beta}\right). \tag{3.122c}$$

The first marginal PDF (3.122a) is equivalent to the symmetry transformation given by Wacławczyk et al. [202], where it is related, as mentioned, to the different behaviour of a turbulent and laminar flow. While inertia driven turbulence is impossible to occur in the given setup of a low-Reynolds active suspension, some researchers describe the behaviour of an active suspensions as active turbulence, see Sec. 1. In Sec. 6 the transformation is used to analyse simulation data and indeed reveals chaotic and deterministic behaviour, i.e intermittency.

4. Direct numerical simulation

Particle resolved Direct Numerical Simulations (DNS) are carried out within the Bounded Support Spectral Solver (BoSSS)[1] [127]. The BoSSS-framework provides a high-order Discontinuous Galerkin (DG) method to solve the fluid equations. The DG method is extended to account for a two-phase flows, leading to the eXtended Discontious Galerkin (XDG) method, which is able to represent the particle surface accurately on a sub-cell level, where cells of the numerical grid, which are cut by the particle surface, are called cut-cells. The combined fluid-particle solver, called eXtended Navier-Stokes plus Rigid Object (XNSERO) solver, enables the solution of an active suspension. As part of the BoSSS framework, XNSERO is able to use all methods implemented by BoSSS for solving the fluid phase. Thus, it employs, as the name states, the Navier-Stokes equation (2.67) to describe the fluid. However, it is possible to reduce the computational load by using the unsteady Stokes equation (2.68) as a linearisation of the problem. Due to the low Reynolds number of a microscopic active suspension, the unsteady Stokes equation is an appropriate choice and used throughout this section. The boundary conditions for the fluid phase at the particle surface, especially the active stress, are implemented by modifying the numerical fluxes at the interface. In addition, XNSERO provides a solver for the particle phase and a collision model for direct interactions between particles. An earlier implementation of the solver has been used to obtain results in the publication Deußen et al. [50]. While some methods, i.e. the XDG-method and the physical equations, have not changed compared to Deußen et al. [50], the implementation of the active boundary conditions, the numerical side of the collision model and the numerical methods to solve the particle equations differ significantly.

In this section, the fluid-particle solver is presented, starting with general properties and definitions of the DG method in Sec. 4.1. Its extension XDG is introduced in Sec. 4.2, including an introductory example of the spatial discretisation. The semi-discrete formulation of the unsteady Stokes equation (2.68) is presented in Sec. 4.3 and the implementation of the active boundary conditions is given in Sec. 4.3.1. Due to the importance of sub-cell accuracy for the representation of the particles, an introduction to the algorithm used for integration on cut-cells is given in Sec. 4.3.2. The discretisation of the Stokes equation is completed in Sec. 4.4 with a presentation of the temporal discretisation. The particle solver is presented in Sec. 4.5, followed by a discussion of the collision model in Sec. 4.6. The three parts of the solver - the fluid XDG solver, the particle solver and the collision model - are put together to a combined solver in Sec. 4.7.

---

[1] https://github.com/FDYdarmstadt/BoSSS

4.1. Discontinuous Galerkin methods

The DG method unifies properties of the Finite Volume Method (FVM) and the Finite Element Method (FEM) Similar to FVM it employs a locally conservative discretisation and numerical fluxes based on the physical problem. By using local ansatz functions, DG provides high-order methods on arbitrary meshes. Due to the local ansatz functions and the flux formulation, cells only need to communicate with their direct neighbour, simplifying the implementation of multi-core, High-Performance Computing (HPC) ready applications. In contrast, high-order FVM needs larger stencils of several neighbouring cells and FEM defines global mass matrices. The DG method also provides good handling of hanging nodes, hence, local Adaptive Mesh Refinement (AMR) can be used straightforwardly. The above advantages are offset by the disadvantage of an increased number of unknowns or Degrees of Freedom (DoF) [126].

Reed and Hill [173] developed the first DG method to solve the neutron transport equation on triangular meshes to describe the hexagonal structure of contemporary nuclear reactors. DG methods to solve fluid flows were developed, firstly for steady first-order partial differential equations [134] and later for steady three dimensional boundary layer problems [38]. Hyperbolic equation in the context of DG were analysed by Chavent and Cockburn [42], Cockburn and Shu [46], and Jaffre et al. [111]. Diffusive terms were first introduced by Nitsche [156]. The development of Symmetric Interior Penalty (SIP) methods [9, 12, 13, 61] finally enabled the usage of the DG method in the context of incompressible convective-dissipative fluid flows [44, 45].

The spatial discretisation of the domain Ω is governed by the following basic definitions, given by Di Pietro and Ern [58] and Kummer [126]

- the two-dimensional domain $\Omega \subset \mathbb{R}^2$ is polygonal and simply connected,
- the numerical mesh consists of cells $\mathfrak{K}_h = \{K_1, ..., K_J\}$, which cover the entire domain $\Omega = \bigcup_{j=1}^{J} K_j$ and do not overlap $K_j \cap K_k = \varnothing, \quad \forall j \neq k$,
- $\Omega = \mathrm{cl}\,\Omega$ and $K_j = \mathrm{cl} K_j$ are closed sets, i.e. they contain their own boundary,
- the mesh size is defined as $h^K = \max\limits_{K_j \in \mathfrak{K}} h_j$, where h_j is the diameter of the cell K_j,
- the set of all edges of the cells $\Gamma^K = \bigcup_{j=1}^{J} \partial K_j$ is split between internal $\Gamma^{\text{int}} = \Gamma^K \setminus \partial\Omega$ and external edges $\Gamma^{\text{ext}} = \Gamma^K \cap \partial\Omega$, where the latter receive boundary conditions of either Dirichlet or Neumann type $\Gamma^{\text{ext}} = \Gamma^D \cup \Gamma^N$,
- a field of normal vectors $n_i^{\Gamma^K}$ at Γ^K exists. At the external surface $n_i^{\Gamma^{\text{ext}}}$ is the outward pointing normal vector,
- the inner $\mathfrak{u}^{\text{in}}$ and outer values $\mathfrak{u}^{\text{out}}$ of the general physical quantity $\mathfrak{u}$ at Γ^K are

$$\mathfrak{u}^{\text{in}}(\boldsymbol{x}) = \lim_{\epsilon \to 0} \mathfrak{u}\left(\boldsymbol{x} - \epsilon \boldsymbol{n}^{\Gamma}\right) \quad \forall \boldsymbol{x} \in \Gamma^K, \tag{4.1}$$

$$\mathfrak{u}^{\text{out}}(\boldsymbol{x}) = \lim_{\epsilon \to 0} \mathfrak{u}\left(\boldsymbol{x} + \epsilon \boldsymbol{n}^{\Gamma}\right) \quad \forall \boldsymbol{x} \in \Gamma^{\text{int}}, \tag{4.2}$$

- the jump operator at Γ^K is

$$[\![\mathfrak{u}]\!]\left(\boldsymbol{x}\right) = \lim_{\epsilon \to 0} \mathfrak{u}^{\text{in}}\left(\boldsymbol{x}\right) - \mathfrak{u}^{\text{out}}\left(\boldsymbol{x}\right) \quad \forall \boldsymbol{x} \in \Gamma^{\text{int}}, \tag{4.3}$$

$$[\![\mathfrak{u}]\!]\left(\boldsymbol{x}\right) = \lim_{\epsilon \to 0} \mathfrak{u}^{\text{in}}\left(\boldsymbol{x}\right) \quad \forall \boldsymbol{x} \in \Gamma^{\text{ext}}, \tag{4.4}$$

- the average operator at Γ^K is

$$\{\mathfrak{u}\}\left(\boldsymbol{x}\right) = \lim_{\epsilon \to 0} \frac{1}{2}\left(\mathfrak{u}^{\text{in}}\left(\boldsymbol{x}\right) + \mathfrak{u}^{\text{out}}\left(\boldsymbol{x}\right)\right) \quad \forall \boldsymbol{x} \in \Gamma^{\text{int}}, \tag{4.5}$$

$$\{\mathfrak{u}\}\left(\boldsymbol{x}\right) = \lim_{\epsilon \to 0} \mathfrak{u}^{\text{in}}\left(\boldsymbol{x}\right) \quad \forall \boldsymbol{x} \in \Gamma^{\text{ext}}. \tag{4.6}$$

Within each cell a polynomial function space is constructed, which forms the broken polynomial space of the entire mesh with the degree k [126]

$$\mathbb{P}_k\left(\mathfrak{K}_h\right) = \left\{\mathfrak{f} \in L^2\left(\Omega\right); \forall K_j \in \mathfrak{K}_h : \mathfrak{f}|_K \text{is polynomial and } \deg\left(\mathfrak{f}|_K\right) \leq k\right\}. \tag{4.7}$$

The local approximation $\widehat{\mathfrak{u}}_j$ in the cell K_j of a general physical field variable $\mathfrak{u}$ is obtained by the summation

$$\widehat{\mathfrak{u}}_j\left(\boldsymbol{x}, t\right) = \sum_{l=1}^{N^k} \tilde{\mathfrak{u}}_{j,l}\left(t\right) \mathfrak{f}_{j,l}\left(\boldsymbol{x}\right), \tag{4.8}$$

where $\tilde{\mathfrak{u}}_{j,l}\left(t\right)$ are called unknowns or DoFs and $\left(\mathfrak{f}_{j,l}\right)_{l=1,\dots,N^k} \in \mathbb{P}\left(\{K_j\}\right)$ is the local polynomial basis [189]. The summation $\sum_{l=1}^{N^k}$ within each cell is carried out for all ansatz functions $\mathfrak{f}_{j,l}$ with the maximum degree of N^k. The ansatz function are modal and fulfil the orthogonality condition [189]

$$\int_{K_j} \mathfrak{f}_{j,m}\mathfrak{f}_{j,n}\,\mathrm{d}\boldsymbol{x} = \delta_{mn}, \tag{4.9}$$

where δ_{mn} is the Kronecker delta.

Due to the presence of two phases, the fluid phase and the particle solid phase, the standard DG method is not sufficient to model the problem. Hence, in order to proceed further, a representation of the phase interface is introduced in the next section, enabling the modelling of multi-phase flows in general and fluid-solid suspension in particular.

4.2. Extend Discontinuous Galerkin methods

A representation for interfaces is necessary to model the particles in an active suspension. The aforementioned level-set method is used to represent such interfaces, see Sec. 2.3.3, leading to the XDG method [126]. The position of the interface with respect to the background mesh is arbitrary, i.e. the interface does not follow the edges of the numerical mesh. Hence, some cells of the mesh are cut by the interface, such cells are referred to as cut-cells. In general the amount of DoFs is doubled in the cut-cells, as a solution is necessary for the physical variables of both phases. In the present work, however, the solid particle phase is described by the Newton-Euler equations (2.54) and (2.55), hence, no field variables are required. Subsequently, the solution simplifies, because the cells occupied by the particles can be considered void. The shape of the cut-cells is arbitrary and they might become infinitely small or ill-shaped. In such cases, obtaining a solution becomes difficult due to high condition numbers. BoSSS averts this problem by employing a cell agglomeration method, i.e. small cut-cells are added towards larger neighbours, see Kummer [126]. An algorithm capable of handling cut-cells, provided by Saye [183], is employed to carry out the integration on the cut-cell mesh, see Sec. 4.3.2.

In a general two-phase setting the domain is split between the part occupied by the phase $\mathfrak{A}$ and the part occupied by the second phase $\mathfrak{B}$

$$\Omega = \Omega^{\mathfrak{A}}(t) \cup \Omega^{\mathfrak{B}}(t), \quad \Omega^{\mathfrak{A}}(t) \cap \Omega^{\mathfrak{B}}(t) = \varnothing, \quad \Gamma(t) = \partial\Omega^{\mathfrak{A}}(t) \cap \partial\Omega^{\mathfrak{B}}(t) \tag{4.10}$$

where the interface $\Gamma(t)$ separates the two phases, which do not overlap. As only two dimensions are considered $\Omega \subset \mathbb{R}^2$ the interface $\Gamma(t)$ is a one-dimensional manifold [126]. It is represented by the zero level set of the function ϕ given in (2.74). In a general multi-phase setup the level-set evolution is governed by the transport equation (2.78)

$$\frac{\partial \phi}{\partial t} + \frac{\partial \phi U_i}{\partial x_i} = 0.$$

In case of rigid particles, however, the interface motion is purely governed by the particle position and orientation, hence, the particle function $\phi_p = \phi_p(\boldsymbol{\chi}_p, \beta_p)$ is prescribed and the global function ϕ is obtained by (2.74). The normal vector at the interface can be determined by (2.76)

$$n_i = \frac{\partial \phi}{\partial x_i} \left|\nabla \phi\right|^{-1}.$$

Due to the representation of the level set by a broken polynomial space, see (4.7) it might not be smooth. However, smoothness of ϕ is necessary for a well-defined interface $\Gamma(t)$ [127]. Hence, BoSSS employs a continuity projection for the level set, where an introduction is given in Sec. 4.4.

Each cell contains two time-dependent sub-domains

$$K_{j,\mathfrak{A}} = K_j \cap \Omega^{\mathfrak{A}}(t) \text{ and } K_{j,\mathfrak{B}} = K_j \cap \Omega^{\mathfrak{B}}(t), \tag{4.11}$$

if it is cut by the interface. Otherwise, the cell K_j is fully occupied by one phase, e.g. $K_{j,\mathfrak{A}} = K_j \wedge K_{j,\mathfrak{B}} = \varnothing$. Hence, the time dependent cut-cell mesh $\mathfrak{K}_h^X(t)$ contains up to twice as many entries as the background mesh $\mathfrak{K}_h$ [127]

$$\mathfrak{K}_h^X(t) = \left\{K_{1,\mathfrak{A}}(t), K_{1,\mathfrak{B}}(t), ..., K_{J,\mathfrak{A}}(t), K_{J,\mathfrak{B}}(t)\right\}. \tag{4.12}$$

Applying the DG polynomial space (4.7) to the cut-cell mesh delivers the XDG polynomial space [127]

$$\begin{aligned} \mathbb{P}_k^X(\mathfrak{K}_h, t) :=& \mathbb{P}_k\left(\mathfrak{K}_h^X(t)\right) \\ =& \left\{\mathfrak{f} \in L^2(\Omega); \forall K_{j,\mathfrak{p}} \in \mathfrak{K}_h^X : \mathfrak{f}|_{K_{j,\mathfrak{p}}} \text{is polynomial and deg} \left(\mathfrak{f}|_{K_{j,\mathfrak{p}}}\right) \leq k\right\}. \end{aligned} \tag{4.13}$$

Subsequently, the XDG local approximation $\widehat{\mathfrak{u}}_j$ of a physical property $\mathfrak{u}$ is

$$\widehat{\mathfrak{u}}_j(\boldsymbol{x}, t) = \sum_{l=1}^{N^k} \left[\tilde{\mathfrak{u}}_{j,l}^{\mathfrak{A}}(t)\, \mathfrak{f}_{j,l}(\boldsymbol{x})\, \gamma^{\mathfrak{A}}(\boldsymbol{x}, t) + \tilde{\mathfrak{u}}_{j,l}^{\mathfrak{B}}(t)\, \mathfrak{f}_{j,l}(t)\, \gamma^{\mathfrak{B}}(\boldsymbol{x}, t)\right], \tag{4.14}$$

where the number of DoFs $\tilde{\mathfrak{u}}^{\mathfrak{P}}_{j,l}$ is doubled compared to the single phase approximation, given by (4.8). The local ansatz functions $\mathfrak{f}^{\mathfrak{A}}_{j,l}(\boldsymbol{x}) = \mathfrak{f}_{j,l}(\boldsymbol{x})\,\gamma^{\mathfrak{A}}$ and $\mathfrak{f}^{\mathfrak{B}}_{j,l}(\boldsymbol{x}) = \mathfrak{f}_{j,l}(\boldsymbol{x})\,\gamma^{\mathfrak{B}}$ ensure a sub-cell accurate representation of the interface as visualised in Fig. 4.1 for a second order polynomial in the phase $\mathfrak{A}$. The indicator functions $\gamma^{\mathfrak{A}}$, $\gamma^{\mathfrak{B}}$ are defined in the same way as the general phase indicator function $\gamma^{\mathfrak{P}}$, see (2.30). In case of the present fluid-particle solver phase $\mathfrak{B}$ is the particle phase, which is not solved based on the XDG method, i.e. is considered void by the fluid solver. Hence, the cell-local approximation of the fluid phase $\mathfrak{A} = F$ in the context of the XNSERO solver is

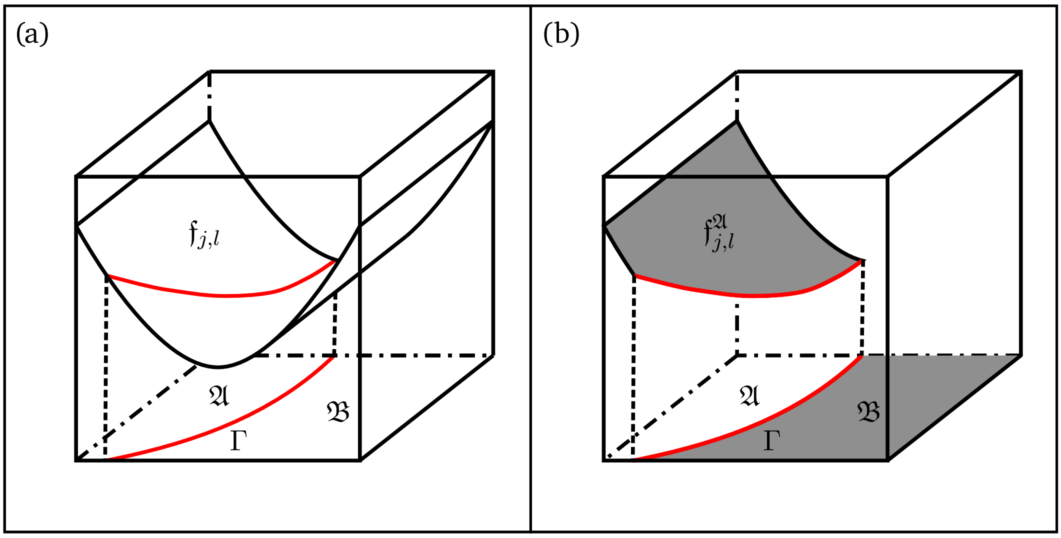

Fig. 4.1.: (a) A cut-cell contains the interface Γ and two sub-domains occupied by the phase $\mathfrak{A}$ and $\mathfrak{B}$ respectively. The depicted two dimensional ansatz function for the entire cell on the left hand side is multiplied with the indicator function $\gamma^{\mathfrak{A}}$ of the phase $\mathfrak{A}$, leading to the sub-cell accurate representation (b) of the ansatz function for the sub-domain occupied by $\mathfrak{A}$.

$$\widehat{\mathfrak{u}}_j(\boldsymbol{x},t) = \sum_{l=1}^{N^k} \tilde{\mathfrak{u}}^{F}_{j,l}(t)\,\mathfrak{f}_{j,l}(\boldsymbol{x})\,\gamma^{F}(\boldsymbol{x},t)\,. \tag{4.15}$$

Apart from the phase indicator function γ^F, the approximation (4.15) is equivalent to the DG approximation (4.8), due to the second phase being void. Solely the computational domain changes from Ω to Ω^F as indicated by the function γ^F.

The following example for a discretisation in an XDG setup builds on Hesthaven and Warburton [95] and Smuda [189]. Consider the one-dimensional conservation law

$$F(x,t;\mathfrak{u}) = \frac{\partial \mathfrak{u}}{\partial t} + \frac{\partial f(\mathfrak{u})}{\partial x} = 0 \quad \forall x \in \Omega = [L,R] \tag{4.16}$$

where $f(\mathfrak{u})$ is the flux of $\mathfrak{u}$ and Ω is a one-dimensional domain with the boundaries L and R. The initial distribution of $\mathfrak{u}$ in Ω is $\mathfrak{u}(x,0) = \mathfrak{u}_0$ and the boundary conditions are of Dirichlet type

$$\mathfrak{u}(x=L,t) = \mathfrak{u}^D, \quad \mathfrak{u}(x=R,t) = \mathfrak{u}^D. \tag{4.17}$$

To find an approximation $\widehat{\mathfrak{u}}$ for the general physical quantity $\mathfrak{u}$, the ansatz (4.15) is used. Hence, the global approximation $\widehat{\mathfrak{u}}$ is obtained by the summation

$$\widehat{\mathfrak{u}}\left(x,t\right)=\sum_{j}^{J}\widehat{\mathfrak{u}}_{j}\left(x,t\right)=\sum_{j}^{J}\sum_{l=1}^{N^{k}}\tilde{\mathfrak{u}}_{j,l}^{F}\left(t\right)\mathfrak{f}_{j,l}\left(x\right)\gamma^{F}\left(x,t\right), \tag{4.18}$$

where $\widehat{\mathfrak{u}}_j$ is the cell-local approximation of $\mathfrak{u}$ in the jth cell, the first summation symbol on the right hand side refers to the different cells and the second one to the ansatz functions of the polynomial basis. Using the ansatz (4.15) together with (4.16) delivers the cell-local residual

$$\mathfrak{R}_{j}=\frac{\partial\widehat{\mathfrak{u}}_{j}}{\partial t}+\frac{\partial f\left(\widehat{\mathfrak{u}}_{j}\right)}{\partial x} \tag{4.19}$$

which is in general non-zero. To obtain a numerical solution it is necessary for the weighted residual to vanish [184]

$$\int_{\Omega}\mathfrak{R}_{j}\mathfrak{g}_{j,l}\,\mathrm{d}\boldsymbol{x}=0\quad\forall l=1,...,N^{k}, \tag{4.20}$$

where $\mathfrak{g}_{j,l}$ is a weight function. Core feature of any Galerkin method is to use the ansatz functions $\mathfrak{f}_{j,l}$ as weight functions, see for example Schäfer [184], leading to

$$\int_{\Omega}\mathfrak{R}_{j}\mathfrak{f}_{j,l}\,\mathrm{d}\boldsymbol{x}=0\quad\forall l=1,...,N^{k}, \tag{4.21}$$

i.e. the residual is required to be orthogonal towards the ansatz functions. Written out, the equation is

$$\int_{K_{j}}\frac{\partial\widehat{\mathfrak{u}}_{j}}{\partial t}\mathfrak{f}_{j,l}\,\mathrm{d}\boldsymbol{x}+\int_{K_{j}}\frac{\partial f\left(\widehat{\mathfrak{u}}_{j}\right)}{\partial x}\mathfrak{f}_{j,l}\,\mathrm{d}\boldsymbol{x}=0\quad\forall l=1,...,N^{k}. \tag{4.22}$$

This formulation is the semi-discrete form, because, while it is discretised in space, the derivative with respect to time is still continuos. Integration by parts delivers the cell local weak formulation of F

$$\int_{K_{j}}\frac{\partial\widehat{\mathfrak{u}}_{j}}{\partial t}\mathfrak{f}_{j,l}\,\mathrm{d}\boldsymbol{x}-\int_{K_{j}}f\left(\widehat{\mathfrak{u}}_{j}\right)\frac{\partial\mathfrak{f}_{j,l}}{\partial x}\,\mathrm{d}\boldsymbol{x}+\int_{\partial K_{j}}n\cdot f\left(\widehat{\mathfrak{u}}_{j}\right)\mathfrak{f}_{j,l}\,\mathrm{d}s=0\quad\forall l=1,...,N^{k}. \tag{4.23}$$

The normal vector $n=\pm1$ in one dimension is a scalar, nevertheless the dot product notation was used to account for a generalisation to higher dimensions. At the edges ∂K_j of the cell K_j, the value of the flux $n\cdot f\left(\widehat{\mathfrak{u}}_j\right)$ is not uniquely defined, because by definition discontinuities are allowed at the cell boundaries. Subsequently, the numerical fluxes

$$\widehat{f}\left(\widehat{\mathfrak{u}}_{j}^{\text{in}},\widehat{\mathfrak{u}}_{j}^{\text{out}},n\right)\approx n\cdot f\left(\widehat{\mathfrak{u}}_{j}\right) \tag{4.24}$$

are introduced to obtain a unique definition of the surface integral in (4.23) [189]. Using (4.23) and (4.24) together with (4.15) delivers

$$\int_{K_{j}}\frac{\partial\tilde{\mathfrak{u}}_{j,n}}{\partial t}\mathfrak{f}_{j,n}\mathfrak{f}_{j,m}\,\mathrm{d}\boldsymbol{x}-\int_{K_{j}}f\left(\tilde{\mathfrak{u}}_{j,n}\mathfrak{f}_{j,n}\right)\frac{\partial\mathfrak{f}_{j,m}}{\partial x}\,\mathrm{d}\boldsymbol{x}+\int_{\partial K_{j}}\widehat{f}\left(\widehat{\mathfrak{u}}_{j}^{\text{in}},\widehat{\mathfrak{u}}_{j}^{\text{out}},n\right)\mathfrak{f}_{j,m}\,\mathrm{d}s=0. \tag{4.25}$$

It is apparent, that this equation can be written in a matrix form, where $\left(M_j\right)_{mn} = \mathfrak{f}_{j,m}\mathfrak{f}_{j,n}$ is called cell local mass matrix. Its global version is a diagonal matrix

$$\boldsymbol{M} = \begin{bmatrix} \boldsymbol{M}_1 & 0 & \dots & 0 \\ 0 & \boldsymbol{M}_2 & \dots & 0 \\ \vdots & \dots & \ddots & \vdots \\ 0 & 0 & \dots & \boldsymbol{M}_J \end{bmatrix}. \tag{4.26}$$

The two following terms of (4.25) form the cell local operator vector

$$\left(O_j^p\right)_m = -\int_{K_j} f\left(\tilde{\mathfrak{u}}_{j,n}\mathfrak{f}_{j,n}\right) \frac{\partial \mathfrak{f}_{j,m}}{\partial x}\,\mathrm{d}\boldsymbol{x} + \int_{\partial K_j} \widehat{f}\left(\widehat{\mathfrak{u}_j^{\mathrm{in}}}, \widehat{\mathfrak{u}_j^{\mathrm{out}}}, n\right) \mathfrak{f}_{j,m}\,\mathrm{d}s, \tag{4.27}$$

leading to the global system of equations

$$M_{mn}\frac{\partial \tilde{\mathfrak{u}}_n}{\partial t} + O_m^p = z_m, \tag{4.28}$$

where the vector z_m contains additional forcing terms and boundary conditions. Solving this system for the solution vector $\tilde{\mathfrak{u}}_n = \left[\tilde{\mathfrak{u}}_{1,1}, \tilde{\mathfrak{u}}_{1,2}, ..., \tilde{\mathfrak{u}}_{j,n}, ..., \tilde{\mathfrak{u}}_{J,N^k}\right]$ delivers an approximation for $\mathfrak{u}$ in the entire domain Ω. In the next section the mass matrix M_{mn}, the operator vector O_m^p and the right hand side vector z_m for the unsteady Stokes equation with an active boundary condition at the particle surface are presented.

4.3. Discrete variational formulation of the Stokes equation

The condition of a low Reynolds number $\mathrm{Re} \ll 1$ allows to substantially simplify the Navier-Stokes equation (2.67) to the unsteady Stokes equation (2.68), see Sec. 2.3.2. As the non-linear convection term is neglected, it is no longer necessary to find an appropriate linearisation of the equations. This is advantageous in terms of computational resources and leads to a significant speed up of the simulation runtime. Hence, only the discretisation of the linear Stokes equation is presented here. The discrete form of the full Navier-Stokes equation in an XDG environment can be found, for example, in Kummer [126]. In order to satisfy the Ladyženskaja-Babuška-Brezzi (LBB) condition [11, 35] the polynomial order of the pressure field is reduced by one compared to the velocity field. A discussion of the stability of the LBB condition can be found in Kummer [126]. The resulting discretisation reads: find

$$\mathfrak{u}^F = \left(\boldsymbol{u}^F, p^F\right) \in \mathbb{P}_k^X\left(\mathfrak{K}_h, t\right) \times \mathbb{P}_{k-1}^X\left(\mathfrak{K}_h, t\right) =: \mathbb{V}_k. \tag{4.29}$$

such that [125, 126, 127, 189]

$$\begin{aligned} \int_{\Omega^F} \frac{\partial u_i^F}{\partial t}\mathfrak{v}_i\,\mathrm{d}\boldsymbol{x} + b\left(\boldsymbol{\mathfrak{v}}, p^F\right) - a\left(\boldsymbol{u}^F, \boldsymbol{\mathfrak{v}}\right) - a^{ac}\left(\boldsymbol{u}^F, \boldsymbol{\mathfrak{v}}\right) - b\left(\mathfrak{q}, \boldsymbol{u}^F\right) \\ = s\left(\boldsymbol{\mathfrak{v}}\right) + r\left(\mathfrak{q}\right) \quad \forall\left(\boldsymbol{\mathfrak{v}}, \mathfrak{q}\right) \in \mathbb{V}_k, \end{aligned} \tag{4.30}$$

where $\mathbb{V}_k$ is the function space of the ansatz and test functions and the function $\mathfrak{v}_i$ is a vector, whereas $\mathfrak{q}$ is a scalar. Clearly, a temporal discretisation is necessary for the integral $\int_{\Omega^F} \frac{\partial u_i^F}{\partial t}\mathfrak{v}_i\,\mathrm{d}\boldsymbol{x}$, which is introduced in Sec. 4.4. Due to the rigidity of the particles, only the fluid domain Ω^F is considered for the integration. Furthermore, following the definition of the Janus particle surface (2.39), the interface Γ is split into two parts, where Γ^{pa} is the passive surface and Γ^{ac} is the active surface. The bilinear forms $b\left(\boldsymbol{\mathfrak{v}}, p^F\right)$ and $b\left(\mathfrak{q}, \boldsymbol{u}^F\right)$ describe the pressure gradient and the velocity divergence, whereas the bilinear form $a\left(\boldsymbol{u}^F, \boldsymbol{\mathfrak{v}}\right)$ represents viscous terms in the bulk, at Dirichlet boundaries and the passive surface Γ^{pa} of the particles [126]. The second viscous bilinear form $a^{ac}\left(\boldsymbol{u}^F, \boldsymbol{\mathfrak{v}}\right)$ represents the action of the active boundary condition at the active particle surface Γ^{ac}. On the right hand side of (4.30) the term $s\left(\boldsymbol{\mathfrak{v}}\right)$ represents boundary conditions for the Stokes equation and $r\left(\mathfrak{q}\right)$ boundary conditions for the continuity equation. In case of the discrete Navier-Stokes equation additional terms occur on both sides of (4.30), one trilinear form to describe convection on the left hand side and one term to describe boundary conditions for the convective terms on the right hand side, see Krause and Kummer [125] and Kummer [126].

To define the bilinear forms in (4.30) it is necessary to introduce the piecewise defined broken gradient $\partial \mathfrak{u}_i / \partial x_j|_h$ and the broken divergence $\partial \mathfrak{u}_i / \partial x_i|_h$, where $\mathfrak{u}_i$ is at least one time continuously differentiable, i.e. $\mathfrak{u}_i \in \mathcal{C}^1\left(\Omega \backslash \Gamma \backslash \partial\Omega\right)$ [126]. The pressure gradient bilinear form is [126]

$$b\left(p^F, \boldsymbol{\mathfrak{v}}\right) = -\int_{\Omega^F} p^F \left.\frac{\partial \mathfrak{v}_i}{\partial x_i}\right|_h \mathrm{d}\boldsymbol{x} - \int_{\Gamma^{\text{int}} \cup \Gamma^D \cup \Gamma(t)} \llbracket \mathfrak{v}_i \rrbracket \, n_i \left\{p^F\right\} \mathrm{d}s. \tag{4.31}$$

Analogously, the velocity divergence is

$$b\left(\mathfrak{q}, \boldsymbol{u}^F\right) = -\int_{\Omega^F} \mathfrak{q} \left.\frac{\partial u_i}{\partial x_i}\right|_h \mathrm{d}\boldsymbol{x} - \int_{\Gamma^{\text{int}} \cup \Gamma^D \cup \Gamma(t)} \llbracket u_i \rrbracket \, n_i \left\{\mathfrak{q}\right\} \mathrm{d}s, \tag{4.32}$$

i.e. the pressure p^F was replaced by the scalar test function $\mathfrak{q}$ and the test function $\boldsymbol{\mathfrak{v}}$ was replaced by the velocity $\boldsymbol{u}^F$ compared to (4.31). The jump $\llbracket u_i \rrbracket$ in the normal direction at the particle surface in (4.32) is defined by $\llbracket u_i \rrbracket \, n_i = \left(u_i^F - u_i^S\right) n_i$ where u_i^S is the product of the translational and rotational part of the particle velocity, see (2.51). Hence, the fluid solver depends on the results of the particle. However, the particle solver also depends on the results of the fluid solver, thus, leading to the necessity to implement an iterative scheme for the coupled solver, see Sec. 4.7. The active stress only occurs in tangential direction and has no effect on the bilinear forms of the pressure and divergence.

The viscous term is formed with a SIP method, which imposes coercivity and positive definiteness of the viscous form $a\left(\boldsymbol{u}^F, \boldsymbol{\mathfrak{v}}\right)$ [9, 10, 126]. The penalty parameter is defined as

$$\eta \coloneqq \max\left\{\mu^{F,\text{in}}, \mu^{F,\text{out}}\right\} \max\left\{\tilde{\eta}^{\text{in}}, \tilde{\eta}^{\text{out}}\right\} \quad \text{on } \Gamma^{\text{int}} \tag{4.33}$$

$$\eta \coloneqq \mu^{F,\text{in}} \tilde{\eta}^{\text{in}} \quad \text{on } \partial\Omega \cup \Gamma\left(t\right), \tag{4.34}$$

where

$$\tilde{\eta} = \eta_0 k^2 \frac{|\partial K_{j,\mathfrak{P}}|}{|K_{j,\mathfrak{P}}|} \tag{4.35}$$

is the local penalty factor, constant within each cut-cell $K_{j,\mathfrak{P}}$ [189]. A discussion of the safety factor $\eta_0 = 4.0$ and the geometrical property $|\partial K_{j,\mathfrak{P}}| / |K_{j,\mathfrak{P}}|$ can be found in Kummer [126]. The viscosity is assumed to be constant within the entire fluid domain Ω^F, hence, the maximum function $\max\left\{\mu^{F,\text{in}}, \mu^{F,\text{out}}\right\} = \mu^F$ returns the fluid viscosity. Once the penalty parameter is obtained, the viscous bilinear form can be written as [126]

$$
\begin{aligned}
a\left(\boldsymbol{u}^F, \mathfrak{v}\right) = &- \int_{\Omega^F} \mu^F \left(\left.\frac{\partial u_i}{\partial x_j}\right|_h \left.\frac{\partial \mathfrak{v}_i}{\partial x_j}\right|_h + \left.\frac{\partial u_j}{\partial x_i}\right|_h \left.\frac{\partial \mathfrak{v}_i}{\partial x_j}\right|_h \right) \\
&+ \int_{\Gamma^{\text{int}} \cup \Gamma^{pa}(t)} \mu^F \left\{ \left.\frac{\partial u_i}{\partial x_j}\right|_h + \left.\frac{\partial u_j}{\partial x_i}\right|_h \right\} n_j \left[\!\left[\mathfrak{v}_i\right]\!\right] \\
&\qquad + \left(\left\{ \mu^F \left(\left.\frac{\partial \mathfrak{v}_i}{\partial x_j}\right|_h + \left.\frac{\partial \mathfrak{v}_j}{\partial x_i}\right|_h \right) \right\} n_j^\Gamma \right) \left[\!\left[u_i\right]\!\right] \mathrm{d}s \\
&- \int_{\Gamma^{\text{int}} \cup \Gamma^{pa}(t)} \eta \left[\!\left[u_i^F\right]\!\right] \left[\!\left[\mathfrak{v}_i\right]\!\right],
\end{aligned} \tag{4.36}
$$

which covers the domain Ω^F and the boundaries Γ^{pa} and Γ^{int} but not the active surface Γ^{ac}, whose bilinear viscous form is introduced in Sec. 4.3.1.

Due to the properties of the Frobenius product, i.e.

$$
\left.\frac{\partial u_j}{\partial x_i}\right|_h \left.\frac{\partial \mathfrak{v}_i}{\partial x_j}\right|_h = \left.\frac{\partial \mathfrak{v}_j}{\partial x_i}\right|_h \left.\frac{\partial u_i}{\partial x_j}\right|_h, \tag{4.37}
$$

the viscous bilinear form (4.36) is symmetric. The symmetry property comes with a disadvantage, because the velocity components in (4.36) are coupled. According to Kummer [126] no ansatz for the viscous form exists, which preserves the symmetry and is decoupled at the same time.

The source terms of the Stokes equations $s\left(\mathfrak{v}\right)$ exclusively stem from Dirichlet boundary conditions at the external boundary $\partial\Omega$ [126]

$$
s\left(\mathfrak{v}\right) = - \int_{\Gamma^D} u_i^D \left(\left.\frac{\partial \mathfrak{v}_i}{\partial x_j}\right|_h n_j + \left.\frac{\partial \mathfrak{v}_j}{\partial x_i}\right|_h n_j - \eta \mathfrak{v}_i \right), \tag{4.38}
$$

because volume forces such as gravity and surface tension are neglected. The reason for the negligence of the latter one is the rigidity of the particles. The source term due to the Dirichlet boundary in case of the continuity equation is [126]

$$
r\left(\mathfrak{q}\right) = \int_{\Gamma^D} \mathfrak{q} u_i^D n_i \, \mathrm{d}s. \tag{4.39}
$$

4.3.1. Active boundary conditions

The bilinear forms $b\left(p^F, \mathfrak{v}\right)$, $b\left(\mathfrak{q}, \boldsymbol{u}^F\right)$ and $a\left(\boldsymbol{u}^F, \mathfrak{v}\right)$ contain integral terms describing the phase interface, which in case of an active suspension is the union of the active and passive boundary of the particles. So far, only passive surfaces have been considered and no active stress was introduced. The active stress only acts in the tangential direction of the particle surface. In the normal direction the surface is still an impermeable wall, the same as for the passive surface. Hence, it is necessary to distinguish between the two directions and formulate the boundary conditions separately. The bilinear pressure form does not depend on the velocity, thus, it remains unchanged. The bilinear velocity divergence only considers the normal component of the velocity $\left[\!\left[u_i\right]\!\right] n_i = \left[\!\left[u_i^F - u_i^S\right]\!\right] n_i \quad \forall \boldsymbol{x} \in \Gamma\left(t\right)$. Accordingly, it does not change at the active surface compared to the passive one. In conclusion, only the viscous form

(4.36) is affected by the change of the boundary condition towards an active boundary. The viscous form at the active boundary is

$$\begin{aligned} a^{ac}\left(\boldsymbol{u}^F, \mathfrak{v}\right) = \int_{\Gamma^{ac}} & \mu^F n_j \left(\left.\frac{\partial u_j}{\partial x_k}\right|_h + \left.\frac{\partial u_k}{\partial x_j}\right|_h \right) n_j \mathfrak{v}_i n_i \\ & + \mu^F n_j \left(\left.\frac{\partial \mathfrak{v}_j}{\partial x_k}\right|_h + \left.\frac{\partial \mathfrak{v}_k}{\partial x_j}\right|_h \right) n_k \left[\!\left[u_i \right]\!\right] n_i \,\mathrm{d}s \\ - \int_{\Gamma^{ac}} & \eta n_i \left[\!\left[u_i^F \right]\!\right] \left[\!\left[\mathfrak{v}_j n_j \right]\!\right] \mathrm{d}s \\ + \int_{\Gamma^{ac}} & P_{jk} f_k^{ac} P_{ji} \mathfrak{v}_i \,\mathrm{d}s. \end{aligned} \tag{4.40}$$

The first two integrals are responsible for the impermeability of the wall in the normal direction (2.41) and the third integral accounts for the active stress in tangential direction (2.42). The tensor P_{ij} in (4.40) is defined as

$$P_{ij} = \delta_{ij} - n_i n_j. \tag{4.41}$$

It should be noted, that the implementation of the active boundary condition is similar to the implementation of the generalised Navier boundary condition given by Smuda [189], due to the identical separation into a normal and tangential component with an additional stress in the tangential direction.

Furthermore, it is important for the implementation, that the level set does not carry any information about the location of the passive and active surfaces of the particles. Hence, to distinguish between the two different boundaries, additional information are necessary. The condition for the active surface is

$$n_i e_{ip} \gamma_p < 0, \tag{4.42}$$

where the definition of the normal vector (2.76) is used. Note that this relation depends on the definition of the function ϕ. In the present work it is negative within the particle domain, hence, n_i points from the particle towards the fluid. However, it is entirely possible to reverse the sign of ϕ, which subsequently requires a reversed sign in (4.42).

4.3.2. Numerical integration on cut-cells

In order to obtain a solution on cut-cells and retain the sub-cell accurate representation of the surface, high order integration methods for integrals of the types

$$\int_{K_{j,\mathfrak{P}}(t)} f \,\mathrm{d}\boldsymbol{x} \text{ and } \int_{\Gamma(t)} g \,\mathrm{d}s \tag{4.43}$$

are necessary. BoSSS supports two different methods for cut-cell integration. Hierarchical Moment Fitting (HMF) is a method proposed by Müller et al. [154], capable of handling different cell types. The second method was proposed by Saye [183] and is generally faster than HMF, however, it is restricted to hyperrectangular cells. During the present work, the cells are restricted to a two-dimensional quadratic shape, hence, the Saye-method is solely used. In the following paragraphs the idea of the method will be briefly outlined based on Saye [183].

As before, we restrict the spatial dimension to $d = 2$, however, Saye [183] derived the method for general d-dimensional hyperrectangles. Thus, the two-dimensional rectangular cell is defined by

$$K_j = \left(x_1^L, x_1^U\right) \times \left(x_2^L, x_2^U\right) \subset \mathbb{R}^2, \tag{4.44}$$

where the notation introduced by Saye [183] for the upper and lower bound of the cell is followed, see Fig. 4.2. Core idea is to reduce multi-dimensional integrals such as the volume integral $\int_{K_{j,\mathfrak{P}(t)}} f \, \mathrm{d}\boldsymbol{x}$ to one-dimensional integrals, which can be approximated by Gaussian quadrature rules with the order q, leading to an order of accuracy of $2q$ [183]. The approximation is obtained by the summation

$$\int_{K_{j,\mathfrak{P}(t)}} f \, \mathrm{d}\boldsymbol{x} \approx \sum_i w_i f\left(x_i\right), \quad \int_{\Gamma(t)} g \, \mathrm{d}s \approx \sum_i \overline{w}_i g\left(\overline{x}_i\right), \tag{4.45}$$

with strictly positive weights w_i, $\overline{w}_i$ and the quadrature nodes x_i, $\overline{x}_i$. Given the order q of the Gauss quadrature, $\mathcal{O}\left(q^2\right)$ quadrature nodes are required for the volume integral and $\mathcal{O}\left(q\right)$ nodes are required for the surface integral.

Let $\boldsymbol{e}^k$ with $k \in \{1, 2\}$ be a coordinate direction where $|\partial_k \phi| = |\partial \phi / \partial x_k| > 0$ on K_j. Then a height function $h = h\left(x_i\right) = h\left(\tilde{x}\right)$ with $i \in \{1, 2\} \setminus k$ exists, describing the local interface $\mathfrak{I} \cap K_j$ as

$$\phi : \mathbb{R}^2 \to \mathbb{R}, \quad \phi\left(\tilde{x}, h\left(\tilde{x}\right)\right) = 0. \tag{4.46}$$

Based on the sign of $\partial_k \phi$, which is constant by assumption, one can determine whether a certain region, say the region where $\phi < 0$, is below or above the graph $x_k = h\left(\tilde{x}\right)$, see Fig. 4.2. To find a suitable direction, the gradient $\partial_k \phi\left(\boldsymbol{x}^c\right)$ at the cell centre x_i^c is tested for its maximum component

$$k = \arg\max_{i=1..2} \left| \frac{\partial \phi\left(\boldsymbol{x}^c\right)}{\partial x_i} \right|. \tag{4.47}$$

A direction $\boldsymbol{e}^k$ is suitable if two conditions are met. To ensure the existence of the height function $|\partial_k \phi| > 0$ must be true. Furthermore, the quotient $|\nabla \phi| / |\partial_k \phi| < C$ must be smaller then a predefined constant C, where Saye [183] gives $C \approx 4$. The conditions ensure good results for the Gaussian quadrature used to evaluate the integrals. If one of these two conditions cannot be met by any direction, a subdivision algorithm is applied. In Fig. 4.3 a circular level set is depicted, fully enclosed by a single cell. The cell is now divided into halves until the interface is sufficiently flat within a single subdivision. Once a suitable height function is found, including possible subdivisions, the new functions ϕ^U and ϕ^L are defined (Fig. 4.2)

$$\phi^U, \phi^L : \mathbb{R} \to \mathbb{R}, \quad \phi^U\left(\tilde{x}\right) = \phi\left(\tilde{x} \oplus x^U e_k\right), \quad \phi^L\left(\tilde{x}\right) = \phi\left(\tilde{x} \oplus x^L e_k\right), \tag{4.48}$$

which are used to introduce a new dimensional reduced integration domain. In case that the sub-domain in question, say the region where $\phi < 0$, is below the height function $x_k = h\left(\tilde{x}\right)$ Saye [183] defines

$$V^U = \left\{\phi^U\left(\tilde{x}\right) < 0 \cup \phi^U\left(\tilde{x}\right) > 0\right\}, \quad V^L = \left\{\phi^L\left(\tilde{x}\right) < 0\right\}, \tag{4.49}$$

see Fig. 4.2. In the opposing case, i.e. the region is above the height function the new domains are reversed

$$V^U = \left\{\phi^U\left(\tilde{x}\right) < 0\right\}, \quad V^L = \left\{\phi^L\left(\tilde{x}\right) < 0 \cup \phi^L\left(\tilde{x}\right) > 0\right\}. \tag{4.50}$$

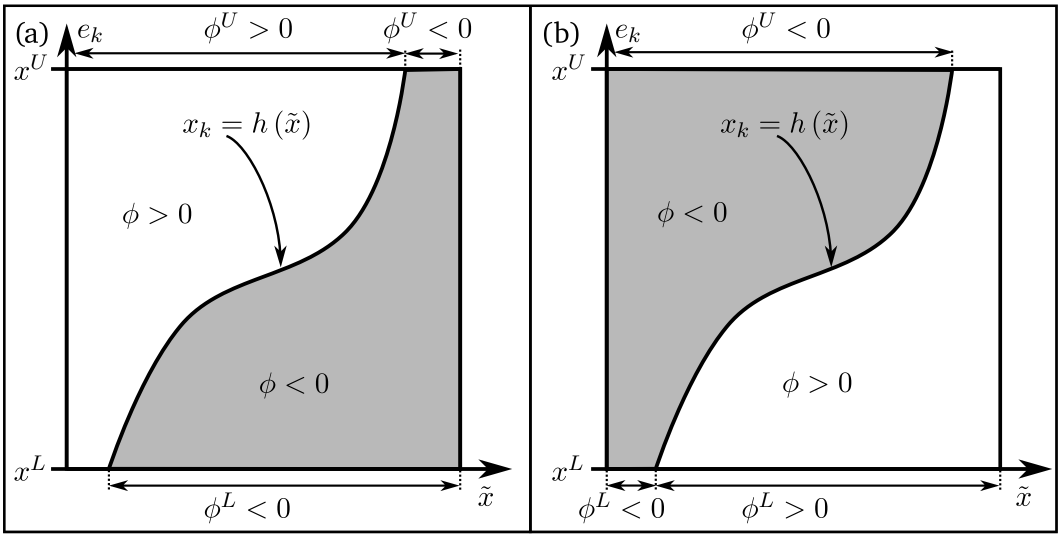

Fig. 4.2.: A region $\phi < 0$ lies either below (a) or above (b) the height function $h(\tilde{x})$, which is equivalent to the zero level set of ϕ. The horizontal axis represents the $\mathbb{R}^{d-1}$ space and the vertical axis the direction of the height function e_k. Illustration based on Saye [183].

In both definitions (4.49) and (4.50) the zero level set of ϕ was excluded to ensure that the function f is smooth on any connected domain. The dimensional reduced volume integral is

$$\int_{K_{j,\mathfrak{P}}(t)} f \,\mathrm{d}\boldsymbol{x} = \int_{\tilde{V}} \int_{I(x)} f(\tilde{x} \oplus y e_k) \,\mathrm{d}y \,\mathrm{d}\tilde{x}, \tag{4.51}$$

where $\tilde{V} = V^U \cap V^L$ and

$$I(x) = \begin{cases} \left\{ y \in \left\{ x_k^U, x_k^L \right\} : s\phi(x \oplus y e_k) > 0 \right\} & \text{if } s = \pm 1 \\ \left\{ y \in \left\{ x_k^U, x_k^L \right\} : \phi(x \oplus y e_k) \neq 0 \right\} & \text{if } s = 0 \end{cases}, \tag{4.52}$$

where $s = \operatorname{sgn}(\phi)$ with $\operatorname{sgn}(0) = 0$ is a sign parameter. The surface integral is treated similar

$$\int_{\Gamma(t) \cap K_j} g \,\mathrm{d}s = \int_{\tilde{V}} g \left. \frac{|\nabla \phi|}{|\partial_k \phi|} \right|_{\tilde{x} + h(\tilde{x}) e_k} \mathrm{d}\tilde{x}. \tag{4.53}$$

Gaussian quadrature is used to obtain a solution for the integrals $\int_{I(x)} f(\tilde{x} \oplus y e_k) \,\mathrm{d}y$ in (4.51) and $\int_{\tilde{V}} g \, |\nabla \phi| / |\partial_k \phi| |_{\tilde{x} + h(\tilde{x}) e_k} \mathrm{d}\tilde{x}$ in (4.53), which requires a root finding algorithm to obtain the height function. In case of the volume integral an additional integration step $\int_{\tilde{V}} \mathrm{d}\tilde{x}$ is necessary to obtain the final result. An in depth explanation of the method and algorithm can be found in the aforementioned publication Saye [183]. The implementation into the BoSSS-framework is described by Beck [19].

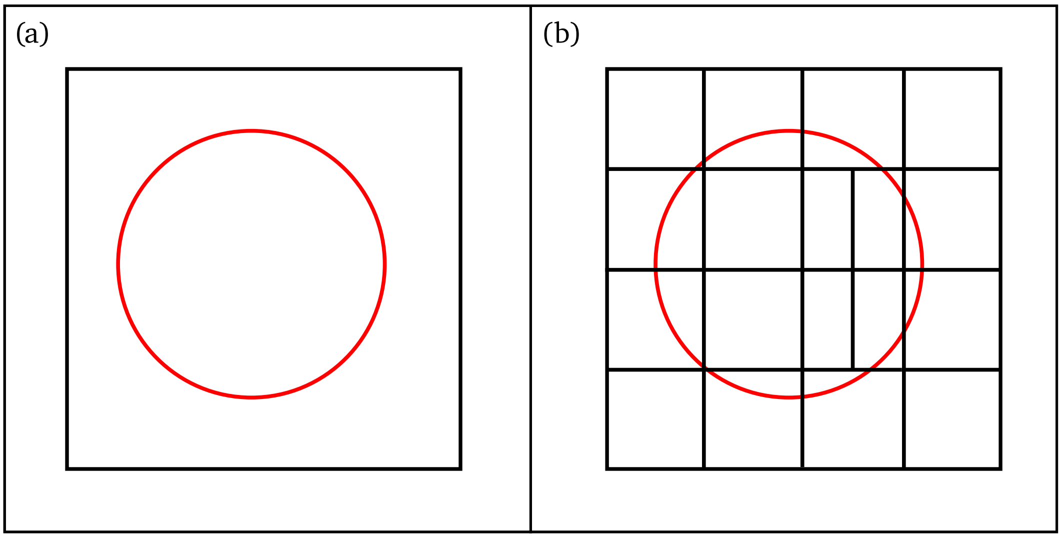

Fig. 4.3.: (a) The circular level set is positioned in a single numerical cell. (b) Through multiple subdivisions of a single cell a favourable level set within each sub-domain is obtained. Illustration based on Saye [183].

4.4. Temporal discretisation of the fluid equations

An implicit second-order Backward Differentiation Formula (BDF2) is used to approximate the temporal derivative in the semi-discrete unsteady Stokes equation (2.68). The entire time-span of the simulation is divided into M time-steps of the constant size Δt. A single time-step is denoted by t^m with $m = \{1, 2, ..., M\}$. The discretisation of the temporal derivative of the unsteady Stokes equation (2.68) with BDF2 delivers [86, 125]

$$u_i^{F,m+1} = \frac{4}{3} u_i^{F*,m} - \frac{1}{3} u_i^{F*,m-1} + \frac{2}{3} \Delta t f_i^{m+1} \quad \forall \boldsymbol{x} \in \Omega^F \left(t^{m+1} \right), \tag{4.54}$$

where f_i^{m+1} is the right hand side of the Stokes equation

$$f_i^{m+1} = \frac{\partial p^{F,m+1}}{\partial x_i} - \frac{1}{Re^F} \frac{\partial^2 u^{F,m+1}}{\partial x_j^2}. \tag{4.55}$$

Additionally the continuity equation (2.65) needs to be fulfilled in every time-step

$$\frac{\partial u_i^{F,m+1}}{\partial x_i} = 0 \quad \forall \boldsymbol{x} \in \Omega^F \left(t^{m+1} \right). \tag{4.56}$$

The spatial discretisation of the right hand side f_i^{m+1} of the unsteady Stokes equation and the continuity equation can be found in the previous Sec. 4.3.

The fluid domain $\Omega^F(t)$ itself is time dependent due to the motion of the phase interface $\Gamma(t)$. Hence, the current solution $u_i^{F,m+1}$, $\forall \boldsymbol{x} \in \Omega^F \left(t^{m+1} \right)$ and the solution of the fluid field at previous time-steps $u_i^{F,m} \, \forall \boldsymbol{x} \in \Omega^F \left(t^m \right)$ and $u_i^{F,m-1} \, \forall \boldsymbol{x} \in \Omega^F \left(t^{m-1} \right)$ are defined on different domains. It is assumed that the displacement of the interface is small within a single time-step, i.e. smaller than the cell diameter h^Γ at the interface. Thus, the solutions $u_i^{F*,m}$ and

$u_i^{F*,m-1}$ used in (4.54) are approximated by

$$u_i^{F*,m} = u_i^{F,m} \, \forall \boldsymbol{x} \in \Omega^F \left(t^{m+1}\right) \cap \Omega^F \left(t^m\right) \tag{4.57a}$$

and

$$u_i^{F*,m-1} = u_i^{F,m-1} \, \forall \boldsymbol{x} \in \Omega^F \left(t^{m+1}\right) \cap \Omega^F \left(t^{m-1}\right). \tag{4.57b}$$

The solution in the missing parts of the domain $\Omega^F \left(t^{m+1}\right) \backslash \Omega^F \left(t^m\right)$ and $\Omega^F \left(t^{m+1}\right) \backslash \Omega^F \left(t^{m-1}\right)$ are obtained by a polynomial extrapolation [125].

Level-Set evolution

Due to the assumption of rigid particles, the level-set evolution is simplified compared to a non-rigid surface. Instead of applying the level-set equation (2.78)

$$\frac{\partial \phi}{\partial t} + \frac{\partial \phi U_i}{\partial x_i} = 0$$

we use that the single-particle function $\phi_p = \phi_p \left(\boldsymbol{\chi}_p, \beta_p\right)$ is solely a function of the position of the centre of mass χ_{ip} and the orientation β_p of the particles. Thus, by using the results of the particle solver, see Sec. 4.5, one can project the new level-set field ϕ_p^{m+1} in every time-step for every particle. Following (2.74) and (2.75) the new field is obtained by

$$\phi^{m+1} = \inf(\Phi^{m+1}), \quad \Phi^{m+1} = \left\{\phi_1^{m+1}, \phi_2^{m+1}, ..., \phi_p^{m+1}, ..., \phi_N^{m+1}\right\}. \tag{4.58}$$

The exact shape of ϕ_p^{m+1} is given by analytical expressions, which might be only piecewise defined to enable complex particle shapes. In the context of this work elliptical particles are used, leading to the following definition of ϕ_p during the time-step $m+1$

$$\begin{aligned} \phi_p^{m+1} =& \frac{\left(\left(\chi_1^{p,m+1} - x_1\right) \cos\left(\beta^{p,m+1}\right) + \left(\chi_2^{p,m+1} - x_2\right) \sin\left(\beta^{p,m+1}\right)\right)^2}{a^2} \\ &+ \frac{\varepsilon^2 \left(\left(\chi_1^{p,m+1} - x_1\right) \sin\left(\beta^{p,m+1}\right) - \left(\chi_2^{p,m+1} - x_2\right) \cos\left(\beta^{p,m+1}\right)\right)^2}{a^2} - 1, \end{aligned} \tag{4.59}$$

where we used the notation χ_i^p and β^p to refer to the properties of a specific particle p. Note that in (4.59) ϕ_p^{m+1} is not a signed distance function, i.e the gradient of ϕ_p^{m+1} has to be normalised in order to return the normal vector, see (2.76). It is entirely possible to reverse the sign of the expression (4.59), which would result in a positive sign of the function ϕ_p within the particle domain Ω_p. Necessarily, the $\inf(\cdot)$ operation in (4.58) needs to change accordingly to a $\sup(\cdot)$ operation.

The particle level-set function ϕ_p^{m+1} is continuous and differentiable. While the combined level-set function ϕ^{m+1} is still continuous it is no longer globally differentiable due to the use of $\inf(\Phi^{m+1})$ in the definition (4.58), which introduces kinks. While ϕ_p^{m+1} is of second polynomial order in case of an elliptical particle and, thus, can be approximated by second order ansatz functions, this is no longer the case for the combined level set. Subsequently, ϕ^{m+1} might contain jumps at the cell boundaries Γ^K, which is a generally undesirable property in the context of the description of an interface.

Smuda and Kummer [190] developed a method to enforce continuity of the level set in a DG-context. A general discontinuous level-set function is $\phi^{DG} \in \mathbb{P}_k\left(\mathfrak{K}_h\right)$. The goal of the continuity projection is to find the optimal L_2-projection of ϕ^{DG} onto the level-set field $\phi^{C0} \in \mathbb{P}_{k+1}$ such that $\phi^{C0} \in \mathcal{C}^0$ is continuous [190]. This conditions can be reformulated as constraints of a quadratic optimisation problem

$$\min \left\|\phi^{C0} - \phi^{DG}\right\|_2^2 \text{ on } \mathfrak{K}_h, \tag{4.60a}$$

$$\text{such that } \left.\phi^{C0}_{j,\text{in}}\right|_{\Gamma^{K,\text{int}}} = \left.\phi^{C0}_{j,\text{out}}\right|_{\Gamma^{K,\text{int}}} \ \forall \Gamma^{K,\text{int}}. \tag{4.60b}$$

The solution for the optimization problem can be found by solving the equivalent system of equations

$$J\left(\widetilde{\boldsymbol{\phi}}\right) = \frac{1}{2}\widetilde{\phi}_i \delta_{ij} \widetilde{\phi}_j - \widetilde{\phi}_i b_i + b_i b_i \rightarrow \min \tag{4.61a}$$

$$\text{such that } A_{ij}\widetilde{\phi}_j = 0. \tag{4.61b}$$

Here, the vector product $\phi^{DG*} = b_i \phi_i$ is the projection of ϕ^{DG} onto $\mathbb{P}_{k^*}$ and the vector $\widetilde{\phi}_i$ is the desired solution, defined by $\phi^{C0} = \widetilde{\phi}\phi_i$, where $\phi_i \in \mathbb{P}_{k+1}\left(\mathfrak{K}_h\right)$. A single row of the constraint matrix A_{ij} is defined by

$$\sum_{n=0}^{k+1} \widetilde{\phi}_{j,n,\text{in}} \phi_{j,n,\text{in}}\left(\boldsymbol{x}\right) - \sum_{n=0}^{k+1} \widetilde{\phi}_{j,n,\text{out}} \phi_{j,n,\text{out}}\left(\boldsymbol{x}\right) = 0, \quad \boldsymbol{x} \in \Gamma^{K,\text{int}}, \tag{4.62}$$

for a sufficient amount of points x_i on the internal surface Γ^{int} [190]. An in depth discussion of the construction and solution of the optimisation problem can be found in Smuda [189] and Smuda and Kummer [190].

4.5. Particle solver

In contrast to the fluid, which is described by the unsteady Stokes equation (2.68) and is solved using the XDG method, the particle equations can be solved with a much simpler method. The translational and rotational motion of the particle is described by the two-dimensional Newton-Euler equation (2.54) and (2.58)

$$V^P \mathfrak{D} \frac{\mathrm{d}v_{ip}}{\mathrm{d}t} = \int_{\Gamma_p} \tau^F_{ij} n_{jp} \,\mathrm{d}s = F_{ip}$$

$$\Theta^S \frac{\mathrm{d}\omega_p}{\mathrm{d}t} = \int_{\Gamma_p} \epsilon_{3ij}\left(x_i - \chi_{iq}\gamma_q\right) \tau^F_{jk} n_{kp} \,\mathrm{d}s = T_p.$$

The integral terms, which are the hydrodynamic forces F_{ip} and torque T_p acting on the particles, are obtained from fluid variables. Thus, it is only necessary to discretise the temporal derivative. Discretisation is carried out using an implicit Adams method

$$v^{m+1}_{ip} = v^m_{ip} + \frac{\Delta t}{12 V^P \mathfrak{D}}\left(5F^{m+1}_{ip} + 8F^m_{ip} - F^{m-1}_{ip}\right), \tag{4.63a}$$

$$\omega^{m+1}_p = \omega^m_p + \frac{\Delta t}{12\Theta^S}\left(5T^{m+1}_p + 8T^m_p - T^{m-1}_p\right), \tag{4.63b}$$

which is a method of third order [86]. The forces F_{ip}^{m+1} and torque T_p^{m+1} are obtained by a numerical integration over the particle surfaces, using the Saye-method described in Sec. 4.3.2. It should be noted that the surface integration is the computationally most expensive function in the particle solver. Due to the implicit character of the Adams method, both, current and previous results for the hydrodynamics are necessary to obtain the particle quantities. Hence, it is necessary to solve the fluid equations before solving the particle equations. The dependency of the particle solver on the results of the fluid solver leads to the implementation of an iterative solver scheme, see Sec. 4.7.

In a second step, the new position and orientation of the particles is determined, again by employing the third order implicit Adams method

$$\chi_{ip}^{m+1} = \chi_{ip}^{m} + \frac{\Delta t}{12}\left(5v_{ip}^{m+1} + 8v_{ip}^{m} - v_{ip}^{m-1}\right), \tag{4.64a}$$

$$\beta_{p}^{m+1} = \beta_{p}^{m} + \frac{\Delta t}{12}\left(5\omega_{p}^{m+1} + 8\omega_{p}^{m} - \omega_{p}^{m-1}\right). \tag{4.64b}$$

4.5.1. Particles at periodic boundaries

Periodic boundary conditions require a special treatment for the particle phase. Consider a rectangular computational domain Ω in two dimensions. Eight virtual domains exists, one for each domain edge Ω_{E_i} and one for each vertex Ω_{V_i}, see Fig. 4.4. Within each virtual domain any particle of the original domain exists at the same position relative to the origin of the virtual domain as in the original domain. The particles within a virtual domain automatically appear at the correct opposing boundary once a particle in the original domain Ω reaches a periodic boundary. Subsequently, it is not necessary to track additional data, because the

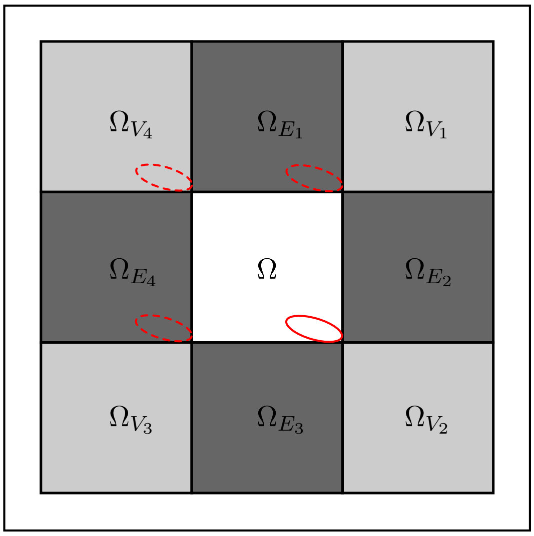

Fig. 4.4.: Each rectangular periodic domain Ω is extended by four virtual domains at the edges $\Omega_{E_1} - \Omega_{E_4}$ and by four virtual domains at the vertices $\Omega_{V_1} - \Omega_{V_1}$. Any particle exists in the original domain Ω and in every virtual domain Ω_{V_i}, Ω_{E_i}. Once a particle in Ω approaches a periodic boundary, its counterparts in the virtual domains automatically appear at the correct opposing boundary as depicted by the dashed particles.

position of the virtual particle can be easily calculated from the position of the original particle, the origin of Ω and the origin of the virtual domain. In the context of calculating the hydrodynamic forces and torques, a sum needs to be formed to obtain the correct results for particles present at the periodic boundary.

4.6. Collisions

Given an infinite resolution of the numerical mesh, i.e. $h^K \to 0$, and an infinite temporal resolution $\Delta t \to 0$, no collisions will occur in an incompressible Newtonian fluid. Instead, the fluid pressure between two approaching particles will increase until it pushes the two particles away from each other. However, if the gap between two approaching particles becomes to small, the unsteady Stokes equation (2.68) is no longer an appropriate model to predict the behaviour of the fluid within the gap. Molecular forces between the particle surfaces, surface roughness, breakdown of lubrication and entanglement of the cilia and flagella might dominate the solution. Furthermore, the continuity assumption no longer holds for very small gaps between the particles, i.e. the Stokes equation becomes invalid.

Besides the physical restriction, a numerical restriction to the minimal distance between two particles exists. As long as the surfaces of two particles are in different cells of the numerical grid, the Saye-algorithm [183] as described in Sec. 4.3.2, is able to distinguish between the separate interfaces. As soon as both particles occupy space in the same cell K_j this is no longer possible, leading to errors in the calculation of the solution for the fluid phase and in the calculation of the hydrodynamic forces and torques acting on the particles. Subsequently, the numerical limit on the minimal distance between two particles is h^Γ, where $h^\Gamma \leq h^K$ is the diameter of the cell at the particle surface.

A collision algorithm is, hence, necessary to

- account for the different physical behaviour of two close particles due to molecular interaction forces, surface roughness, breakdown of lubrication and entanglement of the cilia and flagella,
- prevent that the surfaces of two particles are within the same cell for numerical reasons.

To fulfil this conditions, the collision algorithm needs to contain a physical model for the interaction between two close particles (Sec. 4.6.1) and it is necessary to track the minimal distance between each particle (Sec. 4.6.2). The implementation presented here is highly modular, i.e. one can freely replace the physical model without changing the minimal distance algorithm and vice versa.

4.6.1. Physical collision model

A collision is an interaction between two or more bodies that occurs within a very short period of time compared to a characteristic time interval of the system at hand. The fundamental assumption of the present collision model is conservation of momentum. While each individual particle may have a different momentum before and after the collision, the total momentum of all particles involved remains the same. The surface of the particles is considered smooth,

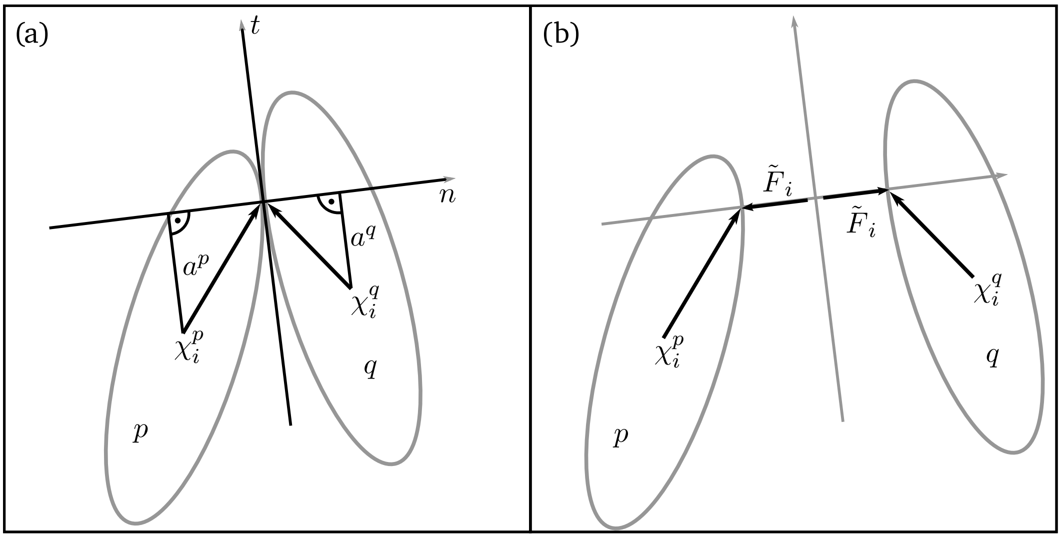

Fig. 4.5.: (a) The geometrical setup for a collision between two particles is defined by the n-t coordinate system. The base vector for the n-axis is the collision normal vector n_i^C. (b) A collision between two particles p and q with smooth surfaces is characterised by the exchange of momentum $\tilde{F}_i$ in the direction of the collision normal vector n_i. Illustration based on Gross et al. [82].

hence, momentum $\widetilde{F}_i$ is only exchanged in the direction of the collision normal vector n_i^C with the magnitude $\widetilde{F} = \widetilde{F}_i n_i^C$, see Fig 4.5.

Another key assumption is that collisions involving multiple particles can be broken down into individual binary collisions. Thus, it is assumed that a many-body collision is in fact simply the rapid succession of multiple binary collisions. As a consequence, the physical model only has to be able to describe the collision between two particles.

To describe the behaviour of a two-particle collision, Gross et al. [82] is followed closely in the current section. A collision consists of two phases. During the compression phase, the particles are pressed into each other and possibly deformed. Quantities describing this phase are indicated by a $+$. The inter-particle forces reach their maximum at $t = t^*$. Hence, the magnitude of the momentum exchanged in the normal direction during this phase can be expressed as

$$\widetilde{F}^+ = \int_{t^+}^{t^*} F(t)\,\mathrm{d}t, \tag{4.65}$$

where the first contact occurs at $t = t^+$ and $F(t)$ is the force between the two particles. After the maximum of the inter-particle forces is reached at t^* the restitution phase follows, in which the particles separate from each other and, depending on their elasticity properties, regain their original shape. Quantities describing the second phase are indicated by $-$. The momentum exchange during the restitution phase is

$$\widetilde{F}^- = \int_{t^*}^{t^-} F(t)\,\mathrm{d}t, \tag{4.66}$$

where the particles loose direct contact at $t = t^-$. Subsequently, the complete momentum exchange during the collision of two particles is

$$\widetilde{F} = \int_{t^+}^{t^-} F\left(t\right) \mathrm{d}t = \widetilde{F}^+ + \widetilde{F}^- . \tag{4.67}$$

Only in the case of ideal elastic behaviour $\widetilde{F}^+$ and $\widetilde{F}^-$ are equal. Under real conditions, it is expected that during the collision kinetic energy is converted into thermal energy and $\widetilde{F}^-$ is smaller than $\widetilde{F}^+$. This is expressed by the means of the coefficient of restitution k

$$\widetilde{F}^- = k\widetilde{F}^+, \quad 0 \leq k \leq 1. \tag{4.68}$$

The coefficient k represents dissipation of energy due to the interaction forces between the particles and deformation, elasticity and plasticity of the individual particles.

The next assumption is that the area of contact between the two particles is small compared to the particle surface. Hence, it can be considered as a single point of contact x_i^C. The normal velocity of the particle p at this point is

$$u^{n,p} = n_i^C u_i^p = n_i^C \gamma_p \left(v_{ip} + \epsilon_{i3j}\omega_p \left(x_j^C - \chi_{jq}\gamma_q\right)\right) \tag{4.69}$$

and the tangential velocity is $u^{t,p} = u_i^p \epsilon_{i3j} n_j^C$. The change of linear momentum between two arbitrary states t^1 and t^2 during the collision is described by

$$\widetilde{F}^{12} = V^P \mathfrak{D} \left(u^{n,p,1} - u^{n,p,2}\right), \tag{4.70}$$

where $u^{n,p,1}$ is the normal velocity at x_i^C of the particle p at the time t_1. Using (4.67), (4.68) together with (4.70) delivers the collision hypothesis

$$k = \frac{u^{n,p,-} - u^{n,q,-}}{u^{n,q,+} - u^{n,p,+}} \tag{4.71}$$

for a collision between two particles p and q.

During the collision, momentum is only exchanged in normal direction, i.e. the surface is assumed to be smooth. Conservation of linear and angular momentum for the first particle p delivers

$$\widetilde{F} = V^P \mathfrak{D} \left(u^{n,p,+} - u^{n,p,-}\right) \tag{4.72}$$

$$a^p \widetilde{F} = -\Theta^S \left(\omega^{p,+} - \omega^{p,-}\right) \tag{4.73}$$

with the eccentricity $a^p = \left(x_i^C - \chi_{ip}\gamma_p\right) \epsilon_{i3j} n_j^C$ (Fig. 4.5). For the second particle q one obtains

$$\widetilde{F} = -V^P \mathfrak{D} \left(u^{n,q,+} - u^{n,q,-}\right) \tag{4.74}$$

$$a^q \widetilde{F} = \Theta^S \left(\omega^{q,+} - \omega^{q,-}\right) \tag{4.75}$$

With (4.71) and (4.72)-(4.75) five equations exists for the five unknowns $\widetilde{F}$, $u^{n,p,-}$, $u^{n,q,-}$, $\omega^{p,-}$ and $\omega^{q,-}$, leading to

$$\widetilde{F} = (1+k) \frac{u^{n,p,+} - u^{n,q,+} + a^p \omega^{p,+} - a^q \omega^{q,+}}{\frac{2}{V^P \mathfrak{D}} + \frac{(a^p)^2 + (a^q)^2}{\Theta^S}}. \tag{4.76}$$

The respective velocities after the collision follow from (4.72)-(4.76)

$$u^{n,p,-} = u^{n,p,+} + \frac{\widetilde{F}}{V^P \mathfrak{D}}, \quad \omega^{p,-} = \omega^{p,+} + a^p \frac{\widetilde{F}}{\Theta^S}, \tag{4.77a}$$

$$u^{n,q,-} = u^{n,q,+} - \frac{\widetilde{F}}{V^P \mathfrak{D}}, \quad \omega^{q,-} = \omega^{q,+} - a^q \frac{\widetilde{F}}{\Theta^S} \tag{4.77b}$$

The velocity of the centre of mass of the particles is obtained by adding the normal velocity after the collision and the undisturbed tangential velocity

$$v_i^p = u^{n,p,-} n_i^C + u^{t,p,+} \epsilon_{i3j} n_j^C. \tag{4.78}$$

It should be noted, that this model is purely based on the kinetics of a rigid body. Molecular effects, such as van der Waals forces are only taken into account indirectly via the coefficient of restitution. Furthermore, entanglement of flagella or cilia is not directly taken into account. All such additional effects need to be taken care of by k. Nevertheless, due to the mentioned modularity of the system it is easily possible to change the physical model without needing to change the entire algorithm.

4.6.2. Numerical implementation

The calculations of the physical model described in the previous section can be carried out explicit, i.e. they are comparably cheap in terms of computation power. The tracking of the distance between all particles is a much more demanding task. For this reason, the tracking algorithm is divided into two parts. In a first step, particles, which are already close to each other, are selected. In a second step the exact distance between those particles is calculated, which is used to decide whether the particle will collide in the current time-step of the simulation.

Pre-selection algorithm

Core of the pre-selection algorithm is the R-tree $\mathcal{R}$, proposed by Guttman [83]. The latter publication forms the basis for the current section. The particles are grouped into a self-balancing tree, where each node N_j^i of the tree is related to a Minimal Bounding Rectangle (MBR) M_j^i. This tree consists of the following elements

- the root node N^0, corresponding to the MBR M^0, where all lower-level MBRs are enclosed in M^0,
- the branch nodes, which enclose a subset of MBRs,
- the leave nodes of the tree, which contain the MBRs of the physical particles.

The root node and the branch nodes contain a number of c child-nodes. The number of child-nodes allowed per parent node is capped by a maximum C, where in the example in Fig. 4.6 $C = 2$. Hence, in the example the root node N^0, which is associated with the MBR M^0, contains two child-nodes N_1^1, N_2^1 and their corresponding MBRs M_1^1, M_2^1. The superscript refers to the level of the tree, where 0 indicates the root level. The subscript on the other

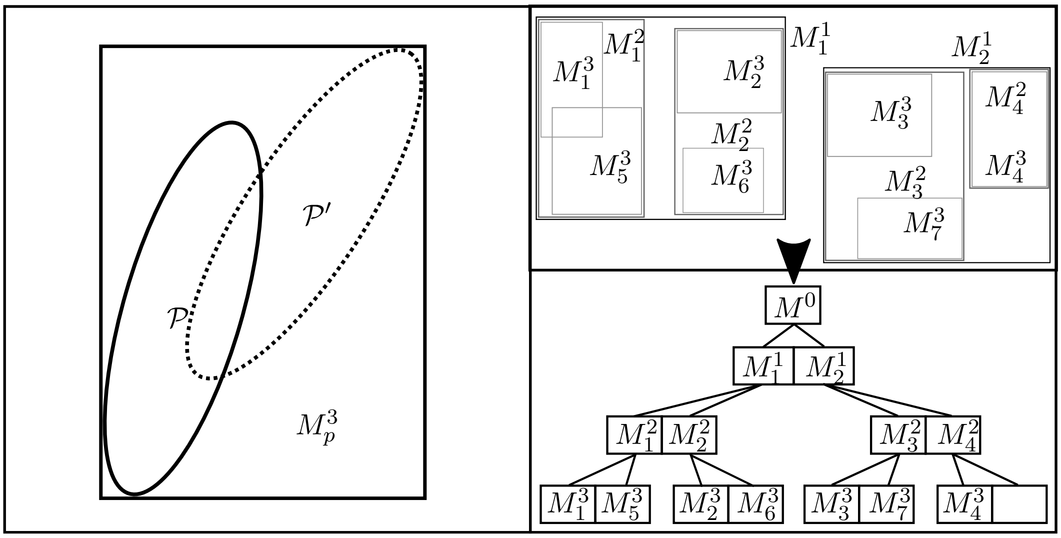

Fig. 4.6.: The lowest level MBR M_p^3 of the R-tree $\mathcal{R}$ contains a particle p, described by a set of points $\mathcal{P} \in \Omega$ and the same particle at the new position and with the new orientation in the next time-step, described by a second set $\mathcal{P}' \in \Omega$. The superscript refers to the level of the tree, where 0 indicates the root level and 3 is the lowest level in this example. The subscript is a counting variable, in case of the lowest level particle MBR it is always equivalent ot the particle ID in the array P. On the right side an exemplary R-tree is constructed for seven particles. Each node contains $m = 2$ MBRs and beside the child-node of M_4^2 every node is fully filled. Due to the low number of MBRs per node M_4^2 and M_4^3 are equivalent. Collisions are detected by finding overlaps between the MBRs, hence, only the particles belonging to M_1^3 and M_5^3 might collide.

hands is a simple counting variable. The child nodes of N_1^1 and N_2^1 again contain up to $C = 2$ child-nodes and so forth. Note that a parent node is not required to contain $c = C$ child-nodes. In the example, the branch node M_4^2 only contains a single child-node M_4^3.

The leaves of the tree, which are at the third level in the given example, contain the physical particles. Due to the self-balancing property of the R-tree, a parent node, which contains a leave node, necessarily only contains leaves. Each particle p is geometrical described by the set of points $\mathcal{P} \in \Omega$. The set $\mathcal{P}' \in \Omega$ describes the geometry of the particle at the next time-step, where the new position and orientation are predicted with the current particle velocities. The union $\widehat{\mathcal{P}} = \mathcal{P} \cup \mathcal{P}'$ of the two sets $\mathcal{P}$ and $\mathcal{P}'$, is enclosed by a single MBR, see Fig. 4.6. Subsequently, a collision can only occur if two of the single-particle MBRs intersect. Particle MBRs between different branches of the tree can only intersect with each other if the higher-level branch node MBRs intersect. Hence, it is, in the most cases, not necessary to check for intersection between all nodes of the tree, leading to a decrease in computational cost.

In the following paragraphs the implementation of the R-tree in BoSSS is presented. The initialisation routine of the R-tree, see Alg. 1 requires two additional recursive sub-algorithms:

- the insertion algorithm, which inserts a single-particle MBR M_p to the tree, see Alg. 2 and Fig. 4.7,

- the split algorithm, which splits a node if the number of child-nodes c exceeds a predefined maximum C, see Alg. 3 and Fig. 4.8.

The initialisation starts with the creation of the root node N^0. MBRs M_p are calculated for each particle. The single-particle MBRs are subsequently inserted to the tree by employing the method InsertMBR (Alg. 2). Periodic boundaries of the computational domain Ω require an additional step in the initialising routine. The twins p^{vd} of a particle p in the virtual domains Ω_{V_i} and Ω_{E_i} automatically appear in the domain Ω if p oversteps a periodic boundary, see Sec. 4.5.1. Thus, the initialisation algorithm (Alg. 2) checks for each particle p^{vd} in a virtual domain, whether it has overstepped a periodic boundary and lies within the original domain Ω. If this is the case the MBR corresponding to the particle p^{vd} is added to the R-tree.

Algorithm 1 Pseudocode implementation of the construction of the particle R-tree.

```
procedure InitialiseTree($P, \Delta t$)    ▷ $P$ is an array, which contains all particles.
    Initialise root node $N^0$
    for p=0; p<$P$.length; p++ do
        $M_p$=CalculateParticleMBR($P[p], \Delta t$)    ▷ see (4.84)
        InsertMBR($M_p^k, N^0$)    ▷ See Alg. 2
        for all $p^{\text{vd}}$, vd $\in \{1, 2, ..., 8\}$ do    ▷ $p^{\text{vd}}$ is the twin of $p$ in a virtual domain to realise periodic boundaries.
            if IsInsidePeriodicDomain($p^{\text{vd}}$) then    ▷ $p^{\text{vd}}$ is partly within the domain $\Omega$.
                $M_{p^{\text{vd}}}$=CalculateParticleMBR($P[p], \Delta t$)    ▷ see (4.84)
                InsertMBR($M_{p^{\text{vd}}}, N^0$)    ▷ See Alg. 2
            end if
        end for
    end for
end procedure
```

The insertion algorithm (Alg. 2, Fig. 4.7) distinguishes two cases. If the node N^i, in which the particle MBR M_p shall be inserted, contains leaves of the tree, the MBR M_p corresponding to the particle p is added as an additional leaf. Subsequently, the node-level MBR M^i needs to be recalculated. The new MBR M^i contains M_p and the old MBR $\widehat{M}^i$, related to the node N^i. Thus, the new MBR M^i is defined by

$$M_p \subset M^i \quad \vee \quad \widehat{M}^i \subset M^i \quad \vee \quad \left|M^i\right| \to \min, \tag{4.79}$$

where the expression $\left|M^i\right| \to \min$ ensures that the area enclosed by M^i is minimal and, thus, the rectangle M^i is actually a MBR.

In the second case N^i is a branch node of the tree. Hence, $c \leq C$ child-nodes N_j^{i+1} exist, which again contain child-nodes N_k^{i+2}. Thus, M_p needs to be inserted into one of the child-nodes N_j^{i+1} of N^i. To prevent unnecessary calls to the collision algorithm, we require that the MBRs of the branch nodes should intersect as little as possible. Hence, in Alg. 2 we search for the child-node N_j^{i+1} of N^i where the minimal bounding rectangle M_j^{test} minimizes

$$\min_{k \neq j, k \in \{1,...,c\}} \left|M_j^{\text{test}} \cap M_k^{i+1}\right|, \quad \forall j \in \{1, ..., c\} \tag{4.80}$$

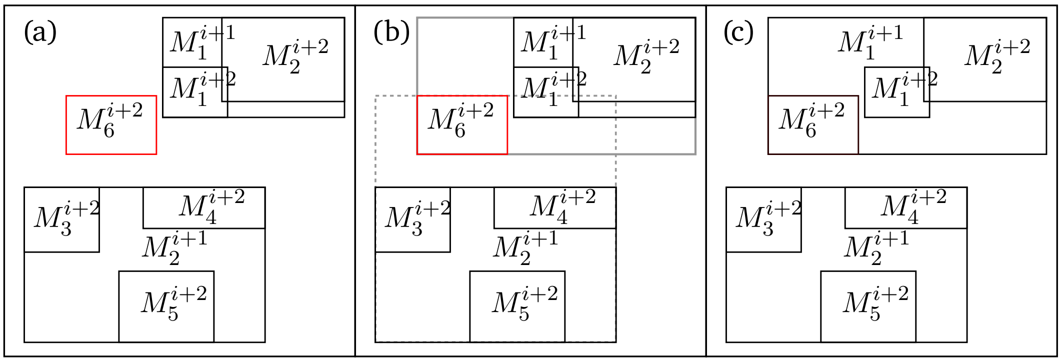

Fig. 4.7.: (a) The MBR M_6^{i+1} shall be inserted into one of the two MBRs M_1^i or M_2^i, which contain already the lower-level MBRs $M_1^{i+1} - M_5^{i+1}$. (b) The insertion is tested for both upper-level MBRs. By requiring a minimal intersection between all MBRs, see (4.80), the MBR M_1^i is chosen for insertion, leading to the result visible in (c).

where

$$M_p \subset M_j^{\text{test}} \quad \vee \quad M_j^{i+1} \subset M_j^{\text{test}} \quad \vee \quad \left|M_j^{\text{test}}\right| \rightarrow \text{min}, \quad j \in \{1, ..., c\}\,, \tag{4.81}$$

i.e. M_j^{test} is the union of one of the child-node MBRs M_j^{i+1} and of M_p. In Fig. 4.7 the condition of minimal intersection (4.80) is visualised. Here, two MBRs M_1^i and M_2^i need to be tested. If M_6^{i+1} is added to M_1^i, the resulting upper level MBRs M_1^i and M_2^i do not intersect. In the case of the insertion of M_6^{i+1} into M_2^i the resulting MBRs M_1^i and M_2^i would clearly intersect. Thus, M_6^{i+1} is inserted into M_1^i as visualised in Fig. 4.7c, which requires the method InsertMBR$\left(M_p, N_j^{i+1}\right)$ to be called again.

Algorithm 2 Pseudocode implementation of the recursive insertion of a new MBR or node.

```
procedure InsertMBR($M_p, N^i$)
    if IsLeaf$\left(N_1^{i+1}\right)$ then                          ▷ $N^i$ contains only leave nodes.
        Add $M_p$ to $N^i$, Update $M^i$
        if $c > C$ then                                  ▷ $c$ is the number of child-nodes of $N^i$
            Split$\left(N^i\right)$
        end if
    else                                                  ▷ $N^i$ has $c \leq C$ child-nodes
        Find child-node $N_j^{i+1}$ of $N^i$ such that
        $\left|M_j^{\text{test}} \cap M_k^{i+1}\right| \rightarrow \text{min} \quad \forall j, k \in \{1, ..., c\}\,, k \neq j$
        InsertMBR$\left(M_p, N_j^{i+1}\right)$                                ▷ Recursive call
        Update $M_j^{i+1}$
        if $c > C$ then
            Split$\left(N^i\right)$
        end if
    end if
end procedure
```

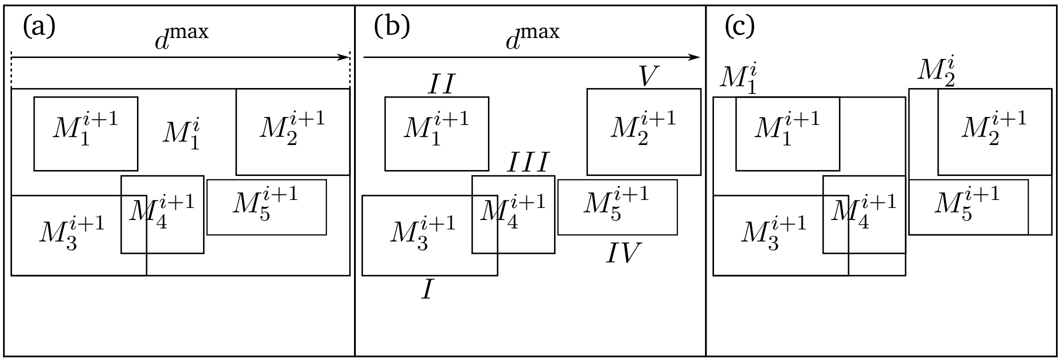

Fig. 4.8.: (a) The MBR M_1^i contains $c = 5$ children, however, it is assumed that the maximum is $C = 4$. Thus, the node needs to be split. The edge of M_1^i in the horizontal direction is the longest, indicated by $d^{\max}$. (b) The children are sorted by their left upper corner in the direction of the vector $d^{\max}\boldsymbol{e}^1$, as indicated by the Roman numbers $I - V$. The new parent MBRs M_1^i and M_2^i are initialised by the two MBRs at the left and right end of the sequence $I - V$,. i.e M_3^{i+1} initialises M_1^i and M_2^{i+1} initialises M_2^i. The remaining MBRs M_1^{i+1}, M_4^{i+1} and M_5^{i+1} are added to the new parents under the condition of minimal intersection, leading to the result presented in (c).

If the node N_j^i is overflown, i.e. its MBR encloses c children and $c > C$, it is necessary to split a node. The split algorithm (Alg. 3, Fig. 4.8) is based on the longest edge $d^{\max}$ of the MBR M_j^i corresponding to the node N_j^i to be split. Hence, either the horizontal $\boldsymbol{e}^1$ or the vertical direction $\boldsymbol{e}^2$ are chosen in two dimensions, where $\boldsymbol{e}^1$ and $\boldsymbol{e}^2$ are the unit vectors of the coordinate frame. Each child-node N_k^{i+1} of N_j^i is sorted according to the $d^{\max}$-coordinate of the left upper point of the MBR M_k^{i+1}, see Fig. 4.8b. The sorted sequence of MBRs is indicated by Roman numbers and the subscript of the constituting MBRs is changed M_l^{i+1}, $l \in \{I, II, III, ..., c\}$. In the example given in Fig. 4.8, the nodes are sorted into the sequence $I - V$. In the next step, the node N_j^i, which will be split, is temporarily removed and reinitialised by the first child-node in the sorted sequence of child-nodes. Furthermore, a new node N_{j+1}^i is initialised with the last child-node of the sorted sequence. In the case of the example given in Fig. 4.8, the child-node M_3^{i+1} is the first node in the sequence $I - V$ and reinitialises the node N_1^i corresponding to the MBR M_1^i. The node N_2^{i+1} corresponding to M_2^{i+1} on the other hand is the last node in the sequence $I - V$ and, thus, initialises the new parent MBR M_2^i. The remaining child-nodes N_l^{i+1}, $l \in \{II, ..., c - I\}$ are added to either of the two nodes N_j^i, N_{j+1}^i under the condition of minimal intersection

$$\min\left\{\left|\left(M_l^{i+1} \cup M_j^i\right) \cap M_{j+1}^i\right|, \left|\left(M_l^{i+1} \cup M_{j+1}^i\right) \cap M_j^i\right|\right\}. \tag{4.82}$$

Hence, in the example given in Fig. 4.8, the two MBRs M_1^{i+1} and M_4^{i+1} are added to M_1^i and the remaining MBR M_5^{i+1} is added to M_2^i. It should be noted that the strategy for splitting a node differs from the original R-tree. Guttman [83] proposed a split algorithm, which requires that the area enclosed by the MBRs is minimal, whereas the present implementation requires that the intersections between MBRs are minimal. In most cases, however, both strategies will lead to the same result. For example, the strategy proposed by Guttman [83] would lead to the same results for the MBRs M_1^{i+1} and M_2^{i+1} in Fig. 4.8.

To obtain the parent node of N_j^i and N_{j+1}^i, two cases need to be considered. If N_j^i was the

Algorithm 3 Pseudocode implementation of the splitting of a node.

```
procedure SPLIT($N^i_j$)
    Find longest edge $d^{\max}$ of $M^i_j$
    Sort child-nodes $N^{i+1}_k$, $k \in \{1, ..., c\}$ into $N^{i+1}_l$, $l \in \{I, II, III, ..., c\}$   ▷ Sequence indicated by Roman numbers
    Remove child-nodes $N^{i+1}_l$, $l > I$ from $N^i_j$
    Initialise $N^i_{j+1}$, add $N^{i+1}_c$ to $N^i_{j+1}$
    for all $N^{i+1}_l$, $l \in \{II, ..., c - I\}$ do   ▷ Insert child-nodes with minimal intersection
        if $\left|\left(M^{i+1}_l \cup M^i_j\right) \cap M^i_{j+1}\right| < \left|\left(M^{i+1}_l \cup M^i_{j+1}\right) \cap M^i_j\right|$ then
            Add $N^{i+1}_l$ to $N^i_j$
        else
            Add $N^{i+1}_l$ to $N^i_{j+1}$
        end if
    end for
    if $N^i_j$ is root node i=0 then
        Initialise new root $N^0$, add $N^i_j$, $N^i_{j+1}$ to $N^0$   ▷ Increase tree depth
    else
        Add $N^i_{j+1}$ to parent $N^{i-1}$
        if (Number of child-nodes in $N^{i-1}$) $> C$ then
            SPLIT($N^{i-1}$)   ▷ Recursive call
        end if
    end if
end procedure
```

old root node $i = 0$ of the tree, a new root node is created as a parent to the split nodes N^i_j and N^i_{j+1}, see Alg. 3. If N^i_j and N^i_{j+1} are branch nodes both are added to the parent N^{i-1}. However, the SPLIT$\left(N^{i-1}\right)$ algorithm might be called again to account for an overflown parent node N^{i-1}.

The calculation of the particle MBRs requires the knowledge about the most extreme point on the particle surface in the directions of the unit vectors $\boldsymbol{e}^1$, $-\boldsymbol{e}^1$, $\boldsymbol{e}^2$ and $-\boldsymbol{e}^2$. Such a point p_i is called support point and is also necessary for the calculation of the minimal distance between two particles. The derivation to obtain the support point can be found in Sec. 4.6.2, see Eq. (4.87). For now we assume that the four necessary support points on the combined set $\widehat{\mathcal{P}} = \mathcal{P} \cup \mathcal{P}'$ of the particle p and its projection to the next time-step are

$$p_i^{+1}\left(\boldsymbol{e}^1\right), \, p_i^{-1}\left(-\boldsymbol{e}^1\right), \, p_i^{+2}\left(\boldsymbol{e}^2\right) \text{ and } p_i^{-2}\left(-\boldsymbol{e}^2\right). \tag{4.83}$$

Thus, one obtains the four vertices of the particle MBR

$$\boldsymbol{V}^1 = \left[p_1^{-1}, p_2^{+2}\right], \, \boldsymbol{V}^2 = \left[p_1^{+1}, p_2^{+2}\right], \, \boldsymbol{V}^3 = \left[p_1^{+1}, p_2^{-2}\right] \text{ and } \boldsymbol{V}^4 = \left[p_1^{-1}, p_2^{-2}\right]. \tag{4.84}$$

The position and orientation of the particles change within each time-step. Hence, it is necessary to update the R-tree constantly. Beside the necessity of updating the particle MBRs the tree itself needs to be restructured to provide an efficient search. However, the reinitialisation of the tree is a costly procedure. Assuming that the displacement of a particle during a single time-step is small, it is not necessary to reinitialise the tree at each time step. Hence, the MBRs are updated within each time-step, following (4.84), and the the tree itself is reinitialised every n time-steps using Alg. 1. No general value of n can be given, however, it has been proven useful to choose a value between ten and one hundred time-steps.

A potential collision is identified by determining overlapping particle MBRs. The search algorithm is presented in Alg. 4. Starting with the root node N^0 each level of the tree is checked for an overlap with the particle MBR M_p, leading to a list of particles, which potentially collide with each other.

Algorithm 4 Pseudocode implementation of the search in a R-tree.

```
procedure SearchForOverlap(particleMBR $M_p$, particleID $p$, currentNode $N^i$)
    List<int> overlappingParticles=new List<int>
    for all Child-nodes $N_j^{i+1}$ in $N^i$ do
        if $M_p \cap M^i \neq \emptyset$ then    ▷ Intersections between $M_p$ and MBR $M^i$ of $N^i$
            if IsLeaf($N_j^{i+1}$) && $j \neq p$ then    ▷ $N_j^{i+1}$ is a leaf and contains a different particle with the ID $j$
                overlappingParticles.Add(j)
            else
                overlappingParticles.AddRange(SearchForOverlap($M_p$, $p$, $N_j^{i+1}$))
            end if
        end if
    end for
    return overlappingParticles
end procedure
```

Distance algorithm

The pre-selection algorithm returns all currently close particles. To determine whether or not this particle collide and to calculate the effects of such an collision it is necessary to determine the minimal distance between the particles. To ensure fast determination of the distance the Gilbert-Johnson-Keerthi (GJK) algorithm [80] is employed. The algorithm computes the distance between convex objects and returns the minimal distance and the closest point on the other object of the two participating objects p and q. An object in case of the present setup might be either a particle or the domain wall. An overview of the algorithm is given in the pseudocode implementation Alg. 5 and a visualisation of a single iteration of GJK can be found in Fig. 4.9.

Instead of comparing every point $\boldsymbol{x}^P \in \mathcal{P}$, $\boldsymbol{x}^Q \in \mathcal{Q}$ in the sets $\mathcal{P}$, $\mathcal{Q}$, corresponding with the objects p, q, to find the minimal distance, the problem is reduced to computing the minimal distance between a simplex and the origin. A simplex is a polytope with $n+1$ vertices, where the order $n \leq d$ of the simplex is restricted by the spatial dimension d of the problem. Thus, in two dimension, GJK generates simplices of maximal second order, i.e. a triangle, in each iteration.

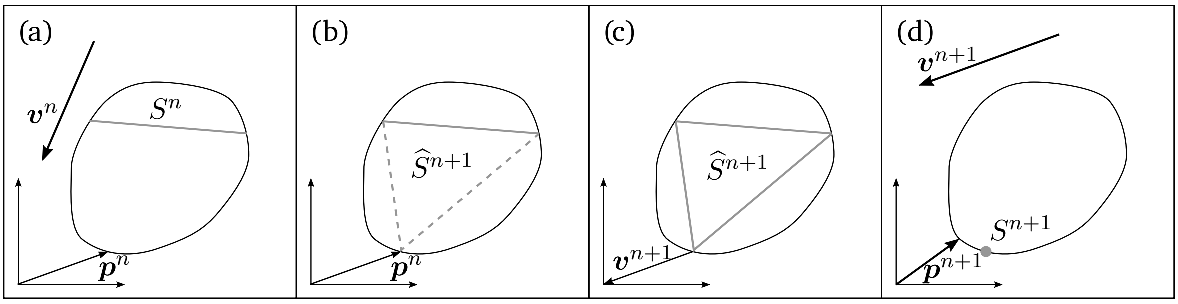

Fig. 4.9.: The image series shows a visualisation of a single step of the GJK-algorithm. In the first panel (a), $p_i^n = s_i^{\mathcal{C}}(\boldsymbol{v}^n)$ is the most extreme point on the set $\mathcal{C}$ in the direction of v_i^n, where $s_i^{\mathcal{C}}$ is the support mapping of $\mathcal{C}$. The point p_i^n is added to the simplex S^n in (b), resulting in the intermediate simplex $\widehat{S}^{n+1} = S^n \cup \boldsymbol{p}^n$. The minimal distance between $\widehat{S}^{n+1}$ and the origin is the lower vertex, i.e. p_i^n itself. In (c) the new vector $v_i^{n+1} = -p_i^n$ is drawn which is used in the next iteration (d) to determine the new support point $p_i^{n+1} = s_i^{\mathcal{C}}\left(\boldsymbol{v}^{n+1}\right)$. The simplex S^{n+1} only contains the vertex p_i^n of the intermediate simplex $\widehat{S}^{n+1}$.

To obtain the simplex, the Minkowski-difference of the two particles is introduced. The Minkowski-difference $\mathcal{C}$ is defined as the difference between each vector of one set $\mathcal{P}$ with each vector of the other set $\mathcal{Q}$

$$\mathcal{C} = \mathcal{P} - \mathcal{Q} = \left\{ \boldsymbol{x}^C = \boldsymbol{x}^P - \boldsymbol{x}^Q \,\middle|\, \boldsymbol{x}^P \in \mathcal{P}, \boldsymbol{x}^Q \in \mathcal{Q} \right\}. \tag{4.85}$$

Hence, the minimal distance vector $r_i{}^{PQ}$ is the vector $x_i{}^C \in \mathcal{C}$ closest to the origin. Thus, the problem at hand is to find

$$r_i{}^{p,q} = \left\{ x_i{}^C \mid \min \left|\boldsymbol{x}^C\right| \quad \forall \boldsymbol{x}^C \in \mathcal{C} \right\}. \tag{4.86}$$

It is, however, not necessary to calculate the entire Minkowski-difference. Instead, the support mapping of the particles is used. It returns the most extreme point p_i on the surface of the object $\mathcal{C}$ in the direction of a vector v_i. A point p_i is called support point of a convex set $\mathcal{C}$ if

$$p_i = s_i^C(\boldsymbol{v}) \tag{4.87a}$$

with

$$v_i p_i = \max \left\{ v_i x_i{}^C | \boldsymbol{x}^C \in \mathcal{C} \right\}, \tag{4.87b}$$

where $s_i^C(\boldsymbol{v})$ is called support mapping of the set $\mathcal{C}$, see Fig. 4.10a. Furthermore, it is known [80] that the support mapping of a Minkowski-difference can be obtained with the support mappings of the constituting sets $\mathcal{P}$ and $\mathcal{Q}$ by

$$s_i^C(\boldsymbol{v}) = s_i^P(\boldsymbol{v}) - s_i^Q(-\boldsymbol{v}). \tag{4.88}$$

For geometric primitives, e.g. spheres and ellipses, an algebraic support function exists, which allows to reach machine precision for the distance vector within a finite number of iterations. The support mapping for a disk with the centre of mass χ_i is [21]

$$s_i^{\text{disk}}(\boldsymbol{v}) = \begin{cases} \chi_i + \dfrac{a v_i}{2\,|\boldsymbol{v}|} & \text{if } |\boldsymbol{v}| \neq 0 \\ 0 & \text{otherwise,} \end{cases} \tag{4.89}$$

Algorithm 5 Pseudo-code implementation of the GJK-algorithm [80] to determine the minimal distance between two convex particles.

```
procedure GJK($\mathcal{P}$, $\mathcal{Q}$)    ▷ Input: Two sets $\mathcal{P}$, $\mathcal{Q}$ defining the geometry of two particles
    Initialize the Simplex ${}^{0}S$ with an arbitrary point ${}^{0}\boldsymbol{v} = \boldsymbol{x}^{C} \in \mathcal{C} = \mathcal{P} - \mathcal{Q}$
    Calculate ${}^{0}p_i = s_i^C\left({}^{0}\boldsymbol{v}\right) = s_i^P\left({}^{0}\boldsymbol{v}\right) - s_i^Q\left(-{}^{0}\boldsymbol{v}\right)$    ▷ See (4.88)
    while $-{}^{n}v_i\,{}^{n}v_i \leq {}^{n}p_i\,{}^{n}v_i$ do    ▷ See (4.97)
        ${}^{n+1}\widehat{S} = {}^{n}S \cup {}^{n}p_i$    ▷ See (4.93)
        Calculate the min. distance ${}^{n+1}v_i$ between ${}^{n+1}\widehat{S}$ and the origin    ▷ See (4.94)
        Reduce order of ${}^{n+1}\widehat{S}$    ▷ See (4.96)
        Calculate ${}^{n+1}p_i = s_i^C\left({}^{n+1}\boldsymbol{v}\right) = s_i^P\left({}^{n+1}\boldsymbol{v}\right) - s_i^Q\left(-{}^{n+1}\boldsymbol{v}\right)$    ▷ See (4.88)
    end while
    Output: Minimal distance $r_i^{p,q} = {}^{n+1}v_i$
end procedure
```

where a is the diameter of the disk and v_i is the direction vector to be tested. The support mapping of objects derived from a disk with an affine transformation

$$T_i\left(\boldsymbol{x}\right) = B_{ij} x_j + c_i \tag{4.90}$$

can be obtained with [21]

$$s_i^T = T_i\left(s_{disk}\left(\boldsymbol{B}^T \boldsymbol{v}\right)\right). \tag{4.91}$$

For particles with an arbitrary shape, i.e. with a non-existing explicit formulation of the support mapping, a binary search is employed to find the current support point p_i. Consider the three points $\left\{\boldsymbol{x},\, \boldsymbol{x}^{\text{left}},\, \boldsymbol{x}^{\text{right}}\right\} \in \mathcal{P}$, where $\mathcal{P}$ is again the set of points describing the surface of the particle p. The points x_i^{left} and x_i^{right} are the left and right neighbour of x_i at the surface Γ. The support point p_i in the direction of v_i is found if the two conditions

$$x_i v_i > x_i^{\text{left}} v_i \tag{4.92a}$$

and

$$x_i v_i > x_i^{\text{right}} v_i \tag{4.92b}$$

are fulfilled, leading to $p_i = x_i$. Otherwise the search is continued on the left or right part of the surface, depending on which of the two scalar products $x_i^{\text{left}} v_i$, $x_i^{\text{right}} v_i$ has the larger result. Since the support mapping only has a unique solution if the particle is convex, GJK is limited to convex particles. Nevertheless, by dividing a concave particle into multiple convex sub-particles, the algorithm may also be employed to arbitrary shapes.

From now on a preceding superscript n indicates the current iteration of the GJK algorithm. After finishing the calculation of the support point, the resulting point ${}^{n}p_i = s_i^C\left({}^{n}\boldsymbol{v}\right)$ is added to the simplex of the previous iteration ${}^{n}S$

$${}^{n+1}\widehat{S} = {}^{n}S \cup {}^{n}\boldsymbol{p}, \tag{4.93}$$

which is the intermediate simplex of the $n+1$ iteration of the distance algorithm. As stated earlier, the order of the simplex is restricted by the dimension of the problem, i.e. in two dimensions ${}^{n+1}\widehat{S}$ contains maximal three points. The restriction is enforced by removing points

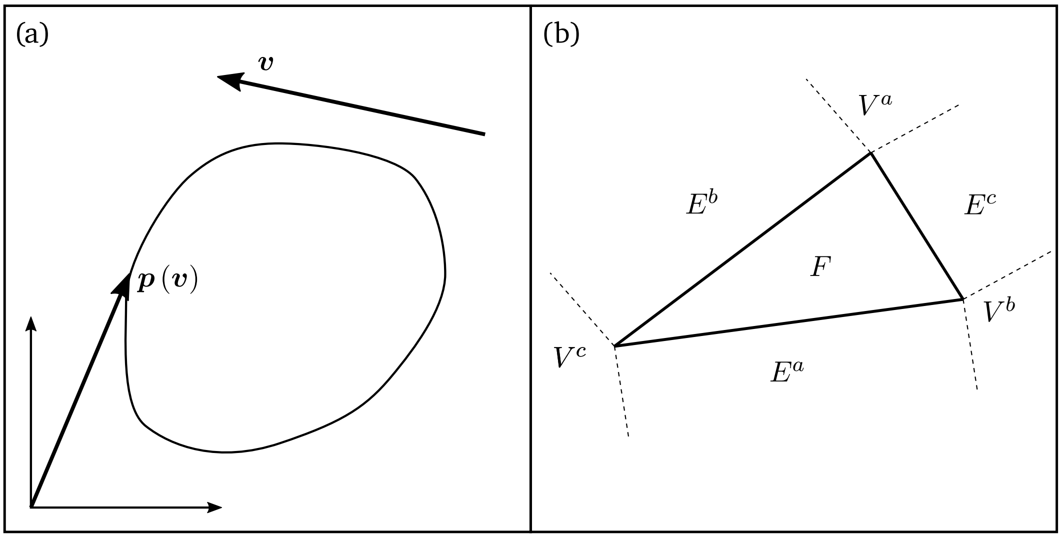

Fig. 4.10.: (a) The graphic visualises the support mapping. $p_i = s_i(\boldsymbol{v})$ is the most extreme point of the object in the direction of v_i. (b) A second order simplex is a triangle. Seven Voronoi-regions [72] are related to the simplex, the face region F, three edge regions E^k and three vertex regions V^k where $k \in \{a, b, c\}$.

from the simplex at a later state in the algorithm, see (4.96). In the first iteration the simplex ${}^0S = \boldsymbol{x}^C \in \mathcal{C}$ is initialised with a single arbitrary point of the set $\mathcal{C}$.

The distance between the simplex ${}^{n+1}\widehat{S} = \left\{\boldsymbol{p}^a, \boldsymbol{p}^b, \boldsymbol{p}^c\right\}$ and the origin is obtained by employing Voronoi-regions [72]. The different regions $R = \left\{F, E^a, E^b, E^c, V^a, V^b, V^c\right\}$ are visualised in Fig. 4.10b for a simplex of second order. To determine the relative position of the simplex towards the origin, each region is tested whether it contains the origin. After the correct region is obtained the distance between the origin and the related sub-simplex can be calculated. A vertex region, say V^a associated with the point $\boldsymbol{p}^a \in {}^{n+1}\widehat{S}$ contains the origin $\boldsymbol{O} = (0, 0)$ if the following conditions are fulfilled

$$p_i^a p_i^a - p_i^a p_i^b \leq 0, \tag{4.94a}$$

$$p_i^a p_i^a - p_i^a p_i^c \leq 0. \tag{4.94b}$$

To test whether the origin is contained in one of the edge regions, e.g the region E^c belonging to the edge between p_i^a and p_i^b, the following conditions have to be fulfilled

$$p_i^a p_i^a - p_i^a p_i^b \geq 0, \tag{4.94c}$$

$$p_i^b p_i^b - p_i^a p_i^b \geq 0, \tag{4.94d}$$

$$p_i^b \epsilon_{ijk} \epsilon_{jlm} \left(p_l^b - p_l^c\right) \left(p_m^b - p_m^b\right) \left(p_k^b - p_k^a\right) \geq 0. \tag{4.94e}$$

If the origin is neither in one of the edge regions nor in one of the vertex regions it must be in the face region of the 2nd-order simplex. Thus, the particle would overlap. In case of higher order simplices in higher dimensions there might be multiple face regions and additionally volume regions, which have to be checked individually. An example for a 3rd-order simplex is given by Ericson [72].

After the correct region is obtained, the distance between the related sub-simplex $R' \subset {}^{n+1}\widehat{S}$ and the origin can easily be calculated. If the origin lies within a vertex region, the vertex itself is the new vector ${}^{n+1}v_i = -p_i^k$, $k \in \{a, b, c\}$, see Fig. 4.9. In case of an edge region the distance vector must be perpendicular to the edge. Let e_i^k, $k \in \{a, b, c\}$ be the unit vector parallel to the edge related to the Voronoi-region E^k. Thus, in two dimensions one obtains the distance vector with

$${}^{n+1}v_i = \pm\epsilon_{ij3} e_j^k \quad k \in \{a, b, c\}\,, \tag{4.95}$$

where the sign of the right hand side depends on the relative position of the origin towards the edge.

The simplex ${}^{n+1}\widehat{S}$ is now reduced to the sub-simplex

$${}^{n+1}S = R' \subset {}^{n+1}\widehat{S}. \tag{4.96}$$

Thus, the order of the simplex is reduced after one iteration to two in case of an edge region or one in case of a vertex region. Accordingly, this reduction enforces the restriction of the order of the simplex to $n \leq d$. The distance vector ${}^{n+1}v_i$ between the sub-simplex R' and the origin is used in the next iteration to calculated the following support point ${}^{n+1}p_i$. However, once the condition

$$-\,{}^{n+1}v_i\,{}^{n+1}v_i \leq {}^{n+1}p_i\,{}^{n+1}v_i \tag{4.97}$$

is fulfilled, the algorithm ends and returns the minimal distance vector $r_i^{p,q} = {}^{n+1}v_i$ [80].

Collision algorithm

The complete collision algorithm is presented in pseudocode in Alg. 6. It is initialised with all particles determined by the pre-selection algorithm to be close to each other. Based on the minimal distance between those particles it is determined whether the particles will collide pairwise in the current time-step Δt. A safe time-step Δt^{safe} is computed, where no collision between any particle occurs

$$\Delta t^{\text{safe}} = \inf\left\{ \Delta t^{p,q} | \, p, q = 1, 2..\widehat{N}, p \neq q \right\}, \quad \Delta t^{p,q} = \alpha \frac{|\boldsymbol{r}^{p,q}|}{\Delta v^{n,p,q}}, \tag{4.98}$$

where $\widehat{N} \leq N$ are all particles selected by the pre-selection algorithm. Within each cycle of the while-loop **while** $\Delta t^{\text{acc}} < \Delta t$ **do** in Alg. 6 the safe time-step is accumulated $\Delta t^{\text{acc}} = \Delta t^{\text{acc}} + \Delta t^{\text{safe}}$. If at some point in the collision routine the accumulated time-step is larger than the time-step of the simulation $\Delta t^{\text{acc}} \geq \Delta t$, no collision is triggered and the simulation will proceed with the next time-step. The velocity $\Delta v^{n,p,q}$ in (4.98) is the difference of the normal velocities of two particles

$$\Delta v^{n,p,q} = v_i^q n_i^C - v_i^p n_i^C, \tag{4.99}$$

where the normal vector n_i^C is approximated with the normalised distance vector

$$n_i^C \approx \frac{r_i^{p,q}}{|\boldsymbol{r}^{p,q}|}. \tag{4.100}$$

The numerical parameter α in (4.98) is used for scaling. Due to the approximation (4.100), Δt^{safe} might be too large, leading to overlapping particles. Overlapping particles need to be

Algorithm 6 Pseudocode implementation of the complete collision algorithm.

```
procedure CalculateCollision(Particles $P$, R-tree $\mathcal{R}$, Time-step $\Delta t$)
    $\Delta t^{\text{acc}} = 0,\ \Delta t^{\text{safe}} = \infty$
    while $\Delta t^{\text{acc}} < \Delta t$ do
        $\left|\boldsymbol{r}^{\text{min}}\right| = \infty$
        while $\left|\boldsymbol{r}^{\text{min}}\right| > \lambda$ do
            for all particle $p \in P$ do
                Update particle state: $\chi_{ip}\left(t^m + \Delta t^{\text{acc}}\right),\ \beta_p\left(t^m + \Delta t^{\text{acc}}\right)$
                $M_p$=CalculateParticleMBR($p$, $\Delta t$)                    ▷ see (4.84)
                $Q$=$\mathcal{R}$.SearchForOverlap($M_p$, $p$, $N^0$)  ▷ See Alg. 4, $N^0$ is root node of $\mathcal{R}$
                for all $q \in Q$ do
                    $\boldsymbol{r}^{p,q}$=GJK($\mathcal{P}$, $\mathcal{Q}$)       ▷ $\mathcal{P}$, $\mathcal{Q}$ are sets related to the particles $p, q$, see Alg. 6
                    if $|\boldsymbol{r}^{p,q}| < \left|\boldsymbol{r}^{\text{min}}\right|$ then
                        $r_i^{\text{min}} = r_i^{p,q}$
                    end if
                    $\Delta t^{p,q} = \alpha|\boldsymbol{r}^{p,q}|/\Delta v^{n,p,q}$
                    if $\Delta t^{p,q} < \Delta t^{\text{safe}}$ then
                        $\Delta t^{\text{safe}} = \Delta t^{p,q}$
                    end if
                end for
            end for
            $\Delta t^{\text{acc}} = \Delta t^{\text{acc}} + \Delta t^{\text{safe}}$
        end while
        for each particle pair $p$, $q$, sorted by $\Delta t^{p,q}$, starting with the smallest $\Delta t^{p,q}$. do
            if $u^{n,q} - u^{n,p} > 0$ then
                Calculate post-collision velocities based on (4.77a)-(4.78)
            end if
        end for
    end while
end procedure
```

reset to a non-overlapping state, leading to additional iterations of the collision algorithm. Hence, a smaller α might reduce the number of iterations resulting from particle overlaps. Overlapping effects result only from the rotational velocity of the particles and different local radii $r_i = x_i - \chi_{ip}\gamma_p$. Hence, for spherical particles with a constant radius α can be chosen close to unity. For elongated, rod-like particles a smaller value for $\alpha < 0.5$ has to be used. Dense suspension might cause high rotational velocities due to the high number of collisions. Thus, in a dense suspension the value of α might be chosen as small as 0.01.

The safe time-step is subsequently used to determine new positions and orientations for the particles $X_{ip}\left(t^m + \Delta t^{\text{acc}}\right),\ \beta_p\left(t^m + \Delta t^{\text{acc}}\right)$, where t^m is the current time of the simulation. No new hydrodynamic forces and torque are calculated, as the collision forces are expected to dominate the solution. Following each update of the position and orientation the minimal distance and the safe time-step has to be calculated again. Only if the euclidean norm of the minimal distance vector

$$\left|\boldsymbol{r}^{\text{min}}\right| = \inf\left\{|\boldsymbol{r}^{p,q}|\, p, q = 1, 2..\widehat{N}, p \neq q\right\} \tag{4.101}$$

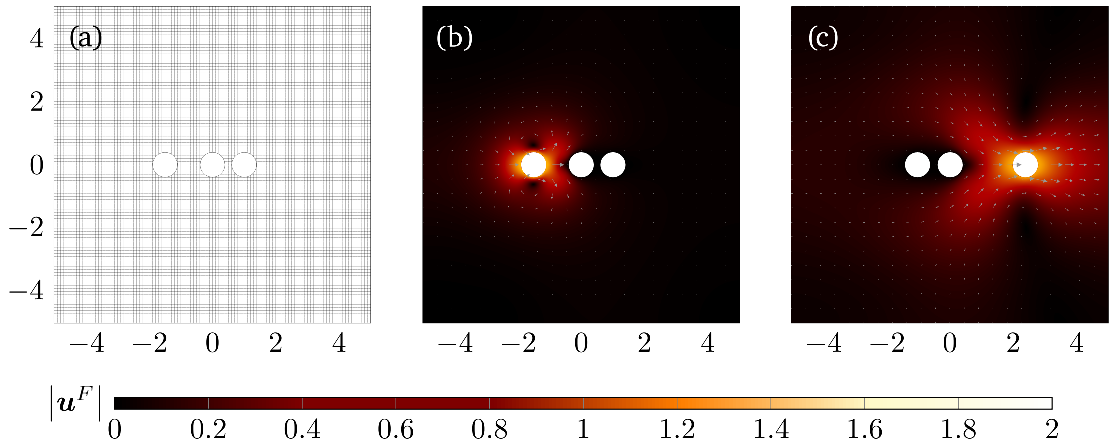

Fig. 4.11.: (a) The collision model is tested by a simple setup. Similar to Newton's cradle, three particles are placed in a quadratic 10×10 domain, where the cell diameter is $h = 0.1$. (b) The left particle is displaced and moves towards the other two particles. The colour scale indicates the absolute value of the fluid velocity and vectors are used to represent the velocity field. (c) After the collision only the right particle is moving with the same velocity as the left particle before the collision.

is smaller than a certain threshold $\lambda = h^{\Gamma}$ the physical collision is calculated.

If one or more particle pairs p, q have been determined with a smaller minimum distance than the threshold $|\boldsymbol{r}^{p,q}| \leq \lambda$ a collision takes place. The particle pairs in question are sorted, starting from the pair with the smallest $\Delta t^{p,q}$ to the largest. Therefore, effects of early collisions on subsequent collisions can be considered. Due to this hierarchy of collisions the velocities of a particle, which participates in a collision, might have changed. Hence, it is necessary to check for every binary collision whether the velocity difference in normal direction between the two particles is positive $u^{n,q} - u^{n,p} > 0$. Otherwise, the particles are already moving away from each other. The post-collision velocities of each binary collision are determined using (4.77a)-(4.78). As long as the accumulated time-step Δt^{acc} is still smaller than the simulation time-step Δt the collision algorithm will be restarted. Hence, even previously undetected collisions which are only possible due to velocity changes in previous collisions are considered and executed.

It should be noted, that the given collision algorithm is highly modular. Thus, the different elements of the entire procedure, the pre-selection algorithm, the GJK algorithm for the distance calculation and the collision model can be changed without interfering with the remaining elements.

4.6.3. Tests for the collision model

The collision model should provide reliable results in accordance to known experiments. In this section simple numerical experiments are presented to show the correctness of the solution. The setup of the first experiment is similar to Newton's cradle, see Fig. 4.11a. Three particles are placed in a 10×10 domain, where the cell diameter is $h = 0.1$. The domain boundaries are defined by a pressure-outlet condition, i.e. a Neumann condition as defined in

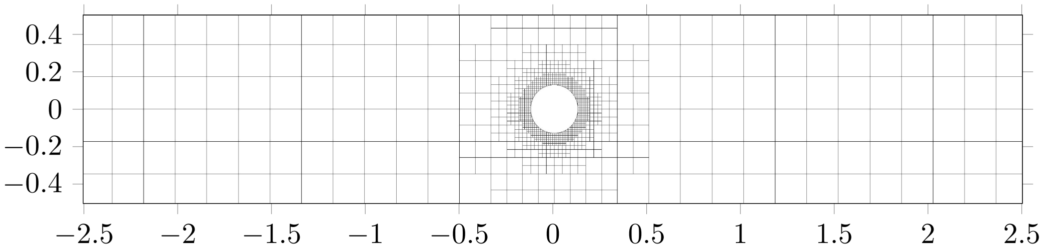

Fig. 4.12.: The image shows the initial setup of the single circular particle moving in the negative vertical direction towards a solid wall. The numerical grid is refined at the particle surface using four refinement levels.

(2.70). The two right particles do not move initially. The left particle is placed with a small distance towards the other two particles and initialised with a velocity of $\boldsymbol{v}^{0,\text{left}} = [1, 0]$. All particles are passive disk-shaped particle with a diameter of $a = 1$. It is expected, that after a series of two collisions between the particles the velocities of the two left particle vanish and the right particle moves with the initial velocity of the left particle, because the coefficient of restitution $k = 1$ is chosen to be unity. Two simulations are carried out. In the first one the fluid is entirely neglected, only the particle solver and the collision model is active. The velocity of the right particle after the collision is $\boldsymbol{v}^{\text{right}} \approx [1, 0]$ with an error of 10^{-15} towards the expected value. Two binary collisions are necessary to shift the momentum from the left particle to the right particle. Both collisions take place within the same time-step, proofing the applicability of the collision algorithm presented in the previous section.

In a second simulation the fluid phase is added. The values of the fluid properties density and viscosity are set to unity. Due to the existence of the fluid it is expected that the combined momentum of all particles is decreased due to dissipation of energy. The resulting flow fields for the situation before and after the collision are shown in Fig. 4.11b and Fig. 4.11c. The velocity of the right particle at $t^5 = 0.4$, the time-step right after the collision, is $\boldsymbol{v}^{5,\text{right}} = [0.991, 1.535 \cdot 10^{-5}]$, whereas the velocity of the left particle immediately before the collision is $\boldsymbol{v}^{4,\text{left}} = [0.993, 4.511 \cdot 10^{-5}]$. Here, the vertical velocity, which ideally would be zero, can be used as a measure for the error, which is mainly introduced by the fluid solver. In the situation depicted in Fig. 4.11c at $t^{23} = 2.2$ the right particle has lost almost no additional momentum and the velocity is $\boldsymbol{v}^{23,\text{right}} = [0.991, -2.23 \cdot 10^{-5}]$.

Further numerical experiments are carried out. A circular passive particle with $a = 0.1$ is placed in a 5×1 domain with a grid size of $h^K = 1/6$, see Fig. 4.12. Four levels of adaptive mesh refinement are applied, where the cell diameter is halved for every level. No external force such as gravity are applied. The particle is initialised with a velocity of $\boldsymbol{v}^0 = [0, -2]$. A collision is expected to take place at the impenetrable wall at the lower boundary with Dirichlet boundary condition $\boldsymbol{u}_{\text{wall}} = 0$. The left, right and upper boundaries are Neumann boundaries, defined by (2.70). The numerical restriction on the distance between two particles does not play any role in this setup, because only one particle is observed. Thus, it is possible to choose the minimal distance threshold for the collision model more freely and we employ $\lambda = 3 \cdot 10^{-3}$. Following Davis et al. [48] and Gondret et al. [81] the relevant parameter for the behaviour of the particle after the collision is the Stokes number

$$\text{St} = \frac{1}{9}\frac{\rho^S U^c L^c}{\mu^F} = \frac{1\rho^F}{9\rho^S}\,\text{Re} = \frac{\mathfrak{D}\,\text{Re}}{9}. \tag{4.102}$$

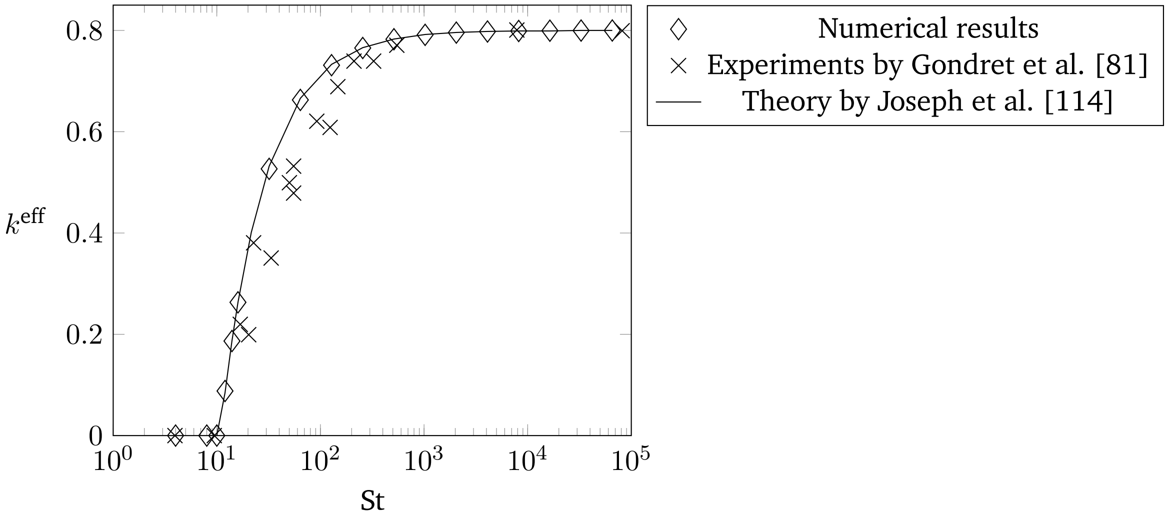

Fig. 4.13.: The diagram shows the dependency of the effective coefficient of restitution k^{eff} on the Stokes number St. Numerical results obtained with XNSERO are compared to experimental [81] and theoretical results [114].

In a series of experiments the density ratio $\mathfrak{D}$ is varied while Re is kept constant. The effective coefficient of restitution $k^{\text{eff}} = v_2^- / v_2^0$ is measured. Note that it is calculated with the initial velocity of the particle and not the velocity right before the collision. Hence, all effects occurring during the approach of the particle are captured by the effective coefficient of restitution. If the particle reached a vertical velocity of $v_2 < v_{crit} = 10^{-4}$ without colliding with the wall, it is assumed that $k^{\text{eff}} = 0$. In order to fit the results to the experimental results of a particle colliding with a wall [81] a dry coefficient of restitution of $k = 0.8$ is employed. The term dry refers to an experiment where the density ratio $\mathfrak{D}$ is large, e.g. the particle is falling in air and no fluid is present. In Fig. 4.13 we compare the present results with the results of Gondret et al. [81] for Teflon particles. As a result of the experimental study a critical Stokes number St_{c} of 10 is calculated. The coefficient of restitution for experiments with a smaller Stokes number is always zero. A similar behaviour is observed in the numerical results, where the critical Stokes number is $St_{\text{c}} \approx 10$ and the first value with $k^{\text{eff}} > 0$ is obtained for $St = 11$. In the initial area of a bouncing particle St < 30 the numerical and experimental results align. However, in a medium interval around $St = 100$ the numerical results for the effective coefficient of restitution tend to be larger than the experimental results. For even larger Stokes numbers, the values converge again and finally reach the dry coefficient of restitution $k = 0.8$.

An analytical model for k^{eff} was developed by Barnocky and Davis [15] and Joseph et al. [114]. Core assumption is the breakdown of lubrication between the colliding particles at a length-scale x_c in the order of the roughness of the surface. Joseph et al. [114] calculated a relation for the effective coefficient of restitution based on the inital position x_0, the length scale x_c and the initial Stokes number St

$$k^{\text{eff}} = k + \frac{1+k}{St} \ln \frac{x_c}{x_0}. \tag{4.103}$$

In Fig. 4.13 the results of the present numerical study are compared with the results of (4.103). The parameter x_c is used to fit the results. The deviation between the numerical and theoretical results is minimized with $x_c = 4.24 \cdot 10^{-3}$, which is in the same order of magnitude as the peak roughness of the particles used by Gondret et al. [81] and of the same order of magnitude as the numerical threshold λ. Hence, the initially purely numerical parameter λ can indeed be used to model the direct interactions of the particles.

4.7. XNSERO-solver scheme

The XNSERO solver contains the XDG fluid solver, the particle solver and the collision procedure presented in the previous sections. A pseudocode implementation of the entire solver can be found in Alg. 7. Due to the coupling of both phases through the hydrodynamic forces and torques in (4.63a) and (4.63b) and the boundary conditions, as implemented in Sec. 4.3 and Sec. 4.3.1, the system is only given implicitly. Let S^F be the solver for the fluid properties $\mathfrak{u}^{F,m+1} = \left\{u_1^{F,m+1}, u_2^{F,m+1}, p^{F,m+1}\right\}$ and S^S the solver for the particle velocities $\mathfrak{u}^{S,m+1} = \left\{v_{11}^{m+1}, v_{21}^{m+1}, \omega_1^{m+1}, ..., v_{1N}^{m+1} v_{2N}^{m+1}, \omega_N^{m+1}\right\}$. Due to the aforementioned coupling, the dependencies are

$$\mathfrak{u}^{F,m+1} = S^F\left(\mathfrak{u}^{F,m+1}, \mathfrak{u}^{F,m}, \mathfrak{u}^{F,m-1}, \mathfrak{u}^{S,m+1}\right) \tag{4.104}$$

$$\mathfrak{u}^{S,m+1} = S^S\left(\mathfrak{u}^{F,m+1}, \mathfrak{u}^{S,m}\right). \tag{4.105}$$

The fluid solver depends on the current fluid and particle solution, i.e. additionally to the implicit formulation of the BDF2-method, the solver depends also implicitly on the particle state. In (4.105) only the particle state $\mathfrak{u}^{S,m}$ appears as an explicit dependency. Nevertheless, due to the occurrence of $\mathfrak{u}^{F,m+1}$ in (4.105), the particle solver depends also on the current state of both the fluid and the particles. Hence, it is necessary to introduce an iteration scheme to solve for $\mathfrak{u}^{F,m+1}$ and $\mathfrak{u}^{S,m+1}$

$${}^{k+1}\mathfrak{u}^{F,m+1} = S^F\left({}^{k}\mathfrak{u}^{F,m+1}, \mathfrak{u}^{F,m}, \mathfrak{u}^{F,m-1}, {}^{k}\mathfrak{u}^{S,m+1}\right) \tag{4.106}$$

$${}^{k+1}\mathfrak{u}^{S,m+1} = S^S\left({}^{k+1}\mathfrak{u}^{F,m+1}, \mathfrak{u}^{S,m}\right), \tag{4.107}$$

where the preceding index k refers to the iteration step. The new fluid properties ${}^{k+1}\mathfrak{u}^{F,m+1}$ can be used for the particle solver, because both solvers are called sequentially, i.e. the call to the particle solver comes after the call to the fluid solver.

4.7.1. Relaxation

Inertia plays a minor role in the present system and any change in the system triggers an immediate reaction. Hence, it is expected that the iteration scheme as presented in (4.106) and (4.107) is unstable. To increase the numerical stability a relaxation method is used. A straightforward implementation delivers the under relaxation method

$${}^{k+1}\mathfrak{u}^{m+1} = \sigma\ {}^{k+1}\tilde{\mathfrak{u}}^{m+1} + (1-\sigma)\ {}^{k}\mathfrak{u}^{m+1}, \quad 0 < \sigma \leq 1. \tag{4.108}$$

The final result of the current iteration step ${}^{k+1}\mathfrak{u}^{m+1}$ is a linear combination of the preliminary result ${}^{k+1}\tilde{\mathfrak{u}}^{m+1}$ obtained directly from the solver (4.106) and (4.107) and the result of the previous iteration step ${}^{k}\mathfrak{u}^{m+1}$. Both terms are linked by the constant relaxation coefficient σ.

Algorithm 7 Pseudocode implementation of a single time-step of the XNSERO-solver.

```
procedure RunSolverOneStep($m$, $t^m$, $\Delta t$)    ▷ Solve for $\mathfrak{u}^{F,m+1}$, $\mathfrak{u}^{S,m+1}$
    Increase time-step counter $m \to m+1$, $t^{m+1} = t^m + \Delta t$
    if $(m+1)\%10 == 0$ then    ▷ Re-initialise R-tree every 10 time-steps
        InitializeTree($P$, $\Delta t$)    ▷ Initialise R-tree
    else UpdateTree($P$, $\Delta t$    ▷ Update MBRs
    end if
    ParticleMPICheck($P$, GridData, MPISize, $m+1$)    ▷ Consistency check of the particle properties on different processes
    procedure Timestepping.Solve(($t^{m+1}$, $\Delta t$))
        $\varphi^{m+1}$=UpdateLevelSet()    ▷ level-set update, see Sec. 4.4
        Perform cell agglomeration    ▷ see Kummer [126] and Kummer et al. [127]
        ${}^{0}\boldsymbol{M}^{m+1}$=ComputeMassMatrix()    ▷ see (4.26)
        ${}^{0}\mathfrak{u}^{F,m+1}$=Extrapolate($\mathfrak{u}^{F,m}$, $\varphi^{m+1}$))    ▷ see (4.57)
        while $|\mathfrak{R}| \geq \epsilon$ do    ▷ convergence criterion $\epsilon$
            Increase iteration counter $k \to k+1$
            ${}^{k+1}\boldsymbol{Op}^{m+1}$,${}^{k+1}\boldsymbol{b}^{m+1}$=ComputeOperatorMatrixAndRHS(${}^{k}\mathfrak{u}^{F,m+1}$)
                ▷ see (4.27), (4.28)
            ${}^{k+1}\mathfrak{u}^{F,m+1} = S^U\left({}^{k}\mathfrak{u}^{F,m+1}, \mathfrak{u}^{F,m}, \mathfrak{u}^{F,m-1}, {}^{k}\mathfrak{u}^{S,m+1}\right)$    ▷ Call to the fluid solver
            ${}^{k+1}\tilde{\mathfrak{F}}^{m+1}$=CalculateHydrodynamics$\left({}^{k+1}\mathfrak{u}^{F,m+1}\right)$
            ${}^{k+1}\mathfrak{F}^{m+1}$=AitkenRelaxation$\left({}^{k+1}\tilde{\mathfrak{F}}^{m+1}, {}^{k}\tilde{\mathfrak{F}}^{m+1}, {}^{k-1}\mathfrak{F}^{m+1}\right)$    ▷ see (4.111)
            ${}^{k+1}\mathfrak{u}^{S,m+1}$=UpdateVelocity$\left({}^{k+1}\mathfrak{F}^{m+1}\right)$    ▷ see (4.63a) and (4.63a)
            $\mathfrak{R}$=ComputeResidual$\left({}^{k+1}\mathfrak{u}^{F,m+1}, {}^{k}\mathfrak{u}^{F,m+1}\right)$
        end while
    end procedure
    CalculateCollision($P$, $\Delta t$)    ▷ see Alg. 6
    CalculateParticlePositonAndAngle($P$, $\Delta t$)    ▷ see (4.64a) and (4.64b)
end procedure
```

Depending on the system in question it might be necessary to choose a small σ to obtain a stable iteration scheme, leading to a slow convergence rate.

It is possible to speed up convergence significantly by introducing a variable relaxation coefficient. A method based on Aitken's Δ^2-process is employed to calculate the coefficient [108]. The present implementation of the relaxation process is based on Küttler and Wall [128]. The hydrodynamic forces and torques acting on the particles are used to determine the variable coefficient σ, because all other particle properties, i.e. the velocities, position and orientation, follow directly and explicitly from the hydrodynamics. The forces and torques acting on all particles are written in a single vector $\mathfrak{F} = [F_{11}, F_{21}, T_1, ..., F_{1N}, F_{2N}, T_N]$. The relaxation coefficient is calculated from results of two previous iteration steps of the XNSERO solver [128]

$$
{}^{k+1}\sigma = -{}^{k}\sigma \frac{{}^{k}\mathfrak{R}_i \left({}^{k+1}\mathfrak{R}_i - {}^{k}\mathfrak{R}_i\right)}{\left|{}^{k+1}\boldsymbol{\mathfrak{R}} - {}^{k}\boldsymbol{\mathfrak{R}}\right|^2}, \tag{4.109}
$$

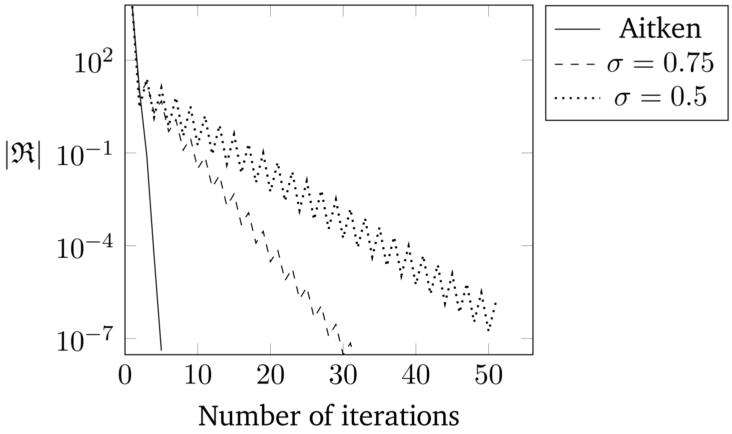

Fig. 4.14.: Comparison between the number of iterations necessary to reach the convergence limit $|\mathfrak{R}| < \epsilon = 10^{-7}$. An iteration with an Aitken relaxation process and an initial coefficient ${}^{1}\sigma^{m} = 1.0$ needs five iterations, an iteration with a static $\sigma = 0.75$ requires 30 iterations and the iteration with $\sigma = 0.50$ does not reach the convergence limit within 50 iterations.

where the residuals ${}^{k}\mathfrak{R}_i$ and ${}^{k+1}\mathfrak{R}_i$ are defined as

$${}^{k}\mathfrak{R}_i = {}^{k}\tilde{\mathfrak{F}}_i - {}^{k-1}\mathfrak{F}_i, \quad {}^{k+1}\mathfrak{R}_i = {}^{k+1}\tilde{\mathfrak{F}}_i - {}^{k-1}\mathfrak{F}_i. \tag{4.110}$$

The resulting relaxation scheme is

$${}^{k+1}\mathfrak{F}_i = {}^{k+1}\sigma\ {}^{k+1}\tilde{\mathfrak{F}}_i + \left(1 - {}^{k+1}\sigma\right)\ {}^{k}\mathfrak{F}_i. \tag{4.111}$$

Two previous values of $\mathfrak{F}_i$ are necessary to calculate the relaxation coefficient. Hence, in the first iteration a constant pre-defined coefficient is used ${}^{1}\sigma = \text{const}$. In the second step it is already possible to apply (4.109) as the iteration is initialised with the results of the previous time-step ${}^{0}\mathfrak{F}_i^{m+1} = \mathfrak{F}_i^{m}$. In Fig. 4.14 static underrelaxation-methods with $\sigma = 0.5$ and $\sigma = 0.75$ are compared to the Aitken relaxation method. The test setup is a 18×18-domain with periodic boundaries and 216 active particles. The particle length is $a = 1$ and their aspect ratio $\varepsilon = 2.5$. Results of the same setup are presented in Sec. 6.2. The convergence limit is $\epsilon = 10^{-7}$ and the maximal number of iterations is 50. Clearly the number of iterations necessary to reach convergence is reduced substantially by the Aitken-relaxation. For $\sigma = 0.5$ no convergence is reached within the limit of 50 iterations. It should be noted, that relaxation methods might increase the number of iterations necessary in some cases compared to $\sigma = 1.0$. However, in many cases no solution can be found in case of the non-relaxated method, as the multi-body system is very sensitive against small perturbations.

4.7.2. Multi-core computing

The solver is HPC-ready, i.e. able to compute the solution on multiple processing cores. Message passing interface (MPI) is used as a standard for inter-process communications. The mesh of the fluid solver is split evenly over all processes. Due to the local ansatz functions of the XDG method inter-process communication is only necessary for the cells at the process

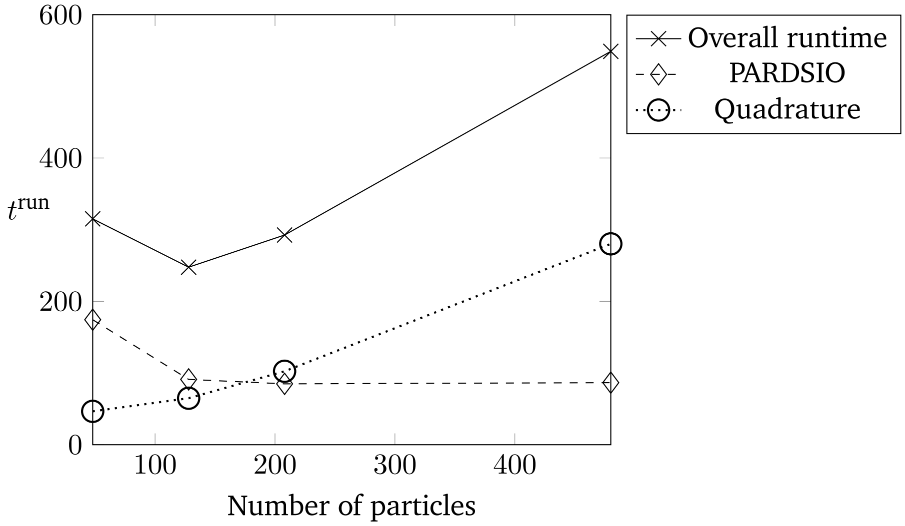

Fig. 4.15.: The diagram shows the comparison of the runtime t^{run} of the most costly algorithms of the XNSERO solver and the overall runtime for the first five time-steps of four different simulations. The numerical backround grid has $38,416$ square numerical cells and $48,\ 128,\ 208,\ 480$ particles are placed within the domain respectively. The simulations are discussed in detal in Sec. 6.2.

boundaries. Consider a grid distributed on two processes p_1 and p_2. Information is shared between both processes about the cells located at the process boundaries. The cells of p_2, which are shared with p_1 are called external cells of p_1 and vice versa. To obtain the necessary numerical fluxes at the cell boundaries, the external cells are treated as source of information the same way as if they were part of the sub-mesh on p_1.

While the fluid solver is completely parallel, this does not fully apply to the particle solver. The integration over the particle surface to obtain hydrodynamic forces and torques acting on the particles is carried out on the sub-meshes of the processes, i.e. in parallel. The relaxation (4.111) and the solution for (4.63a), (4.63b), (4.64a) and (4.64b) are obtained on a single process and afterwards shared with the other processes to minimise inter-process communication. As all mentioned relations are given explicit for each iteration the computational demand is low compared to the potential communication costs, which justifies the sequential approach.

4.7.3. Runtime test

The runtime of the XNSERO solver is mainly governed by the linear fluid solver S^F and the integration routines. In Fig. 4.15 the runtime for different simulations for five time-steps is compared. All simulations are carried out in a domain with solid wall boundaries and $38,416$ square cells. The number of particles is varied. Each simulation is discussed in detail, including a figure of the initial conditions, in Sec. 6.2. The polynomial order of the fluid velocity is $k = 2$, the polynomial order of the pressure field is $k = 1$, subsequently, the number of DoFs is $576,240$. The DoFs are distributed over eight processes, hence, each process need to solve a system of approximately $72,030$ DoFs. The exact number of DoFs per process might change based on the load balancing, which is done by a BoSSS method, see Kummer et al. [127]. Each simulation is carried out on a machine with an Intel® Core© i7-9700K CPU and 32GB installed physical memory (RAM). In Fig. 4.15 the most costly procedures are compared, based on their runtime on the first process.

The number of DoFs in the fluid phase changes with the number of particles considered. For a dilute suspension $N \rightarrow 0$ one obtains the limiting case of $576,240$ DoFs, however, with increasing density, the number of DoFs declines. Hence, the computational costs for the linear fluid solver, where the PARallel DIrect Solver (PARDISO) is used for all simulations [2, 29, 30], decrease with increasing particle density. A plateau is reached for high density suspension, because, while the number of DoFs in the fluid phase is decreased further, the costs for the communication between processes does not decrease with the same rate. At the same time, the amount of cut-cells increases, hence, it is necessary to formulate quadrature rules for an increased number of complex-shaped cells, see Sec. 4.3.2. Subsequently, the load caused by the formulation and execution of the quadrature rules increases with increasing number of particles. Both procedures, the linear solver and the quadrature, account for approximately $2/3$ of the overall runtime. The remaining $1/3$ is mostly consumed by the computation of the mass- and operator matrix, i.e. other methods to solve for the fluid properties. The particle solver, including the tracking of the distance of the particles by the R-tree and GJK-algorithm account for less then one percent of the runtime in the given example.

5. Homogenised two-phase model

The particle-resolved model presented in the previous section requires enormous amounts of computation power for large systems, see Sec. 4.7.3. In order to simulate systems with a large number of particles, i.e. $N > 1000$, it is therefore necessary to further simplify the model by using a coarse-grained representation. Coarse-grained models are widely used in the fields of chemistry and physics. Core idea of a coarse-grained model is to represented several smaller entities, e.g. atoms or molecules, by a larger imaginary entity, which groups the individual atoms together, see for example Kmiecik et al. [122]. In a similar way, the individual elements of the active suspension, a specific number of particles and the fluid, can be combined into a new pseudo-material that has the same statistical properties as the individual components. The idea is similar to the transition from the molecular representation of a fluid to a continuum. The properties of the suspension, such as the velocity of the particles and the fluid, are averaged over a representative volume element, a technique known as Eulerian spatial averaging [63, 102, 109, 174]. A similar approach has been chosen by Wolgemuth [208] to model an active suspension, whose phenomenological approach leads to similar equations of motion. However, the model is restricted to particle volume fractions below 20% and does not consider important interactions forces such as the Saffman lift force [180]. Other studies, e.g. Dunkel et al. [65, 66], restrict themselves to an incompressible suspension, i.e. changes in the particle density are not considered.

Eulerian spatial averaging has been applied to a wide variety of systems, e.g debris flows and avalanches [33, 167], partially molten material [20, 150] and bubble induced turbulence [64, 179]. To the authors knowledge, besides our own publication Deußen et al. [55] no direct application of the Eulerian spatial averaging theory to active suspensions based on first principles exists. By considering the mean value, it is possible to observe very large numbers of particles. However, information about the behaviour of the suspension on small scales is lost, making it necessary to model corresponding fluctuation terms. This problem is thus related to the modelling of the Reynolds stress terms in turbulence research. The derivation of the spatially averaged model equation and the closure relations were presented first in Deußen et al. [55], which is, thus, closely followed in the present section.

5.1. Spatial averaging

Let the representative averaging volume element V be a subset of Ω

$$V \subset \Omega. \tag{5.1}$$

The volume element V needs to be significantly smaller than the domain Ω and at the same time larger than the the particle volume V^P, where V^P is defined as the area enclosed by the particle domain Ω_p, see (2.56). Both phases are present in V. The number of particles in V is N', where we assume that $1 \ll N' \ll N$ is fulfilled. Hence, by applying the condition of non-overlapping particles (2.26) and phases (2.33), the averaging volume is defined by

$$V = V^F \cup V^S = V^F \cup \bigcup_{p=1}^{N'} \Omega_p, \tag{5.2}$$

where V^F is the subdomain of V occupied by the fluid. In Fig. 5.1 V is visualised in two dimensions. While it is depicted as rectangular in the figure, the choice of the shape of V is arbitrary. The Eulerian coordinate of the averaged model is $\boldsymbol{x}$ which is the centre of V. The local coordinate $\boldsymbol{x}^* = \boldsymbol{x} + \boldsymbol{\zeta}$ consist of the position vector $\boldsymbol{x}$ and the relative position $\boldsymbol{\zeta}$ within the averaging volume V [174]. In general the boundary ∂V might cut through particles. Subsequently, it might be necessary to consider stresses within the rigid particles. However, it is assumed that the number N' of particles within V is large and one can neglect the particles cut by ∂V. Consequently, all particles are completely immersed within V. Each particle and each phase occupies a certain fraction of V. The resulting volume fractions are defined as

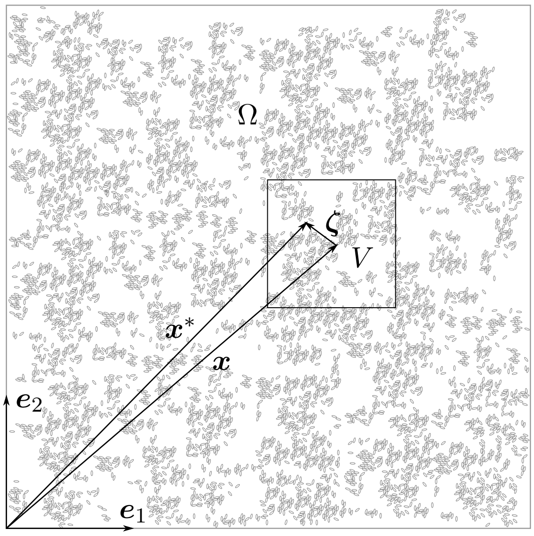

Fig. 5.1.: A visualisation of the averaging volume in two dimensions. The representative averaging volume element V is a subset of Ω. In this section the local Eulerian coordinate is denoted by $\boldsymbol{x}^* = \boldsymbol{x} + \boldsymbol{\zeta}$, where $\boldsymbol{x}$ is the centre of V and ζ is the position vector within V. Reproduced from Deußen et al. [55], with the permission of AIP Publishing

$$\alpha_p = \frac{V^P}{V}, \quad \alpha^S = \sum_{p=1}^{N'} \alpha_p = \frac{V^S}{V}, \quad \alpha^F = \frac{V^F}{V} = 1 - \alpha^S, \tag{5.3}$$

where the saturation condition (2.33) was used to relate α^F and α^S.

Two different averages are necessary to derive the model. Volume integration of the arbitrary non-dimensional physical quantity $\mathrm{u}^{\mathfrak{P}}$ over the representative volume element V delivers

$$\left\langle \mathrm{u}^{\mathfrak{P}} \right\rangle (\boldsymbol{x}, t) = \frac{1}{V} \int_V \mathrm{u}^{\mathfrak{P}} (\boldsymbol{x}^*, t)\, \gamma^{\mathfrak{P}} (\boldsymbol{x}^*, t)\, \mathrm{d}\boldsymbol{x}^*, \tag{5.4}$$

where the indicator function $\gamma^{\mathfrak{P}}$ is defined in (2.30). In the most simple case $\mathrm{u}^{\mathfrak{P}} = 1$, one obtains the previously introduced volume fractions

$$\frac{1}{V}\int_V \gamma^{\mathfrak{P}}\,\mathrm{d}\boldsymbol{x}^* = \alpha^{\mathfrak{P}}. \tag{5.5}$$

The particles are rigid, hence, one can assume that the property u_p is constant within the particle volume V^P. Subsequently the volume average delivers for the solid phase

$$\left\langle \mathrm{u}^S \right\rangle (\boldsymbol{x}, t) = \frac{\mathrm{u}_p \Omega_p}{V}, \tag{5.6}$$

where the summation convention is applied. The second necessary average is called the true physical average, which only considers the volume occupied by the phase $\mathfrak{P}$

$$\overline{\mathrm{u}^{\mathfrak{P}}}(\boldsymbol{x}, t) = \frac{1}{V^{\mathfrak{P}}}\int_V \mathrm{u}^{\mathfrak{P}}(\boldsymbol{x}^*, t)\,\gamma^{\mathfrak{P}}(\boldsymbol{x}^*, t)\,\mathrm{d}\boldsymbol{x}^*. \tag{5.7}$$

Both averaged quantities are related via the volume fraction of $\mathfrak{P}$

$$\frac{\left\langle \mathrm{u}^{\mathfrak{P}} \right\rangle}{\overline{\mathrm{u}^{\mathfrak{P}}}} = \frac{V^{\mathfrak{P}}}{V} = \alpha^{\mathfrak{P}}. \tag{5.8}$$

As mentioned, in the context of the Eulerian spatial averaging theory a new pseudo-material is considered, which consists of the particles and the fluid [63]. Thus, transport equations for each property of the new material are derived using the volume average (5.4). The averaged quantities describe the continuous material similar to the replacement of the individual molecular velocity by the continuous velocity and pressure in a fluid continuum. Nevertheless, the true physical average (5.7) is the desired result of the examination. Subsequently, (5.8) is used to replace the volume average in the newly derived equations.

5.1.1. Reynolds decomposition

Similar to the Reynolds decomposition in turbulence research, Reis and Wang [174] introduced the decomposition

$$\mathrm{u}^{\mathfrak{P}} = \overline{\mathrm{u}^{\mathfrak{P}}} + \tilde{\mathrm{u}}^{\mathfrak{P}}, \tag{5.9}$$

i.e. the physical quantity $\mathrm{u}^{\mathfrak{P}}$ can be described as a sum of its true average and the fluctuations $\tilde{\mathrm{u}}^{\mathfrak{P}}$. Again, in analogy to the derivation of the RANS equation in turbulence research, one obtains

$$\overline{\mathrm{u}^{1,\mathfrak{P}}\mathrm{u}^{2,\mathfrak{P}}} = \overline{\overline{\mathrm{u}^{1,\mathfrak{P}}}\,\overline{\mathrm{u}^{2,\mathfrak{P}}} + \overline{\mathrm{u}^{1,\mathfrak{P}}}\,\tilde{\mathrm{u}}^{2,\mathfrak{P}} + \tilde{\mathrm{u}}^{1,\mathfrak{P}}\,\overline{\mathrm{u}^{2,\mathfrak{P}}} + \tilde{\mathrm{u}}^{1,\mathfrak{P}}\tilde{\mathrm{u}}^{2,\mathfrak{P}}} = \overline{\mathrm{u}^{1,\mathfrak{P}}}\,\overline{\mathrm{u}^{2,\mathfrak{P}}} + \overline{\tilde{\mathrm{u}}^{1,\mathfrak{P}}\tilde{\mathrm{u}}^{2,\mathfrak{P}}} \tag{5.10}$$

for a product of two physical quantities $\mathrm{u}^{1,\mathfrak{P}}$ and $\mathrm{u}^{2,\mathfrak{P}}$. In order to obtain this result, some basic calculation rules for averaged variables must be followed [174]. First, the average of the fluctuations vanishes

$$\overline{\tilde{\mathrm{u}}^{\mathfrak{P}}} = 0 \tag{5.11}$$

and the average of the average returns

$$\overline{\overline{\mathrm{u}^{\mathfrak{P}}}} = \overline{\mathrm{u}^{\mathfrak{P}}}. \tag{5.12}$$

Subsequently, one obtains

$$\overline{\overline{\mathrm{u}^{1,\mathfrak{P}}}\,\overline{\mathrm{u}^{2,\mathfrak{P}}}} = \overline{\mathrm{u}^{1,\mathfrak{P}}}\,\overline{\mathrm{u}^{2,\mathfrak{P}}}. \tag{5.13}$$

The first term on the right hand side of (5.10) is the product of two averages and as such part of the desired results. The second term $\overline{\tilde{\mathrm{u}}^{1,\mathfrak{P}}\tilde{\mathrm{u}}^{2,\mathfrak{P}}}$ introduces new correlation quantities. The closure problem at hand is related to the infinite hierarchy of the PDF-equations, see Sec. 3.4. Similar to the closure problem in turbulence, models are required, because the information about the fluctuations are lost during the averaging process.

5.1.2. Volume averaged derivatives

It is necessary to express averages of derivatives as derivatives of averages for the derivation of the transport equations for the quantities of the new pseudo-material. Hence, in the present section relations are derived to change the sequence of averaging and derivation. By using the transport equation for the phase indicator function $\gamma^{\mathfrak{P}}$ (2.78), one obtains for the temporal derivative

$$\frac{\partial \gamma^{\mathfrak{P}}}{\partial t} = \mp\delta\left(\phi\right) u_i \frac{\partial \phi}{\partial x_i^*} = \mp\delta\left(\phi\right) u_i^{\Gamma} n_i = \mp\delta\left(\phi\right) u_i^{S} n_i, \tag{5.14}$$

where n_i is the normal vector at the surface, see (2.76). Throughout this section it is assumed that the condition $|\nabla\phi| = 1$ holds. The sign of the right hand side is negative for the fluid phase $\mathfrak{P} = F$ and positive for the solid phase $\mathfrak{P} = S$. Due to the rigidity of the particles, the surface velocity $u_i^{\Gamma} = u_i^{S}$ equals the particle velocity. The averaging volume is static, i.e. it does not change over time. Subsequently, it is possible to switch a temporal derivative and a spatial integration. Leibniz product rule yields

$$\left\langle \frac{\partial \mathrm{u}^{\mathfrak{P}}}{\partial t} \right\rangle = \frac{1}{V}\int_V \frac{\partial \mathrm{u}^{\mathfrak{P}}}{\partial t}\gamma^{\mathfrak{P}}\,\mathrm{d}\boldsymbol{x}^* = \frac{1}{V}\frac{\partial}{\partial t}\int_V \mathrm{u}^{\mathfrak{P}}\gamma^{\mathfrak{P}}\,\mathrm{d}\boldsymbol{x}^* - \frac{1}{V}\int_V \mathrm{u}^{\mathfrak{P}}\frac{\partial \gamma^{\mathfrak{P}}}{\partial t}\,\mathrm{d}\boldsymbol{x}^*. \tag{5.15}$$

Rewriting the integrals as volume averages and using (5.14) and the definition of the phase interface (2.34) delivers

$$\left\langle \frac{\partial \mathrm{u}^{\mathfrak{P}}}{\partial t} \right\rangle = \frac{\partial \left\langle \mathrm{u}^{\mathfrak{P}} \right\rangle}{\partial t} \pm \frac{1}{V}\int_V \delta\left(\phi\right)\mathrm{u}^{\mathfrak{P}} u_i^{S}\frac{\partial \phi}{\partial x_i^*}\,\mathrm{d}\boldsymbol{x}^* = \frac{\partial \left\langle \mathrm{u}^{\mathfrak{P}} \right\rangle}{\partial t} \pm \frac{1}{V}\sum_{p=1}^{N'}\int_{\Gamma_p} \mathrm{u}^{\mathfrak{P}} u_i^{S} n_i\,\mathrm{d}s, \tag{5.16}$$

where the sign of the integral term is positive for a fluid property u^F and negative for a solid phase property u^S. The additional integral term in (5.16) represents the transport of $\mathrm{u}^{\mathfrak{P}}$ at the phase interface [63].

Similarly, one obtains for the averaged gradient

$$\begin{aligned}\left\langle \frac{\partial \mathrm{u}^{\mathfrak{P}}}{\partial x_i^*} \right\rangle &= \frac{1}{V}\frac{\partial}{\partial x_i}\int_V \mathrm{u}^{\mathfrak{P}}\gamma^{\mathfrak{P}}\,\mathrm{d}\boldsymbol{x}^* - \frac{1}{V}\int_V \mathrm{u}^{\mathfrak{P}}\frac{\partial \gamma^{\mathfrak{P}}}{\partial x_i^*}\,\mathrm{d}\boldsymbol{x}^* \\ &= \frac{\partial \left\langle \mathrm{u}^{\mathfrak{P}} \right\rangle}{\partial x_i} \mp \frac{1}{V}\int_V \delta\left(\phi\right)\mathrm{u}^{\mathfrak{P}}\frac{\partial \phi}{\partial x_i^*}\,\mathrm{d}\boldsymbol{x}^* = \frac{\partial \left\langle \mathrm{u}^{\mathfrak{P}} \right\rangle}{\partial x_i} \mp \frac{1}{V}\sum_{p=1}^{N'}\int_{\Gamma_p} \mathrm{u}^{\mathfrak{P}} n_i\,\mathrm{d}s,\end{aligned} \tag{5.17}$$

where $\partial x_j^*/\partial x_j = 1$ and

$$\frac{\partial \gamma^{\mathfrak{P}}}{\partial x_i^*} = \pm\delta\left(\phi\right)\frac{\partial \phi}{\partial x_i^*} = \pm\delta\left(\phi\right) n_i \tag{5.18}$$

are used. The sign of the additional surface integral in (5.17) is negative for the fluid phase $\mathfrak{P} = F$ and positive for the solid phase $\mathfrak{P} = S$.

5.2. Averaged transport equations

A general transport equation for the arbitrary physical quantity $\mathfrak{u}^{\mathfrak{P}}$ and the flux $\Psi_i^{\mathfrak{P}}$ of the same variable is

$$\frac{\partial \mathfrak{u}^{\mathfrak{P}}}{\partial t} + \frac{\partial \mathfrak{u}^{\mathfrak{P}} u_i^{\mathfrak{P}}}{\partial x_i^*} = \frac{\partial \Psi_i^{\mathfrak{P}}}{\partial x_i^*} + \Pi_i^{\mathfrak{P}}, \tag{5.19}$$

where $\Pi_i^{\mathfrak{P}}$ is a source of the quantity $\mathfrak{u}^{\mathfrak{P}}$. The variable $\mathfrak{u}^{\mathfrak{P}}$ is of arbitrary tensorial order. The tensorial order of the flux and the source term is, accordingly, increased by one. Forming the volume average (5.4) of the general transport equation (5.19) yields

$$\left\langle \frac{\partial \mathfrak{u}^{\mathfrak{P}}}{\partial t} \right\rangle + \left\langle \frac{\partial \mathfrak{u}^{\mathfrak{P}} u_i^{\mathfrak{P}}}{\partial x_i^*} \right\rangle = \left\langle \frac{\partial \Psi_i^{\mathfrak{P}}}{\partial x_i^*} \right\rangle + \left\langle \Pi_i^{\mathfrak{P}} \right\rangle . \tag{5.20}$$

The averaged derivatives $\left\langle \partial \mathfrak{u}^{\mathfrak{P}} / \partial t \right\rangle$ and $\left\langle \partial \mathfrak{u}^{\mathfrak{P}} / \partial x_i^* \right\rangle$ can be transformed into derivatives of averages $\partial \left\langle \mathfrak{u}^{\mathfrak{P}} \right\rangle / \partial t$ and $\partial \left\langle \mathfrak{u}^{\mathfrak{P}} \right\rangle / \partial x_i$ by applying (5.16) and (5.17). The resulting transport equation for the volume average of $\mathfrak{u}^{\mathfrak{P}}$ is

$$\begin{aligned} &\frac{\partial \left\langle \mathfrak{u}^{\mathfrak{P}} \right\rangle}{\partial t} \pm \frac{1}{V} \sum_{p=1}^{N'} \int_{\Gamma_p} \mathfrak{u}^{\mathfrak{P}} u_i^S n_i dS + \frac{\partial \left\langle \mathfrak{u}^{\mathfrak{P}} u_i^{\mathfrak{P}} \right\rangle}{\partial x_i} \mp \frac{1}{V} \sum_{p=1}^{N'} \int_{\Gamma_p} \mathfrak{u}^{\mathfrak{P}} u_i^{\mathfrak{P}} n_i \, \mathrm{d}s \\ =&\frac{\partial \left\langle \Psi_i^{\mathfrak{P}} \right\rangle}{\partial x_i} \mp \frac{1}{V} \sum_{p=1}^{N'} \int_{\Gamma_p} \Psi_i^{\mathfrak{P}} n_i \, \mathrm{d}s + \left\langle \Pi_i^{\mathfrak{P}} \right\rangle . \end{aligned} \tag{5.21}$$

The velocity of both phases in normal direction at the interface is equal due to the impermeability condition (2.41) at the entire particle surface Γ_p. Subsequently, both surface integrals at the left hand side of (5.21) vanish due to opposing signs. As before, the upper sign of the combined plus-minus refers to the fluid phase and the lower sign to the solid phase.

In the next step, the true physical averaged is introduced. Using (5.8) and the decomposition (5.9) yields

$$\frac{\partial \alpha^{\mathfrak{P}} \overline{\mathfrak{u}^{\mathfrak{P}}}}{\partial t} + \frac{\partial \alpha^{\mathfrak{P}} \overline{\mathfrak{u}^{\mathfrak{P}}}\, \overline{u_i^{\mathfrak{P}}}}{\partial x_i} = \frac{\partial \alpha^{\mathfrak{P}} \overline{\Psi_i^{\mathfrak{P}}}}{\partial x_i} - \frac{\partial \alpha^{\mathfrak{P}} \overline{\tilde{\mathfrak{u}}^{\mathfrak{P}} \tilde{u}_i^{\mathfrak{P}}}}{\partial x_i} + \alpha^{\mathfrak{P}} \overline{\Pi_i^{\mathfrak{P}}} \mp \frac{1}{V} \sum_{p=1}^{N'} \int_{\Gamma_p} \Psi_i^{\mathfrak{P}} n_i \, \mathrm{d}s, \tag{5.22}$$

which is the transport equation of the true physical average of $\mathfrak{u}^{\mathfrak{P}}$. In the following sections (5.22) is used to obtain averaged balance equations for the fluid mass, the solid mass, fluid and solid linear and rotational momentum and the particle orientation. With the exception of the mass balance equations, all equations will require models for the Reynolds-stress type term $\partial \alpha^{\mathfrak{P}} \overline{\tilde{\mathfrak{u}}^{\mathfrak{P}} \tilde{u}_i^{\mathfrak{P}}} / \partial x_i$ and for the interaction term $V^{-1} \sum_{p=1}^{N'} \int_{\Gamma_p} \Psi_i^{\mathfrak{P}} n_i \, \mathrm{d}s$.

5.2.1. Averaged mass balance

The transport equations are derived in a dimensionless form. The mass densities of the fluid phase ρ^F and solid phase ρ^S are non-dimensionalised by using the fluid density itself. Hence, the dimensionless fluid density is unity and the dimensionless solid density is the density ratio $\mathfrak{D} = \rho^S/\rho^F$. As a result, one obtains from (5.22) together with (5.5) the fluid phase mass balance

$$\frac{\partial \alpha^F}{\partial t} + \frac{\partial \alpha^F \overline{u_i^F}}{\partial x_i} = 0, \tag{5.23}$$

where the general variables in (5.22) are set to $\mathfrak{u}^F = 1$, $\Psi_i^F = 0$ and $\Pi_i^F = 0$.

In case of the solid phase, the mass balance is formed with $\mathfrak{u}^S = \mathfrak{D}$, $\Psi_i^S = 0$ and $\Pi_i^S = 0$. The mass densities are considered to be constant in Ω. Hence, the true average of the mass density ratio is

$$\overline{\mathfrak{D}} = \mathfrak{D}. \tag{5.24}$$

Using aforementioned values together with (5.22) delivers the solid phase mass balance

$$\frac{\partial \alpha^S}{\partial t} + \frac{\partial \alpha^S \overline{u_i^S}}{\partial x_i} = 0. \tag{5.25}$$

The true physical average of the solid phase velocity $\overline{u_i^S}$ equals the average of the translational velocity $\overline{v_i^S}$ of the particles

$$\overline{u_i^S} = \frac{1}{V^S} \int_V v_{ip} \gamma_p \, \mathrm{d}\boldsymbol{x}^* + \frac{1}{V^S} \int_V \epsilon_{ijk} \omega_{jp} \left(x_k - \chi_{kq} \gamma_q \right) \gamma_p \, \mathrm{d}\boldsymbol{x}^* = \frac{v_{ip} \Omega_p}{V^S} = \overline{v_i^S}. \tag{5.26}$$

The rotational velocity is constant within each particle, leading to a vanishing contribution to the average

$$\int_V \epsilon_{ijk} \omega_{jp} \left(x_k - \chi_{kq} \gamma_q \right) \gamma_p \, \mathrm{d}\boldsymbol{x}^* = \epsilon_{ijk} \omega_{jp} \int_V \left(x_k - \chi_{kq} \gamma_q \right) \gamma_p \, \mathrm{d}\boldsymbol{x}^* = 0. \tag{5.27}$$

Therefore, as expected, the rotational velocity of the particles does not contribute to the convection of the particle mass. Accordingly, the mass balance (5.25) together with (5.27) yields

$$\frac{\partial \alpha^S}{\partial t} + \frac{\partial \alpha^S \overline{v_i^S}}{\partial x_i} = 0. \tag{5.28}$$

The saturation condition (2.33) has to be followed, hence, the sum of the volume fractions returns unity

$$\alpha^S + \alpha^F = 1, \tag{5.29}$$

delivering an additional equation. This relation is necessary to retrieve an equal number of unknowns and equations, due to the occurrence of the fluid pressure in the momentum balance equations.

5.2.2. Averaged linear momentum balance

The local linear momentum balance of the fluid phase can be either described by the Navier-Stokes equation (2.67) or the unsteady Stokes equation (2.68). In case of the particle resolved model the unsteady Stokes equation was used, mainly to reduce the computational load of the solver. In case of the spatially averaged model the linearisation might no longer be possible, because an additional length scale is introduced by the representative volume element V. The volume averaged Navier-Stokes equation is obtained from (5.22) with $\mathfrak{u}_i^F = u_i^F$, $\Psi_{ij}^F = \tau_{ij}^F$ and $\Pi_i^F = 0$.

$$\frac{\partial \alpha^F \overline{u_i^F}}{\partial t} + \frac{\partial \alpha^F \overline{u_i^F}\,\overline{u_j^F}}{\partial x_j} + \frac{\partial \alpha^F \overline{\tilde{u}_i^F \tilde{u}_j^F}}{\partial x_j} - \frac{\partial \alpha^F \overline{\tau_{ij}^F}}{\partial x_j} + \frac{1}{V}\sum_{p=1}^{N'} \int_{\Gamma_p} \tau_{ij}^F n_j \,\mathrm{d}s = 0. \tag{5.30}$$

It is, alternatively, possible to obtain the volume averaged momentum balance by averaging the Navier-Stokes equation directly. The averaged fluid stress tensor $\overline{\tau_{ij}^F}$ depends on a material law. Throughout the present work a Newtonian fluid is assumed; the average of the respective material law is formed in Sec. 5.3.5.

Two unclosed terms enter (5.30). The term $\partial \alpha^F \overline{\tilde{u}_i^F \tilde{u}_j^F} / \partial x_j$ resembles the Reynolds stress term in the RANS equation and has to be modelled. The surface integral $V^{-1} \sum_{p=1}^{N'} \int_{\Gamma_p} \tau_{ij}^F n_j \,\mathrm{d}s$ represents interaction forces between the fluid and the solid phase and will be represented by a linear combination of known forces, see Sec. 5.3.2 [109]. Contrary to the approach used to derive the PDF equations, where the active Navier-Stokes equation (2.97) was employed, the active stress does not directly appear in (5.30). Because of the volume averaging process, the active stress enters the equation as a force. Hence, the active force is merged into the interaction force term, i.e. the surface integral. Alternatively, it is entirely possible to add the active stress as a production term, which would need to be introduced to the momentum balance of the solid phase accordingly.

The linear momentum of the solid phase is $\mathfrak{u}_i^S = \mathfrak{D} u_i^S$. Due to the rigidity of the particles and the assumption, that all particles cut by the surface ∂V can be neglected, the flux $\overline{\Psi^S} = 0$ vanishes. The only source of momentum in the system is the active stress, however, it is introduced into the model via the interaction force term. Thus, no source occurs $\Pi_i^S = 0$. At the surface of the particles the jump condition

$$[\![\tau_{ij} n_j]\!] = 0, \quad \forall \boldsymbol{x}^* \in \Gamma_p \tag{5.31}$$

is applied, leading to

$$\int_{\Gamma_p} \tau_{ij}^S n_j \,\mathrm{d}s = \int_{\Gamma_p} \tau_{ij}^F n_j \,\mathrm{d}s. \tag{5.32}$$

Using (5.22) together with (5.27) and (5.32) delivers the averaged solid phase linear momentum balance equation

$$\mathfrak{D}\left[\frac{\partial \alpha^S \overline{v_i^S}}{\partial t} + \frac{\partial \alpha^S \overline{v_i^S}\,\overline{v_j^S}}{\partial x_j} + \frac{\partial \alpha^S \overline{\tilde{v}_i^S \tilde{v}_j^S}}{\partial x_j}\right] - \frac{1}{V}\sum_{p=1}^{N'} \int_{\Gamma_p} \tau_{ij}^F n_j dS = 0. \tag{5.33}$$

The unclosed integral term $-V^{-1}\sum_{p=1}^{N'}\int_{\Gamma_p}\tau_{ij}^{F}n_j dS$ is equal to the surface integral term in (5.30) with reversed sign. Again, an additional Reynolds stress type term $\partial\alpha^S\overline{\tilde{v}_i^S\tilde{v}_j^S}/\partial x_j$ enters the equation, which has to be modelled. As for the fluid phase, (5.33) can be obtained from the local physical equations, i.e. the translational Newton-Euler equation (2.54). While the local quantity of the translational velocity $v_{ip} = v_{ip}\,(t)$ only depends on the time t, the averaging process introduced a spatial dependency via the phase indicator function $\gamma^{\mathfrak{P}}$ in (5.4). Subsequently, the averaged equation for the linear momentum contain a convective term, which is not the case in the local linear momentum balance.

5.2.3. Averaged angular momentum balance

The local angular momentum of the fluid phase with respect to the centre of V is $\mathfrak{u}_i^F = \epsilon_{ijk}\zeta_j u_k^F$. The flux is $\Psi_{ij}^F = \epsilon_{ijk}\zeta_j\tau_{kl}$. Using (5.20) delivers the averaged angular momentum balance

$$\left\langle\epsilon_{ijk}\zeta_j\frac{\partial u_k^F}{\partial t}\right\rangle+\left\langle\epsilon_{ijk}\zeta_j\frac{\partial u_k^F u_l^F}{\partial x_l^*}\right\rangle-\left\langle\epsilon_{ijk}\zeta_j\frac{\partial \tau_{kl}^F}{\partial x_l^*}\right\rangle+\left\langle\epsilon_{ijk}\tau_{jk}^F\right\rangle=0. \tag{5.34}$$

The first three terms in (5.34) represent the angular momentum of the linear momentum. Using Navier-Stokes equation (2.67) these terms vanish and one obtains with (5.8) the symmetry of the fluid stress tensor

$$\overline{\tau_{ij}^F}=\overline{\tau_{ji}^F}, \tag{5.35}$$

which is a property of a Newtonian fluid and preserved during the averaging process.

The angular momentum of the solid phase with respect to the coordinate origin is $\mathfrak{D}\epsilon_{ijk}x_j^*u_k^S$. The averaged angular momentum is

$$\overline{\mathfrak{D}\epsilon_{ijk}x_j^*u_k^S}=\mathfrak{D}\epsilon_{ijk}\left[\overline{x_j^*v_k^S}+\epsilon_{ijk}\sum_{p=1}^{N'}\chi_{ip}\overline{v_k^S}+\overline{\Theta_{ij}\omega_j^S}\right], \tag{5.36}$$

where the first two terms on the right hand side are contributions of the angular momentum of the linear momentum. Subsequently, their contributions to the balance equation for the angular momentum vanish similar to the fluid phase angular momentum. The last term $\overline{\Theta_{ij}^S\omega_j^S}$ describes the average angular momentum of the particles with respect to their centre of mass. In general, both, the moment of inertia tensor Θ_{ij}^S and the rotational velocity ω_j^S are functions of the time t . Changing the reference frame to a body-fixed frame delivers a constant Θ_{ij}^S. Furthermore, it is assumed that the axes of the body reference frame align with the primary axes of the particle, leading to a diagonal moment of inertia tensor Θ_{ij}^S. However, due to the rotating nature of the body reference frame the temporal derivative changes. Let $\boldsymbol{e}^{a,P}$ with $a = 1, 2, 3$ be the body reference frame and the principle axes of inertia. In this case the moment of inertia tensor contains only diagonal elements. Due to the rotation the temporal derivative of the unit vector system $\boldsymbol{e}^{a,P}$ is

$$\frac{\mathrm{d}e_i^{a,P}}{\mathrm{d}t}=\epsilon_{ijk}\omega_j e_k^{a,P}\quad\forall a\in\{1,2,3\}\,. \tag{5.37}$$

Using (5.37), the general averaged transport equation (5.22), the decomposition (5.9) and the definition (2.52) of the particle radial vector r_i one obtains the transport equation for the averaged particle angular momentum

$$\Theta_{ij}^S \frac{\partial \alpha^S \overline{\omega_j^S}}{\partial t} + \Theta_{ij}^S \frac{\partial \alpha^S \overline{\omega_j^S}\, \overline{v_k^S}}{\partial x_k} + \Theta_{ij}^S \frac{\partial \alpha^S \overline{\tilde{\omega}_j^S \tilde{v}_k^S}}{\partial x_k} + \epsilon_{ijk} \alpha^S \Theta_{kl}^S \overline{\omega_j^S}\, \overline{\omega_l^S} + \epsilon_{ijk} \alpha^S \Theta_{kl}^S \overline{\tilde{\omega}_j^S \tilde{\omega}_l^S}$$
$$- \frac{1}{V} \sum_{p=1}^{N'} \int_{\Gamma_p} \epsilon_{ijk} r_j \tau_{kl}^F n_l \, \mathrm{d}s = 0, \tag{5.38}$$

where the fourth and fifth terms on the right hand side arise due to the temporal change of the body reference frame (5.37), similar to the local three rotational Newton-Euler equation (2.55). The moment of inertia tensor Θ_{ij}^S is constant, hence, it is no longer necessary to include it in the averaging process. Both terms $\epsilon_{ijk} \alpha^S \Theta_{kl}^S \overline{\omega_j^S}\, \overline{\omega_l^S} + \epsilon_{ijk} \alpha^S \Theta_{kl}^S \overline{\tilde{\omega}_j^S \tilde{\omega}_l^S}$ vanish in case of a two-dimensional problem, reducing the amount of modelling necessary. The integral term $V^{-1} \sum_{p=1}^{N} \int_{\Gamma_p} \epsilon_{ijk} r_j \tau_{kl}^F n_l dS$ represents hydrodynamic torques acting on the particles. Similar to the hydrodynamic forces in case of the linear momentum balance, it will be modelled as a linear combination of well-known torques. Additionally, the fluctuation terms $\Theta_{ij}^S \partial \alpha^S \overline{\tilde{\omega}_j^S \tilde{v}_k^S} / \partial x_k$ and $\epsilon_{ijk} \alpha^S \Theta_{kl}^S \overline{\tilde{\omega}_j^S \tilde{\omega}_l^S}$ need to be modelled as they are unclosed.

5.2.4. Particle orientation balance

Although the orientation of the particles is not a conservation variable, it has a great influence on the behaviour of an active suspension. For several of the interaction forces and torques, which will be used to model the surface integrals in the momentum equations, the orientation vector defines the direction of the forces respectively the torque. As we will see, the behaviour of the averaged orientation differs significantly from the orientation of the individual particles. The volume averaged model is derived for three dimensions, hence, the orientation vector $\boldsymbol{e}_{ip}$ is used as the transport variable. Its local temporal derivative is (2.48)

$$\frac{\mathrm{d} e_{ip}}{\mathrm{d} t} = \epsilon_{ijk} \omega_{jp} e_{iq} \gamma_q .$$

Subsequently, (5.22) is used together with $\mathfrak{u}^S = e_i^S$, $\Psi_i^S = 0$ and $\Pi_i^S = \epsilon_{ijk} \omega_{jp} e_{iq} \gamma_q$, leading to

$$\frac{\partial \alpha^S \overline{e_i^S}}{\partial t} + \frac{\partial \alpha^S \overline{e_i^S}\, \overline{v_j^S}}{\partial x_j} + \frac{\partial \alpha^S \overline{\tilde{e}_i^S \tilde{v}_j^S}}{\partial x_j} - \epsilon_{ijk} \alpha^S \overline{\omega_j^S}\, \overline{e_k^S} - \epsilon_{ijk} \alpha^S \overline{\tilde{\omega}_j^S \tilde{e}_k^S} = 0. \tag{5.39}$$

The length of the particle orientation vector $e_i = e_{ip} \gamma_p$ is always unity. However, the averaged orientation vector, which transport and change is described by (5.39), has a variable length. As such, it measures not only the orientation, but also the orderliness of the particles. In the case that all particles are orientated parallel and in the same direction, the length $e^S = \left| \overline{e_i^S} \right|$ becomes unity. In the opposing case, when all particles are pairwise opposite orientated $e^S = 0$ approaches zero. While the term $\epsilon_{ijk} \alpha^S \overline{\omega_j^S}\, \overline{e_k^S}$ is a source term for the element $\overline{e_i^S}$ of the averaged orientation vector, it does not change the length of the vector. Hence, the two unclosed fluctuation terms $\partial \alpha^S \overline{\tilde{e}_i^S \tilde{v}_j^S} / \partial x_j$ and $\epsilon_{ijk} \alpha^S \overline{\tilde{\omega}_j^S \tilde{e}_k^S}$ in (5.39) are responsible for the length change and need to be modelled.

5.2.5. Relation between the PDF equations and the volume averaged equations

The PDF equations derived in Sec. 3.4 contain all information about the averaged equations derived in the present section, hence, they provide an alternate way to derive the averaged equations. The average or expectation value of a general variable $\mathfrak{u}$ can be defined by using the PDF $f^{\mathfrak{U}}$

$$\langle \mathfrak{u} \rangle = \int \mathfrak{U} f^{\mathfrak{U}} \,\mathrm{d}\mathfrak{U}, \tag{5.40}$$

i.e. by an integration with respect to the sample space variable $\mathfrak{U}$. As an example, the averaged fluid linear momentum equation (5.30) is derived. The velocity marginal PDF equation is given for the single-field velocity U_i. Considering only the velocity in the bulk of the fluid phase by multiplying (3.88) with the sample space indicator function ${}_1g^F$ delivers the following reduced equation

$$\begin{aligned}
&\int \frac{\partial\, {}_1g^F\, {}_1f}{\partial t} + \frac{\partial\, {}_1g^F\, {}_1V_i\, {}_1f}{\partial x_i} \,\mathrm{d}\boldsymbol{X}\,\mathrm{d}\boldsymbol{b} \\
&\quad = \frac{1}{4\pi}\frac{\partial}{\partial\, {}_1V_i}\int {}_1g^F \frac{\partial}{\partial\, {}_1x_i}\frac{1}{|{}_2\boldsymbol{x} - {}_1\boldsymbol{x}|}\left({}_2V_i\frac{\partial}{\partial\, {}_2x_i}\right)^2 {}_2f\,\mathrm{d}\,{}_2\boldsymbol{x}\,\mathrm{d}\,{}_2\boldsymbol{V}\,\mathrm{d}\boldsymbol{X}\,\mathrm{d}\boldsymbol{b} \\
&\quad - \frac{1}{\mathrm{Re}}\frac{\partial}{\partial\, {}_1V_i}\int \delta\left({}_2\boldsymbol{x} - {}_1\boldsymbol{x}\right) {}_1g^F\, {}_2V_i \frac{\partial^2\, {}_2f}{\partial\, {}_2x_j{}^2}\,\mathrm{d}\,{}_2\boldsymbol{x}\,\mathrm{d}\,{}_2\boldsymbol{V}\,\mathrm{d}\boldsymbol{X}\,\mathrm{d}\boldsymbol{b},
\end{aligned} \tag{5.41}$$

which, apart from the indicator function ${}_1g^F$, is equivalent to the equation for the single point PDF given by Lundgren [142]. Applying (5.40) to (5.41) and integrating by parts delivers

$$\begin{aligned}
&\frac{\partial}{\partial t}\int {}_1g^F\, {}_1V_i\, {}_1f\,\mathrm{d}\,{}_1\boldsymbol{V}\,\mathrm{d}\boldsymbol{X}\,\mathrm{d}\boldsymbol{b} + \frac{\partial}{\partial x_j}\int {}_1g^F\, {}_1V_i\, {}_1V_j\, {}_1f\,\mathrm{d}\,{}_1\boldsymbol{V}\,\mathrm{d}\boldsymbol{X}\,\mathrm{d}\boldsymbol{b} \\
&\quad = -\frac{1}{4\pi}\int {}_1g^F \frac{\partial}{\partial\, {}_1x_i}\frac{1}{|{}_2\boldsymbol{x} - {}_1\boldsymbol{x}|}\left({}_2V_i\frac{\partial}{\partial\, {}_2x_i}\right)^2 {}_1f\left({}_2\boldsymbol{V}\right)\mathrm{d}\,{}_2\boldsymbol{x}\,\mathrm{d}\,{}_2\boldsymbol{V}\,\mathrm{d}\boldsymbol{X}\,\mathrm{d}\boldsymbol{b} \\
&\quad + \frac{1}{\mathrm{Re}}\int {}_1g^F\, {}_1V_i \frac{\partial^2\, {}_1f}{\partial\, {}_2x_j{}^2}\,\mathrm{d}\,{}_1\boldsymbol{V}\,\mathrm{d}\boldsymbol{X}\,\mathrm{d}\boldsymbol{b},
\end{aligned} \tag{5.42}$$

where ${}_1f\left({}_2\boldsymbol{V}\right)$ is the single-point PDF at ${}_2\boldsymbol{x}$. The equation (5.42) can be rewritten as

$$\frac{\partial\left\langle \gamma^F u_i^F \right\rangle}{\partial t} + \frac{\partial\left\langle \gamma^F u_i^F u_j^F \right\rangle}{\partial x_j} = -\left\langle \gamma^F \frac{\partial p^F}{\partial x_i}\right\rangle + \left\langle \frac{\gamma^F}{\mathrm{Re}}\frac{\partial^2 u_i^F}{\partial u_j^2}\right\rangle = \left\langle \gamma^F \frac{\partial \tau_{ij}}{\partial x_j}, \right\rangle . \tag{5.43}$$

The averaged occurring in (5.40) and (5.43) are ensemble averages in contrast to the volume averages in (5.30). It is possible to transform the averages by using the ergodic hypothesis [31]. A statistically stationary random process is called ergodic, i.e. the PDF of the respective process does not depend on a time-shift Δt

$$f^{\mathfrak{U}}(t) = f^{\mathfrak{U}}(t + \Delta t)\,. \tag{5.44}$$

In case of such a process both the time average and the ensemble average are equivalent.

$$\lim_{T\to\infty}\frac{1}{T}\int_0^T \mathfrak{u}\left(\boldsymbol{x}, t\right)\mathrm{d}t = \int \mathfrak{U} f^{\mathfrak{U}}\,\mathrm{d}\mathfrak{U}. \tag{5.45}$$

Transferring this idea to a volume average delivers

$$\lim_{V \to \infty} \frac{1}{V} \int_V \mathfrak{u}\left(\boldsymbol{x}, t\right) \mathrm{d}\boldsymbol{x} = \int \mathfrak{U} f^{\mathfrak{U}} \, \mathrm{d}\mathfrak{U}, \tag{5.46}$$

which requires an infinite averaging volume $V \to \infty$. In a real system the domain and subsequently the averaging volume are finite. To ensure that still a large number of possible realisations of the ensemble occur in the averaging volume, it is required that the number of particle within the averaging volume is large. This requires $V^P/V \ll 1$, leading to the approximation

$$\frac{1}{V} \int_V \mathfrak{u}\left(\boldsymbol{x}, t\right) \mathrm{d}\boldsymbol{x} \approx \int \mathfrak{U} f^{\mathfrak{U}} \, \mathrm{d}\mathfrak{U}. \tag{5.47}$$

Using this approximation (5.47) together with (5.16), (5.17) and (5.43) delivers

$$\frac{\partial \left\langle u_i^F \right\rangle}{\partial t} + \frac{\partial \left\langle u_i^F u_j^F \right\rangle}{\partial x_j} = \frac{\partial \left\langle \tau_{ij} \right\rangle}{\partial x_j} - \frac{1}{V} \sum_{p=1}^{N'} \int_{\Gamma_p} \tau_{ij} n_j \, \mathrm{d}s, \tag{5.48}$$

where the averaging operator $\langle \cdot \rangle$ now again refers to the volume average (5.4). Introducing the decomposition (5.9) and the true physical volume average (5.7) delivers the volume averaged linear momentum balance for the fluid as given in (5.30).

5.3. Closure relations

The different transport equation of both phases for the mass (5.23), (5.28), linear momentum (5.30), (5.33), angular momentum (5.38) and the orientation of the solid phase (5.39) contain different unclosed terms. All terms can be grouped into two different types. The first type of unclosed terms contains the interaction terms between the two phases, represented by the surface integrals

$$\frac{1}{V} \sum_{p=1}^{N'} \int_{\Gamma_p} \tau_{ij}^F n_j \, \mathrm{d}s \quad \text{and} \quad \frac{1}{V} \sum_{p=1}^{N'} \int_{\Gamma_p} \epsilon_{ijk} r_j \tau_{kl}^F n_l \, \mathrm{d}s. \tag{5.49}$$

The second type of unclosed term contains the fluctuations of the physical variables. The equations (5.30), (5.33), (5.38) and (5.39) contain such terms, which will be modelled by phenomenological considerations. Additionally, the averaged fluid stress tensor $\overline{\tau_{ij}^F}$ needs to be defined in this section.

5.3.1. Mixture viscosity and mixture Reynolds number

Up until know, friction, dissipation and viscosity does not explicitly enters the volume averaged model, it is, however, implied due to the occurrence of the averaged stress tensor $\overline{\tau_{ij}^F}$. The rigid particles cause additional resistance against deformation, which leads to an increase of the Reynolds number compared to a single phase fluid flow [109]. This was first described by Einstein [68, 69], who introduced a mixture viscosity μ^M, leading to a mixture Reynolds number Re^M. For small volume fractions $\alpha^S \ll 1$ and spherical particles the mixture viscosity is [69]

$$\mu^M = \mu^F \left(1 + \frac{5}{2}\alpha^S\right). \tag{5.50}$$

Ishii and Hibiki [109] extended this relation by using a power law to account for higher particle densities

$$\mu^M = \mu^F \left(1 - \frac{\alpha^S}{\alpha^S_{\text{max}}}\right)^{-\mu^{\text{int}}\alpha^S_{\text{max}}}, \tag{5.51}$$

where α^S_{max} is the maximum volume fraction of the solid phase. In general, α^S_{max} is smaller than unity, because even at the highest density packing cavities still exist. Spherical particle have a maximum random packing fraction of $\alpha^S_{\text{max}} = 0.64$ [198], whereas for ellipsoidal particles this value increases up to 0.74 [39, 60]. The intrinsic viscosity μ^{int} in (5.51) accounts for the shape of the particles. For ellipsoidal particles Pabst et al. [164] gave the following relation

$$\mu^{\text{int}} = \frac{5}{2} + 0.123\,(\varepsilon - 1)^{0.925}, \tag{5.52}$$

with the aspect ratio ε of the particles. In case of spherical particles the intrinsic viscosity becomes $\mu^{\text{int}} = 5/2$, subsequently, the linear expansion of (5.51) delivers (5.50).

The particle Reynolds number is

$$\mathrm{Re}^P = \frac{\rho^F U^c a}{\mu^F}, \tag{5.53}$$

where the particle length a is used as the characteristic length scale $L^c = a$. Using the mixture viscosity delivers the mixture Reynolds number

$$\mathrm{Re}^M = \frac{\rho^F U^c a}{\mu^M} = \frac{\rho^F U^c a}{\mu^F}\left(1 - \frac{\alpha^S}{\alpha^S_{\text{max}}}\right)^{\mu^{\text{int}}\alpha^S_{\text{max}}}, \tag{5.54}$$

which will be used throughout the following sections.

5.3.2. Interface forces

The integral terms in the transport equations for the linear momentum (5.30) and (5.33) represent forces at the phase interface. The forces acting on the solid phase are

$$\left\langle F_i^S \right\rangle = \frac{F_{ip}\Omega_p}{V} = \frac{V^P}{V}\sum_{p=1}^{N'}\int_{\Gamma_p} \tau_{ij}^F n_j dS \tag{5.55}$$

Due to momentum conservation the forces acting on the fluid phase have the same absolute value but opposing sign

$$\left\langle F_i^S \right\rangle = -\left\langle F_i^F \right\rangle \tag{5.56}$$

The interface forces are modelled as a linear combination of well establish forces

$$\left\langle F_i^S \right\rangle = \left\langle F_i^A \right\rangle + \left\langle F_i^D \right\rangle + \left\langle F_i^B \right\rangle + \left\langle F_i^V \right\rangle + \left\langle F_i^L \right\rangle + \left\langle F_i^P \right\rangle. \tag{5.57}$$

The active stress at the particle surface causes the averaged active force $\left\langle F_i^A \right\rangle$. The averaged drag force $\left\langle F_i^D \right\rangle$ is caused by the friction between the two phases. The averaged Basset-force

$\langle F_i^B \rangle$ and the virtual mass force $\langle F_i^V \rangle$ have their origin in the relative acceleration of the two phases. However, due to the low Reynolds number assumed in an active suspension, it will be shown, that both force contributions can be neglected. The averaged lift force $\langle F_i^L \rangle$ has three contributions, the Saffman-force $\langle F_i^{LS} \rangle$, the Magnus-force $\langle F_i^{LM} \rangle$ and the circulation lift force $\langle F_i^{LC} \rangle$. The last contribution to (5.57) is the averaged pressure force $\langle F_i^P \rangle$, caused by a pressure gradient at the interface.

Active force

The active stress at the surface of the particles is a source of momentum, necessary to drive the particles forward. According to the definition of the active source term (2.98) the local active stress exerted on the fluid phase is

$$A_i = \delta \left(\boldsymbol{x}^* - \Gamma^{ac} \right) A^c t_i, \tag{5.58}$$

with the non-dimensional active stress magnitude A^c. Forming the average delivers

$$\begin{aligned} \frac{V^P}{V} \int_V \delta \left(\boldsymbol{x}^* - \Gamma^{ac} \right) A^c t_i \, \mathrm{d}\boldsymbol{x}^* =& \frac{V^P}{V} \sum_{p=1}^{N'} \int_{\Gamma_p^{ac}} A^c t_i \, \mathrm{d}s \\ =& -\frac{2aA^c}{\varepsilon} \frac{e_{ip}\Omega_p}{V} \int_{\frac{\pi}{2}}^{\pi} \sin(\theta) \sqrt{\varepsilon^2 \sin^2(\theta) + \cos^2(\theta)} \, \mathrm{d}\theta \\ =& -\alpha^S \mathfrak{A}^c \overline{e_i^S} \end{aligned} \tag{5.59}$$

for a two-dimensional pusher particle, where θ is the polar angle, see Fig. 2.2. In case of a puller particle, the sign in (5.59) has to be reversed, leading to an particle moving in the opposite direction. Alternatively, the integration domain of the elliptic integral can be change to $\int_0^{\pi/2}$, effectively switching the active and passive part of the particle. Instead of using the magnitude A^c and the elliptic integral directly, the active force magnitude, see (2.95) is introduced

$$\mathfrak{A}^c = \frac{2aA^c}{\varepsilon} \int_{\frac{\pi}{2}}^{\pi} \sin(\theta) \sqrt{\varepsilon^2 \sin^2(\theta) + \cos^2(\theta)} \, \mathrm{d}\theta.$$

The averaged active force $\mathfrak{A}^c$ simply can be prescribed, removing the necessity to distinguish between cases of different spatial dimensions. The force derived in (5.59) is the force acting on the fluid, hence, due to momentum conservation the averaged active force on the particle is

$$\langle F_i^A \rangle = \alpha^S \mathfrak{A}^c \overline{e_i^S}. \tag{5.60}$$

As stated in Sec. 5.2.4, the averaged orientation $\overline{e_i^S}$ is not a unit vector. Thus, the length of the averaged orientation might vanish $e^S = 0$, leading to an suspension with no effective averaged active force, despite the existence of active particles. The fluctuation correlations in the averaged transport equations will be used to model effects of the active stress on smaller scales, where information are lost in the averaged system.

Drag force

The averaged drag force $\left\langle F_i^D \right\rangle$ accounts for the friction between the two phases. It ensures that velocity differences are evened out. The drag force on a single particle in an uniform flow has two contributions, the form drag F_i^{form} and the friction drag F_i^{friction} [132] and it is proportional to the relative velocity between the two phases

$$w_i^S = u_i^F - u_i^S. \tag{5.61}$$

The form drag is caused by the pressure and the friction drag by viscous forces. Leith [132] wrote Stokes' law for a spherical particle in the following form

$$F_i^D = \frac{3\pi a}{\text{Re}^P} w_i^S = F_i^{\text{form}} + F_i^{\text{friction}}, \tag{5.62}$$

where F_i^D is the drag force acting on a single particle, $F_i^{\text{form}} = 1/3 F_i^D$ and $F_i^{\text{friction}} = 2/3 F_i^D$. The form drag is proportional to the cross sectional area $A_\perp$ of the particle perpendicular to the relative velocity vector w_i^S. The friction drag on the other hand is associated with the longitudinal cross sectional area $A_\|$ parallel to w_i. For an non-spherical particle, the deviation of the spherical form is measured by the sphericity

$$\Phi_\| = \frac{a_v^2}{a_s^2} = \frac{\pi^{\frac{1}{3}} \left(6V^P\right)^{\frac{2}{3}}}{\Gamma_p}, \tag{5.63}$$

where a_v is the diameter of a volume equivalent sphere with respect to the particle and a_s is the diameter of a surface equivalent sphere. Furthermore, the cross sectional sphericity is defined as

$$\Phi_\perp = \frac{a_v^2}{a_\perp^2}, \tag{5.64}$$

where $a_\perp$ is the diameter of the disk with the same surface area as $A_\perp$ of the particle. While a_v and a_s are constants depending on the geometry of the particle, $a_\perp$ is a function of the relative velocity w_i and the orientation of the particle. Using the sphericity (5.63) and the cross sectional sphericity (5.64) together with Stokes' law for a spherical particle (5.62), one obtains for a non-spherical particle [132]

$$F_i^D = \frac{\pi a}{\text{Re}^P} \left(\frac{1}{\sqrt{\Phi_\perp}} + \frac{2}{\sqrt{\Phi_\|}} \right) w_i^S. \tag{5.65}$$

Hölzer and Sommerfeld [98] derived a more complex relation for the drag on a non-spherical particle, however, for low Reynolds number their relation also reduces to (5.65).

So far, only a passive particle with a uniform no-slip boundary condition in an infinite domain has been considered. Both, the active boundary of the Janus particle and the possible no-slip boundary condition at the outer surface of the domain Ω might influence the effective drag on the particle. Considering an ideal slip-sphere, Happel and Brenner [90] gave a correction factor of $2/3$ compared to a no-slip sphere, i.e. the friction drag F_i^{friction} vanishes due to the slip boundary, however, the form drag F_i^{form} is increased by a factor of two. The active surface of a Janus particle is not an ideal slip boundary. Hence, the relation between the no-slip drag $F_i^{\text{no-slip}}$ and the slip drag force F_i^{slip} is not clear. However, a numerical study [57] suggests, that

$F_i^{\text{Janus}} = 0.5\left(F_i^{\text{no-slip}} + F_i^{\text{slip}}\right)$. Subsequently, the correction factor for an active Janus particle with two equally sized surfaces Γ^{ac} and Γ^{pa} is

$$c_{Ac}^{D} = \frac{5}{6}. \tag{5.66}$$

Domain boundaries might have two separate effects. On the one hand, they might influence the general behaviour of a particle independent of its position. On the other hand, the drag on a particle close to a solid wall is generally increased. However, numerical studies [92] for a particle in a duct showed that if the size of the particle is much smaller than the height of the duct $\frac{a}{\varepsilon H} \ll H$, the influence of the relative position towards the wall is negligible. The general increase of the drag force due to the solid walls of a duct according to Hensley and Papavassiliou [92] is

$$c_H^D = 1 + 2.33\varepsilon^{\frac{2}{5}}\frac{a}{\varepsilon H}, \tag{5.67}$$

which again is close to unity for small ratios $a/\varepsilon H$. With $c_{\text{corr}}^D = c_{Ac}^D c_H^D$ one obtains the drag force on a Janus particle

$$F_i^D = \frac{\pi a c_{\text{corr}}^D}{\text{Re}^P}\left(\frac{1}{\sqrt{\Phi_\perp}} + \frac{2}{\sqrt{\Phi_\parallel}}\right) w_i^S. \tag{5.68}$$

So far, the particle Reynolds number Re^P was used, because only a single particle was considered. In the next step, the drag force is extended to an active suspension, hence, the mixture Reynolds number Re^M is used. Averaging (5.68) delivers

$$\left\langle F_i^D \right\rangle = \frac{\alpha^S \pi a c_{\text{corr}}^D}{\text{Re}^M}\left(\frac{1}{\overline{\sqrt{\Phi_\perp}}} + \frac{2}{\sqrt{\Phi_\parallel}}\right)\overline{w_i^S}, \tag{5.69}$$

where all correlations of fluctuations where neglected and the average of the relative velocity is defined as

$$\alpha^S \overline{w_i^S} = \alpha^S\left(\overline{u_i^F} - \overline{v_i^S}\right). \tag{5.70}$$

Note that, due to the fact that the cross sectional sphericity is a function of the orientation and the relative velocity, it is also an averaged variable. Specifically, in (5.69) the average of the square root $\overline{\sqrt{\Phi_\perp}}$ is formed. The sphericity $\Phi_\parallel$ on the other hand is constant and no average has to be taken.

The circulation lift force F_i^{LC} will be defined as a function of the drag coefficient C^D. Hence, by considering a three dimensional particle with the longitudinal cross sectional area $\pi a^2/4\varepsilon$ one obtains

$$C^D = \frac{8\varepsilon c_{\text{corr}}^D}{a\left|\overline{\boldsymbol{w}^S}\right| \text{Re}^M}\left(\frac{1}{\overline{\sqrt{\Phi_\perp}}} + \frac{2}{\sqrt{\Phi_\parallel}}\right), \tag{5.71}$$

which leads to

$$\left\langle F_i^D \right\rangle = \frac{\alpha^S \pi a^2}{8\varepsilon} C^D \left|\overline{\boldsymbol{w}^S}\right| \overline{w_i^S}. \tag{5.72}$$

Basset-force and virtual mass force

The Basset-force arises due to viscous effects of the relative acceleration of the two phases, whereas the virtual mass force accounts for inertia effects of the relative acceleration [109]. As mentioned, both contribution to the interface forces can be neglected due to the low Reynolds number condition, which will be shown in the following assessment. According to Ishii and Hibiki [109] the Basset-force on a spherical particle is

$$F_i^B = 3a^2\sqrt{\frac{\pi\mathfrak{D}}{\mathrm{Re}^P}}\int_t \frac{\mathrm{d}w_i^S}{\mathrm{d}t'}\frac{\mathrm{d}t'}{\sqrt{t-t'}}, \tag{5.73}$$

where the relative acceleration between the two phases is

$$\frac{\mathrm{d}w_i^S}{\mathrm{d}t} = \frac{\partial w_i^S}{\partial t} + \frac{\partial w_i^S u_j^S}{\partial x_j^*}. \tag{5.74}$$

Comparing F_i^B to the drag force on a spherical particle delivers the proportionality coefficient

$$\frac{F_i^B}{F_i^D} \propto \sqrt{\mathrm{Re}^P\, a^2} = O\left(10^{-7.5}\right), \tag{5.75}$$

where $\mathrm{Re}^P = 10^{-3}$ and a micrometer sized particle $a = 10^{-6}$ was assumed.

The virtual mass force is [109, 110, 218]

$$F_i^V = \frac{\alpha_p}{2}\frac{1+2\alpha^S}{1-\alpha^S}\frac{\mathrm{d}w_i^S}{\mathrm{d}t}. \tag{5.76}$$

Again, by considering the drag for a spherical particle, one obtains the coefficient

$$\frac{F_i^V}{F_i^D} \propto \mathrm{Re}^P\, a^2 = O\left(10^{-15}\right) \tag{5.77}$$

with the above values for Re^P and a. Subsequently, the Basset-force and the virtual mass force are negligable for small particles and small Reynolds numbers.

Lift force

The lift force acting on a single particle comes from three contributions. A fluid velocity gradient causes a lift force at the particle, called Saffman-force F_i^{LS}. If the particle itself has a rotational velocity the Magnus-force F_i^{LM} is induced. The third component of the lift force is caused by the circulation of the fluid F_i^{LC}, similar to the lift force acting on an airfoil.

Saffman [180] established a formulation for the lift force due to a fluid velocity gradient acting on a spherical particle

$$F_i^{LS} = 1.615\sqrt{\frac{a}{\mathrm{Re}}}\left|\boldsymbol{\omega}^F\right|^{-\frac{1}{2}}\epsilon_{ijk}w_j^S\omega_k^F, \tag{5.78}$$

where we used a non-dimensional formulation given by Ishii and Hibiki [109]. Here, ω_i^F is the rotation of the fluid flow

$$\omega_i^F = \epsilon_{ijk}\frac{\partial u_j^F}{\partial x_k^*}. \tag{5.79}$$

Results of Hölzer and Sommerfeld [99] indicate, that (5.78) also holds for non-spherical particles under the condition $\mathrm{Re} \ll 1$. To obtain the average of (5.78) it is assumed that the fluid rotation (5.79) is constant within the averaging volume

$$\overline{\omega_i^F} = \epsilon_{ijk} \frac{\partial \overline{u_j^F}}{\partial x_k}. \tag{5.80}$$

Thus, no products of the form $\overline{\mathfrak{u}^{1,\mathfrak{P}}\mathfrak{u}^{2,\mathfrak{P}}}$ occur and one obtains for the averaged Saffman-force

$$\left\langle F_i^{LS} \right\rangle = 1.615 \alpha^S \sqrt{\frac{a}{\mathrm{Re}^M}} \left| \overline{\boldsymbol{\omega}^F} \right|^{-\frac{1}{2}} \epsilon_{ijk} \overline{w_j^S}\, \overline{\omega_k^F}, \tag{5.81}$$

where the mixture Reynolds number is used to account for the suspension.

The relative rotation of the fluid and the particle $1/2\omega_i^F - \omega_i^S$ determines the Magnus-force. It causes a drift in the perpendicular direction of the relative translational velocity and the relative rotational velocity. For spherical particles the non-dimensional relation reads [178]

$$F_i^{LM} = \frac{\pi}{8} a^3 \epsilon_{ijk} \left(\frac{1}{2} \omega_i^F - \omega_i^S \right) w_k^S. \tag{5.82}$$

Similar to the Saffman-force, Hölzer and Sommerfeld [99] showed that Rubinow's theory is in good agreement with the numerically obtained values for the Magnus-force of an ellipsoidal particle. Averaging and neglecting any terms arising due to fluctuations delivers

$$\left\langle F_i^{LM} \right\rangle = \frac{\alpha^S \pi a^3}{8} \epsilon_{ijk} \left(\frac{1}{2} \overline{\omega_i^F} - \overline{\omega_i^S} \right) \overline{w_k^S}, \tag{5.83}$$

which is the averaged Magnus-force acting on the active particles in the suspension. Note that the Magnus-force also depends on the fluid density, however, throughout this work it is assumed that the non-dimensional fluid density is unity. Hence, it does not explicitly appear in the relations for the Magnus-force (5.82) and (5.83).

A non-spherical, ellipsoidal particle experiences an additional lift force F_i^{LC}, if the orientation vector $e_i = e_{ip}\gamma_p$ does not align with the vector of the relative velocity w_i^S. The resulting circulation is the main source of the lift on an airfoil. In the theory of airfoils the Kutta-Joukowski theorem relates the magnitude of F_i^{LC} to the circulation G

$$F^{LC} = \rho^F w^S G, \tag{5.84}$$

which is based on invisicid theory and not applicable to an active suspension due to its high-viscous, low-Reynolds nature. The lift force on a single particle with an angle of incidence φ^I towards the relative velocity is [151]

$$F_i^{LC} = \mathrm{sgn}\left(w_i^S e_{ip}\gamma_p\right) \frac{\pi}{8} a^2 C^L \epsilon_{ijk} \left(\epsilon_{klm} w_l^S e_{mq}\gamma_q\right) w_k^S, \tag{5.85}$$

where the angle of incidence φ^I is

$$\cos\varphi^I = \frac{e_{ip}\gamma_p w_i^S}{\left|\boldsymbol{e}_q\gamma_q\right| \left|\boldsymbol{w}^S\right|}. \tag{5.86}$$

It should be noted, that the relative velocity of the two phases is expected to be rather small due to the low Reynolds number. Hence, as the circulation lift force depends quadratically on the relative velocity w_i^S, compared to the linear dependency of the Magnus- and Saffman-force, the influence of the circulation lift force is expected to be smaller. The drag coefficient C^D is used to define the lift coefficient C^L and subsequently the magnitude of the circulation lift force. Hoerner [97] derived the relation

$$C^L = C^D \sin^2\left(\varphi^I\right)\cos\left(\varphi^I\right). \tag{5.87}$$

To improve the calculation of the lift coefficient a fit based on Hoerner [97] and numerical data is derived

$$C^L\left(\varphi^I\right) = C^D a_0 \sin\left(a_1\varphi^I\right)\sin\left(a_1\varphi^I + a_2\right)\cos\left(a_1\varphi^I + a_3\right) \tag{5.88}$$

with the coefficients a_1, a_2 and a_3. Simulations in BoSSS for a single particle with a diameter $a = 1$ and an aspect ratio $\varepsilon = 2$ are used to obtain exemplary values for the coefficients. The particle is placed in a uniform flow with an inflow a the right and an outflow at the left side of the domain Ω. Boundary conditions at the upper and lower side are periodic. The resulting coefficients are

$$a_0 = 0.92, \quad a_1 = 0.647, \quad a_2 = 0.351\pi, \quad a_3 = 0.177\pi, \tag{5.89}$$

which do not depend on the particle Reynolds number Re^P.

Especially the signum function in (5.85) is difficult to model, because the result of the average $\overline{\mathrm{sgn}\left(w_i^S e_{ip}\gamma_p\right)}$ is unknown. The assumption

$$\overline{C^L(\varphi)^I \mathrm{sgn}\left(w_i^S e_{ip}\gamma_p\right)} \approx c^e C^L\left(\widehat{\varphi^I}\right)\mathrm{sgn}\left(\overline{e_i^S}\cdot\overline{w_i^S}\right). \tag{5.90}$$

is used as an approximation. The additional model parameter $c^e = c^e\left(e^S\right)$ is a function of the length of the averaged orientation vector e^S. The parameter is meant to introduce a dependency on the orderliness of the suspension state. Perpendicular orientation vectors of many particle pairs and an effective orientation of each pair parallel to the relative velocity leads to a vanishing averaged signum function. Thus, the parameter c^e has a minimum in case of $e^S = \sqrt{2}/2$, because the probability for all particles to be perpendicular to each other in pairs reaches a maximum. However, it is not possible to assume a vanishing circulation lift force in general, leading to the model constant c_1^e, accounting for the minimum circulation lift. In the case $e^S = 1$ all particles move parallel. Hence, the averaged signum function reaches its maximum value and $c^e = 1$. The opposing case $e^S = 0$ delivers a second maximum, which is defined by the second model parameter $c_2^e \leq 1$. This behaviour is mapped by the ansatz

$$\begin{aligned} c^e = &\left(\frac{c_2^e - c_1^e}{2}\cos\left(\frac{2\pi}{\sqrt{2}}e^S\right) + \frac{c_2^e + c_1^e}{2}\right)\left(1 - \mathcal{H}\left(e^S - \frac{\sqrt{2}}{2}\right)\right) \\ &+ \left(\frac{1 - c_1^e}{2}\cos\left(\frac{2\pi}{2-\sqrt{2}}\left(e^S - 1\right)\right) + \frac{c_2^e + c_1^e}{2}\right)\mathcal{H}\left(e^S - \frac{\sqrt{2}}{2}\right). \end{aligned} \tag{5.91}$$

Furthermore, it is necessary to define a model for the averaged angle of incidence. The following approximation is used

$$\cos\left(\widehat{\varphi}^I\right) = \frac{\overline{e_i^S}\,\overline{w_i^S}}{\left|\overline{\boldsymbol{e}^S}\right|\left|\overline{\boldsymbol{w}^S}\right|}, \tag{5.92}$$

where the circumflex indicates an approximated quantity obtained from averaged quantities and not a mathematical average. Using the two approximations (5.90) and (5.92), one obtains the averaged circulation lift force

$$\left\langle F_i^{LC} \right\rangle \approx \alpha^S \mathrm{sgn}\left(\overline{\boldsymbol{e}^S} \cdot \overline{\boldsymbol{w}^S} \right) \frac{\pi a^2 c^e}{8} C^L\left(\widehat{\varphi}^I\right) \epsilon_{ijk} \epsilon_{jlm} \overline{w_l^S}\, \overline{e_m^S}\, \overline{w_k^S}, \tag{5.93}$$

where any fluctuations were neglected.

Pressure force

A pressure gradient over the surface of a particle causes an additional force. Assuming the pressure gradient to be constant at the entire surface, delivers for a single particle

$$F_i^P = -V^P \frac{\partial p^F}{\partial x_i^*}. \tag{5.94}$$

Averaging (5.94) delivers

$$\left\langle F_i^P \right\rangle = -V^P \frac{\partial \alpha^S \overline{p^F}}{\partial x_i}, \tag{5.95}$$

where a constant pressure gradient within the averaging volume was assumed.

5.3.3. Interface torques

The torque at the interface

$$\langle T_i \rangle = \frac{V^P}{V} \sum_{p=1}^{N'} \int_{\Gamma_p} \epsilon_{ijk} r_j \tau_{kl}^F n_l \, \mathrm{d}s \tag{5.96}$$

emerges as a source in the solid phase angular momentum balance (5.38). The torque has two contributions. For spherical particles or particles with an aspect ratio close to unity the main contribution is the drag torque T_i^D, caused by the friction between the two phases. For elongated particles the pitching torque T_i^P becomes more important, caused by an off-centred point of attack of the interface forces. Hence, the averaged torque is

$$\langle T_i \rangle = \left\langle T_i^P \right\rangle + \left\langle T_i^D \right\rangle. \tag{5.97}$$

Pitching torque

Depending on the angle of incidence φ^I and the aspect ratio ε of a particle, the centre of pressure is the point of attack of all interface forces $\left\langle F_i^S \right\rangle$. Rosendahl [175] gave the expression

$$r^{CP}\left(\varphi^I\right) = \left| \left(\boldsymbol{\chi}_p^{CP} - \boldsymbol{\chi}_p \right) \gamma_p \right| = \frac{a}{4}\left(1 - e^{1-\varepsilon}\right)\left(1 - \sin^3 \varphi^I\right) \tag{5.98}$$

for the length of the distance vector r_i^{CP} between the centre of mass χ_{ip} and the centre of pressure χ_{ip}^{CP} of a single particle. It is assumed that the direction of r_i^{CP} is defined by the orientation vector $e_i = e_{ip}\gamma_p$

$$r_i^{CP} = \mathrm{sgn}\big(w_j^S e_{jp}\gamma_p\big) r^{CP}\big(\varphi^I\big) e_{ip}\gamma_p. \tag{5.99}$$

Similar to the circulation lift force, a signum function and the angle of incidence occurs in (5.99). Thus, it is necessary to find an approximation for the averaged distance vector $\overline{r_i^{CP}}$. The angle of incidence is again approximated by (5.92) and it is assumed that the averaged distance vector can be described by

$$\overline{r_i^{CP}} = \mathrm{sgn}\left(\overline{w_j^S}\,\overline{e_j^S}\right) r^{CP}\left(\widehat{\varphi}^I\right)\overline{e_i^S}. \tag{5.100}$$

Following Mandø and Rosendahl [145] the cross product

$$T_i^P = \epsilon_{ijk} r_j^{CP} F_k^S. \tag{5.101}$$

defines the pitching torque. Averaging and neglecting any emerging fluctuation term delivers the averaged pitching torque

$$\left\langle T_i^P \right\rangle = \epsilon_{ijk}\overline{r_j^{CP}}\left\langle F_k^S \right\rangle. \tag{5.102}$$

Drag torque

The cause of the drag torque is solely the friction in tangential direction at the interface between a particle and the surrounding fluid. In case of a single spherical particle the drag torque is [75, 118]

$$T_i^D = \frac{\pi a^3}{\mathrm{Re}^P}\left(\frac{1}{2}\omega_i^F - \omega_i^S\right). \tag{5.103}$$

There is no form component of the drag torque as it is in the case of the drag force. Subsequently, by using the sphericity $\Phi_{\|}$ one obtains the drag torque for a non-spherical passive particle

$$T_i^D = \frac{\pi a^3}{\mathrm{Re}^P\,\Phi_{\|}^{\frac{3}{2}}}\left(\frac{1}{2}\omega_i^F - \omega_i^S\right). \tag{5.104}$$

An additional correction factor is necessary to account for the active boundary condition and the slip velocity caused by it. For an ideal slip-particle the entire drag torque vanishes. While the active boundary is not an ideal slip boundary condition due to the active stress, the latter is symmetric. Hence, it does not contribute to the net torque on the particle and the correction factor is $c_{\mathrm{corr}}^{DT} = 0.5$, leading to

$$T_i^D = \frac{\pi a^3 c_{\mathrm{corr}}^{DT}}{\mathrm{Re}^P\,\Phi_{\|}^{\frac{3}{2}}}\left(\frac{1}{2}\omega_i^F - \omega_i^S\right). \tag{5.105}$$

Averaging yields

$$\left\langle T_i^D \right\rangle = \frac{\alpha^S \pi a^3 c_{\mathrm{corr}}^{DT}}{\mathrm{Re}^M\,\Phi_{\|}^{\frac{3}{2}}}\left(\frac{1}{2}\overline{\omega_i^F} - \overline{\omega_i^S}\right), \tag{5.106}$$

where the mixture Reynolds number accounts for the suspension. The averaged drag torque (5.106) is proportional to the difference of the rotation $\frac{1}{2}\overline{\omega_i^F} - \overline{\omega_i^S}$ and aims to reduce said difference.

5.3.4. Fluctuation correlation tensors

The averaged balance equations for the linear momentum (5.30), (5.33), for the angular momentum (5.38) and the particle orientation (5.39) contain tensors of fluctuation correlations. These terms transport information about smaller scales influencing the macroscopic behaviour of the suspension. The information about small scales is lost during the averaging process, hence, it is necessary to describe the fluctuation correlations by model relations. The most simple model would be to neglect any fluctuation correlation. However, important and characteristic behaviour of an active suspension can not be mapped by such a model. For example, the averaged active force only acts on the suspension if $e^S \neq 0$. Nevertheless, the active stress of the particles in such a suspension still acts as a source for the linear momentum, which has to be introduced by a model for the fluctuation tensors. The tensors $\overline{\tilde{\mathfrak{u}}_i^{\mathfrak{P}}\tilde{u}_j^{\mathfrak{P}}}$ are of an equivalent type as the Reynolds stress tensor in the RANS equation describing turbulent flows. Following the line of thought employed in turbulence research, a Boussinesq ansatz is formulated in analogy to the fluid stress tensor τ_{ij}^F

$$\overline{\tilde{\mathfrak{u}}_i^{\mathfrak{P}}\tilde{u}_j^{\mathfrak{P}}} = \frac{2}{3}K\delta_{ij} - \mu^S\left(\frac{\partial \mathfrak{u}_i^{\mathfrak{P}}}{\partial x_j} + \frac{\partial \mathfrak{u}_j^{\mathfrak{P}}}{\partial x_i}\right), \tag{5.107}$$

which is employed as a model for the fluctuation correlations in all of the transport equations mentioned before. Here, $K = 0.5\,\overline{\tilde{\mathfrak{u}}_i^{\mathfrak{P}}\tilde{u}_i^{\mathfrak{P}}}$ is a generalised turbulent kinetic energy, analogously to turbulence research. The diffusion coefficient μ^S is introduced in analogy to the turbulent eddy viscosity.

Translational velocity correlation

The correlation tensor

$$\frac{\partial \alpha^S \overline{\tilde{v}_i^S \tilde{v}_j^S}}{\partial x_j} \tag{5.108}$$

occurs in the averaged solid phase linear momentum balance (5.33). It is assumed that it describes interactions between individual particles. The diffusive part of the Boussinesq ansatz (5.107) describes collision effects, which in a low-Reynolds flow have a negligible effect on the particle distribution but a large effect on the momentum equilibrium due to friction. It is assumed that the mixture viscosity accounts for the momentum diffusion $\mu^S = \frac{1}{\mathrm{Re}^M}$, i.e. the lubrication of the particle surface does not break.

The turbulent kinetic energy $0.5\,\overline{\tilde{v}_i^S \tilde{v}_i^S}$ is a measure for the energy stored in the fluctuations of the flow field. It is assumed that the main source of such fluctuations is the active stress at the particle surface. The flow in the vicinity of each particles resembles the flow field of a force dipole (1.3), decaying with $1/r^2$ in three dimensions, where r is the length of the distance vector $r_i = {}_2x_i^* - {}_1x_i^*$. The dipole is situated at ${}_1x_i^*$ and induces a velocity at ${}_2x_i^*$. Using the magnitude of the active force $\mathfrak{A}^c$ as strength of the dipole in (1.3) and introducing the angle κ, defined by $\cos(\kappa) = {}_1e_{ip}\,{}_1\gamma_p r_i$, delivers [217]

$${}_2u_i^{ac} = \frac{\mathfrak{A}^c a Re^M}{8\pi r\left(r^2 + c^K\right)}\left(3\cos^2(\kappa) - 1\right) r_i, \tag{5.109}$$

where ${}_2u_i^{ac}$ is the velocity induced due to the active stress at the point ${}_2x_i^*$. In (5.109) a model parameter c^K is used to flatten the velocity gradient in the closest proximity to the particle surface in order to resemble experimental results of the flow field around an active particle [62]. This modification is especially necessary within a distance of half a particle length around the surface. Hence, $c^K = (a/2)^2$ is chosen. A second particle at ${}_2x_i^*$ is accelerated by the action of the force dipole (5.109). By moving the second particle closer to the first particle at ${}_1x_i^*$ the work per volume

$$K^{ac} = -\frac{\mathfrak{D}}{2}\left(\frac{\mathfrak{A}^c Re^M a}{8\pi\left(r^2 + c^K\right)}\right)^2 \left(3\cos^2\left(\kappa\right) - 1\right)^2 \tag{5.110}$$

is done. In order to find the average of K^{ac}, it is assumed that the average of r is

$$\overline{r} = \left(\frac{V}{N'}\right)^{\frac{1}{3}} = \left(\frac{V^P}{\alpha^S}\right)^{\frac{1}{3}}. \tag{5.111}$$

Furthermore, to obtain the average

$$\overline{\left(3\left(\cos\left(\kappa\right)\right)^2 - 1\right)^2} = 9\overline{\cos^4\left(\kappa\right)} - 6\overline{\cos^2\left(\kappa\right)} + 1 = \frac{11}{8} \tag{5.112}$$

an equal distribution of all particles within the averaging volume is assumed, leading to the averaged kinetic energy

$$\overline{K^{ac}} = -\frac{11\mathfrak{D}}{\left(\overline{r}^2 + c^K\right)^2}\left(\frac{\mathfrak{A}^c Re^M a}{32\pi}\right)^2. \tag{5.113}$$

Similarly, if a particle is positioned close to a solid wall, wall and particle will interact through the fluid. The so called mirror system of a force dipole at a solid wall consists of a superposition of a force dipole, a force quadrupole and a source quadrupole [22, 25]. Subsequently, one obtains the averaged work done by moving a particle closer to the wall

$$\overline{K^W} = -\frac{\mathfrak{D}}{2\left(h^2 + c^K\right)^2}\left(\frac{3\mathfrak{A}^c a Re^M}{64\pi}\right)^2 \left(1 - 3\cos^2\left(\kappa^W\right)\right)^2, \tag{5.114}$$

by using Berke et al. [22] as a basis. The cosine $\cos\left(\kappa^W\right) = n_i^W \overline{e_i^S}$ is defined by the averaged orientation vector $\overline{e_i^S}$ and the normal vector n_i^W of the wall and h is the distance of the particle towards the wall.

The sum of $\overline{K^{ac}}$ and $\overline{K^W}$ is $\overline{K} = \overline{K^{ac}} + \overline{K^W}$ leading to the following Boussinesq ansatz for the translational velocity correlation tensor

$$\mathfrak{D}\alpha^S \overline{\tilde{v}_i^S \tilde{v}_j^S} = \frac{2}{3}\alpha^S \overline{K}\delta_{ij} - \frac{\mathfrak{D}\alpha^S}{\mathrm{Re}^M}\left(\frac{\partial \overline{v_i^S}}{\partial x_j} + \frac{\partial \overline{v_j^S}}{\partial x_i}\right). \tag{5.115}$$

Rotational-translational velocity correlations

The expression

$$\Theta_{ij}^S \frac{\partial \alpha^S \overline{\tilde{\omega}_j^S \tilde{v}_k^S}}{\partial x_k} + \epsilon_{ijk} \alpha^S \Theta_{kl}^S \overline{\tilde{\omega}_j^S \tilde{\omega}_l^S} \tag{5.116}$$

occurs in (5.38). The following model is derived under the assumption, that the first term represents interactions between particles based on the active stress and transfer of rotational kinetic energy into translational kinetic energy due to collisions and vice versa. The latter assumption was made due to the occurrence of both the translational and the rotational particle velocity in the first term. The second term on the other hand only contains fluctuations of the rotational velocity, connected by the Levi-Civita symbol. Hence, it is assumed that it represents transfer of rotational kinetic energy between particles during collisions. Because of the Levi-Civita symbol only the antisymmetric part of the tensor $\Theta_{kl}^S \overline{\tilde{\omega}_j^S \tilde{\omega}_l^S}$ is necessary to model.

Similar to the translational correlations the Boussinesq ansatz is used to model the term $\Theta_{ij}^S \partial \alpha^S \overline{\tilde{\omega}_j^S \tilde{v}_k^S} / \partial x_k$. It should include interactions due to the active stress and transfer of energy between the translational and the rotational velocities. Hence, it is proposed based on the Boussinesq ansatz

$$\Theta_{ij}^S \frac{\partial \alpha^S \overline{\tilde{\omega}_j^S \tilde{v}_k^S}}{\partial x_k} = \frac{2}{3} \alpha^S \overline{W} - \Theta_{ij}^S \frac{\partial}{\partial x_k} \frac{\alpha^S}{\mathrm{Re}^M} \left(\frac{\partial \overline{\omega_j^S}}{\partial x_k} + \frac{\partial \overline{\omega_k^S}}{\partial x_j} \right), \tag{5.117}$$

where $\overline{W} = \overline{W^{ac}} + \overline{W^W}$ represents the interactions between other particles due to the active stress and interactions with a solid wall. The second term in the Boussinesq approximation introduces collision effects by applying the mixture Reynolds number to model diffusion. Both contributions of the parameter $\overline{W}$ are modelled in analogy to $\overline{K^{ac}}$ and $\overline{K^W}$. Following Zöttl and Stark [217] the magnitude of the rotational velocity induced by the particle q to another particle p at a certain distance r is

$$\omega^{ac} = \frac{\mathfrak{A}^c a Re^M}{8\pi \left(r^3 + (c^K)^{\frac{3}{2}} \right)} \cos(\kappa) \sin(\kappa) \left[3 - \frac{\varepsilon^2 - 1}{\varepsilon^2 + 1} \left(6 \cos(\kappa)^2 + 1 \right) \right], \tag{5.118}$$

which is directed perpendicular to the $\boldsymbol{e}_q$-$\boldsymbol{r}$-plane. Subsequently, we obtain for the averaged rotational kinetic energy

$$\overline{W^{ac}} = \frac{\overline{\Theta_{er}^S}}{\left(\overline{r}^3 + (c^K)^{\frac{3}{2}} \right)^2} \left(\frac{\mathfrak{A}^c a Re^M}{32\pi} \right)^2 \left(3 - 4 \frac{\varepsilon^2 - 1}{\varepsilon^2 + 1} \right)^2. \tag{5.119}$$

Here, the moment of inertia Θ_{er}^S is the component of the tensor Θ_{ij}^S related to the perpendicular direction of the $\boldsymbol{e}_q$-$\boldsymbol{r}$-plane. However, due to the averaging process, the information about the parameters of this plane are lost. The moment if inertia is, thus, modelled by taking the average of the elements of the known tensor of inertia Θ_{ij}^S, leading to the averaged moment of inertia $\overline{\Theta_{er}^S}$. The rotational energy obtained by moving a particle closer to the wall is derived from the induced rotational velocity due to the mirror system as given by Berke et al. [22] and the distance from the wall h, leading to

$$\begin{aligned}\overline{W^W} =& \frac{\overline{\Theta_{er}^S}}{2\left(h^3+(c^K)^{\frac{3}{2}}\right)^2}\left(\frac{3\mathfrak{A}^c aRe^M}{64\pi}\right)^2 \times \\ & \times \cos\left(\kappa^W\right)^2 \sin\left(\kappa^W\right)^2 \left[1+\frac{\varepsilon^2-1}{2\left(\varepsilon^2+1\right)}\left(1+\cos\left(\kappa^W\right)^2\right)\right]^2 .\end{aligned} \tag{5.120}$$

As mentioned in the introduction of this section, the second term of (5.116) is meant to represent further collision effects. It should be noted, that due to the Levi-Civita symbol and the antisymmetric nature of the tensor the term will only have an effect in fully three dimensional systems. We propose the ansatz

$$\begin{aligned}\overline{\tilde{\omega}_j^S \Theta_{kl}^S \tilde{\omega}_l^S} =& \frac{1}{2}\epsilon_{jmn}\overline{\frac{\partial \tilde{u}_m^S}{\partial x_n}\Theta_{kl}^S\tilde{\omega}_l^S} = \frac{1}{2}\epsilon_{jmn}\left(\overline{\frac{\partial \tilde{u}_m^S \Theta_{kl}^S \tilde{\omega}_l^S}{\partial x_n}} - \overline{\tilde{u}_j^S \frac{\Theta_{kl}^S \tilde{\omega}_l^S}{\partial x_n}}\right) \\ \approx& \frac{1}{2}\varepsilon_{jmn}\left[\frac{\partial}{\partial x_n}\left(\frac{1}{\mathrm{Re}^M}\left(\frac{\partial \Theta_{kl}^S \overline{\omega_l^S}}{\partial x_m} - \frac{\partial \Theta_{ml}^S \overline{\omega_l^S}}{\partial x_k}\right)\right)\right. \\ & \left. - \frac{1}{2}\varepsilon_{jmn}\frac{1}{\mathrm{Re}^M}\frac{\partial}{\partial x_n}\left(\frac{\partial \Theta_{kl}^S \overline{\omega_l^S}}{\partial x_m} - \frac{\partial \Theta_{ml}^S \overline{\omega_l^S}}{\partial x_k}\right)\right] \\ =& \frac{1}{2}\varepsilon_{jmn}\frac{\partial\left(\mathrm{Re}^M\right)^{-1}}{\partial x_n}\left(\frac{\partial \Theta_{kl}^S \overline{\omega_l^S}}{\partial x_m} - \frac{\partial \Theta_{ml}^S \overline{\omega_l^S}}{\partial x_k}\right) .\end{aligned} \tag{5.121}$$

In the second last step of (5.121) a modified version of the Boussinesq approximation was used

$$\overline{\tilde{\mathfrak{u}}_i^{\mathfrak{P}} \tilde{u}_j^{\mathfrak{P}}} = \mu^S\left(\frac{\partial \mathfrak{u}_i^{\mathfrak{P}}}{\partial x_j} - \frac{\partial \mathfrak{u}_j^{\mathfrak{P}}}{\partial x_i}\right), \quad \mu^S = \frac{1}{\mathrm{Re}^M} \tag{5.122}$$

which will be called antisymmetric Boussinesq approximation.

Orientation-velocity correlations

In the transport equation for the averaged particle orientation additional fluctuation terms

$$\frac{\partial \alpha^S \overline{\tilde{e}_i^S \tilde{v}_j^S}}{\partial x_j} - \epsilon_{ijk}\alpha^S \overline{\tilde{\omega}_j \tilde{e}_k} \tag{5.123}$$

occur. The first term is a correlation between the fluctuations of the orientation vector and the fluctuations of the translational velocity. Accordingly, it is straightforward to assume, that it represents the influence of the translational velocity on the orientation due to collisions and the active stress. In the second term the rotational velocity occurs, hence, it represents the interactions between the rotational velocity and the orientation during collisions.

In analogy to the velocity correlations the Boussinesq approximation is used to model the translational velocity-orientation correlation

$$\overline{\tilde{e}_i^S \tilde{v}_j^S} = \frac{2}{3}\alpha^S K^E \delta_{ij} - \frac{1}{\mathrm{Re}^M}\left(\frac{\partial \overline{e_i^S}}{\partial x_j} + \frac{\partial \overline{e_j^S}}{\partial x_i}\right). \tag{5.124}$$

The first term accounts for interactions due to the active stress and the second term represent collisions between particles. It is a viscous term modelled with the mixture Reynolds number Re^M, i.e. in this model collisions enforce realignment of particles. The diagonal part K^E is modelled by introducing the quantity

$$e_{ip} u_i^{ac} = \frac{\mathfrak{A}^c a Re^M}{8\pi r\left(r^2 + c^K\right)}\left(3\left(\cos\left(\kappa\right)\right)^2 - 1\right) r_i e_{ip}, \tag{5.125}$$

representing the influence of the active fluid velocity, i.e. the velocity induced by a force dipole (5.109), on the orientation. It vanishes during the averaging process in the domain far away from the wall, because $\overline{\left(3\left(\cos\left(\kappa\right)\right)^2 - 1\right) r_i e_{ip}} = 0$, where it is necessary to neglect fluctuations and to assume an equal distribution of the particles within the averaging volume. In the near wall region the averaged orientation-velocity correlation becomes

$$\overline{K^E} = \overline{e_i^S u_i^W} = \frac{3\mathfrak{A}^c a Re^M}{64\pi\left(h^2 + c^K\right)}\left(3\left(\cos\left(\kappa^W\right)\right)^2 - 1\right)\cos\left(\kappa^W\right), \tag{5.126}$$

which completes the Boussinesq approximation (5.124).

The rotational velocity-orientation correlation in (5.123) is modelled by the antisymmetric Boussineq ansatz, introduced in the previous section Sec. 5.3.4. Because of the occurrence of the Levi-Civita symbol in (5.123) only the non-diagonal, antisymmetric elements of the tensor are relevant, leading to

$$\overline{\tilde{\omega}_j \tilde{e}_k} = \frac{1}{2}\varepsilon_{jmn}\frac{\partial}{\partial x_n}\left(\frac{1}{\mathrm{Re}^M}\right)\left(\frac{\partial \overline{e_k^S}}{\partial x_m} - \frac{\partial \overline{e_m^S}}{\partial x_k}\right). \tag{5.127}$$

Similar to (5.121) the antisymmetric correlation (5.127) only occurs in fully three dimensional systems.

Fluid velocity correlation

The transport equation for the averaged fluid velocity contains the correlation of the fluctuations of the fluid velocity $\alpha^F \overline{\tilde{u}_i^F \tilde{u}_j^F}$. It is the well-known Reynolds-stress term from turbulence research, which occurs in the RANS equation due to the ensemble average and in large eddy simulations due to the spatial filtering. Hence, it can be modelled in analogy to turbulent eddy viscosity models by a Boussinesq ansatz

$$\alpha^F \overline{\tilde{u}_i^F \tilde{u}_j^F} = \frac{2}{3}\alpha^F K \delta_{ij} - \alpha^F \mu^t \left(\frac{\partial \overline{u_i^F}}{\partial x_j} + \frac{\partial \overline{u_j^F}}{\partial x_i}\right). \tag{5.128}$$

The diagonal term K of the ansatz is modelled by $-\overline{K^{ac}}$ in analogy to the particle translational velocity. The assumption behind this ansatz is, that fluctuations in a low-Reynolds active suspension mainly originate from the active stress at the fluid-particle interface. The eddy viscosity in turbulence research μ^t represents energy dissipation on small scales. However, due to the condition of a low-Reynolds flow $\mathrm{Re} \ll 1$ and in general small scales, it can be assumed that $\mu^t \ll \mu^F$. Subsequently, it is possible to neglect the eddy viscosity for a model of an low-Reynolds suspension.

5.3.5. Fluid stress tensor

Beside the Reynolds stress tensor discussed in the previous section, the averaged fluid velocity equation also contains the averaged stress tensor $\overline{\tau^F_{ij}}$. Throughout the entire work a Newtonian fluid is assumed, hence, the local stress tensor is

$$\tau^F_{ij} = -p^F \delta_{ij} + \frac{1}{\mathrm{Re}} \left[\frac{\partial u^F_i}{\partial x^*_j} + \frac{\partial u^F_j}{\partial x^*_i} \right] , \tag{5.129}$$

where the derivatives are taken with respect to the local spatial coordinate x^*_i. The first step is to replace the fluid Reynolds number Re by the mixture Reynolds number Re^M to account for the increased resistance against deformation due to the rigid particles. The average of of the stress tensor is

$$\overline{\tau^F_{ij}} = -\overline{p^F} + \frac{1}{\mathrm{Re}^M} \left[\frac{\partial \overline{u^F_i}}{\partial x_j} + \frac{\partial \overline{u^F_j}}{\partial x_i} \right] - \frac{1}{\mathrm{Re}^M} \sum_{p=1}^{N'} \left(\int_{\Gamma_p} u^F_i n^S_j dS + \int_{\Gamma_p} u^F_j n^S_i dS \right) , \tag{5.130}$$

where it is assumed that α^S is constant within the averaging volume V. Thus, the mixture Reynolds number Re^M is not averaged. The integral terms result from the average of the gradient of the velocity, see (5.17). The particles are rigid, hence, the contribution of the integral terms vanish. Subsequently, one obtains for the divergence of the averaged stress tensor

$$\frac{\partial \alpha^F \overline{\tau^F_{ij}}}{\partial x_j} = -\frac{\partial \alpha^F \overline{p^F}}{\partial x_i} + \frac{\partial}{\partial x_j} \frac{\alpha^F}{\mathrm{Re}^M} \left[\frac{\partial \overline{u^F_i}}{\partial x_j} + \frac{\partial \overline{u^F_j}}{\partial x_i} \right] . \tag{5.131}$$

5.3.6. Closed system

In the previous sections closure relations for the entire system of averaged transport equations are derived. The system consists of fifteen equations for fifteen unknown variables in three dimensions. The averaged variables are the volume fractions of both phases α^F, α^S, the fluid pressure $\overline{p^F}$, the fluid velocity $\overline{u^F_i}$, the solid translational velocity $\overline{v^S_i}$, the solid rotational velocity $\overline{\omega^F_i}$ and the solid orientation vector $\overline{e^S_i}$. All equations necessary to solve for the given variables are, including the saturation condition (2.33),

$$
\begin{aligned}
&\frac{\partial \alpha^S}{\partial t} + \frac{\partial \alpha^S \overline{v_i^S}}{\partial x_i} = 0, \quad \frac{\partial \alpha^F}{\partial t} + \frac{\partial \alpha^F \overline{u_i^F}}{\partial x_i} = 0, \quad \alpha^S + \alpha^F = 1, \\
&\frac{\partial \alpha^F \overline{u_i^F}}{\partial t} + \frac{\partial \alpha^F \overline{u_i^F}\,\overline{u_j^F}}{\partial x_j} + \frac{\partial \alpha^F \overline{p^F}}{\partial x_i} - \frac{2}{3}\frac{\partial \alpha^S \overline{K}}{\partial x_i} - \frac{\partial}{\partial x_j}\frac{\alpha^S}{\mathrm{Re}^M}\left[\frac{\partial \overline{u_i^F}}{\partial x_j} + \frac{\partial \overline{u_j^F}}{\partial x_i}\right] - \frac{\langle F_i^F \rangle}{V^P} = 0, \\
&\mathfrak{D}\left[\frac{\partial \alpha^S \overline{v_i^S}}{\partial t} + \frac{\partial \alpha^S \overline{v_i^S}\,\overline{v_j^S}}{\partial x_j} + \frac{2}{3}\frac{\partial \alpha^S \overline{K}}{\partial x_i} - \frac{\partial}{\partial x_j}\left[\frac{\alpha^S}{\mathrm{Re}^M}\left(\frac{\partial \overline{v_i^S}}{\partial x_j} + \frac{\partial \overline{v_j^S}}{\partial x_i}\right)\right]\right] - \frac{\langle F_i^F \rangle}{V^P} = 0, \\
&\Theta_{ij}^S\left[\frac{\partial \alpha^S \overline{\omega_j^S}}{\partial t} + \frac{\partial \alpha^S \overline{\omega_j^S}\,\overline{v_k^S}}{\partial x_k} - \frac{\partial}{\partial x_k}\left[\frac{\alpha^S}{\mathrm{Re}^M}\left(\frac{\partial \overline{\omega_j^S}}{\partial x_k} + \frac{\partial \overline{\omega_k^S}}{\partial x_j}\right)\right]\right] + \frac{2}{3}\alpha^S \overline{W}_{ij} 1_j \\
&\qquad + \alpha^S \epsilon_{ijk}\left[\Theta_{kl}^S \overline{\omega_j^S}\,\overline{\omega_l^S} - \frac{\epsilon_{jmn}}{2}\frac{\partial}{\partial x_n}\left(\frac{1}{\mathrm{Re}^M}\right)\left(\frac{\partial \Theta_{kl}^S \overline{\omega_l^S}}{\partial x_m} - \frac{\partial \Theta_{ml}^S \overline{\omega_l^S}}{\partial x_k}\right)\right] - \frac{\langle T_i \rangle}{V^P} = 0, \\
&\frac{\partial \alpha^S \overline{e_i^S}}{\partial t} + \frac{\partial \alpha^S \overline{e_i^S}\,\overline{v_j^S}}{\partial x_j} - \frac{\partial \alpha^S K^E}{\partial x_i} - \frac{\partial}{\partial x_j}\left[\frac{\alpha^S}{\mathrm{Re}^M}\left(\frac{\partial \overline{e_i^S}}{\partial x_j} + \frac{\partial \overline{e_j^S}}{\partial x_i}\right)\right] \\
&\qquad - \alpha^S \epsilon_{ijk}\left[\overline{\omega_j^S}\,\overline{e_k^S} + \frac{\epsilon_{jlm}}{2}\frac{\partial}{\partial x_m}\left(\frac{1}{\mathrm{Re}^M}\right)\left(\frac{\partial \overline{e_k^S}}{\partial x_l} - \frac{\partial \overline{e_l^S}}{\partial x_k}\right)\right] = 0.
\end{aligned}
\tag{5.132}
$$

5.4. Implementation

Results in this work, see Sec. 6.3, are obtained for steady planar flows. Thus, the model is implemented using MATLAB's (Version 9.2.0.556344, R2017a) built-in one-dimensional partial differential equations solver *pdepe.m*. It employs a finite difference method (FDM) [187] for the spatial discretisation. Another built-in method *ode15s.m* provides the numerical integration in time, based on numerical differentiation formulas up to fifth order [185, 186]. This implementation can be used to obtain stationary results for planar flows, leading to the results given in Sec. 6.3. The MATLAB-scripts related to the publication Deußen et al. [55] are publicly available via TUdatalib [54]. The scripts in [54] form the basis for the scripts used in the present work, which are also publicly available, including the results presented in Sec. 6.3, via TUdatalib [52].

In order to make the numerical procedure more robust and to comply with the limits

$$0 \leq \alpha^S \leq \alpha^S_{\mathrm{max}}, \quad 0 \leq e^S \leq 1 \tag{5.133}$$

additionally auxiliary functions are introduced. Especially for iterative procedures it is necessary to provide additional limitations to prevent overestimations. Furthermore, due to the dependency of the mixture Reynolds number Re^M on the particle volume fraction α^S, the inverse Reynolds number $1/\mathrm{Re}^M$ might become very large. This singularity is a numerically unfavourable behaviour, because it leads to non-converging solutions. Lets assume that the particle volume fraction α^S is a function of an auxiliary variable g^α

$$\alpha^S = \frac{\alpha^S_{\text{max}}}{1 + \exp\left(-g^\alpha\right)}. \tag{5.134}$$

This equation represents a logistic function, which image α^S is restricted to the interval $\left(0, \alpha^S_{\text{max}}\right)$. Introducing (5.134) into the transport equation for the mass of the solid phase (5.28) delivers

$$\frac{\partial g^\alpha}{\partial t} + \overline{v^S_i}\frac{\partial g^\alpha}{\partial x_i} + \left(\exp\left(g^\alpha\right) + 1\right)\frac{\partial \overline{v^S_i}}{\partial x_i} = 0. \tag{5.135}$$

Solving the new transport equation for g^α instead of the unmodified mass balance delivers a numerically stable procedure to determine the solution of the system (5.132).

Analogously, a logistic function is introduced for the length e^S of the orientation vector $\overline{e^S_i}$

$$e^S = \frac{1}{1 + \exp\left(-g^e\right)}, \tag{5.136}$$

restricting e^S to the interval $(0, 1)$. However, no equation is known which directly describes the behaviour of e^S. Forming the dot product of $\overline{e^S_i}$ and the transport equation for the orientation (5.39) delivers such an equation

$$\begin{aligned}
\frac{\alpha^S}{2}\left(\frac{\partial e^S}{\partial t} + \frac{\partial e^S\overline{v^S_i}}{\partial x_i}\right) &= \overline{e^S_i}\frac{\partial}{\partial x_i}\frac{\alpha^S\mathfrak{A}^c a Re^M}{96\pi\lambda^2} - \overline{e^S_i}\frac{\partial}{\partial x_j}\left[\alpha^S\mu^E\left(\frac{\partial\overline{e^S_i}}{\partial x_j} + \frac{\partial\overline{e^S_j}}{\partial x_i}\right)\right] \\
&- \alpha^S\overline{e^S_i}\epsilon_{ijk}\frac{\epsilon_{jlm}}{2}\frac{\partial}{\partial x_m}\frac{1}{\mathrm{Re}^M}\left(\frac{\partial\overline{e^S_k}}{\partial x_l} - \frac{\partial\overline{e^S_l}}{\partial x_k}\right) = 0.
\end{aligned} \tag{5.137}$$

The solution of (5.137) is then used to rescale the solution provided by (5.39) for the individual components of the orientation vector.

6. Results

Results for the particle-resolved model and for the homogenised model are presented in this section. Starting with a single-particle setup solved with BoSSS, basic properties of active particles are investigated and discussed (Sec. 6.1). With the help of the single particle simulation, it can be shown how individual particles interact with a solid wall and how pusher and puller particles differ in this respect. Furthermore, the correctness of the approximation of the active particle by a Stokes dipole is shown by using a line-out plot. In the course of the section, the complexity of the system is continuously increased. In the next step, a system with two particles in a domain with periodic boundaries is examined (Sec. 6.2.1). Special attention is paid to the mutual attraction or repulsion of the particles, which is predicted by the velocity equation of the Stokes dipole and was already used in the modelling process of the homogenised model, see Sec. 5.3.4.

Based on these simple systems, suspensions with multiple particles can be analysed. For this purpose, nine particles are first investigated in a channel domain in Sec. 6.2.2. The differences between pusher and puller particles will be discussed again, where the focus is on the stability of the trajectory followed. This investigation will lead to the conclusion that pusher particles have a significantly more unstable behaviour than puller particles. Since the main focus of this work is on the examination of chaotic systems, the following numerical experiments will only be carried out with pusher particles. Real suspensions with many particles are investigated in the last section on particle-resolved systems (Sec. 6.2.3). A large number of particles are introduced into a domain closed with walls, whereby the number of particles and, thus, the particle density is varied between different experiments. Due to the high number of particles, it is possible to determine statistical values such as the PDF. Therefore, the theoretical findings from Sec. 3 can be used to directly link the occurring phenomena with the physical and statistical equations. Limitations in the available computing power force a switch to the homogenised model presented in Sec. 5 for even larger systems. Results for various planar flows are examined in Sec. 6.3. It is found that in the presence of velocity gradients of the background flow, additional forces occur that amplify known effects such as wall attraction. Furthermore, it can be observed that different aggregate states of the solid phase occur, a finding that also results from the analysis of the statistical Lie symmetries.

6.1. Single particle simulation

In this simple setup a single active particle is placed in the centre of a closed domain Ω. As the name implies, all outer boundaries $\partial\Omega$ of the domain are impermeable, no-slip walls. The particle is of elliptical shape; its length is $a = 1$ and the aspect ratio is $\varepsilon = 2.5$. The dimensionless active stress at the active boundary Γ^{ac} is $A_c = 10$. This particle is used throughout

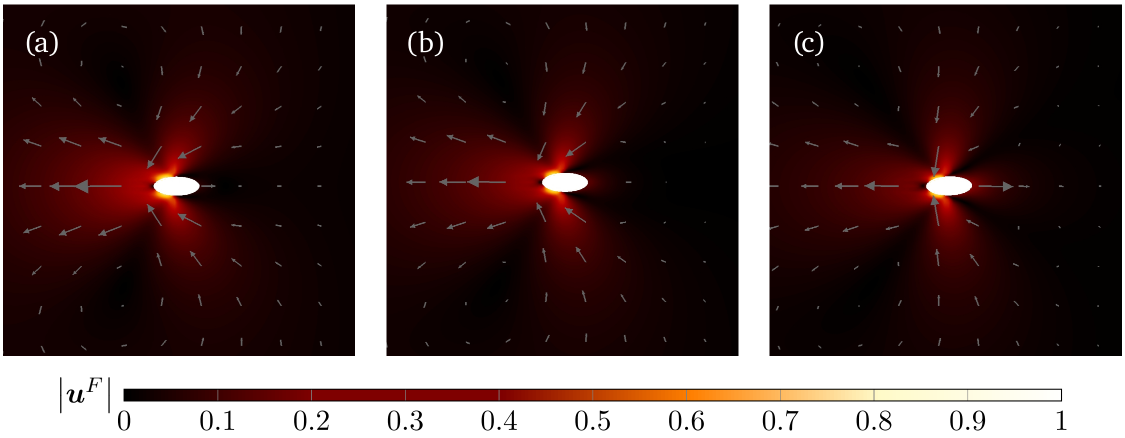

Fig. 6.1.: The flow field in the vicinity of a particle changes during the acceleration phase. The vectors indicate the fluid flow and the colour scale the absolute value of the fluid velocity. A slow moving particle accelerates (a) by pushing fluid in the opposing direction. (b) Due to the movement of the particle, the fluid in front of the particle also starts to move together with the particle. This slows down the acceleration. (c) The particle has reached its cruising speed. The flow field now resembles the flow field of a force dipole, see Fig. 1.2.

multiple numerical experiments, which are presented in the current and following sections. Hence, it will be referred to as *standard particle*. The domain is a square with the edge length $a_\Omega = 19.6$, subdivided into $38,416$ square numerical cells, where the cell diameter is $h = 0.1$. Again, this domain is used throughout multiple numerical experiments and will be referred to as *standard domain*. The polynomial order for the velocity is set to two, subsequently, the polynomial order for the pressure is one. This leads to a maximum number of $576,240$ DoFs for the fluid solver. This number is, however, reduced by the presence of the particles, because cells fully occupied by the particles are considered void.

In Fig. 6.1 the acceleration phase of a single pusher particle is shown, where the colour scale refers to the speed of the fluid, i.e. the absolute value of the velocity, and the vectors indicate the velocity field. This combination of colour and vectors is used throughout all figures in this section. The particle is orientated in the right direction, hence, the active surface is located at the left half of the particle surface. At the beginning of the simulation the particle velocity is zero, hence, the fluid is solely accelerated in the left direction by the active stress. Once the particle starts moving, fluid material is accelerated in the right direction together with the particle due to the no-slip boundary condition at the passive half of the surface (Fig 6.1a+b). The flow field of the particle resembles that of a two-dimensional Stokes dipole (Fig 1.2) once the particle has reached its terminal velocity (Fig 6.1c). A line-out plot of the fluid velocity during the terminal phase is shown in Fig. 6.2. The plots are taken at the right and left side of the particle as well as at the upper and lower side, which will be referred to by compass directions. The characteristic behaviour of a Stokes dipole, which decays with $1/r$ in two dimensions, is especially visible in the Northern and Southern direction. In a large area, both plots decay with an exponent $m = 1$ similar to the Stokes dipole. The behaviour is only different close to the particle surface $r/a \to 0$ and close to the domain wall $r/a \to 10$. The latter one is caused by the no-slip and impermeable wall, which causes the velocity to decay

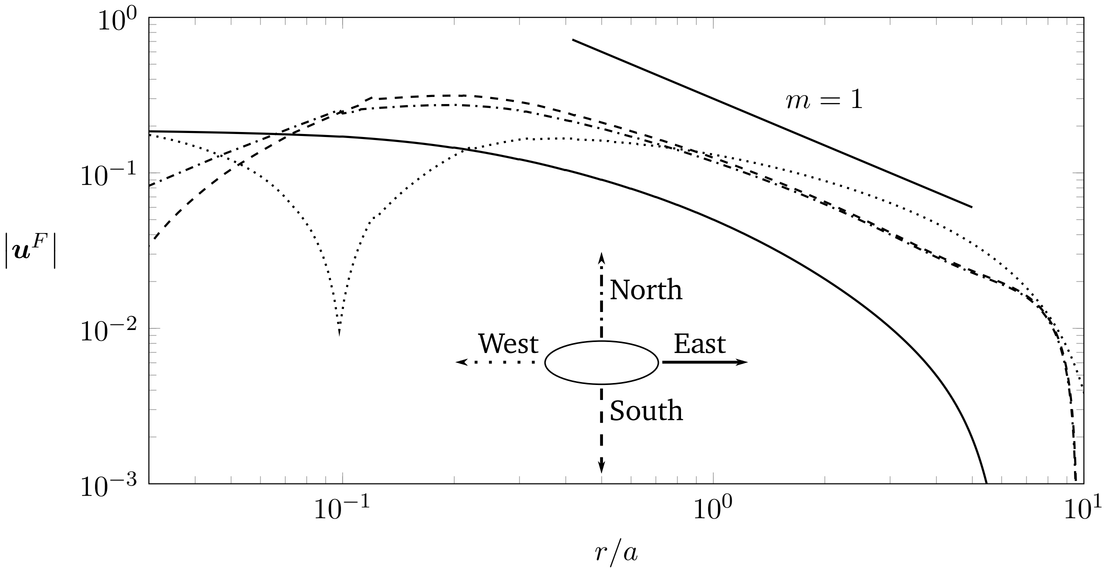

Fig. 6.2.: The velocity of the fluid is plotted into four directions starting at the surface of a single particle. The direction of the plots are given using compass directions.

faster. Close to the particle surface, the approximation of a Stokes dipole is no longer valid, which is known throughout the literature, see for example Bechinger et al. [18]. A stagnation point is visible at the Northern and Southern direction, directly at the particle surface, which is indicated by a decrease in the velocity in Fig. 6.2. It is caused by the connection between the active and the passive surface, where the active surface accelerates the fluid in one direction and the passive no-slip boundary condition accelerates the fluid in the opposing direction, which is the direction of the particle velocity.

The Western plot shows a singularity at $r/a \approx 0.1$, which is caused by the active boundary condition. At the Northern and Southern surface of the particle the fluid is accelerated in the Western direction alongside the particle surface. Due to the curvature of the surface, the two flows at the Northern and Southern side have an opposing direction at the westernmost point of the particle, leading to a stagnation point. On both sides, the Western and the Eastern one, the decay of the velocity is overall smaller and subsequently increased in the wall region compared to the Northern and Southern side. Note that the particle was initialised at the centre of the domain and has since then moved in the Eastern direction. Hence, the distance to the wall for the Eastern line-out plot is shorter than the Western one. Furthermore, the particle has started to slowly rotate, causing the velocity difference in the Northern and Southern direction in the proximity of the particle.

The cause of the rotation of the particle, i.e. its unstable orientation, is a small perturbation, e.g. a numerical error. Pusher particles in general are sensitive towards even very small perturbations, a fact which will be examined further in Sec. 6.2.2. The instability is reinforced by the interactions between the particle and the domain wall. Active particles aligning and being attracted to solid walls is a well known behaviour, see for example Volpe et al. [201] and Zöttl and Stark [217]. In the exemplary image strip Fig. 6.3 the three main phases of the interactions between a active pusher particle and a wall are visible. As described by Volpe et al. [201] the three phases are approach (Fig. 6.3a-e), contact (Fig. 6.3f) and detachment

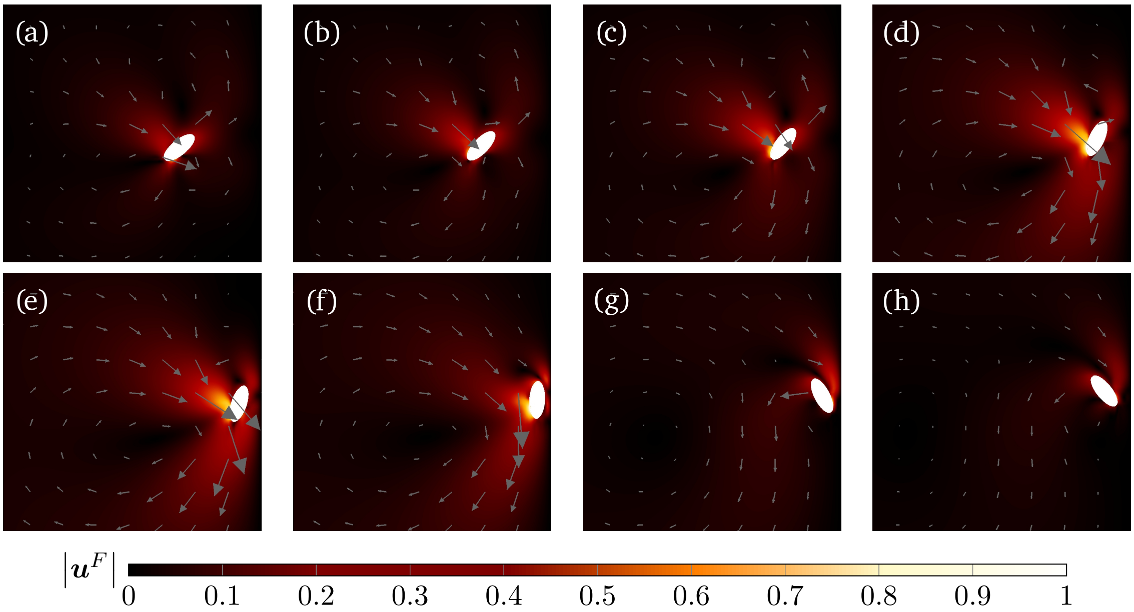

Fig. 6.3.: A single particle approaches a solid wall at the right side of each image. (a) The particle is tilted and moves in the upper right direction. (a)-(e) Due to the wall the fluid flow towards the particle at the side facing the wall is cut off. Hence, due to the remaining flow on the other particle side, the particle moves towards the wall. (f) The particle has aligned towards the wall, moving even closer will lead to a collision between particle and wall. (g)-(h) A collision has taken place and the particle slowly leaves the wall.

(Fig. 6.3g+h). During the process, the particle orientation first aligns parallel to the wall. During the detachment, the particle rotates further and detaches from the wall, i.e. one could say that the particle is reflected at the wall, in analogy to the behaviour of waves. The active stress causes the particle not only to move in the direction of its orientation, but also in the normal direction of the wall, where hydrodynamic interactions between wall and particle cause the particle to be attracted towards the wall. Subsequently, even after the detachment of the particle from the wall, the particle will, over time, realign and again approach the wall starting the process depicted in Fig. 6.3 anew. The attraction towards the wall can be explained by a so called mirror system. The idea is to replace the wall by flow singularities similar to the Stokes dipole, which represents the particle. In order to fulfil the no-slip boundary condition, it is necessary to introduce a Stokes dipole, a force quadrupole and a source quadrupole as a mirror system [25]. Berke et al. [22] derives the velocity induced on the particle in the wall-normal direction, which has been used in the present work to determine the translational velocity correlations of the homogenised model, see (5.114). If the angle κ^W between the particle orientation vector and the wall normal vector is $\kappa^W > \arccos\left(1/\sqrt{3}\right)$, the particle is attracted towards the wall, otherwise it is repulsed [22]. Hence, a particle moving in an already tilted manner towards the wall, as given in Fig. 6.3, will, most likely, move constantly alongside the wall, repeating the three phases approach, contact and detachment if no additional perturbations exist [18].

A puller particle can be obtained by reversing the orientation vector and changing the sign

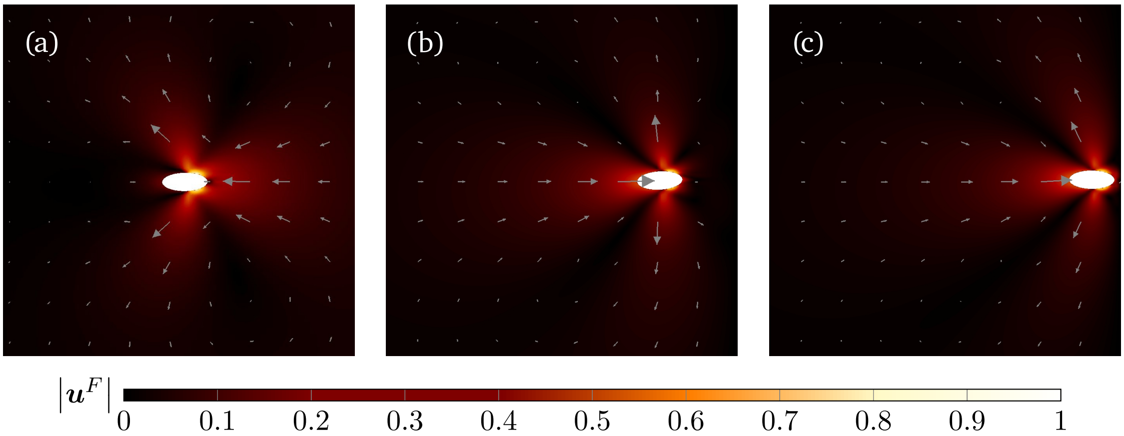

Fig. 6.4.: The fluid flow around a puller particle (see Fig. 1.2), which swims into the right direction, is reversed compared to flow in the vicinity of a pusher particle (Fig. 6.1). (a) Fluid is moved primarily in the left direction during the acceleration phase of the pusher particle. (b) The particle approaches the domain wall at the right boundary of the image. Note, that the flow field closely resembles the ideal flow field of a Stokes dipole, however, the fluid flow on the Eastern side of the particle is suppressed due to the wall. (c) The particle approaches the wall in the horizontal direction. The small angle visible in (b) vanished.

of the active stress. The resulting flow field (Fig. 6.4) is reversed compared to the pusher particle, i.e. fluid is accelerated towards the particle in the Western and Eastern direction and accelerated away from the particle in the Northern and Southern direction. During the acceleration phase (Fig.6.4a) the particle velocity is small, hence, the flow field differs from the ideal Stokes dipole. Once the acceleration is finished (Fig.6.4b), the flow field more closely resembles the singularity. While perturbations still lead to changes in the orientation of the particle (Fig.6.4b), the interaction with the vertical wall at the right side of the image causes the particle to realign with the horizontal axis. The parallel alignment of the particle orientation vector and the wall normal vector holds even after the particle has reached the wall (Fig.6.4c), i.e. the particle is trapped at the wall. The alignment towards the normal vector of the wall is again a well observed property of puller particles, see for example Bechinger et al. [18] and Lauga and Powers [130].

6.2. Multi particle simulations

While the behaviour of a single particle is certainly interesting, the main focus of this work is the behaviour of a suspension, i.e. a multi-particle system and the emergence of chaotic and deterministic states. The increased sample-size enables the usage of statistical quantities and, subsequently, the possibility to apply the results of the probability theory and Lie-symmetry analysis to the numerical results. First, in Sec. 6.2.1 interactions between two particles are investigated. From this, fundamental properties of active particles can be derived, which then explain the behaviour of larger systems. The differences between pusher and puller particles are further examined in a series of numerical experiments in a periodic channel. The length

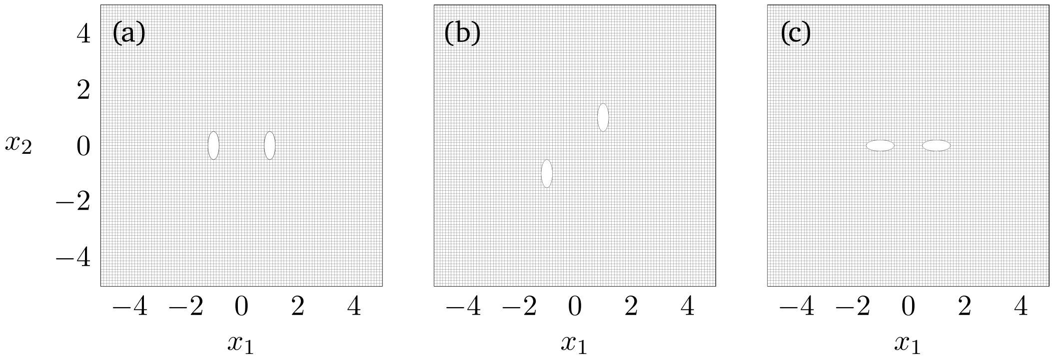

Fig. 6.5.: Initially, two particles are placed close to the centre of the periodic domain. The diameter of the numerical cells is $h = 0.1$ and the particles are *standard particles*. (a) Two parallel particles with a horizontal distance of two. (b) Two parallel but opposing particles with a horizontal and vertical distance of two. (c) Two opposing particles with a horizontal distance of two.

of the averaged orientation vector (Sec. 5.2.4) is used to indicate chaotic and deterministic behaviour. In a third series of numerical experiments the complexity of the system is further increased. While the channel experiments only contain nine particles, now suspensions with up to 480 particles are examined. The domain is fully closed, hence, it is possible to observe

- wall agglomeration effects,
- bulk agglomeration effects,
- orientational alignment.

The particle volume fraction of the suspensions is varied by changing the number of particles within the domain, while keeping the size of the domain constant. The effects are first described qualitatively by analysing snapshots of the simulations at certain time-steps. In a second step, the analysis is carried out quantitatively by using different statistical measures.

6.2.1. Two particle interactions

In this section, numerical experiments with two *standard particles* in a periodic 10×10 domain with $h = 0.1$ are discussed. In the first experiment two pusher particles are initially placed close to the centre of the domain, see Fig 6.5a. The distance for each particle from the centre is unity, i.e. one particle length. Subsequently, the centres of mass for both particles are separated by a distance of $r = 2$. Both particles are initially orientated in the vertical direction. The active part of the surface is facing downwards and the orientation vector is facing upwards. The results for this experiment are presented in Fig. 6.6. Relatively quickly, the particles begin to move towards each other and deviate from their original trajectories. The orientation vector of each particle points more strongly in the direction of the other particle (Fig. 6.6b). As soon as the particles are close, they again begin to move in an approximately parallel direction, while still attracting each other (Fig. 6.6c). This behaviour is well-known in the literature, see for example Bechinger et al. [18] and Berke et al. [22]. It is a property which can be directly deduced from the velocity field around a Stokes dipole (1.5). In the case of the two particles

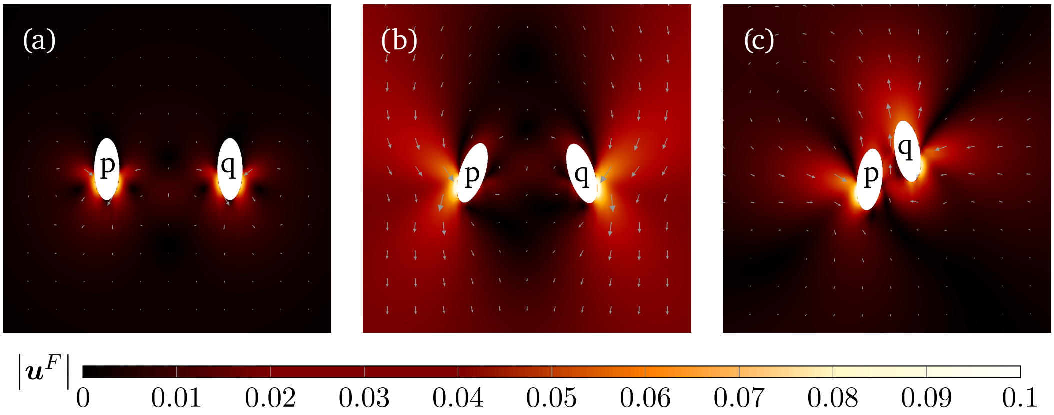

Fig. 6.6.: Two particles are placed in a periodic domain. (a) Initially, the particles are placed parallel towards each other with a horizontal distance of two particle lengths between the centre of mass. (b) The particles reorientate towards another at $t = 4.3$. (c) At $t = 12.3$ the particles are positioned closely and start to realign in a parallel direction.

in the experiment, the distance vector r_i between the particles and the orientation vectors are approximately perpendicular to each other due to the initial arrangement. It follows from (1.5) that each particle induces a velocity in the opposite direction of r_i. Hence, both particles are attracted towards each other. This circumstance was used, for example, in this work to model the velocity correlations in the homogenised model, see (5.113).

In the next experiment, both particles are placed in an opposing direction on parallel trajectories. The vertical and horizontal distance between the centre of mass is equal to two particle lengths, see Fig. 6.5b. In the first time-steps of the simulation, both particles move undisturbed from their opponent on their initial path (Fig. 6.7a). The particle p is orientated upwards, i.e. the active stress accelerates the surrounding fluid in the downward direction. The right particle q on the other hand, moves downwards, hence, the active stress acts upwards. Once the particles reach a similar vertical position, they start to reorientate towards another (Fig.6.7b), similar to the previous experiment. However, because of the opposing movement, the attraction due to the active stress is not strong enough to cause direct contact between the two particles. Instead, it induces a moment and, subsequently, a rotational velocity, which causes the particles to leave their initial path. Once a particle has left the near field of its opponent, it will follow the new trajectory undisturbed. The rotational velocity, induced by the moment, will decline over time. Nevertheless, the particle trajectory is not a straight line. However, the problem is symmetric, hence, both particle will always have an approximately parallel orientation. For example, at $t = 12.4$ (Fig. 6.7c) the orientation angle towards the horizontal axis of the lower particle q is $\beta_q = 1.17\pi$ and the orientation angle of the upper particle p is $\beta_p = 0.16\pi$. The deviation from an actual parallel alignment of the particles is therefore only 0.01π.

In case of two directly opposing particles, see Fig. 6.8, the two pusher particles try to evade another. The left particle p is orientated towards the right side, whereas its opponent q faces left. Both particles are initialised on the horizontal axis with a distance from the centre of the domain of $r = 1$, i.e. the particles are separated by two particle lengths (Fig. 6.5c). Instead

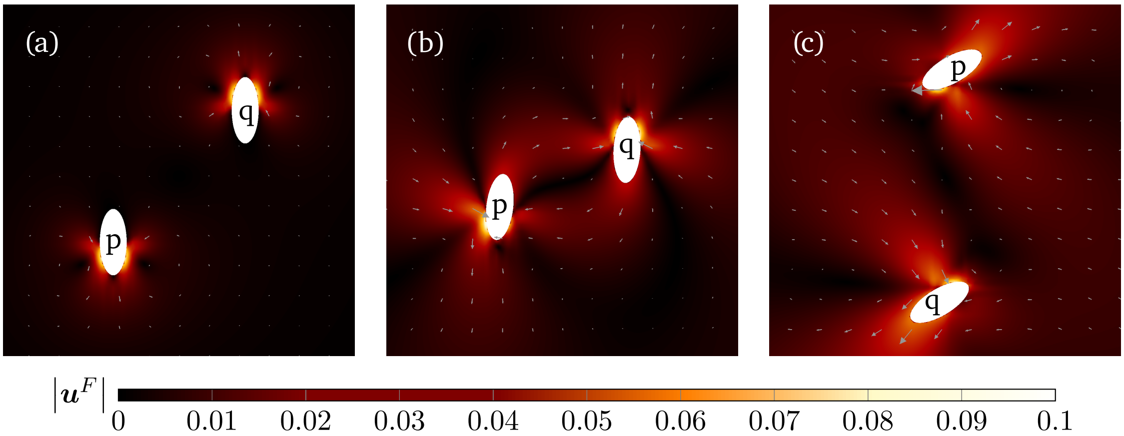

Fig. 6.7.: Two particles are placed in a periodic domain. (a) Initially, the particles are placed parallel towards each other with a horizontal and vertical distance of two particle lengths between the centre of mass. (b) The particles start interacting with another at $t = 4.3$. (c) At $t = 12.3$ the particles have left their initial vertical trajectory. The new path of both particles is still parallel.

of rotating towards the other particle and thus facing in the direction of the other particle, which was the case in the experiments investigating parallel particles (Fig. 6.6, Fig. 6.7), the particle orientation vector starts pointing away from the opposing particle (Fig. 6.8b). However, as both particles continuously move forward, at some point they are aligned parallel, while still having opposing directions. Accordingly, the interaction from now on follows a similar scheme as in the second experiment (Fig. 6.7) and the particles will follow parallel trajectories in opposing directions. The absolute value of the orientation angle towards the horizontal axis of both particles is approximately equal to $45°$, where the angle of the upper particle is $\beta_p = 0.26\pi$ and the orientation angle for the lower particle is $\beta_q = 1.28\pi$. The deviation towards a perfect parallel alignment is again small and takes a value of 0.02π. The evading behaviour of the particles is again a result of the Stokes dipole nature of an active pusher particle. The distance vector r_i and the orientation vector of each of the particles are initially parallel, hence, the resulting velocity induced by one particle on the other is in the positive distance vector direction, see (1.5). Accordingly, both particles try to push away the opposing particle. The own active stress of the particles acts against this push-back and combined with the inherent instability of a pusher particle, as investigated in the single-particle simulations and in the following Sec. 6.2.2, this leads to the evasion visible in Fig. 6.8b+c. Once the particles are no longer aligned towards the horizontal axis, a moment and, subsequently, a rotational velocity is induced by the respective opponent.

So far, the initial axes of orientation of both particles have been parallel in all three presented experiments. The next two-particle experiment will show, that this is not a necessary property in order to obtain parallel movement after the interaction. In Fig. 6.9 the results are presented. The left particle p is initially placed with a vertical and horizontal distance of two towards the right particle q. Furthermore the orientation angle towards the horizontal axis is $\beta_p = \pi/4$. The second particle faces in the downward direction $\beta_q = -\pi/2$. The initial setup is preserved until the two particles are close to each other, see Fig. 6.9. The left particle p induces a negative rotational velocity on the right particle q, leading to a rotation to the left lower corner.

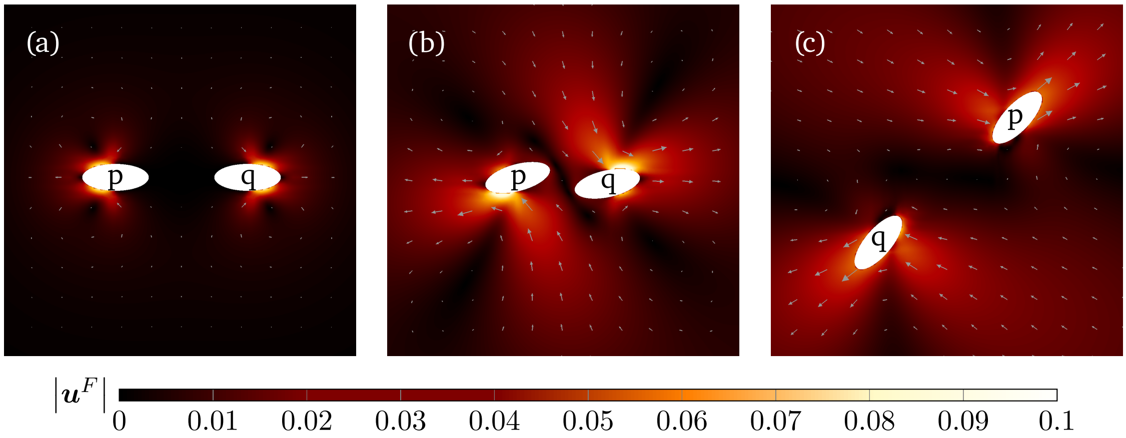

Fig. 6.8.: Two particles are placed in a periodic domain. (a) Initially, the particles are placed opposing towards each other with a horizontal distance of two particle lengths between the centre of mass. (b) The particles try to evade each other at $t = 4.3$. (c) Both particles move on approximatly parallel trajectories in the opposing direction at $t = 12.4$.

The induced velocity on the first particle p, however, is minimal, because it is located in the blind spot of the particle q. By blind spot the area is meant, where the outward pointing and inward pointing flow of the Stokes dipole come into contact and, subsequently, the induced velocity vanishes, see Fig. 1.2. Thus, the orientation angle towards the horizontal axis of the particle p remains $\beta_p = \pi/4$ and the orientation angle of the second particle q becomes $\beta_q = 1.21\pi$, see Fig. 6.9c. Additionally, the two particles are relatively close to the boundary and already interact with another over the periodic boundary, leading to the asymmetrical flow field visible in Fig. 6.9c. Independently of the initial setup, two particles show a clear tendency of aligning their trajectories parallel to each other. While this behaviour might be disturbed by the presence of solid walls or additional particles, it is expected to observe alignment towards other particles also in multi-particle experiments.

6.2.2. Particles in a channel

The initial setup for all numerical experiments in this section is presented in Fig. 6.10. Nine particles are placed in the left half of the domain, orientated towards the right side. Depending on the experiment, the particles might be either pusher or puller particles and have different geometrical properties. Depicted in Fig. 6.10 are nine *standard particles*. The upper and lower domain boundaries are solid walls, whereas the right and left side are periodic boundaries. The length of the channel is 19.6 and the height is 3.92, i.e. the length of the channel is the same as the length of the *standard domain* and the height to length ratio is five. The cell diameter is again $h = 0.1$, leading to $2,952$ cells and a maximum of $44,280$ DoFs. Both numbers are reduced by the number of cells occupied by the particles.

The series starts with an experiment containing nine pusher *standard particles* as depicted in Fig. 6.10. The progression of the simulation is shown in Fig. 6.11. During the initial acceleration phase (Fig. 6.11a) the fluid flow opposes the motion of the particles. While the particles

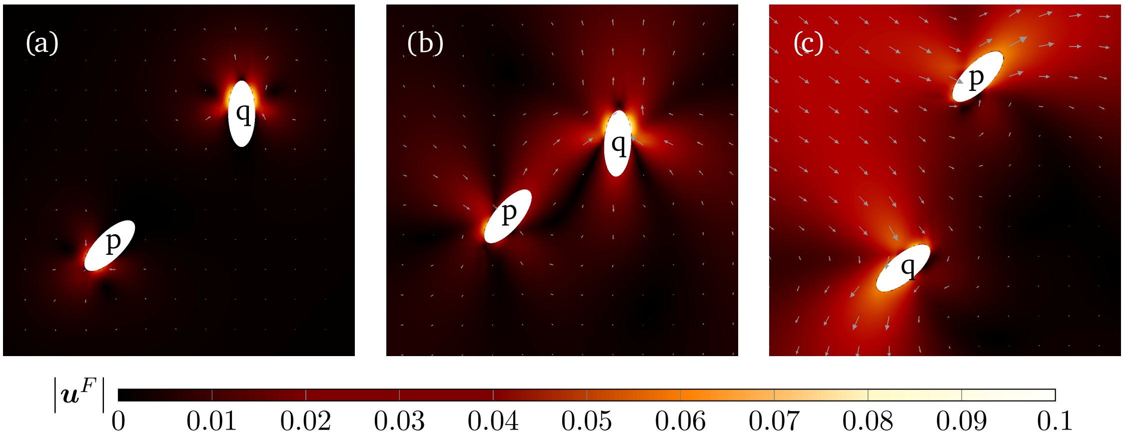

Fig. 6.9.: Two particles are placed in a periodic domain. (a) Initially, one particle is tilted with an angle of $\beta_p = \pi/4$, whereas the other particle faces downwards $\beta_q = -\pi/2$. (b) The particles keep their orientation at $t = 4.3$. (c) At $t = 12.3$ the particles move on approximately parallel trajectories in opposing directions.

move approximately parallel in the right direction, the fluid is accelerated to the left. The ordered initial state will eventually break down (Fig. 6.11b+c) and the particles will accumulate at the channel walls. Note, that the fluid flow is now reversed, i.e. the particles accelerate each other indirectly via the fluid. However, due to the unordered, chaotic state of the particles, regions with vertical or reversed fluid flow might appear, leading to an overall slower acceleration of the particles compared to the initial parallel motion.

Puller particles on the other hand show a much more stable behaviour. Nine puller *standard particles* are placed in the domain as shown in Fig. 6.10. Compared to the pusher particles, the puller particles are able to better hold the parallel formation, see Fig. 6.12. A direct results from the parallel orientation is an increased averaged particle velocity compared to the system with pusher particles.

The differences between pusher and puller particles can be quantified by analysing their averaged orientation and velocity. The averaged quantities are obtained in each time-step by calculating the mean value of all nine particles, similar to the procedure of obtaining the homogenised model (Sec. 5). The results for the absolute value of the averaged orientation vector and velocity are presented in Fig. 6.13. The behaviour, which is visible in the already discussed snapshots of the simulations, is clearly expressed in the diagrams. The averaged length of the orientation vector decreases over time for the pusher particles, indicating the chaotic orientation visible in Fig. 6.11. Maxima, as they appear in the diagram at $t = 35$, are the product of random equal orientation. In this case, several particles move simultaneously and parallel to the upper wall (Fig. 6.11b). Despite such local peaks, e^S trends downwards in case of pusher particle until a steady state of $e^S \approx 0.5$ is reached. The overall orientation of the puller particles on the other hand is almost constant, hence, $e^S \approx 1$. The differences in the orientation result in a significantly different averaged velocity. Due to the parallel motion of the puller particles, almost no collisions occur and the particles are able to accelerate much more efficiently than the pusher particles. Ergo, the acceleration phase lasts longer and the averaged terminal velocity of the puller particles $\left|\overline{\boldsymbol{u}^{S,Pl}}\right| \approx 0.32$ is higher than the terminal

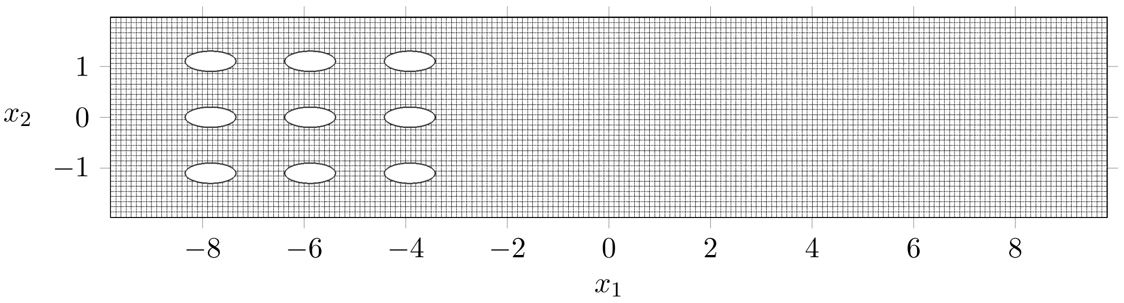

Fig. 6.10.: The initial particle position in the first time-step. Nine standard particles are placed in the left half of the domain, which is five times longer than high. Upper and lower boundary are solid walls, whereas a periodic boundary is used at the left and right side. All particles are orientated towards the right side of the resulting channel, leading to an initial motion in the right direction. This setup holds for both, pusher and puller particle simulations.

velocity of the pusher particles $\left|\overline{\boldsymbol{u}^{S,Ps}}\right| \approx 0.17$ (Fig. 6.13b). In fact, the ratio between the orientation of the pusher and the puller particle is approximately equal to the ratio of the velocities. Hence, one concludes a linear relationship between the two quantities orientation and velocity. Such a linear relationship can easily computed by setting $F_i^A = F_i^D$ and neglecting all other interaction forces, where F_i^A is the active force and F_i^D the drag force acting on the particle. One obtains from (2.94) and (5.68)

$$F_i^A = F_i^D \Rightarrow \mathfrak{A}^c e_{ip}\gamma_p = \frac{\pi a c^D_{\text{corr}}}{\text{Re}^P}\left(\frac{1}{\sqrt{\Phi_\perp}} + \frac{2}{\sqrt{\Phi_\|}}\right) w_i^S. \tag{6.1}$$

Assuming $\Phi_\perp = \text{const.}$ delivers a linear relationship between the orientation vector $e_i = e_{ip}\gamma_p$ and the relative velocity w_i^S. Note that, in general the cross sectional sphericity $\Phi_\perp$ is not a constant but itself a function of the relative velocity w_i^S and the orientation. Nevertheless, in the given example, it seems to play a minor role for the terminal velocity.

It should be noted that the attraction of the pusher particles towards the wall is not caused by their elliptical shape. The shape of the particles might reinforce certain behaviour patterns, however, the attraction itself is solely due to the pusher property. In the next experiment the *standard particles* are replaced by disk-shaped pusher particles to show the shape independency of the attraction. The volume of the particle is kept constant in order to not change the particle volume fraction α^S. Subsequently, the diameter of the disk is $a = \sqrt{0.4}$. Furthermore, to account for the decreased particle surface, the dimensionless active stress is increased to $A^c = 11.85$. All other parameters are kept constant compared to the previous simulations. A snapshot of the simulation at $t = 93.4$ is shown in Fig. 6.14a. Similar to the previous experiment with pusher particles the disk-shaped pusher particles tend to move towards the wall. Due to the different shape, however, their movement is slower despite the increased active stress.

Going into the opposing direction, i.e. increasing the aspect ratio of the particles, leads to similar results. In Fig. 6.14b, a snapshot for a simulation with elongated pusher particles is shown. The particles have a length of $a = 1.414$ and an aspect ratio of $\varepsilon = 5$, i.e. the particle volume fraction α^S is kept constant compared to the previous experiments. The active stress is

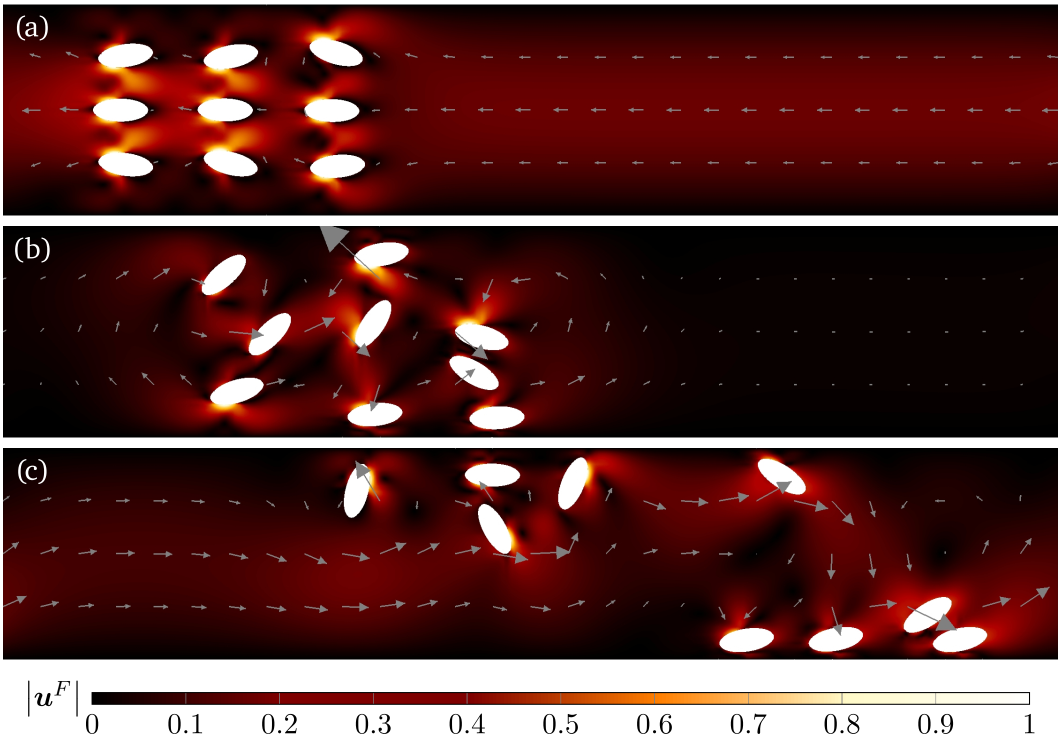

Fig. 6.11.: During the progression of the simulation the initial, ordered state is replaced by a more chaotic state in case of pusher particles. (a) At $t = 10$ the particle setup is almost the same as it was at $t = 0$. (b) After a longer time-span ($t = 35$) the particles lost their parallel alignment and orientate themselves towards the wall. (c) The particles stay at the wall at $t = 70$. The particle orientation is mostly random, there is no longer a preferred direction.

decreased to $A^c = 7.75$ to account for the increased particle surface. The snapshot was taken at $t = 50$; the velocity of the particle has significantly increased compared to the previous simulations. Most importantly, the particle again are attracted towards the wall. The particles show an tendency to align parallel to the wall, a phenomenon which was not visible that clearly in the simulation of the *standard particles* in the channel, however, has been deduced from the single particle behaviour, see Fig. 6.3.

In the channel experiments, it became apparent that pusher particles show an overall more unstable behaviour than puller particles. While pullers keep themselves on a stable trajectory in the middle of the channel, pusher particles are attracted towards the wall and do not necessarily keep a parallel alignment. Such a behaviour is well-known in the literature, see for example Alonso-Matilla et al. [5]. To generate chaotic systems in the following section only pusher particles are employed.

6.2.3. Many particles in a closed domain

In this section, the behaviour of many *standard particles* in the *standard domain* is examined, where the data base is publicly available via TUdatalib [53]. The main parameter is the particle

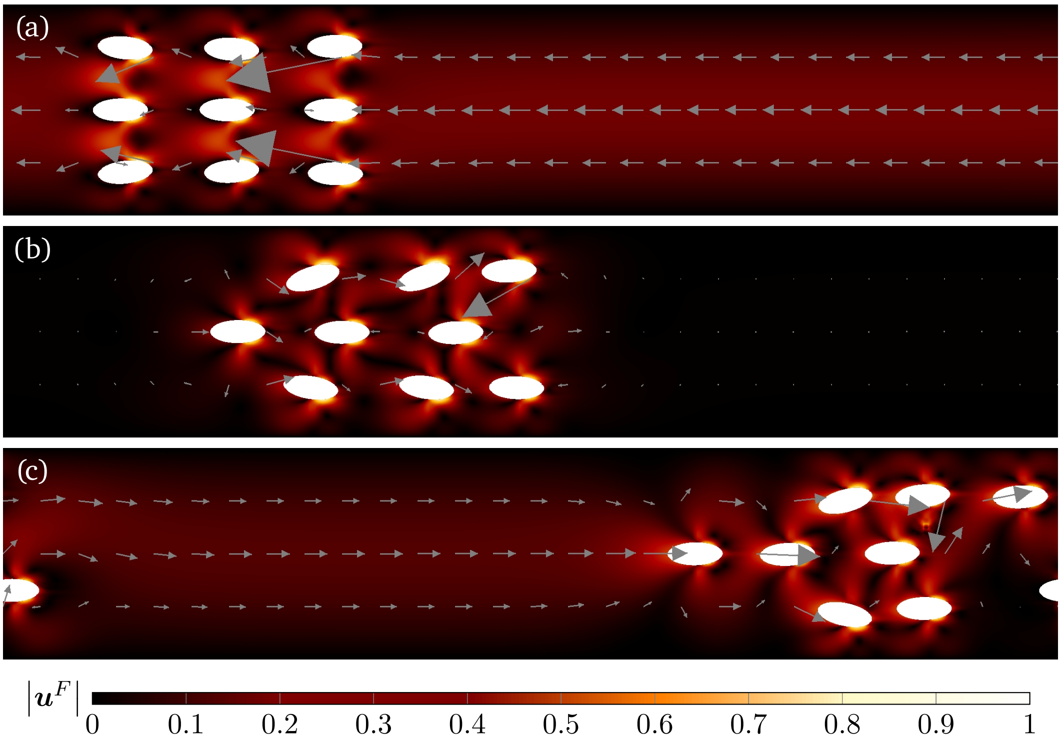

Fig. 6.12.: During the progression of the simulation with puller particles the initial, parallel state is preserved over the entire simulation time. (a) At $t = 10$ the particle setup is almost the same as it was at $t = 0$. Due to the initially strong acceleration of the particles in the right direction, the fluid velocity vector faces the left side. (b) After a longer time-span ($t = 35$) the particles mostly kept their parallel orientation. The bulk fluid flow almost vanished and will in the following time-steps reverse into the right direction. (c) The particles stay in the centre of the channel at $t = 70$. The preferred direction to the right side is kept and the overall fluid flow follows the particle motion. Note that one particle has already reached the periodic boundary and reappears at the left side of the domain.

volume fraction α^S, i.e. the density of the suspension. In Fig. 6.16 and Fig. 6.17, multiple examples of the numerical experiment with different α^S are shown. The Reynolds number for all setups is of the order $\mathcal{O}\left(10^{-1}\right)$. The initial orientation of all particles is horizontal, facing either to the right or the left side, see Fig. 6.15. The distance between the horizontal axes, which contain the particles, is varied to generate suspensions with different volume fractions α^S. The systems examined here were already analysed with respect to their run-time behaviour in Sec. 4.7.3.

The particles in a dilute suspension $\alpha^S = 0.04$ (Fig. 6.16a) swim almost undisturbed, similar to a single particle experiment. However, if multiple particles reach a wall, the rotation mechanism to leave the wall, as described in section 6.1, is prohibited by neighbouring particles. Subsequently, multiple particles form a stable cluster at the wall, which in the example Fig. 6.16a is located at the lower boundary. The location of the cluster at the wall is a product of chance, i.e. there is no mechanism such as gravity enforcing the particles to accumulate at the lower wall. Increasing the volume fraction to $\alpha^S = 0.11$ (Fig. 6.16b) preserves the clus-

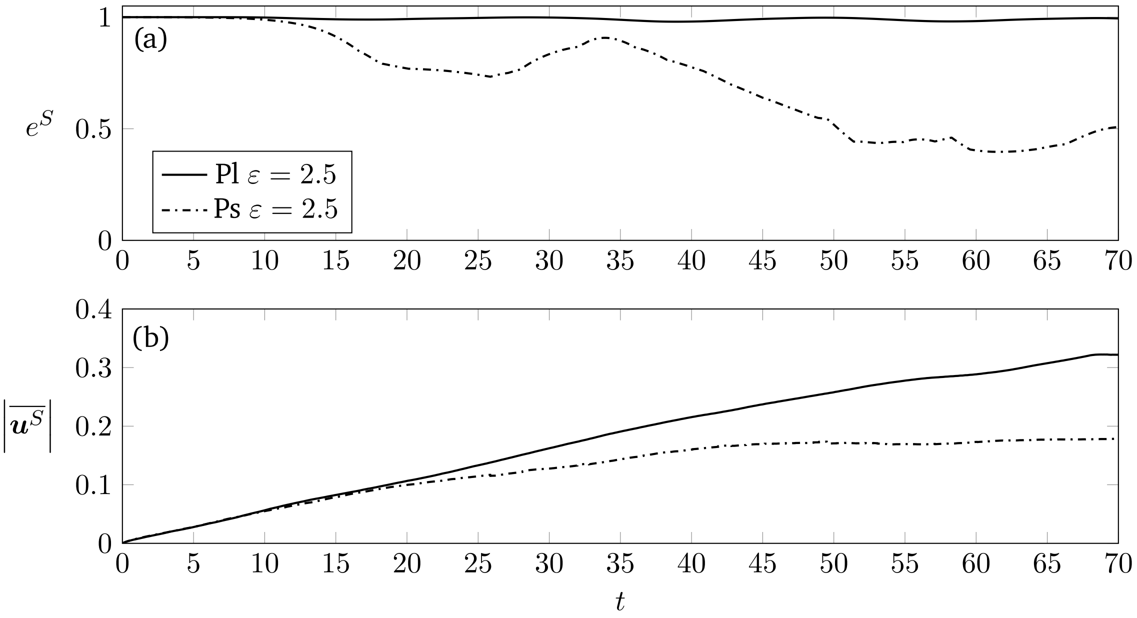

Fig. 6.13.: The diagrams show results for the averaged length of the orientation vector (a) and the absolute value of the averaged particle velocity (b) for different channel experiments. Puller particles are indicated by Pl, pusher particles by Ps.

ters at the lower boundary. Additionally, the particles in the bulk region also form clusters, leading to some regions of the domain with no particles and other regions with a high particle density. Compared to the structures emerging at the domain wall, the bulk-clusters are less densely packed and also less stable. Similar to the attraction of active particles towards the wall, which was investigated in the previous sections (Sec. 6.1- Sec. 6.2.2), active particles are attracted towards each other, permitting the formation of clusters. The particle-particle attraction has been used to find a model for the translational velocity correlation of the homogenised model, see Sec. 5.3.4. The clustering effect is reinforced by a further increase of the volume fraction to $\alpha^S = 0.17$ (Fig. 6.17a). Apart from the pure density increase due to the formation of local clusters, particles show a tendency to align towards the orientation of their neighbours. This alignment strengthens with a further increase of the volume fraction to $\alpha^S = 0.39$ (Fig. 6.17b). Because of the high particle density, the structure resembles crystalline lattices. Similar to crystals, small voids form in the lattice, which in the case of the present suspension continue to ensure that the particles can move in a constrained manner.

Mean squared displacement

In this section, the previous qualitative statements are quantified. This requires the introduction of the mean square displacement (MSD), which is defined as follows

$$\mathfrak{L}\left(\Delta t\right) = \left\langle \left|\boldsymbol{\chi}_p\left(t + \Delta t\right) - \boldsymbol{\chi}_p\left(t\right)\right|^2 \right\rangle, \tag{6.2}$$

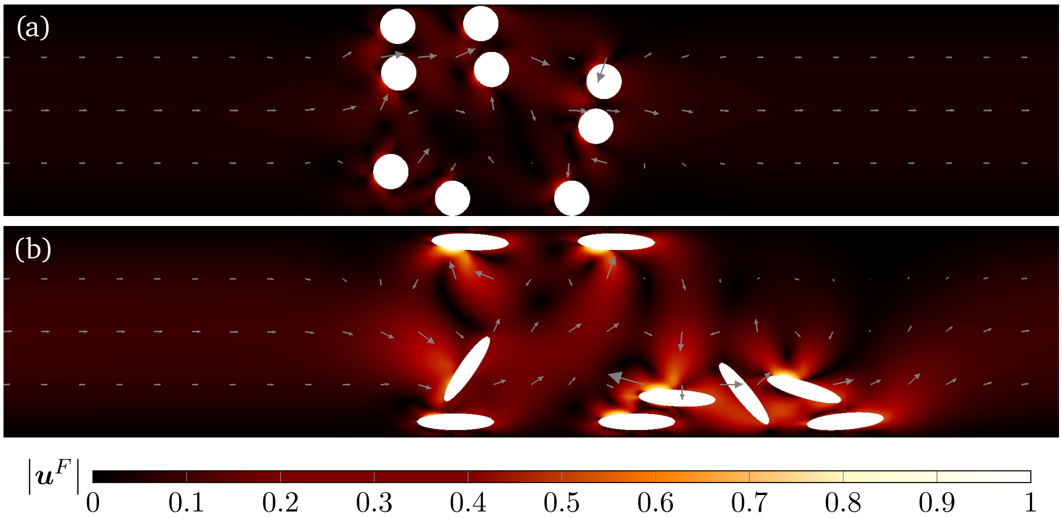

Fig. 6.14.: (a) Disk-shaped pusher particles moving in a channel. Their movement is overall slower comparded to elongated particles, however, they are also attracted towards the channel walls. (b) Elongated pusher particles with $\varepsilon = 5$ align parallel towards the wall.

where the average $\langle\cdot\rangle$ is taken over all particles and the time. For a passive Brownian particle a simple relation between the MSD and the time interval Δt exists

$$\mathfrak{L}(\Delta t) = 2dD\Delta t, \tag{6.3}$$

where d is the number of spatial dimension and D is the diffusion coefficient [67, 188]. Processes described by (6.3) are often referred to as normal diffusion, implying that anomalous diffusion exists. In fact, normal diffusion is only a special case, a more general formulation of (6.3) is obtained by adding an exponent κ [152]

$$\mathfrak{L}(\Delta t) = D_\kappa \Delta t^\kappa, \tag{6.4}$$

where D_κ is the generalized diffusion coefficient and $\kappa = 1$ leads to (6.3). In principle, κ can take any positive value, leading to the three diffusive regimes visualized in Fig. 6.18a. Subdiffusion $0 < \kappa < 1$ occurs, for example, during molecular transport in cells and is caused by molecular crowding [14, 203]. The transport due to diffusion is slowed down compared to normal diffusion. The superdiffusive regime $1 < \kappa < 2$ describes an accelerated diffusive process, caused for example by an active stress. As we will see in the following results, ballistic diffusion $\kappa = 2$ occurs in the limiting case of a dilute active suspension. Superballistic diffusion might occur in the transport of waves in photonic lattices, see for example Anderson [7] and Hufnagel et al. [105], it is not visible in an active suspension.

The theoretical MSD for an active particle is known and given by [18, 78, 103, 147] in two dimensions

$$\mathfrak{L}(\Delta t) = \left(4D + 2\left(v^p\right)^2 \Delta t_R\right) \Delta t + 2\left(v^p\right)^2 \Delta t_R^2 \left(e^{-\frac{\Delta t}{\tau^R}} - 1\right), \tag{6.5}$$

where v^p is the particle speed and

$$\tau^R = \frac{\pi \mu^F a^3}{k_B T} \tag{6.6}$$

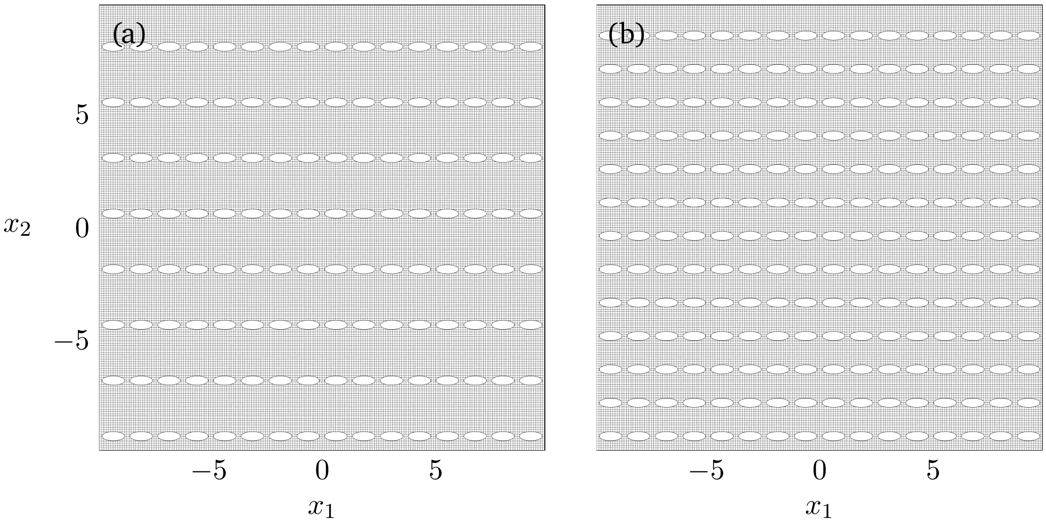

Fig. 6.15.: Initially, all particle of the multi-particle simulation are placed in rows. Each particle has the opposing orientation of its neighbour in the same row, i.e. the orientation angle of the first particle is $\beta_1 = 0$, subsequently, the orientation angle of the second particle is $\beta_2 = \pi$. Different particle densities are obtained by changing the distance between the rows. (a) Setup with 128 particles, $\alpha^S = 0.11$. (b) Setup with 208 particles, $\alpha^S = 0.17$.

is a characteristic time-scale for the rotational diffusion of a spherical particle, see Bechinger et al. [18]. The time-scale depends on the fluid viscosity μ^F, the particle diameter a, the Boltzmann constant k_B and the temperature T. For short time scales $\Delta t \ll \tau^R$, (6.5) becomes the normal diffusion relation (6.3). For medium times $\Delta t \approx \tau^R$, the active particles undergo ballistic diffusion and (6.5) becomes $\mathfrak{L}(\Delta t) = 4D\Delta t + 2\,(v^p)^2\,\Delta t^2$. For large time scales $\Delta t \gg \tau^R$, (6.5) again is a linear function of Δt [18].

In Fig. 6.18b the MSDs for five numerical experiments are presented. The time-step size of the simulations is $\Delta t = 10^{-2}$, which is consequently the minimum value on the horizontal axis of the diagram. For short and medium time intervals Δt, a power-law is found in accordance to (6.4). For larger time intervals the assumption of a power law no longer holds. Crowding leads to a decrease of the diffusion exponent κ. To obtain the exponent κ, time intervals up to 1000 time-steps, i.e. $\Delta t = 10$, are taken into account. Clearly, all examined systems lie within the superdiffusive regime (Fig. 6.18c). Due to the accelerated motion of the particles compared to passive Brownian particles this result is expected.

In case of a single particle $\kappa \approx 2$, i.e. ballistic diffusion, is reached for medium time intervals in accordance to (6.5). Particles can still move relatively undisturbed in a dilute suspension, i.e. $\alpha^S = 0.04$. Hence, the decrease of the exponent κ is small compared to the single particle simulation, see Fig. 6.18. The results for a single particle and the dilute suspension are in good agreement with the theoretical MSD for active particles (6.5), where Bechinger et al. [18] distinguished three different regimes, one for small, one for medium and one for large time scales. In the short time regime normal diffusion is observed in experiments [215], however, only if the strength of the propulsion mechanism is small [18]. In the presented numerical experiments this regime is not visible, because the magnitude of the active stress

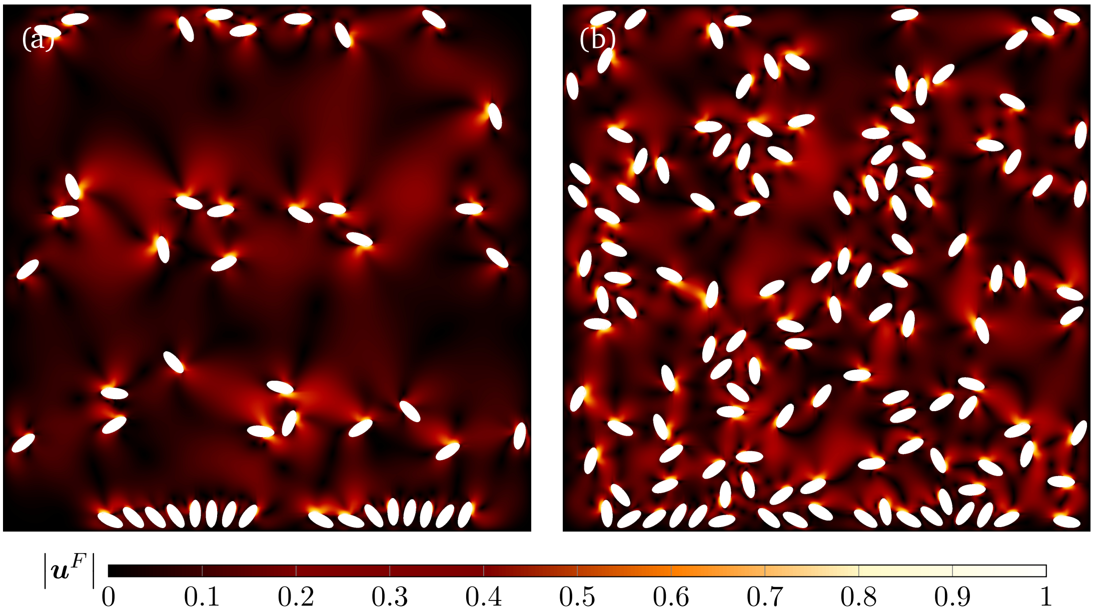

Fig. 6.16.: The particle volume fraction α^S is an important parameter for the behaviour of the suspension. The particles in both images are identical with $a = 1$ and $\varepsilon = 2.5$. (a) Some particles accumulate at the walls of the domain in a dilute suspension with $\alpha^S = 0.04$. Particles in the bulk swim almost undisturbed from other particles. (b) The volume fraction is increased to $\alpha^S = 0.11$. Distinct accumulations at the wall are still visible. Additionally, particles form structures within the domain.

is comparably large and the short time regime is, subsequently, expected to be only visible on time intervals smaller than the time-step of the simulation. In the medium time scale regime, theory predicts an exponent $\kappa = 2$, which is obtained for both, the single particle experiment and the dilute suspension. Furthermore it is visible in Fig.6.18 that κ decays for larger time scales $\Delta t > 10$, which agrees with the theoretical examination (6.5). Note, however, that the normal diffusion regime is not reached, i.e. the exponent is still larger than unity. With increasing particle volume fraction α^S the behaviour of κ changes. It decreases due to the formation of clusters, which restrict the motility of individual particles, as visible in Fig 6.16b. Increasing the volume fraction even higher than the given examples would lead to freezing, i.e. all motion of any individual particle vanishes. In this case only bulk motion, i.e. the collective motion by all particles in the same direction, is possible.

Minimal distance PDF and alignment PDF

In the previous section the formation of clusters has already been mentioned several times. A cluster describes a number of particle close to each other. The particles within a cluster have a tendency to align towards the same direction and move with similar velocities. Clusters can break up and reassemble again and again. The exact behaviour depends on the parameters of the simulation, especially the particle volume fraction. In the following paragraph the formation of clusters is quantified by investigating the minimal distance PDF. All PDFs derived in this work are obtained by using MATLAB-scripts, which are publicly available via TUdatalib

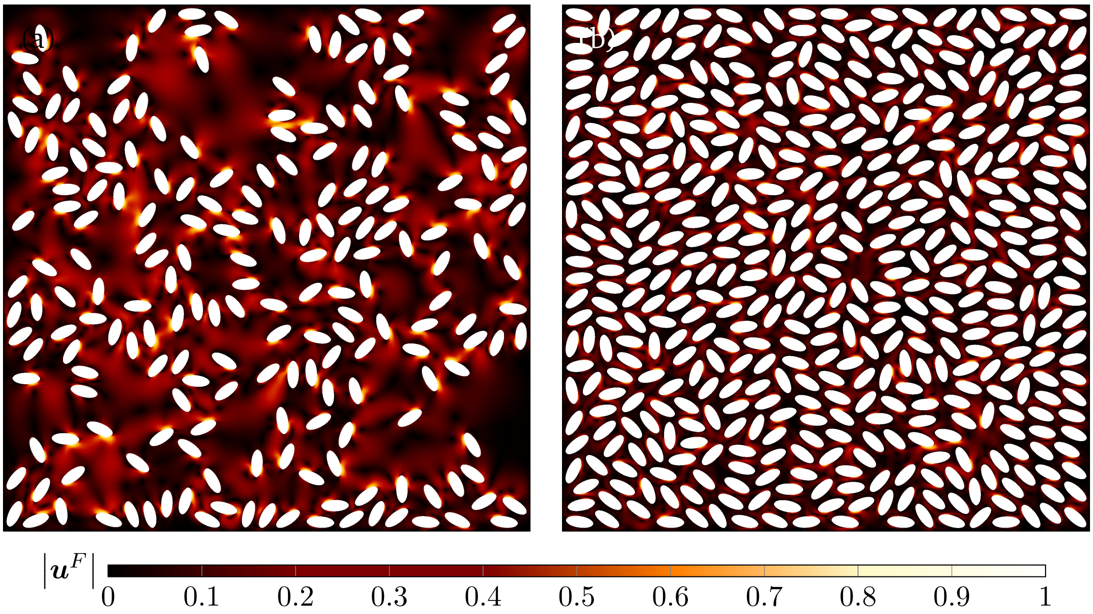

Fig. 6.17.: Suspensions with higher particles densities form clearer structures. (a) The volume fraction is $\alpha^S = 0.17$. Several particle cluster haven been formed. (b) High volume fractions, in this example $\alpha^S = 0.39$, lead to almost crystalline structures.

[53]. The PDF is calculated by finding the position $\boldsymbol{\chi_p}$ of the closest particle p towards a probing particle

$$f^{\mathfrak{r}^{\min}} = \left\langle \delta\left(\mathfrak{r}^{\min} - r^{\min}\right)\right\rangle, \quad r^{\min} = |\boldsymbol{\chi}_p - \boldsymbol{\chi}_1|\,, \tag{6.7}$$

where $\boldsymbol{\chi}_1$ is the position of the probing particle and $\mathfrak{r}^{\min}$ is the sample space variable. Furthermore, lets define the particle near-field, which is bounded by a circle around $\boldsymbol{\chi}_1$ with the radius $a/2 + \lambda$, where λ is the tolerance parameter necessary to numerically distinguish the surfaces of different particles, see Sec. 4.6. As visible in Fig. 6.19 the behaviour of the PDF in the near field area and the far field is substantially different, where the densest suspension $\alpha^S = 0.39$ constitutes a special case as the entire PDF lies within the near field region. The splitting in the near and far field indicates the application of the shape symmetry (3.109), relating two different fractions of the PDF towards each other. In the case of the minimal distance PDF, the shape symmetry is given by

$$f^{\mathfrak{r}^{\min}*} = f^{\mathfrak{r}^{\min}} + \psi\left(\mathfrak{r}^{\min}\right). \tag{6.8}$$

On a side note, it might also be possible to use the general formulation of the intermittency symmetry (3.118), because of the similarity of both symmetry transformation in the general form, see (3.119). Apart from the reduction property (3.110) nothing is known about the free function $\psi\left(\mathfrak{r}^{\min}\right)$. However, it is possible to derive properties from the data presented in Fig. 6.19. Assume that $f^{\mathfrak{r}^{\min}}$ describes the PDF in the far field and $\psi\left(\mathfrak{r}^{\min}\right)$ modifies the PDF to fit to the data in the near field. In the case of the far field PDF $f^{\mathfrak{r}^{\min}}$ it is possible to derive an invariant solution from the intermittency symmetry for the particle position (3.122b) and the constant Galilean symmetry, i.e. a constant spatial shift. This specific symmetries were chosen, because it is apparent from the simulation snapshots that active suspensions form locally dense

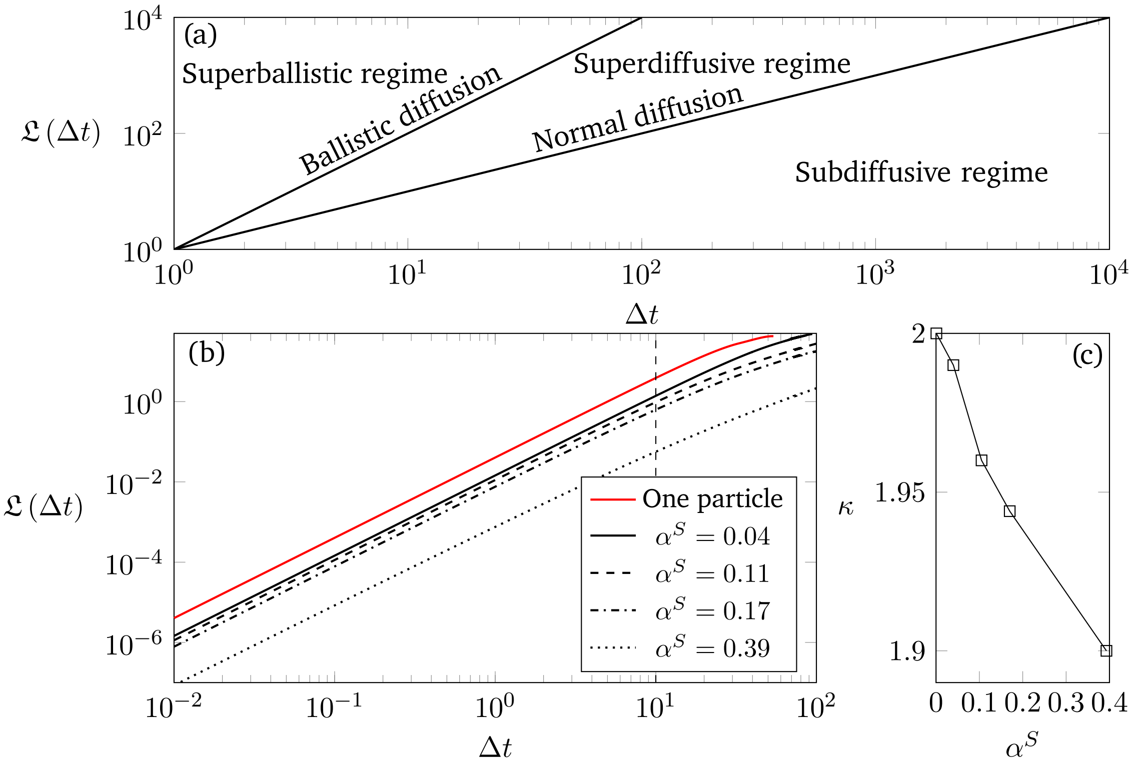

Fig. 6.18.: (a) The three diffusive regimes, the superballistic $2 < \kappa$, the superdiffusive $1 < \kappa < 2$ and the subdiffusive regime $0 < \kappa < 1$, exist. The three regimes are separated by the special cases of ballistic diffusion $\kappa = 2$ and normal diffusion $\kappa = 1$. Illustration based on Palyulin et al. [165]. (b) The Mean Squared Displacement (MSD) for numerical experiments with different α^S. The script necessary to obtain the data is publicly available via TUdatalib [53]. (c) Active particles exist in the superdiffusive regime. The particle volume fraction α^S determines the value of κ, where $\lim\limits_{\alpha^S \to 0} \kappa = 2$.

structures, i.e. show intermittent behaviour. Intermittency here refers to the phenomenon of locally deterministic or ordered behaviour within an overall more chaotic system. Secondly, the spatial shift was chosen, because it fits the intended result, which is a distance. The result of the derivation of the invariant solution, which can be found in appendix A.2.1, is an exponential distribution

$$f^{\mathfrak{r}^{\mathrm{min}}} = C\mathcal{H}\left(\mathfrak{r}^{\mathrm{min}} - a'\right) e^{-C\left(\mathfrak{r}^{\mathrm{min}} - a'\right)}, \tag{6.9}$$

which contains two parameters a' and C to fit the solution to the data. In Fig. 6.19 a fitting for the far field region of the PDF is presented. The parameter C is responsible for the slope in the logarithmic diagram, i.e. the exponent of the PDF. As expected it increases with increasing α^S, because the particles are more densely packed, thus, leading to more deterministic states. The minimal distance PDF for the suspension with $\alpha^S = 0.39$ does not reach the far field, nevertheless, it is still possible to fit the exponential distribution (6.9) to the tail of the PDF. Furthermore, it is straightforward to assume that in the limiting case $\alpha^S \to \alpha^S_{\mathrm{max}}$ the distribution turns into a Dirac impulse at $\mathfrak{r}^{\mathrm{min}} = a'$, turning (6.9) into the intermittency trans-

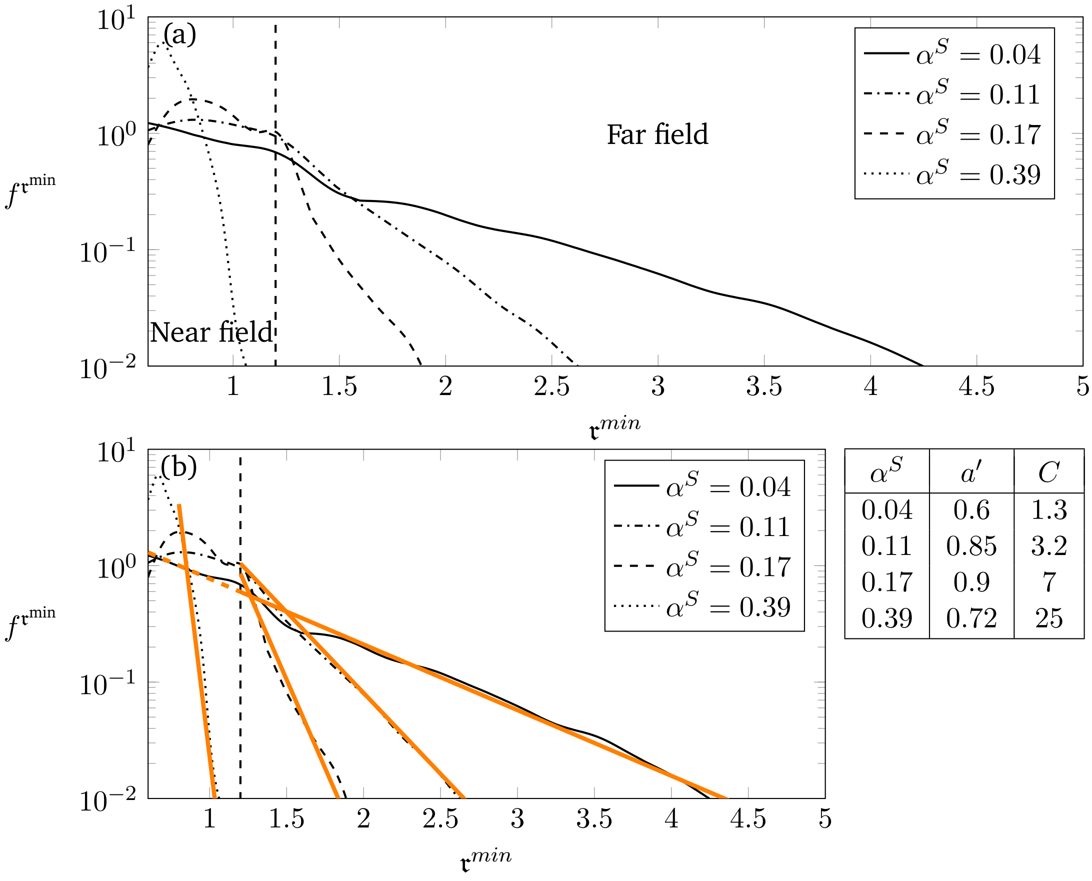

α^S	a'	C
0.04	0.6	1.3
0.11	0.85	3.2
0.17	0.9	7
0.39	0.72	25

Fig. 6.19.: (a) The structure of the minimal distance PDF $f^{\mathfrak{r}^{\min}}$ changes depending on the particle volume fraction α^S. Furthermore, clear differences between the near and the far field are visible. (b) Invariant solutions for the far field region are plotted in orange. The employed coefficients are displayed in the table on the right.

formation (3.122a) with $c_{\text{int}} = 0$. The Dirac distribution can be reached from (6.9) by letting C become infinitely large. At the other end of the density spectrum $\alpha^S = 0.04$, it is possible to fit (6.9) to the entire distribution in the near and far field, indicated by the dashed extension into the near field.

The variance of the exponential distribution (6.9) is defined as $1/C^2$. Subsequently, with increasing particle volume fraction the variance decreases significantly, indicating a more and more deterministic behaviour. For the high density suspension $\alpha^S = 0.39$, it is certain to find the next particle in the near field region, which is enforced by the high density and missing empty space. In a suspension of equally distributed particles, the distance towards the next particle is 0.89, a value which is already within the near field region. The maximum of the PDF is even closer to the minimal possible value at $\mathfrak{r}^{\min} = 0.6$, indicating an additional attraction of the particles towards each other. For the medium density suspensions $\alpha^S = 0.11$ and $\alpha^S = 0.17$, the variance is already significantly decreased compared to the dilute suspension. Again, consider a suspension of equally distributed particles, for the suspension $\alpha^S = 0.11$ this leads to a distance towards the next particle of 1.73 and for the suspension $\alpha^S = 0.17$ to distance of 1.36. Both values are in the far field region, nevertheless, the maximum of the PDF

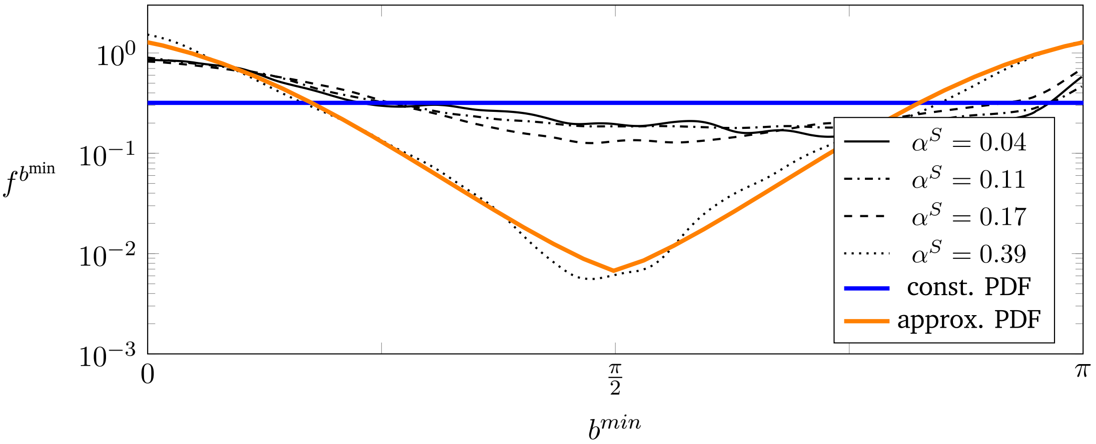

Fig. 6.20.: The alignment PDF $f^{b^{min}}$ is obtained by calculating the relative angle between a probing particle and the particle closest towards the probing particle.

for both suspensions $\mathfrak{r}^{\min}_{0.11} = 0.82$, $\mathfrak{r}^{\min}_{0.17} = 0.81$ lies within the near field region. Clearly, active particles have a tendency to attract each other and form regions with high particle densities.

While the parameter C can be interpreted straightforward as the influence of the particle density on the PDF, the interpretation of a' is a little more complex. In case of the dilute suspension $\alpha^S = 0.04$, $a' = 0.6$ is the minimal distance two particle can achieve due to the smaller particle diameter $b = 0.4$ and the numerical tolerance parameter $h = 0.1$. The latter is applied for each particle, hence, the minimal possible distance for each particle pair is $b' = 0.6$. In the diagram 6.19, b' is the onset for the horizontal axis. The value of a' increases with increasing α^S and seems to be related to the position of the local maximum of the PDF in the near field region. While related to the maximum of the PDF, a' does in general not equal the position of the maximum. For medium densities the maxima lie in the centre of the near field region. In case of the highest density suspension the local maximum is closer to $b' = 0.6$, thus, a' is decreased compared to the previous suspensions. A second PDF is necessary to understand the behaviour of the minimal distance PDF in the near field. Therefore, the alignment PDF $f^{b^{\min}}$ is introduced, which describes the probability distribution of the relative angle $\beta_p - \beta_1$ of the closest particle p towards a probing particle. The data is given in Fig. 6.20. For dilute suspensions, e.g. $\alpha^S = 0.04$, the probability between zero and π is almost equally distributed. Maxima exists at $b^{min} = 0$ and $b^{min} = \pi$, however, the difference towards the rest of the distribution is small. Such an PDF indicates a small preference of the particles to align parallel towards each other, i.e. to obtain a relative angle of $b^{min} = 0$ or $b^{min} = \pi$, nevertheless, enough space is available to allow mostly free rotation of each particle. The free rotation explains the identical behaviour of the minimal distance PDF of the dilute suspension $\alpha^S = 0.04$ in the near and far field. Increasing the particle volume fraction leads to a stronger tendency of the particles for a parallel alignment. The minimum at $b = \pi/2$ and the two maxima become stronger. Parallel aligned particles can be closer towards each other due to the ellipse shape of the particles. Hence, one can observe a larger and distinctive maximum of the minimal distance PDF $f^{\mathfrak{r}^{\min}}$ in the near field region for higher particle densities, which shifts towards the minimal possible distance $b' = 0.6$, see Fig. 6.19.

A constant PDF $f^{b^{min}} = c(\boldsymbol{x}, t) = 1/\pi$ independent of b^{min} for the orientation angle is an invariant solution of the orientation symmetry (3.50f), see appendix A.2.2. It is given by the blue constant in Fig. 6.20. The Lie operator $\mathfrak{X} = \partial/\partial b_p$ is only defined for passive disks, i.e. the active boundary condition and the ellipse-shape break the symmetry. Thus, the constant PDF is a solution for passive disk-shaped particles and can only be considered as a limiting case for an active suspension. Using the shape symmetry

$$f^{b^{\min}*} = f^{b^{\min}} + \psi\left(b^{\min}\right). \tag{6.10}$$

one obtains the PDF $f^{b^{\min}*}$ as a linear combination of the constant PDF $f^{b^{\min}}$ and the shape function $\psi\left(b^{\min}\right)$. Hence, the shape function introduces the dependency on the particle shape and the active stress. For the densest suspension $\alpha^F = 0.39$ the PDF is approximated by the addition of the free function

$$\begin{aligned}\psi\left(b^{min}\right) =& \frac{\exp\left(c_1\left|\cos\left(b^{min}\right)\right|^{c_2} + c_3\left|\frac{\pi}{2} - b^{min}\right|\right)}{c_4} - \frac{1}{\pi}\\ =& \frac{\exp\left(3\left|\cos\left(b^{min}\right)\right|^{1.4} + 1.439\left|\frac{\pi}{2} - b^{min}\right|\right)}{150} - \frac{1}{\pi}\end{aligned} \tag{6.11}$$

to the constant PDF. In Fig. 6.20 the approximate PDF for the highest particle volume fraction $\alpha^S = 0.39$, obtained with the shape symmetry, is given in orange colour. For even higher particle densities it is expected that the particles will align more and more towards each other, which allows the maximum of the minimal distance PDF $f^{\mathfrak{r}^{\min}}$ to shift closer to the minimal possible distance $b' = 0.6$. It is possible to retrieve the limiting case of only parallel aligned particles from (6.11) by letting the exponent c_2 become infinite and choosing the other constants c_1, c_3, c_4 appropriately in order to not violate the reduction property (3.66). The result is a deterministic distribution containing two Dirac impulses at 0 and π. Thus, in the limiting case the intermittency symmetry (3.122c)

$$f^{b*} = c_{\text{int}} f^{b} + (1 - c_{\text{int}})\delta\left(\boldsymbol{b} - \boldsymbol{\beta}\right),$$

where $c_{\text{int}} = 0$, is retrieved.

Clearly, the behaviour of the minimal distance PDF and the alignment PDF are related, leading to the introduction of a joint PDF. Simulation data for the joint PDF, formed with the sample space variable for the minimal distance $\mathfrak{r}^{\min}$ and the relative angle $b^{\min}$, is shown in Fig. 6.21 for the two suspensions $\alpha^S = 0.11$ and $\alpha^S = 0.39$. The joint PDF clearly shows the different behaviour of the particles in the near field $0.6 \leq \mathfrak{r}^{\min} \leq 1.2$ depending on the volume fraction and confirms the previously made observations. In the case of the densest suspension $\alpha^S = 0.39$ the particles most likely are located in the closest proximity of each other. This is only possible if the relative angle is either zero or π, i.e. the particle move either in the same or in the opposing direction. The setup is symmetric, i.e. there is no significant difference between the two maxima in Fig. 6.21b. The more dilute suspension on the other hand, has a much wider range of possible outcomes. Two distinct maxima exist, one at approximately $(0.6, 0)$ and on at approximately $(1.2, \pi)$, see Fig. 6.21a. Thus, two different preferred state exist. The first maximum is related to to configuration, where two particles are placed right next to each other in parallel and facing in the same direction. Such a situation is most commonly found at the domain wall, see Fig. 6.16. The second maxima is related to two particles opposing each other and being located at the westernmost or easternmost point of the opposing particle, similar to the situation shown in Fig. 6.8a. Particle states outside of the maxima regions are relatively likely to happen compared to the denser suspension, which is similarly visible

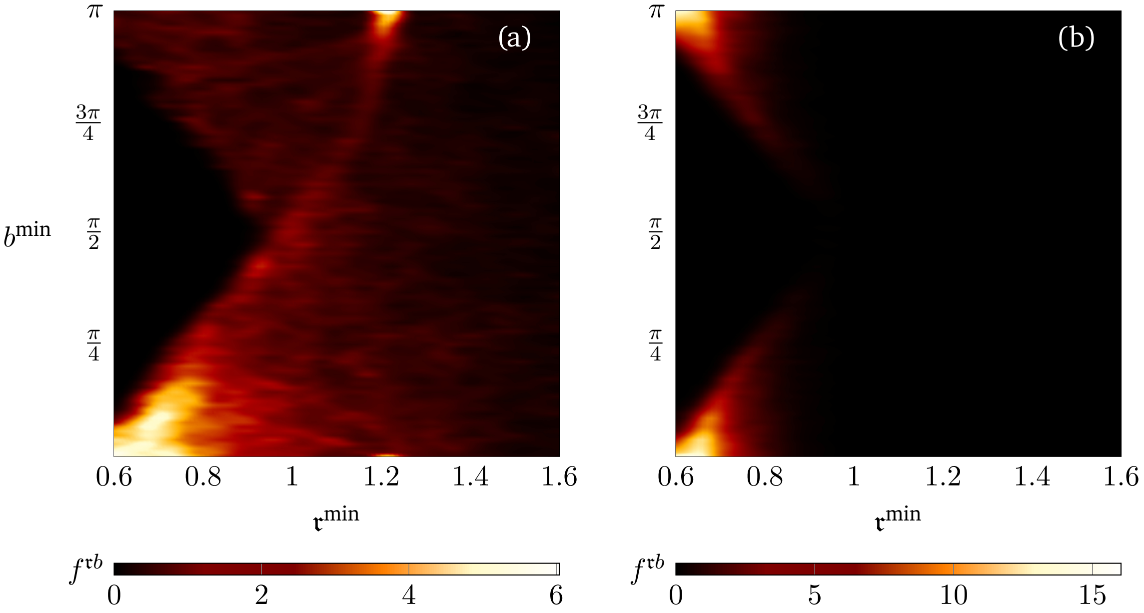

Fig. 6.21.: The joint PDF formed with the minimal distance and the alignment of two particles towards each other reveals the reason for the different behaviour in the near field region. (a) The joint PDF for $\alpha^S = 0.11$ contains two maxima, however, a wide range of states are possible. (b) The joint PDF for $\alpha^S = 0.39$ shows two maxima. All particles align parallel, either in the same direction $b^{\text{min}} = 0$ or in the opposing direction $b^{\text{min}} = \pi$.

in the marginal minimal distance PDF in Fig. 6.19. The joint PDF for all four suspensions can be found in App. A.3. In conclusion, higher particle densities lead to more deterministic probability distributions of the minimal distance and the relative orientation, whereas dilute suspension show a chaotic behaviour with respect to the two variables mentioned before.

Particle velocity PDF

In the minimal distance and relative angle PDFs no clearly chaotic behaviour could be found for dense suspensions. In fact, with increasing particle density the behaviour becomes more and more deterministic. For the dilute suspension $\alpha^S = 0.04$, on the other hand, the alignment PDF shows behaviour which could be interpreted as chaotic, because no preferred direction of alignment exists. The analysis of the particle velocity PDF in the following paragraph will reveal partially deterministic and partially chaotic behaviour. The velocity PDF in its most general form

$$f^V = \langle \delta \left(\boldsymbol{V} - \boldsymbol{U} \right) \rangle \tag{6.12}$$

describes the probability of finding a certain velocity at a specific point in space and time in both phases. In this paragraph, the focus lies on the probability distribution of the particle velocity, hence, the particle velocity PDF is defined

$$f^{V^S} = \left\langle \delta \left(\boldsymbol{V}^S - \boldsymbol{u}^S \right) \right\rangle . \tag{6.13}$$

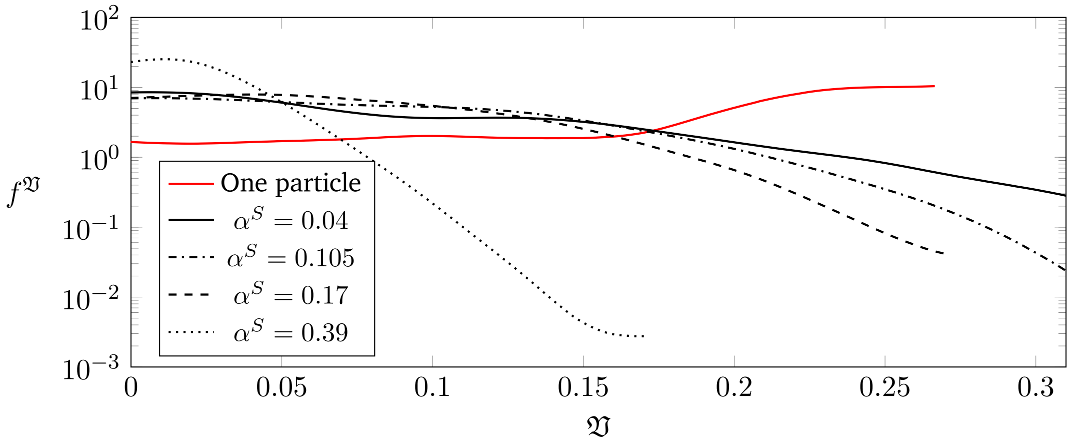

Fig. 6.22.: The diagram shows the probability distribution for the speed, i.e. the absolute value of the velocity, of the particles. Four suspensions and a single-particle experiment are depicted.

The systems under investigation do not contain any preferred direction, due to the symmetric shape of the physical domain. Hence, the velocity components in both directions of the $\mathbb{R}^2$-space form the database. Furthermore, the speed PDF is defined, i.e. the probability distribution of the absolute value of the particle velocity

$$f^{\mathfrak{V}} = \langle \delta \left(\mathfrak{V} - |\boldsymbol{U}| \right) \rangle . \tag{6.14}$$

The speed PDF is depicted in Fig. 6.22 for a single active particle and four different active suspensions. A single particle will reach its terminal velocity after the acceleration phase. Subsequently, the PDF takes the form of an equal distribution for the lower velocities, describing the acceleration phase. The most likely state for such a system is the particle moving with the terminal velocity, hence, one obtains a maximum at the right end of the distribution. This behaviour changes completely once multiple particles are considered. Due to the interactions between the particles, each particle is constantly accelerated and decelerated. Hence, the maximum is shifted towards zero with increasing particle density. In dilute suspensions ($\alpha^S = 0.04$ and $\alpha^S = 0.11$), the maximum speed exceeds that of the single particle. This increase is caused by the interactions and collisions between particles. While some particles might slow down, others might be accelerated further by their neighbours. Furthermore, in the case of the suspension with $\alpha^S = 0.04$ the behaviour of the single particle system is still visible. The PDF forms a plateau around $\mathfrak{V} = 0.1$, reminiscent of the equal distribution of the single particle for smaller speeds. Increasing the particle volume fraction α^S further leads to a decreasing maximum speed and an increased probability of lower speeds, i.e. a maximum of the PDF located close to zero.

The PDF for the velocity components shows, as expected, a similar behaviour to the speed-PDF. The main difference is the maximum for all velocity-PDFs at $V = 0$, which is not visible in the speed-PDF. Components of the velocity vector might become zero while the particle is moving parallel to one of the axes of the coordinate system. Thus, even if the speed of the particle is non-zero, individual components might vanish, leading to the visible maximum at $V = 0$. As mentioned earlier, no preferred direction exists in the fully closed quadratic domain, hence, the velocity PDF is symmetric. Subsequently, it is sufficient to show the PDF of the absolute

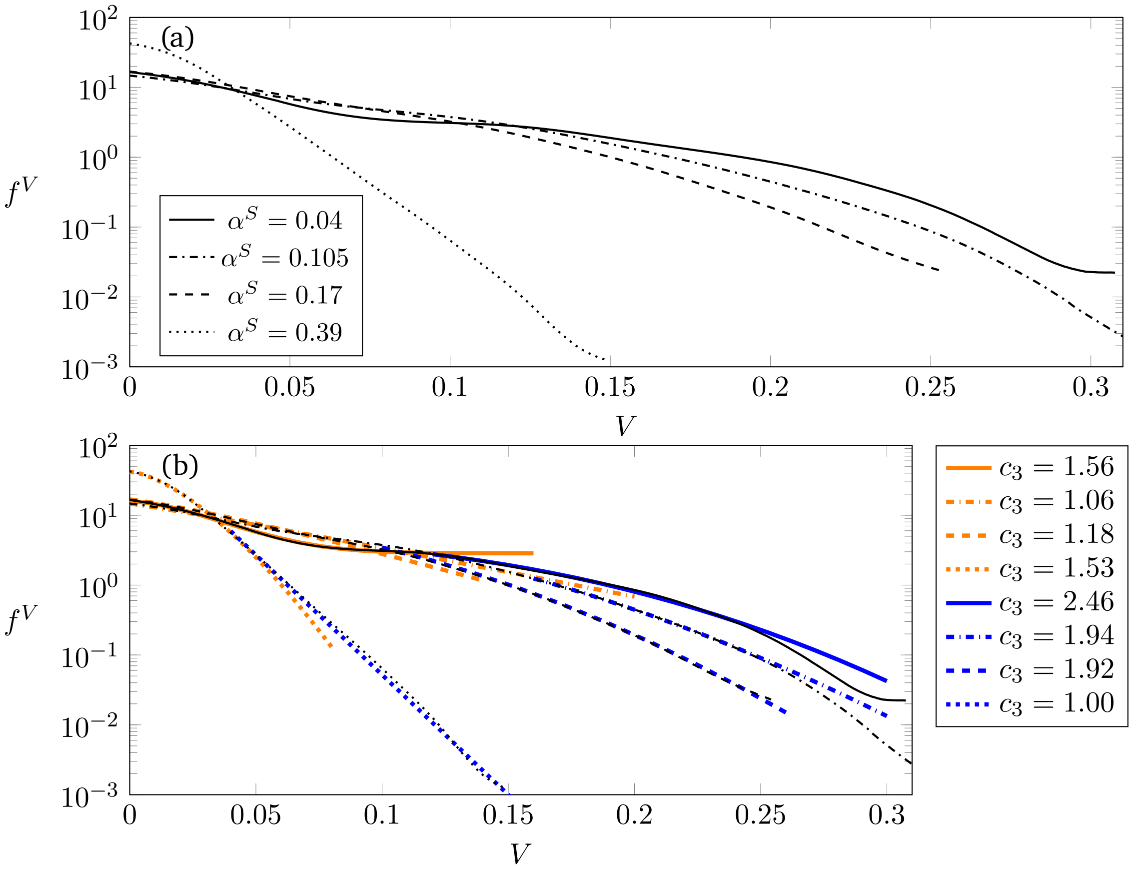

Fig. 6.23.: (a) The diagram shows the velocity PDF for four different suspensions. (b) An approximation for the velocity PDF is obtained by using a linear combination of two functions of the type (6.16).

value of the velocity components, which is done in Fig. 6.23, where the absolute value of the components is denoted by V. To investigate the velocity PDF, the invariant solution obtained from the shape symmetry of the velocity PDF is used. This solution is the single-point shape symmetry itself

$$f^{*V} = f^V + \psi(V). \tag{6.15}$$

The free function $\psi(V)$ allows the PDF to be represented as a linear combination of individual functions. Again, the general intermittency symmetry (3.118) can be used equivalently due to (3.119). Choosing the ansatz

$$\psi^n(V) = c_1 e^{-c_2|V|^{c_3}} + \psi^{n+1}(V) \tag{6.16}$$

permits to identify heavy and light tailed distribution. A heavy tailed PDF decreases more slowly compared to a standard normal distribution, i.e. rare events become more likely. Such a slowly decaying distribution indicates chaotic behaviour, because the system can enter a wider variety of states. As such it is related to the definition of intermittency given in Sec. 3.6.2, i.e. intermittency describes the sudden outburst of an otherwise rare event [135, 206]. A light tailed distribution on the other hand decays faster than a comparable normal distribution. Hence, it is related to more deterministic states. The ansatz function (6.16) can become a

Tab. 6.1.: All coefficients necessary to define the function depicted in Fig. 6.23b are denoted in this table.

α^S	0.04			0.11		0.17		0.39	
	ψ^1	ψ^2	ψ^3	ψ^1	ψ^2	ψ^1	ψ^2	ψ^1	ψ^2
c_1	13.19	2.85	4.52	14.73	8.33	16.8	9.67	1.43	140
c_2	161.12	90.36	0	16.92	66.54	27.16	85.91	272.84	79.00
c_3	1.56	2.46	0	1.06	1.94	1.18	1.92	1.53	1.00

normal distribution if $c_3 = 2$, hence, a heavy tailed distribution is obtained for $c_3 < 2$ and a light tailed one for $c_3 > 2$. Necessarily, the next ansatz function $\psi^{n+1}(V)$ needs to ensure that the reduction property (3.66) of the PDF is preserved.

In Fig. 6.23b, two functions ψ^1, ψ^2 are used to approximate the velocity PDF. A third function $\psi^3 = f^V$ is used to preserve the reduction property leading to the PDF

$$f^{*V}_{\alpha^S} = \psi^1 + \psi^2. \tag{6.17}$$

Only in case of the dilute suspension $\alpha^S = 0.04$, an additional free function is necessary, which reduces to a constant. All coefficients are shown in Tab. 6.1. As already mentioned, to distinguish between heavy and light tailed distributions, the coefficient c_3 is of interest. The inner PDF, depicted in orange in Fig. 6.23b and described by ψ^1, and by $\psi^1 + \psi^3$ in case of the dilute suspension $\alpha^S = 0.04$, is a heavy tailed distribution $c_3 < 2$ for all given examples. Nevertheless, significant differences are visible between the suspension. The second $\alpha^S = 0.11$ and third suspension $\alpha^S = 0.17$ have a much smaller exponent, i.e. heavier tails, than the densest suspension $\alpha^S = 0.39$ and the dilute suspension $\alpha^S = 0.04$. Due to the comparably small exponent c_3 both inner PDFs for $\alpha^S = 0.11$ and $\alpha^S = 0.17$ have a wide range of possible outcomes, thus, indicating chaotic behaviour. The inner PDF is a valid approximation of the data in the interval $0 \leq V \leq 0.12$. The maximum value of the inner PDF for both suspensions is at $V = 0$, where $f^V_{0.11}(V = 0) = 8.33$ and $f^V_{0.17}(V = 0) = 9.67$. The minimum values within the given interval are $f^V_{0.11}(V = 0.12) = 2.81$ and $f^V_{0.17}(V = 0) = 2.23$. Hence, both suspensions behave similar, despite the visual differences between the suspensions (Fig. 6.16a, Fig. 6.17a). Clusters are formed, as indicated by the minimal distance PDF. However, the particle velocity shows a high variance even within such clusters, leading to the constant break up and re-formation of local structures.

In case of the high density suspension $\alpha^S = 0.39$ on the other hand, the inner PDF is more similar to a normal distribution with an exponent $c_3 = 1.53$ compared to the suspensions with medium densities. It is a valid approximation for small velocities $0 \leq V \leq 0.05$. While it is still a heavy tailed PDFs, outcomes close to zero $f^V_{0.39}(V = 0) = 41.97$ are up to 16.79 times more likely than outcomes closes to 0.05, where $f^V_{0.39}(V = 0.05) = 2.5$. Hence, the densely packed particles move much slower and with a smaller variance compared to the suspensions with medium density, indicating the formation of stable structures.

It is already visible in the speed-PDF that the dilute suspension behaves differently. The inner PDF is formed by a linear combination of the function ψ^1 and the constant ψ^3 and shows good agreement with the data in the interval $0 \leq V \leq 0.12$. The maximum value at $V = 0$ is 16.04, i.e. it is 3.55 times higher than the value of ψ^3. Compared to the densest suspension, the distribution is much closer to an equal distribution, i.e. all events within the area of the inner distribution are approximately equally likely. This behaviour is reminiscent of the behaviour of a single particle, see Fig. 6.22. Clearly, the time-span between particle-particle interactions is large enough for the particles to constantly accelerate towards the single particle terminal velocity, which itself is part of the outer PDF. In accordance to the almost equal distribution of the PDF no cluster is formed in the centre of the domain (Fig. 6.16a). The increase of the PDF towards zero and the maximum at zero is caused by the emergence of particle formations at the domain wall, see Fig. 6.16a.

The outer PDF, depicted in blue in Fig. 6.23b and described by ψ_2, shows a change in behaviour for all suspensions. The heavy-tail behaviour of the densest suspension is reinforced, whereas the other three suspensions get lighter tails. While the terminal velocity of a single particle can be exceeded in a suspension, due to collisions and indirect particle-particle interactions, a limit for the maximum velocity exists. This limit has to be understood as a soft limit, i.e. higher velocities become simply unlikely, jet are not impossible. In order to comply with this soft maximum limit, the decay of the velocity PDFs of the three more dilute suspension needs to accelerate compared to the inner PDF, which is achieved by a higher exponent c_3. In case of the densest suspension, the inner PDF already decayed quickly. Hence, in the region of the outer PDF no additional limitation exists, which would cause an increasing decay of the PDF, leading to the exponent $c_3 = 1.0$, i.e. a very light tail, indicating intermittent behaviour.

To further the understanding of the interactions of the particles, especially in a dense suspension, one might investigate a joint PDF. The PDF formed with the sample space variable of the minimal distance $\mathfrak{r}^{\text{min}}$, see (6.7), and the sample space variable $\mathfrak{v}^{pq}$ of the relative speed of two particles

$$v^{pq} = |\gamma_p \boldsymbol{v}_p - \gamma_q \boldsymbol{v}_q| \tag{6.18}$$

is

$$f^{\mathfrak{r}\mathfrak{v}} = \left\langle \delta\left(\mathfrak{r}^{\text{min}} - r^{\text{min}}\right) \delta\left(\mathfrak{v}^{pq} - v^{pq}\right) \right\rangle . \tag{6.19}$$

Due to the correlation of the minimum distance r^{min} and the relative velocity v^{pq} in (6.19), it is possible to derive conclusions about the stability of the structures visible in the snapshots of the simulations, see Fig. 6.16 and Fig. 6.17. Data from the simulations for the joint PDF is presented in Fig. 6.24 for two suspension. Results for all investigated systems can be found in App. A.3. The differences between the two suspensions are immediately noticeable. The lower density suspension, see Fig. 6.24a, shows two maxima, whereas the high density suspension, see Fig. 6.24b, only shows one maximum. The latter maximum is a direct result of the geometrical constraints in a dense suspension, which are also visible in the marginal PDF for the minimal distance, see Fig. 6.19 and the joint PDF for the minimal distance and the alignment, see Fig. 6.21b. Due to the low relative velocity in the dense suspension, structures such as clusters are relatively stable and the spatial configuration of the suspension only changes slowly. Note that a structure formed with several particles might still have a significant velocity, only the relative velocity between the particles vanishes. States outside of the immediate near-field region are very unlikely for the suspension $\alpha^S = 0.39$, while the particles in the other suspension $\alpha^S = 0.11$ have a wide range of possible states. Thus, any structure emerging in a lower density suspension is relatively unstable due to the high relative velocities. The maximum at approximately $(1.2, 0)$ for the suspension presented in Fig. 6.24 is related to the maximum $(1.2, \pi)$ in the joint PDF for the minimal distance and the alignment, see Fig. 6.21a. It is related to the two particle interaction investigated in Fig. 6.8. Two opposing

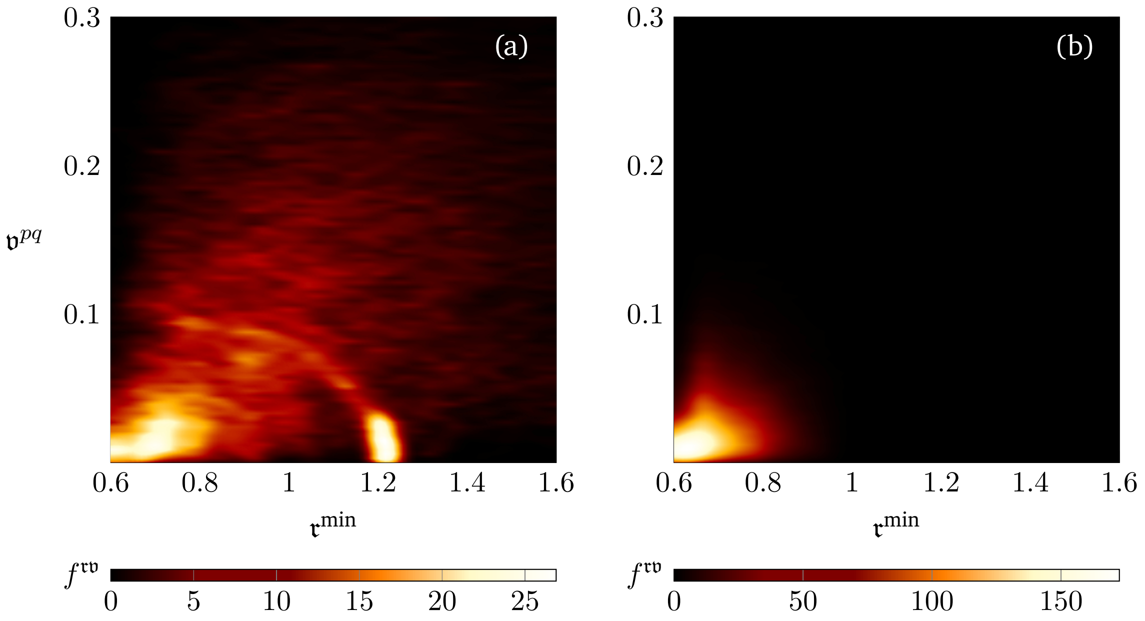

Fig. 6.24.: (a) The diagram shows the joint PDF formed with the minimal distance and relative velocity for the suspension $\alpha^S = 0.11$. (b) Only the maximum in the lower left corner remains for the densest suspension $\alpha^S = 0.39$.

particles block their paths, thus, leading to a decaying relative velocity. Hence, opposing particles might have a stabilising effect on clusters formed within the domain. The maximum in the left lower corner, on the other hand, is mostly caused by particles at the wall. As visible in Fig. 6.16b, particles directly at the wall align parallel and are orientated towards the wall. Due to the blocking nature of the wall, the absolute and the relative velocities decay.

The behaviour of the velocity-PDFs is reminiscent of the definition of intermittency. This term describes both the consistent alternation of deterministic and stochastic behaviour and the sudden eruption of an otherwise rare event. Both definitions have already been used in the definition of intermittency symmetry (3.122a). Forming the limiting case of the ansatz function (6.16) delivers the Dirac function

$$\lim_{c_1, c_2 \to \infty} c_1 e^{-c_2 |V|^{c_3}} = \delta\left(V\right). \tag{6.20}$$

Subsequently, by forming the limiting case for the inner PDF ψ^1 it is possible to retrieve the single-point version of the intermittency symmetry (3.122a)

$$f^{*V} = c_{\text{int}} f^V + \left(1 - c_{\text{int}}\right) \delta\left(V - U\right). \tag{6.21}$$

Here, U represents the velocity of an ideal cluster, where all particle share the same velocity. The parameter c_2 increases steadily for the three suspensions $\alpha^S = 0.11$, $\alpha^S = 0.17$ and $\alpha^S = 0.39$ as visible in Tab. 6.1. Hence, it is expected for c_2 to increase further with increasing particle density, leading to the limiting case (6.20). Accordingly, the parameter c_1 can be directly related to c_{int}, i.e. $c_{\text{int}} = c_1$.

A system with a global particle volume fraction $\alpha^S = \alpha^S_{\text{max}}$ freezes, hence, the velocity vanishes once the limiting case is reached. If a cluster of particles locally approaches the maximum volume fraction, but the overall domain is much larger than the cluster, motion is still possible. The velocity U in (6.21) then represents the cluster velocity $U = U^{\text{cluster}}$, which is identical for all particles within the cluster as no relative motion between the particles is possible. In other words, one would observe a phase separation, where the cluster is a solid phase and the surroundings with lower particle density are occupied by a fluid phase of a new pseudo-material, which contains the particles as molecules. Subsequently, while the name intermittency symmetry was adopted from turbulence research, in the context of active particles *cluster* or *phase-separation* symmetry would be a more fitting name. Reformulating the general intermittency symmetry (3.118) for an ideal cluster delivers

$$ {}_K f^* = c_{\text{int}}\, {}_K f + (1 - c_{\text{int}}) \prod_{k=1}^{K} \delta\left({}_k\boldsymbol{V} - \boldsymbol{U}^{\text{cluster}}\right) \delta\left(\boldsymbol{X} - \boldsymbol{\chi}\right) \prod_{p=1}^{N} \delta\left(b_p - \beta^{\text{cluster}}\right). \tag{6.22} $$

The two variables cluster velocity U^{cluster} and orientation β^{cluster} are used to describe the deterministic part of the PDF. Due to the separation property, the symmetry transformation (3.120) is only valid in a finite domain, hence, this formulation of the symmetry transformation returns the probability $(1 - c_{\text{int}})$ of the formation of an ideal cluster with a uniform cluster velocity and orientation. In reality small deviations from the cluster velocity and orientations might exist, which are small enough to not break the cohesion of the cluster. Such a real cluster can be, for example, represented by a product of normal distributions $\delta_\epsilon\left(x\right) = \left(2\pi\epsilon\right)^{-0.5} e^{-x^2/(2\epsilon)}$, where the limiting case $\lim\limits_{\epsilon\to 0} \delta_\epsilon\left(x\right) = \delta\left(x\right)$ returns the Dirac delta. Hence, the cluster-symmetry transformation for real clusters reads

$$ {}_K f^* = c_{\text{int}}\, {}_K f + (1 - c_{\text{int}}) \prod_{k=1}^{K} \delta_\epsilon\left({}_k\boldsymbol{V} - \boldsymbol{U}^{\text{cluster}}\right) \prod_{p=1}^{N} \delta\left(\boldsymbol{X}_p - \boldsymbol{\chi}_p\right) \delta_\epsilon\left(b_p - \beta^{\text{cluster}}\right) \tag{6.23} $$

where the parameter ϵ, $\boldsymbol{U}^{\text{cluster}}$ and β^{cluster} need to be chosen appropriately such that ${}_K f^*$ is a solution of the PDF hierarchy (3.96). Particle-resolved simulations of a system with visible phase separation would require an enormous computational power due to the large number of particles. Hence, to investigate the *cluster*- or *phase-separation* symmetry further, the homogenised model is used.

It should be noted that intermittency and shape symmetry also occur in systems with passive particles without the presence of active particles. However, for the formation of clusters, especially in the centre of the domain without direct participation of walls, the activity of the particles is mandatory. It can therefore be assumed that the parameters c_1, c_2 and c_3 are functions of the active stress.

6.3. Results for the homogenised model

The homogenised model, as presented in Sec. 5, is used to simulate larger systems of active suspensions. All data presented in this section is publicly available via TUdatalib [52]. Consider a steady planar flow, i.e. all derivatives in the x_1 and x_3 direction vanish. Furthermore, the pressure gradient in the x_2 direction is considered to be zero, due to the steady state of the system, which requires vanishing vertical transport of material. The domain setup is given in Fig. 6.25. At first, classical planar flows with a constant initial particle distribution are examined. Difference and similarities between the behaviour of a Poiseuille flow, a Couette flow

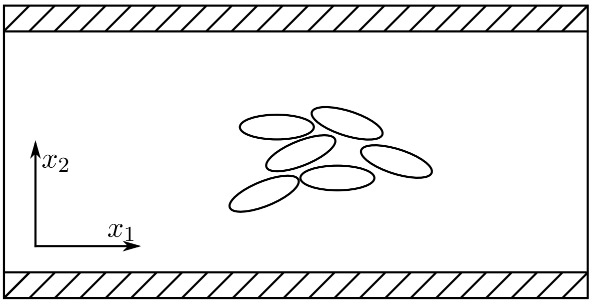

Fig. 6.25.: The setup for all planar channel flows. The upper and lower boundaries are solid impermeable walls. All gradients in the x_1-direction beside a possible constant pressure gradient vanish, hence, one-dimensional profiles are sufficient to describe the flow through the channel.

and the combination of both are investigated. A planar Poiseuille flow is driven by a constant pressure gradient parallel to the walls. A Couette flow is a planar shear flow, achieved by prescribing a velocity in the tangential direction at the wall. Special attention is given to the influence of the different interaction forces between the phases. In a second series of numerical experiments, the *phase separation* symmetry is investigated, which was already derived from the behaviour of the multi-particle simulation in the previous section.

It is necessary to define boundary conditions for all physical quantities for both phases at the domain boundary. The upper and lower boundaries are considered to be impermeable, hence, all velocities in x_2-direction vanish at the boundary. Furthermore, a no-slip condition is applied for the fluid velocity. Particles, however, tend to slide alongside the wall, which can be deduced from numerical experiments using the BoSSS framework, see Sec. 6.2.2. Hence, a Neumann condition is used for the averaged solid phase velocity $\overline{v_1^S}$ in the horizontal direction, i.e. the derivative $\partial\overline{v_1^S}/\partial x_2 = 0$ vanishes, permitting a slip velocity tangential to the wall. The wall is still considered impermeable, hence, the velocity $\overline{v_2^S} = 0$ vanishes at the wall. In this respect, the results presented here differ from those presented by Deußen et al. [55, 54]. In the aforementioned publication, a vanishing velocity at the wall was assumed for the horizontal velocity of the solid phase. However, considering the results from the particle-resolved simulations, see Fig. 6.11, a Neumann condition for the velocity parallel to the wall seems more reasonable. Further quantities, i.e. the particle rotational velocity $\overline{\omega_i^S}$, the particle orientation $\overline{e_i^S}$ and the solid phase volume fraction α^S are also bounded by a Neumann condition.

The first test case is a Poiseuille flow with a constant pressure gradient $\partial\overline{p^F}/\partial x_1 = -10^4$ in the x_1 direction. The magnitude of the active force acting on the particles is varied between the experiments. The averaged orientation of the particle is enforced to be constant. While this is clearly an assumption, it is a physical one. In all numerical experiments shear flows are investigated. It is known that under the presence of a shear flow particles in a suspension tend to align towards another [47, 213]. Furthermore, the particle resolved simulations in a channel indicate, that a steady state is reached for the averaged orientation, see Fig. 6.13. The averaged orientation vector is chosen to be $\overline{\boldsymbol{e}^S} = [0.855, 0]$.

In case of a single-phase Newtonian Poiseuille flow, such an experiment results in a parabolic velocity profile. The parabolic profile can be used to benchmark the implementation of the model. While it is not possible to simulate single-phase problems due to the logistic function

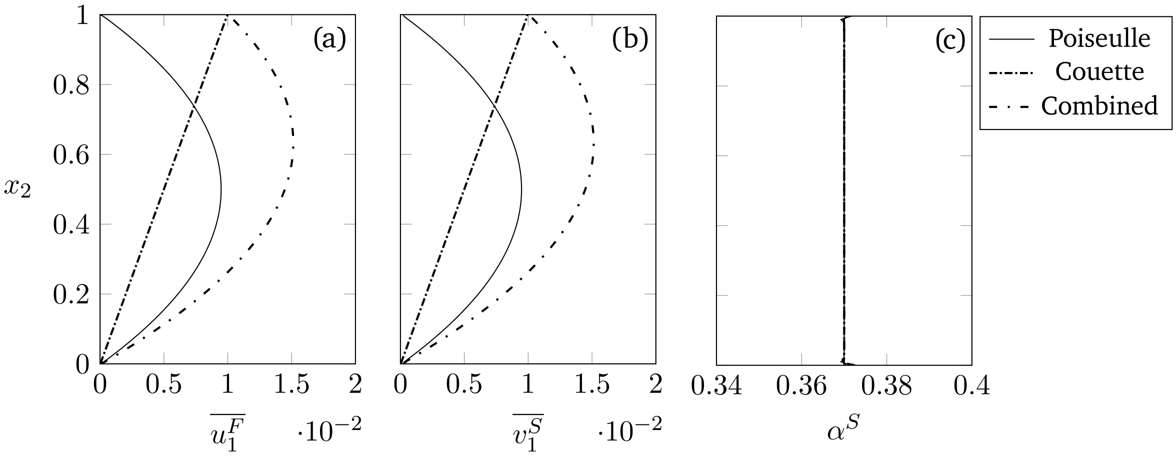

Fig. 6.26.: (a) The fluid velocity profile, (b) the solid phase velocity profile and (c) the volume fraction α^S profile in case of a passive suspension for three classical flows.

bounding the particle volume fraction (5.134), a simulation with $\alpha^S \to 0$ is possible. Comparing the solution obtained with $\alpha^S = 3.36 \cdot 10^{-5}$ with the analytical solution of a planar Poiseuille flow $\overline{u_1^F} = x_2 / (2\,\mathrm{Re})\,(-\partial \overline{p^F} / \partial x_2)\,(H - x_2)$, where H is the height of the channel, and calculating the L_2-norm of the resulting Residual vector yields a relative error of $1.6 \cdot 10^{-3}$.

Similarly, passive suspensions, i.e. $\mathfrak{A}^c = 0$, also develop a parabolic velocity profile as shown in Fig. 6.26. As mentioned in Sec. 2.3.1 small passive particles are subject to Brownian motion, which was not considered in the derivation of the model equations in Sec. 5. However, due to the volume average, the stochastic effect of the Brownian motion vanishes, because its probability is normal distributed with an expectation value of zero, see Einstein [67]. In this experiment and all following experiments the Reynolds number is set to $\mathrm{Re}^P = 10^{-4}$. Due to the low value, passive particles are expected to closely follow the fluid phase. Subsequently, the relative velocity $\overline{w_i^S}$ between the two phases approaches zero and the interaction forces vanish, because of their dependency on $\overline{w_i^S}$. It should be noted that $\overline{w_i^S}$ does not become exactly zero. However, the resulting deviation of the particle distribution from the initial, constant distribution is small and, subsequently, negligible, see Fig. 6.26c. Besides the solution for the Poiseuille flow of a passive suspension, Fig. 6.26 also presents results for a Couette and a Couette-Poiseuille flow. In case of the Couette flow a linear velocity profile is obtained, equivalent to the solution of a single phase fluid flow. The resulting profiles for the Poiseuille-Couette flow are linear combinations of the two constituting flows. Due to the low Reynolds number, the convective terms in (5.132) vanish, leading to a linearisation of the system. Furthermore, the evolution equation for the particle position (2.46) was not used in the derivation of the homogenised model, because the information about the exact position of the particles is lost. Thus, the linear symmetry (3.36g) is present in the system, leading to the linear combination of the results of the Poiseuille and Couette flow in case of the combined Couette-Poiseuille flow.

In the case of active suspensions, the situation is different. The active force creates a velocity difference between the phases. This permits the interaction terms to become effective. In Fig. 6.27, the resulting velocity profiles and particle distributions are shown. As expected, the active force causes a significant relative velocity $\overline{w_i^S}$ between the two phases of the system.

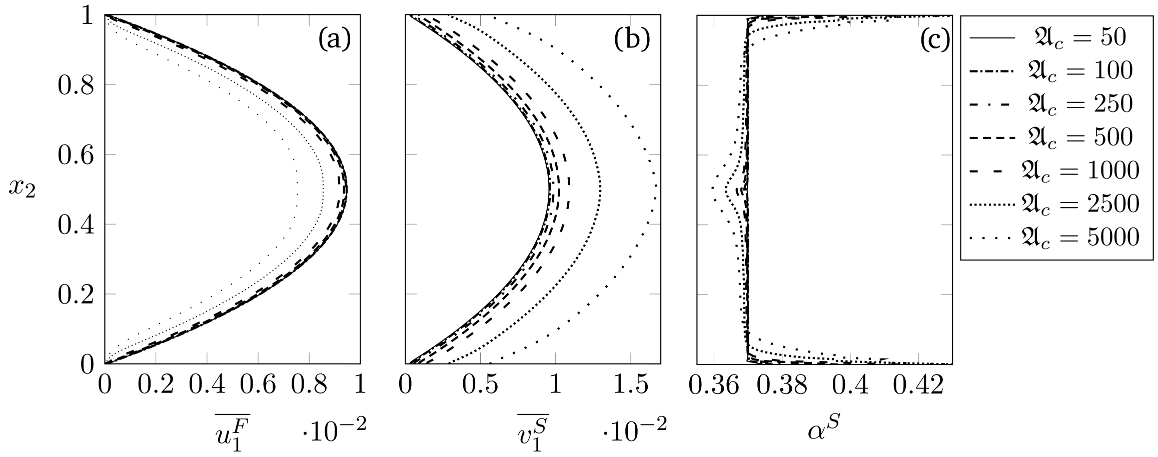

Fig. 6.27.: The velocity profiles of a planar active Poiseuille flow deviate strongly from the classical parabolic profile with increasing active force. (a) On the left panel the averaged fluid velocity is shown. (b) The averaged solid phase velocity increases with increasing active force. (c) The velocity difference between the two phases permits lift forces in the x_2 direction, leading to an increase in particle density at the boundaries and a depletion in the centre of the domain.

With increasing $\mathfrak{A}^c$ the gap between the two phases widens, as the particle velocity increases, including the slip velocity at the boundary, whereas the fluid velocity decreases. Subsequently, due to the dependency of the interaction forces between the phases on $\overline{w_i^S}$, vertical force components cause an accumulation of solid material at the domain boundaries. Such an effect is well-known in the literature, see for example Bechinger et al. [18], Berke et al. [22], and Ezhilan and Saintillan [74], and was also observed in the particle resolved simulations, see Sec. 6.2. Similar results were obtained by Deußen et al. [55], where as mentioned the only difference to the present setup is the permitted slip velocity of the horizontal averaged particle velocity. Due to the constant particle orientation parallel to the x_1 direction, the averaged active force does not directly contribute to the movement of solid material in the vertical direction. Rather, the lift forces are responsible for this behaviour. The velocity difference is relatively small, hence, the circulation lift force F_i^{LC} is still negligible. Furthermore, the difference $0.5\,\overline{\omega_3^F} - \overline{\omega_3^S}$ vanishes due to the drag torque, leading to an negligible Magnus-force. The attraction of the active particles towards the wall as modelled in (5.114) decays with $1/h^4$. Thus, in the centre of the present channel such effects play a minor role. Subsequently, the Saffman-force is the only remaining cause of the shift in the distribution of the particles [55]. Such an behaviour is unknown from passive suspensions, where Saffman-forces play an overall minor role, i.e. no change in the particle distribution can be observed. Especially for passive spheres, it was shown that the Saffman-force is negligible [1, 49, 131]. Other examinations of active particles mainly focus on the active wall attraction [18, 22, 74, 208] and do not consider the Saffman-force as a relevant parameter.

In the following paragraph, an active Couette flow is analysed. The particles are the same as in case of the Poiseuille flow and their orientation is again fixed. A constant velocity $\overline{u_{\text{wall}}^F} = 10^{-2}$ is prescribed as a boundary condition for the fluid velocity at the upper wall. The slip velocity for the solid phase is still permitted at both walls. The resulting velocity profiles and particle

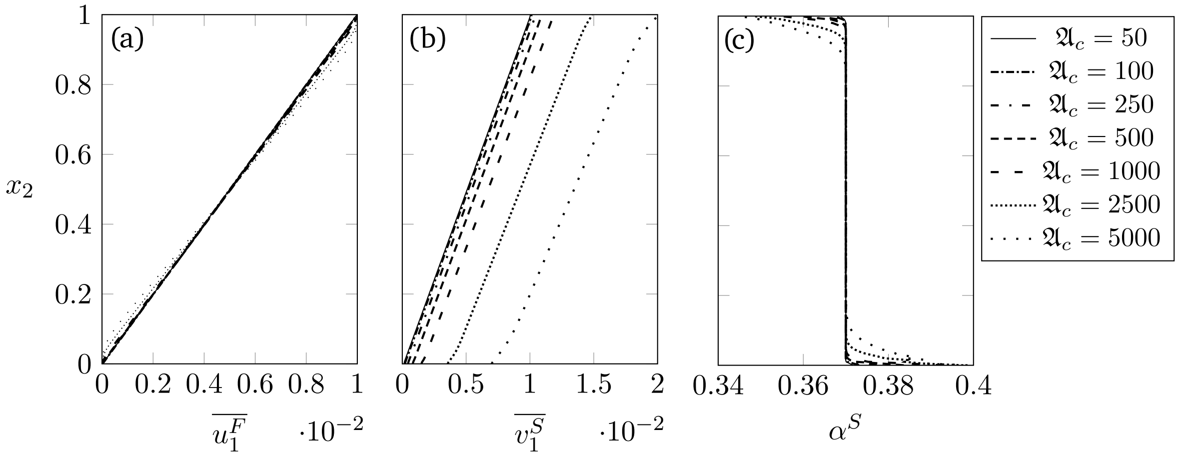

Fig. 6.28.: The velocity profiles of a planar active Couette flow deviate from the classical linear profile with increasing active force. (a) On the left panel the averaged fluid velocity is shown. (b) The averaged solid phase velocity increases with increasing active force. (c) The velocity difference between the two phases permits lift forces in the x_2 direction, leading to an increase in particle density at the fixed lower boundary and a depletion at the upper moving boundary.

distributions are presented in Fig. 6.28. For vanishing active forces $\mathfrak{A}^c = 0$, the linear velocity profile of a Newtonian planar Couette flow is retrieved, see Fig. 6.26a+b. With increasing active force the velocity profiles deviate from this linear profile. The fluid velocity is decreased in the near wall region of the lower boundary and increased at the upper boundary compared to a linear profile. The slip velocity of the particle phase becomes more dominant. At the lower wall, the solid phase velocity profile deviates from a linear profile. The velocity decreases faster than linear, corresponding with the increase of the particle volume fraction α^S. At the moving upper wall, the particle velocity increases stronger than linear, corresponding with a decrease of the particle density in the same region. The depletion of the particle phase at the upper wall shows that interaction forces, namely the Saffman-force, are dominant in this setup. The active wall attraction is not able to counter the Saffman-force, hence, driving particle material away from the upper wall towards the lower wall. Similar to the Poiseuille flow, the active force exerted by the particles is indirectly responsible for the change in the particle distribution. It creates the velocity difference between the two phases, which permits the Saffman-force and is not visible in a passive suspension. Similar results have been obtained for a setup with vanishing slip velocity [55], however, the slip velocity strengthens the effect of the Saffman-force due to the higher velocity difference.

Combining the two previous classical flows delivers a Couette-Poiseuille flow, i.e. the flow is driven by the pressure gradient $\partial\overline{p^F}/\partial x_1 = -10^4$ and the prescribed fluid velocity $\overline{u^F_{\text{wall}}} = 10^{-2}$ at the upper boundary. Results are shown in Fig. 6.29. Effects of both constituting flows are visible. The depletion of solid material in the centre of the domain and the maximum of the velocity profiles is shifted towards the upper wall compared to the Poiseuille flow. Particles accumulate at both boundaries, however, the accumulation is stronger at the lower wall due to the Couette part of the flow. Again, for small active forces (Fig. 6.29a+b) and passive suspensions (Fig 6.26a+b), the well-known profile of a Newtonian Coeutte-Poiseuille flow is retrieved. In case of a single phase Newtonian fluid in a low Reynolds setup, the velocity

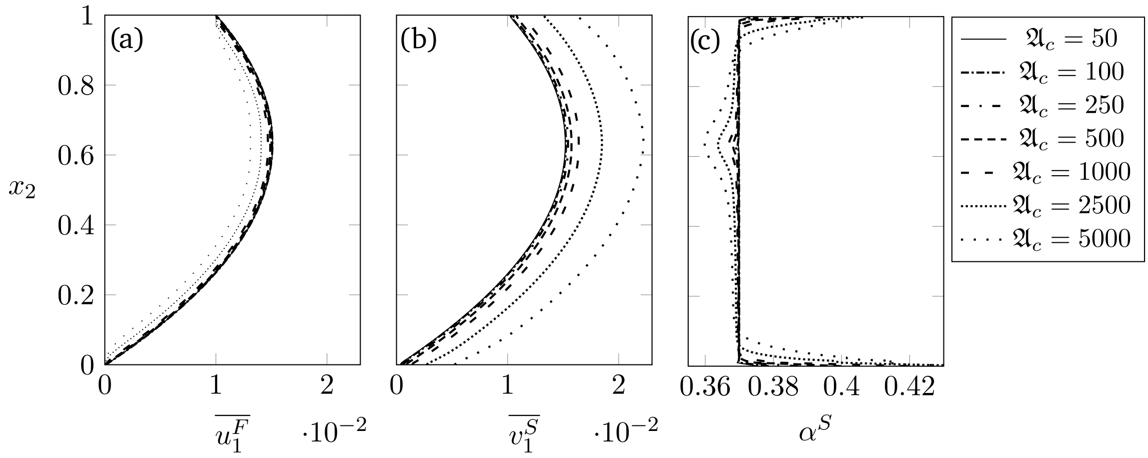

Fig. 6.29.: The velocity profiles of a planar active Couette-Poiseuille flow deviate from the classical profile with increasing active force. (a) On the left panel the averaged fluid velocity is shown. (b) The averaged solid phase velocity increases with increasing active force. (c) The velocity difference between the two phases permits lift forces in the x_2 direction, leading to an increase in particle density at the fixed lower boundary and a smaller increase at the upper moving boundary. The depletion of material from the bulk flow is off-centred.

profile is a linear combination of the velocities of the Couette and the Poiseuille flow due to the linearity of the Stokes equation. This linear feature of the single-phase unsteady Stokes equation becomes visible in the symmetry (3.36g), allowing the addition of any solution of the Stokes equation to another solution. As remarked in Sec. 3.3.2, this symmetry is not generally applicable to a suspension. It is the temporal evolution of the particle position, see (2.46), which breaks the symmetry. All information about the specific location of an individual particle is lost due to the averaging process. Thus, (2.46) is not used for the derivation of the homogenised system (5.132) and the symmetry transformation (3.36g) is applicable.

To analyse the differences between the three flows and the situation at the upper and lower wall, a boundary layer thickness δ_h is introduced. The length scale δ_h is defined as the distance from the wall where α^S deviates only by 1% from the mean value of α^S. A linear interpolation is used to find the correct value of δ_h between grid-points. The results are presented in Fig. 6.30. As expected δ_h increases with increasing active force $\mathfrak{A}^c$, however, the behaviour differs slightly between the different examined flows. In case of the Poiseuille flow, which is used as a reference, the increase is linear with a proportionality constant $c = 1.29 \cdot 10^{-5}$. At the lower boundary of the Couette flow, the thickness of the boundary layer also increases linearly with $c = 1.48 \cdot 10^{-5}$, whereas on the upper, moving wall a deviation from the linear behaviour is visible. While for smaller values of $\mathfrak{A}^c$ it increases faster than the Poiseuille reference, for higher active forces it shows a tendency to align with the curve of the Poiseuille flow. The boundary layer thickness δ_h of the Couette-Poiseuille flow seems to behave similar to an average of the Poiseuille and Couette flows in accordance to the aforementioned superposition principle. The thickness is overall increased at the lower boundary compared to the aforementioned flows. However, the slope is decreased compared to the Couette case; the constant is $c = 1.34 \cdot 10^{-5}$. At the upper boundary the curve aligns more strongly towards the curve of the Poiseuille flow for high active stresses, while it deviates similar to the Couette case from

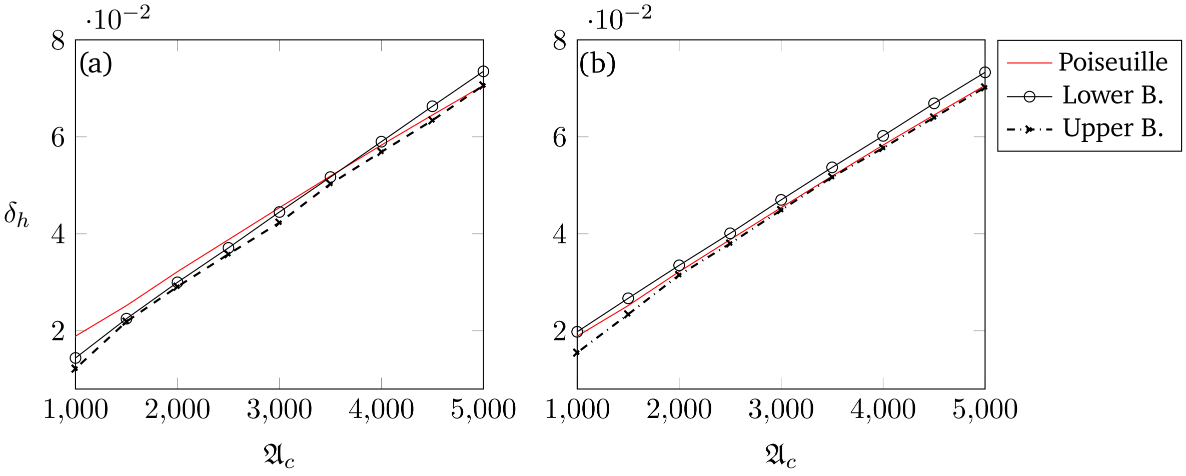

Fig. 6.30.: The boundary layer thickness δ_h behaves differently for the upper and lower boundary. (a) In the left panel the situation for the Couette flow is shown and δ_h at the lower boundary of the Poiseulle flow is used as reference. (b) In the right panel the boundary layer of the Couette-Poiseulle flow is depicted.

the linear behaviour at lower $\mathfrak{A}^c$.

Until now the starting distribution of the particles was always constant over the entire height of the domain. Uneven starting distributions might enforce interesting behaviour. In the next experiment, a cubic polynomial is used to initialise the logistic function $g^{\alpha}_{\text{init}} = (2.5\,(0.5 - x_2))^3$, which defines the particle volume fraction. The flow is driven by the active force of the particles and a prescribed velocity at the upper wall $\overline{u^F_{\text{wall}}} = 10^{-2}$, i.e. it is a Couette flow. The resulting velocities and particle distribution are presented in Fig. 6.31. Two things become apparent on first sight. The magnitude of the fluid velocity in the x_1 direction might become negative and α^S vanishes at the upper moving boundary for larger active forces $\mathfrak{A}^c$. The depletion leads to an interesting behaviour of the fluid velocity. In the quasi single-phase region, where almost only fluid is present, a linear velocity profile for the fluid phase is retrieved. The flow in this region can be represented by a single-phase Couette flow with two moving walls. The velocity of the upper wall would equal the prescribed boundary velocity of the present experiment and the velocity of the lower wall equals the fluid velocity of the last point with two phases present. Depletion is only reached for high active forces, i.e. the described behaviour is only visible for $\mathfrak{A}^c = 2500$ and $\mathfrak{A}^c = 5000$. Furthermore, the depletion is not complete, i.e. there are still particles preset in very small numbers.

The single-phase and two-phase regions are separated by a jump in the particle distribution. Subsequently, as predicted by the analysis of the shape and intermittency symmetry in combination with the particle resolved simulations, see Sec. 6.2.3 and Eq. (6.21), separation into different phases is a property of active suspensions. If one considers the suspension to be a new pseudo-material, where the active particles are the equivalent to the molecules of a physical material, the single-phase region is occupied by a gaseous phase of this new material, leading to the name *active gas* phase. Fitting this analogy, the remaining particles in the *active gas* phase move relatively fast, see Fig. 6.31b. Particle resolved simulations show that in the case of dilute suspensions no structures are formed in the domain, see Fig. 6.16a. In combination with the high averaged velocity it can be assumed that the particles move in a

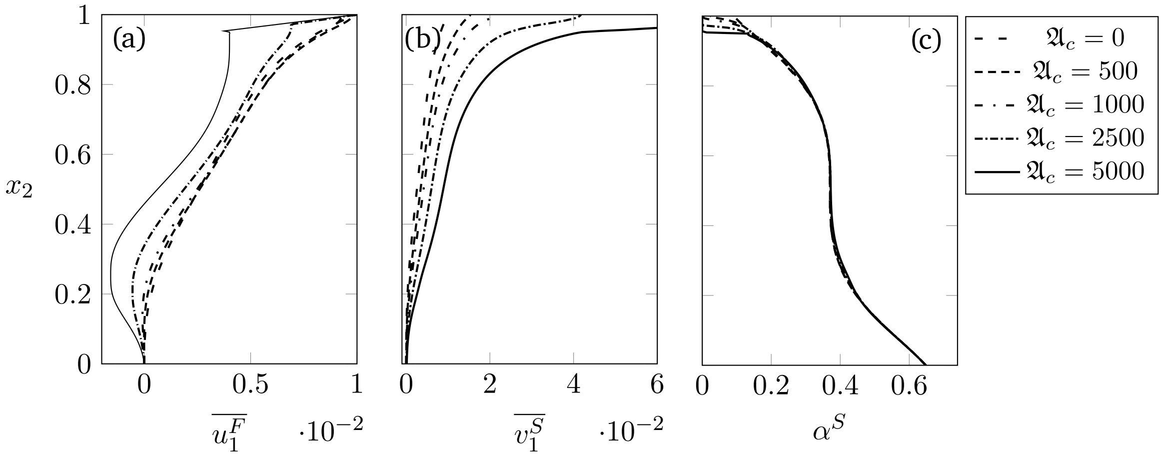

Fig. 6.31.: Unevenly distributed particle material can lead to interesting phase separation behaviour. A cubic polynomial was used as initial particle distribution, leading to a complete depletion of the particle phase at the upper moving boundary.

Tab. 6.2.: The position of the phase interfaces between the three active phases in the experiment shown in Fig. 6.31 are shown in this tabular.

$\mathfrak{A}^c$	liquid/solid	gas/liquid
500	0.044	-
1000	0.033	-
2500	0.02	0.973
5000	0.013	0.957

chaotic manner. Hence, the particle behaviour in the *active gas* can be related to the stochastic term of the *phase separation* symmetry (6.23) and the fluid behaviour can be related to the deterministic term in the aforementioned symmetry.

In large parts of the two-phase region, the state of matter of the pseudo-material is liquid, i.e. it is an *active liquid*. The active particles are packed much more densely than in the *active gas* phase, but velocity gradients on large and small scales are still possible. Not quite as obvious as in the case of the transition from gaseous to liquid, the suspension near the lower wall changes to a state resembling a solid. There is no visible jump in the particle distribution. However, the particle velocity at the lower wall decreases to an almost constant value close to zero. In analogy to the molecules in a solid, which from a macroscopic point of view all move at the same speed, we call the material in this region an *active solid*. It should be noted, that the change of the particle volume fraction in this region from the initial state is negligible, i.e the pseudo-material is frozen, which is the main reason for the missing jump and the clear separation between liquid and solid phase. Hence, in this experiment the *active solid* behaves like a glass, i.e. a frozen melt. For the purpose of this examination the position of the interface will be defined as the point where the local velocity gradient is smaller than 10% of the averaged velocity gradient of the two-phase region. The position of the phase interfaces is given in Tab. 6.2. The *active solid* phase is another example for the action of the *phase separation symmetry*, given by (6.23) for a realistic cluster. While in other regions of the domain the gradient of the velocity is large and might change quickly, the velocity in

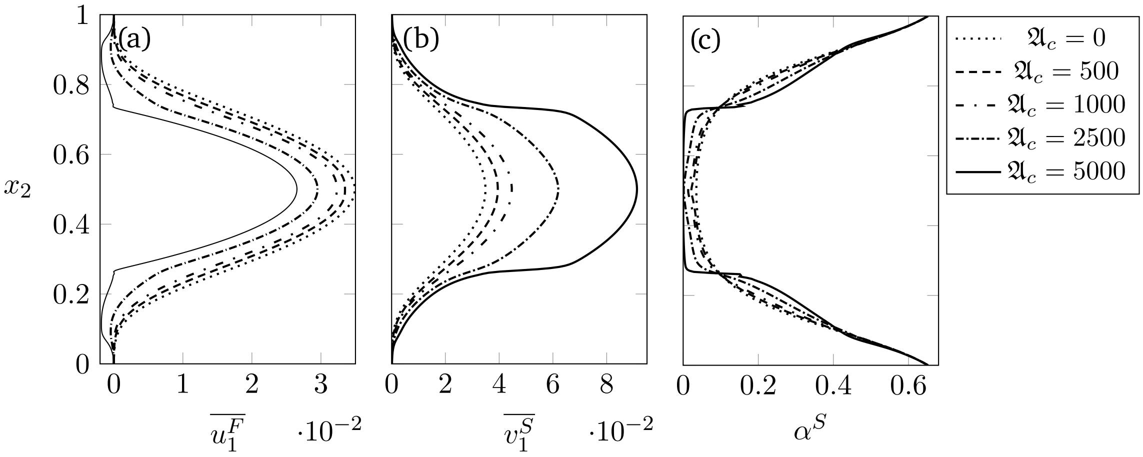

Fig. 6.32.: Unevenly distributed particle material can lead to interesting phase separation behaviour. A cubic polynomial was used as initial particle distribution, leading to a complete depletion of the particle phase at the upper moving boundary.

the *active solid* phase is approximately constant, i.e. related to the cluster velocity introduced in Sec. 6.2.3. The fluid phase on the other hand behaves much more dynamic, including a region of backflow for high averaged active forces. Thus, it is related to the stochastic part of the *phase separation* symmetry. The observation of phase separation in an active suspension is well documented, including the terminology *active gas, active liquid* and the glass-like *active solid*, see for example Berthier and Kurchan [23], Buttinoni et al. [36], Henkes et al. [91], Marchetti et al. [146], and Paoluzzi et al. [166]. To the authors knowledge, the connection, which is derived with the help of Lie symmetries, between the simulation results showing clustering and phase separation and the underlying theory is a new idea, developed in the present work. A further discussion of this connection can be found in the final section of this thesis, see Sec. 7.5.

A second experiment with a non-constant particle distribution delivers an even clearer picture of the phase separation. The particle volume fraction is initialised by a parabolic profile for the logistic function $g^\alpha = 20\,(x_2 - 0.5)^2 - 3$, i.e. most particles are already at the boundaries, whereas the centre of the domain contains a smaller number of particles. Additionally to the activity of the particles, the flow is driven by a pressure gradient $\partial\overline{p^F}/\partial x_1 = -10^4$. The results for the velocities in the x_1 direction and the particle distribution are given in Fig. 6.32. In the centre of the domain, the *active gas* is present for high active forces. Similar to the linear profile in case of a Couette flow, the fluid velocity forms a parabolic profile in the region occupied by the *active gas*, which is known from single-phase Newtonian flows and passive suspensions, see Fig. 6.26. Especially for large active forces, the transition between the *active liquid* and the *active solid* also becomes clearly visible in the form of a kink in the particle distribution. In the *active solid* region, the particle distribution shows almost no deviation from the initial distribution and the particle velocity is close to zero, i.e. the suspension is frozen. In the *active liquid* region, the particle distribution profile deviates clearly for high active forces from the initial parabolic profile, which is still intact for suspensions with lower active forces $\mathfrak{A}^c \leq 1000$. In the present experiment the *active gas* only develops for the highest active force $\mathfrak{A}^c = 5000$, the interfaces are located at $x_2 = 0.28$ and $x_2 = 0.72$. The kinks in the particle distribution are located at $x_2 = 0.08$ and $x_2 = 0.92$ for $\mathfrak{A}^c = 5000$ and at $x_2 = 0.07$ and $x_2 = 0.93$ for $\mathfrak{A}^c = 2500$.

It should be noted that this position differs from the position of the interface resulting from the previously used definition, i.e. the local particle velocity gradient being smaller than 10% of the averaged velocity gradient. The positions of the interfaces resulting from this definition are $x_2 = 0.03$ and $x_2 = 0.97$ for $\mathfrak{A}^c = 5000$ and $x_2 = 0.04$ and $x_2 = 0.96$ for $\mathfrak{A}^c = 2500$. The position of the kink should, however, be considered as a more reliable definition, because it is based on a single, deterministic feature of the suspension. From Fig. 6.32 it becomes apparent, that the *phase separation symmetry* (6.21) acts differently on the solid and on the fluid phase. In the subdomain occupied by the *active gas*, the fluid velocity profile is deterministic, as the well-known parabolic profile of a Newtonian fluid is retrieved. Due to the low number of particles present, local fluctuations are expected to be minimal for the fluid velocity. Hence, the deterministic part of the symmetry is dominant in this region for the fluid velocity. On the other hand, it is known from the particle resolved simulation of a dilute suspension that the particle velocity PDF is wider than for a dense suspension, i.e. a more chaotic state is reached, see Fig. 6.23. In the region occupied by the *active liquid* and the *active solid*, the variance of the particle velocity PDF shrinks, i.e. more deterministic states are reached, as indicated by the velocity PDF for denser suspensions, see Fig. 6.23. The fluid velocity, however, behaves more chaotic, including areas with reversed averaged flow. Furthermore, it can be expected due to the densely packed particles, that the microscopic fluctuations of the fluid velocity are large.

7. Discussion

Several different methods to examine an active suspension have been derived in this work. One could consider the different methods as tools in a toolbox, which contents can help gaining a deeper understanding of active suspensions. The classical symmetries, the PDF approach and the statistical symmetries developed in Sec. 3 represent the first tool in the toolbox. The second tool is the particle resolved XNSERO solver presented in Sec. 4. Last but not least we have the homogenised model, which represent the third tool (Sec. 5). All tools for itself have been proven valuable to provide insight on the behaviour of active suspensions. However, they become even more powerful in combination as shown in Sec. 6. The present section serves as a conclusion, to discuss the achieved results and the interaction of the individual tools.

7.1. The model

First, the underlying model is discussed, which is identical for all the different methods mentioned above. To the authors knowledge, most models for active particles consider only the solid phase, see for example Bechinger et al. [18], Jayaram et al. [113], and Vicsek et al. [200]. Models, which do consider the fluid, often simplify the motor of the particle and only apply a point force [84, 85, 93, 94]. In contrast, in the presently used model the particles are considered as extended objects, which exert an active stress on their surroundings. Thus, it belongs to the same model family as used for example by Kanevsky et al. [116] and Saintillan and Shelley [182]. The active stress is motivated by biological structures such as flagella and cilia [116]. Due to the increased level of detail, the computational costs increase compared to simpler models. This becomes especially apparent during the usage of the particle resolved XNSERO solver. Nevertheless, while dry models, i.e. models which do not consider the fluid phase, show interesting behaviour such as phase separation and the formation of large-scale cluster [36, 113], the fluid-particle interactions and particle-particle interactions provide an additional level of information. The presented model employs a sharp interface approach by representing the particle surface with the level-set method, see Sec. 2.3.3. The sharp interface representation combined with the sub-cell accuracy of the XDG method is especially useful for the particle resolved DNS. Disadvantages of the level-set method such as the necessity for high order implicit solvers for the transport equations of ϕ vanish due to the explicit formulation of ϕ based on the particle geometry.

Probably the biggest assumption of the model is the rigidity of the particles. Artificial active particles often consists of polymers [18] or of metallic compounds [212]. Thus, the assumption of rigidity is close to reality of artificial particles, because the small forces acting on each particle are not able to deform such artificial structures. Biological and, by extension, biohybrid active particles, on the other hand, mostly consist of soft tissue and fluid material.

Nevertheless, microorganisms are able to keep their body shape stable and will recover their native state after strong deformations [209]. Hence, the rigid model is also valid for many biological particles. However, species of the genus *Amoeba* [148] and similar organisms, who change their shape in order to drive themselves forward, might need a different modelling approach. Nonetheless, if the body deformations are sufficiently small, for example in the case of *Euglena gracilis*, experiments show a flow field similar to a Stokes dipole in the vicinity of the particles [71], as it is the case with the presented model. In fact, Ergin [71] mentions the necessity to remove the body features of *E. gracilis* for micro particle image velocimetry, because the movement of the organism is not related to the motion of the fluid. Accordingly, while small scale deformations of the particle body might exist, their effect on the hydrodynamics is negligible or possibly unrelated to the motion of the fluid, supporting the choice of a rigid particle model.

Active stress as a model for the particle motor is derived from organisms with cilia [116]. These micro-paddles are much smaller than the actual organism and exert a force on the surrounding fluid. The model of a mechanical stress distributed over the surface is, thus, a natural choice. Artificial Janus particles are closely related, because such particles rely on a slip velocity at the surface, caused by chemical reactions [212], as method of propulsions. A slip velocity is permitted by the active stress in the present model. However, the chemical reaction at the surface of artificial Janus particles might create a gradient of a chemical species, which, additionally to the hydrodynamic interactions, influences the behaviour of the active suspension [140]. Another method of propulsions is the helical movement, as exerted by the flagella of *Escherichia coli* [62] or *Euglena gracilis* [71]. As shown by the aforementioned authors Drescher et al. [62] and Ergin [71], the far-field approximation of the Stokes dipole is valid for such active particles. Far field in this context refers to the domain surrounding the particle with a diameter of only a few particle diameters, i.e. still in a close range of the particle. It excludes the region in the closest vicinity of the particle surface, which cannot be approximated by a Stokes dipole, see Fig. 6.2 and Bechinger et al. [18]. Thus, while differences might exist in the closest vicinity of the particle, the overall hydrodynamic behaviour of many active particles can be described by a Janus particle model with active stress as method of propulsion.

To reduce computational cost, especially in the case of the DNS, the Stokes approximation for the Navier-Stokes equation was introduced, see (2.17) for the steady case and (2.68) for the unsteady case. The non-linear convective terms of the Navier-Stokes equation are neglected, which is a reasonable approximation due to the condition of low Reynolds numbers $\mathrm{Re} \ll 1$. However, in the case of only two spatial dimensions no non-trivial steady solution exists for a particle in a uniform flow in an infinite domain, which is known as Stokes paradox [196]. Oseen [162] solved the paradox by introducing an additional term, which accounts for the inertia in the far field of the fluid flow. In the present work, the resulting Oseen equation (3.35) was derived from the symmetries of the unsteady Stokes equation, see (3.34). While no solution for a steady, uniform flow in two dimensions exists, solutions for unsteady [76] and non-uniform [43] flows are known, including solutions for the Stokes dipole, see (1.5) [43]. Due to the use of the unsteady Stokes equation (2.68), a finite domain and the general non-uniformity of the local fluid flow in an active suspension, see for example Fig. 6.17, the Stokes paradox poses no problem in the present work.

Brownian motion [67, 188] is neglected entirely in the present model, see Sec. 2.3.1. The term Brownian motion describes the random motion of a small particle dispersed in a fluid due to the collisions of the particle with the molecules of the fluid. The particles in consideration in the present work are certainly small enough to experience relevant accelerations due to Brownian motion. It is, however, assumed, that the Péclet number Pe $\equiv v^{ac}/\sqrt{D^T D^R}$ as given by Bechinger et al. [18] is large, i.e. the strength of the active transport, represented by the velocity v^{ac}, is larger than the diffusive transport due to Brownian motion, represented by the two diffusion coefficients $\sqrt{D^T D^R}$. Hence, any random term in the model system containing the Navier-Stokes respective Stokes equation and the Newton-Euler equation is neglected. For systems with small Péclet number it might be necessary to consider stochastic terms in the defining equations. Throughout this work, systems with small Péclet numbers are analysed only with the homogenised model. Here, passive suspension with Pe $= 0$ are considered, see Sec. 6.3. However, Brownian motion is described by a normal distribution with vanishing expectation value, see Einstein [67]. Thus, due to the averaging process, the diffusive effects of Brownian motion are not depicted in the homogenised model.

7.2. Symmetries

In Sec. 3 Lie-symmetries of the physical and statistical descriptions of the systems were presented, starting with the symmetries of a single-phase fluid system. The generalised Galilean symmetry of the Navier-Stokes equation is unavailable for the unsteady Stokes equation and reduced to a constant spatial shift. The steady Stokes equation, on the other hand, contains the classical Galilean symmetry, i.e. a function linear in time can be added to the unmodified Eulerian coordinate x_i. Due to the linearity of the Stokes equation, an additional symmetry appears, which is related to the superposition principle of linear differential equations. Furthermore, the scaling symmetry T_{Sc1} of the Navier-Stokes equation is split into two scaling symmetries T_{Sc2} and T_{Sc3}, where the combination of the latter two results in the first scaling symmetry T_{Sc1}, see (3.37).

Applying the rotation operator $\nabla\times$ to the unsteady Stokes equation delivers a transport equation for the vorticity. It is equivalent to the heat equation, which symmetries in the one-dimensional case are given by Ibragimov [106]. In Sec. 3.2.1 the set of symmetries in two spatial dimensions for the vorticity equation was presented. Interestingly, while derived from the unsteady Stokes equation, the vorticity equation has a time-dependent Galilean symmetry, where the spatial shift depends linearly on the time [106]. Furthermore, the transformation group of the vorticity equation contains a symmetry directly related to the dissipation of the vorticity, see (3.41g).

Once the solid phase is added to the system and an active suspension is observed, most of the additional symmetries (3.36) of the unsteady Stokes equation (2.68) are broken by (2.46) and (2.47). The symmetry breaking affects the two scaling symmetries $T_{\text{Sc2}}, T_{\text{Sc3}}$ which only appear in the combined form T_{Sc1} and the linearity symmetry T_{lin}. Furthermore, all additional symmetries of the vorticity equation are broken due to the evolution equation of the orientation angle (2.47). They might be, however, applicable to a passive suspension of disk-shaped particles in two dimensions or spherical particles in the three-dimensional case. As such they are related to the shifting symmetry of the orientation angle (3.50f), which is also only present in the isotropic case of non-polar disk-shaped or spherical passive particles. While not applicable to an active suspension, due to the polarity of an active particle, the orientation symmetry (3.50f) serves as a limiting case in the investigation of multi-particle suspensions, see Sec. 6.2.3. As mentioned earlier in this section in case of the unsteady Stokes equation the choice of $f_{i,G}$ is restricted and only a constant space shift is allowed. This is not the case if the full Navier-Stokes equation is employed. In this case the system of equations contains either the classical Galilean symmetry if $\mathfrak{D} \neq 1$ or the generalised Galilean symmetry if $\mathfrak{D} = 1$.

It is necessary to emphasise that although the unsteady Stokes equation itself is linear, the linear symmetry (3.36g) is broken by (2.46) and (2.47), i.e. it is no longer a symmetry of the entire system of equations. Nevertheless, as the information about the exact position of the particles is lost in the homogenised model (see Sec. 5), the system of averaged equations (5.132) contains the linearity symmetry (3.36g) if the convective terms are neglected. The Couette-Poiseuille flow (Fig. 6.29) is an example for the application of this symmetry, because it can be considered as a superposition of a Couette and a Poiseuille flow. Notably, the linearity symmetry of the vorticity equation is still not part of the transformation group of the averaged system, because (2.47) has been used directly to derive the transport equation for the averaged orientation (5.39). On a side note, in case of a passive suspension with circular or spherical particles the additional symmetries of the vorticity equation might be applicable, a setup, which is outside the scope of the present work.

7.2.1. Statistical theory

In the next step, a statistical description of an active suspension is derived. Solely based on the three multi-dimensional sample space variables V_i, X_{ip} and b_p, which are related to the three physical variables velocity U_i, particle position χ_{ip} and orientation β_p, the PDF description of a system contains all statistical information. The derivation is based on first principles, i.e. the conservation of mass and momentum. It should be noted, while the derivation for the PDF hierarchy was carried out in two dimensions, the adaption to three dimensions is straightforward, as only the terms describing the particle rotation need to be adapted. Similar to the LMN hierarchy [142, 153, 157] an infinite hierarchy of transport equations for the multi-point joint PDF for the three aforementioned variables is derived [51]. Comparably to turbulence research the PDF hierarchy for an active suspension reveals a closure problem, due to being an infinite hierarchy. While it is not solvable directly, the PDF hierarchy shows interesting properties. First and foremost, it consists only of linear equations, even though it contains an equivalent term $\sum_{k=1}^{K} V_i \partial_{\,K} f / \partial_{\,k} x_i$ to the convective term in the physical space. Furthermore, the PDF transports information about the entire statistic of the system, hence, containing all statistical moments. Subsequently, it is possible to derive statistical models for an active suspension directly from the PDF hierarchy, which has been shown in Sec. 5.2.5 for the homogenised two-phase model. In fact, all statistical models are part of the PDF equations. In order to derive such a model one needs an appropriate termination condition for the hierarchy and model equations for terms of a higher order. In case of the homogenised model, the desired output is the average of the physical quantities, i.e the first moment of the single-point PDF. Accordingly, all information about higher moments such as covariance or multi-point correlations is lost. It is necessary to find an appropriate model for the emerging unclosed terms, which are multi-variable moments of second order.

In combination with the Lie symmetry theory the PDF hierarchy can be used without solving the equations and without introducing artificial termination conditions for the hierarchy of equations. Similar to the Stokes and vorticity equation, all equations in the hierarchy are linear. Hence, additionally to the classical symmetries of the physical space (Sec. 3.5), it contains a linear symmetry, which allows to form the sum of arbitrary solutions of the hierarchy. Due to the specific properties of a PDF, particularly the reduction property (3.66), two variants of the linear transformation are possible. One was introduced by Wacławczyk et al. [202] as shape symmetry, the other as intermittency symmetry.

7.3. Particle-resolved simulations

In Sec. 4 a solver for the Janus particle model, implemented as part of the BoSSS framework, is presented. No additional simplifications were introduced, hence, the XNSERO solver carries out DNS. The solid phase and the fluid phase are solved separately. The two phases are connected by the interface interactions, i.e. the boundary conditions acting on the fluid phase at the particle surface and the hydrodynamic forces and torques acting on each particle. All equations considered separately are linear, because the fluid phase is described by the unsteady Stokes equation. For a single phase problem a direct linear solver such as PARDISO might be sufficient to obtain a solution. As revealed by the symmetry analysis, the linear symmetry does not exists in the system of equations describing an active suspension. Due to the aforementioned interface interactions, precisely the active and passive boundary condition and the hydrodynamic forces and torques, an iterative procedure is necessary, which is presented in Alg. 7. In terms of computational costs, the fluid solver and the formulation and execution of the quadrature rules dominate the runtime of the solver, see Fig. 4.15. Especially for high numbers of particles the performance of the Saye-algorithm (Sec. 4.3.2), responsible for the integration on cut-cells, becomes increasingly important. As the Saye-algorithm relies on a subdivision routine for the handling of unfavourable surface configurations in cut-cells, see Fig. 4.3, the number of recursive levels necessary might become large especially for dense suspensions. Improvements to the algorithm in general and the subdivision routine in particular are necessary in order to solve larger problems than presented in this work and to extend the solver to three dimensions.

For the present problem size a direct solver such as PARDISO is the most efficient choice to obtain a solution for the fluid phase as a sub-routine of the XNSERO solver scheme presented in Alg. 7. For even larger systems it might be necessary to switch to more complex solvers, e.g. multigrid solvers, to obtain a solution in a reasonable time span. Consider the presented *standard domain* with $576,240$ DoFs. In case of the highest particle volume fraction, i.e. $\alpha^S = 0.39$, this leads to approximately $43,938$ DoFs per process in the fluid phase if eight cores are used. In case of such a comparably small number of DoFs, PARDISO is still on par with multigrid solvers, see Kummer et al. [127].

Besides the performance challenges, the model itself poses difficulties to the implementation, which are necessary to discuss. When considering the flow field of a Stokes dipole, four singularities immediately catch the readers attentions. Two singularities are located at the Northern and Southern side of the particle surface, where the active and passive boundaries are connected. The other two singularities are located at the westernmost and easternmost points of the surface, where the up- and downstream of the Northern and Southern side of the particle meet. Due to the discontinuous nature of the XDG method, such singularities are handled well by the fluid solver, especially if located directly at a cell boundary. If the singular point is located within a numerical cell the ansatz polynomials need to be capable of capturing the singularity. While this necessarily introduces an error into the problem, this error can be reduced by either increasing the polynomial order of the ansatz functions or by choosing a sufficiently small cell size $h^\Gamma \leq h^K$ at the surface of the particles. To achieve small values of h^Γ it might be useful to employ AMR techniques, which are readily available in BoSSS. AMR is most useful in dilute suspensions, where enough particle-free spaces exist where larger grid sizes are acceptable. For dense suspensions the additional costs of the AMR routines might outweigh the benefits of a coarser background grid. Hence, for the multi-particle suspensions no AMR technique was applied (Fig. 6.15), whereas AMR is used to investigate the collision between a particle and the wall, see Fig. 4.12. If no AMR is applied, an appropriate global mesh size has to be selected to minimize the error, while keeping the complexity of the problem contained.

The purpose of the collision model is twofold. On the one hand, it is necessary to ensure a minimal distance between the particles based on the numerical grid of the fluid solver. The minimal distance is defined by the cell diameter h^Γ at the particle surface, because the Saye-algorithm requires the particles to be at least one cell apart to be able to distinguish between particles. Hence, with smaller cell diameters particles are allowed to come closer towards each other. In the hypothetical case of infinite spatial and temporal resolution, i.e $h^\Gamma \to 0$ and $\Delta t \to 0$, no collision model would be necessary. The reason is, that in an ideal incompressible flow no collision between two objects can occur. The pressure would become large and forces the two objects to separate. However, physical effects, such as surface roughness, breakdown of lubrication, weak interaction forces and entanglement of cilia and flagella require a different handling of small gaps between particles than the bulk fluid phase. For very small gaps between particles the assumption of a continuum is no longer valid. However, assuming a particle size of $a = 10^{-6}$ and a mean free path of the molecules in the surrounding fluid of the order of $\lambda \approx 10^{-10}$ delivers a minimum gap size of $r = 10^{-3}a$ where one would expect the onset of a Knudsen flow with a Knudsen number of $\mathrm{Kn} = \lambda / r \approx 0.1$, the Navier-Stokes (2.67) and Stokes equation (2.68) are no longer valid. Direct interaction forces such as the van der Waals force are in general short ranged. Thus, interactions based on van der Waals forces between ideal surfaces also require small gap sizes. However, given non-ideal surfaces and ciliated particles, such forces might become relevant on much larger scales. It is known, that cilia can increase adhesion by van der Waals forces, which was studied by analysing the foot of the golden mussel *Limnoperna fortunei* [8]. The length of an individual cilium might vary depending on the organism. Let's assume a length of $L^{\mathrm{Cil}} = 0.1a$ for a microorganism [160]. Hence, already for a gap size of a tenth of the particle length one can expect weak interaction forces. Furthermore, cilia or flagella of neighbouring particles might entangle, leading to additional mechanical interactions forces between two particles. Hence, the choice of $h^K = 0.1a$ in the multi-particle simulations (Sec. 6.2) is reasonable.

The particle solver of XNSERO contains a formulation for the Newton-Euler equations (2.54), (2.55) and the evolution of the position and the orientation of the particle (2.46), (2.47) which depends only on the previous particle solutions and the current solution of the flow field. A method of third order is chosen, given by (4.63a)-(4.64b). For the presented results the simulations were carried out with a polynomial order of $k = 2$ for the fluid velocity. If the polynomial order of the XDG ansatz polynomials is increased it might be necessary to also change the integration method of the particle solver in order to preserve the high-order characteristics of the entire XNSERO solver.

7.4. Homogenised fluid-particle simulations

Due to high computational costs, large systems with thousands of particles are currently not possible to simulate with the XNSERO solver. Hence, the homogenised model is introduced, which is based on volume averaged physical quantities of both phases, see Sec. 5. Results are presented for a planar configuration, leading to one-dimensional profiles. Nevertheless, the underlying system, including the particle behaviour, is modelled in three spatial dimensions. The averages of the fluid and particle velocities, the fluid pressure, the particle rotational velocity, the particle orientation and the volume fraction of the fluid and the particle phase together describe a new pseudo-material, which occupies the entire domain. The transport equations for all aforementioned variables need to be solved for all space-time points, i.e. at any point in the domain both constituting phases are always present.

Instead of using the fluid Reynolds number Re, the mixture Reynolds number Re^M is introduced. It is defined by the mixture viscosity μ^M, which accounts for the increased resistance towards deformation due to the presence of the particles [110]. The concept of a mixture viscosity was first introduced by Einstein [68, 69], however, to account for non-spherical particles a version introduced by Ishii and Zuber [110], Ishii and Hibiki [109], and Pabst et al. [164] is employed, see (5.51). The mixture viscosity is a function of the aspect ratio ε, the local solid phase volume fraction α^S and the maximum volume fraction α^S_{max}. Depending on the exact shape of the particles, α^S_{max} takes values between zero and unity. The limiting case of $\alpha^S_{max} = 1$ is only reached for ordered rectangular cuboids in three dimensions. Packings of other particles exhibit gaps that cannot be filled with evenly shaped particles. For example, the highest possible packing fraction for uniform spheres is $\alpha^S_{max} = \pi/\sqrt{18} \approx 0.74$, which is known as Kepler conjecture [88]. This value is only reached in an ordered state, the maximum random packing fraction is $\alpha^S_{max} \approx 0.64$ for spherical particles [198]. For ellipsoidal particles the maximum random packing fraction is increased up to $\alpha^S_{max} = 0.74$ [39, 60]. The mixture Reynolds number vanishes in the limiting case, where $\alpha^S = \alpha^S_{\text{max}}$. Thus, the viscosity becomes infinite and the suspension behaves similarly to a solid object. But even before α^S_{max} is reached, the suspension begins to freeze, i.e the suspension glassifies. This effect is noticeable in an active suspension, for example, when the state of an *active solid* is reached, see Fig. 6.31 and Fig 6.32. In the opposing case, where the solid phase volume fraction vanishes, i.e. a single phase flow is obtained, the mixture Reynolds number equals the unmodified fluid Reynolds number. The influence of the averaged particle orientation was not taken into account when modelling the mixture viscosity and the mixture Reynolds number. It is known [47], that some suspensions show shear thinning behaviour, especially if elongated particles are present. Due to the shear rate, the particles orientate themselves towards each other, assuming a sufficient particle density. Layers of particles on top of each other can simply slide off, thus decreasing the mixture viscosity. This would not be the case in a disordered system, as the particles would block each other. Incorporating the dependency on the orientation would surely increase the applicability of the entire model. However, in the present work only planar flows between two infinite planes are considered. Given the results of the DNS for a channel flow with elongated pusher particles (Fig. 6.14) one can assume, that after some time a steady state for the length of the averaged orientation vector is reached (Fig. 6.13). Hence, for the channel flows presented in Sec. 6.3 a constant length of the averaged orientation vector is assumed, thus, it is not necessary to model the mixture viscosity based on the particle orientation.

Due to the averaging process additional unclosed terms occur in the equations for the homogenised model. One type of terms describes interface interaction forces, which are modelled as linear combination of known forces. Such a procedure is well established in the derivation of volume averaged models, see for example Ishii and Hibiki [109]. The other class of unclosed terms are of the same type as the Reynolds stress tensor in the RANS equations of turbulence research. In the present work a phenomenological approach to model these terms is chosen. The Boussinesq ansatz is used (5.107) as a foundation. Phenomena such as the attraction of active particles towards each other and towards solid walls are then used to describe the generalised turbulent kinetic energy. The diffusion coefficient is modelled on the assumption that collisions between particles have a diffusive effect on the distribution of the linear and rotational momentum. Thus, the mixture Reynolds number is employed to model collisions and friction within the solid phase. The results obtained with this model are in good agreement both with the DNS carried out in this work and the literature about similar planar flows. However, there is no guarantee that such an approach results in a complete model, which is applicable to a wide range of configurations. A forward-looking approach to define model equation is presented by Klingenberg and Oberlack [121] in the context of turbulence research. Based on a full set of Lie-symmetries, i.e. containing both classical symmetries of the Navier-Stokes equation and statistical symmetries, Klingenberg and Oberlack [121] derive a more general turbulence model compared to existing models. The resulting modified $k - \varepsilon$ model is capable of improving the results of classical models [121, 120]. Due to the structural similarities of the classical and the statistical symmetries of an active suspension towards their counterpart in turbulence research it is expected that this approach is transferable to the present problem.

7.5. Connecting data and theory

The classical and the statistical symmetries are used to analyse data provided by simulations carried out with the XNSERO solver and the homogenised model. The focus is particularly on the statistical symmetries. The shape symmetry is applied to the PDF of the minimal distance towards the next particle (6.8), the relative orientation (6.11) and the particle velocity (6.16). The intermittency symmetry is used to derive the exponential distribution of the far-field section of the minimal distance PDF, see (6.9). It also appears as the limiting case for the shape symmetry in case of dense suspensions, see for example (6.20). Thus, it is possible to connect commonly known phenomena of active suspension, such as the formation of cluster or emerging chaotic states, to the theoretical foundations.

In case of the joint intermittency symmetry the new names *cluster* or *phase separation* symmetry are proposed. The ideal, discrete version of this symmetry is given by (6.22). Considering that the boundaries between different *active phases* might not necessarily be sharp, a second version of the symmetry is given (6.23), which allows a range of values for the velocity and orientation within the cluster or phase. The usage of the term *cluster* or *phase separation* depends on the size of the emerging structures. While clusters in the comparably small systems analysed with the BoSSS code are restricted to a small space, *active phases* in the results for the homogenised model might consist of a large number of particles and occupy significant percentages of the domain. It is possible to identify three different *active phases* in analogy to the aggregate states of normal matter. In this analogy, the particles are molecules of a new pseudo-material. An *active gas* is characterised by a particle density close to zero, i.e. the mean free path between particles is large, and the fluid behaves similar to a single phase flow with the same characteristic velocity profiles. The interface towards the *active liquid* is sharp and kinks and jumps are visible in the velocity profiles, see Fig. 6.31 and Fig. 6.32. The *active solid* phase is characterised by high particle densities and almost constant velocities, especially for the particle phase. The interface towards the *active liquid* phase is, however, less sharp than the interface between the *active gas* and *active liquid* phase. Nevertheless, while observing the Poiseuille flow with non-uniform initial particle distribution, a kink in the profile of the particle density at the solid-liquid interface becomes visible, see Fig. 6.32. In fact, in the presented simulations, the *active solid* behaves similar to a glass in the sense that it represents a frozen melt. The *active liquid* phase poses a intermediate state, where fluid and particles can move relatively freely, which becomes visible in the averaged quantities by comparably large gradients. The deterministic term of the *phase separation* symmetry describes both, the deterministic behaviour of the fluid phase in the *active gas* and the constant particle velocity in case of the *active solid* phase. The behaviour of the other phase, i.e. the solid phase in the *active gas* and the fluid phase in the *active solid*, is then described by the chaotic term of the *phase separation* symmetry. Furthermore, the separation into two phases, especially the sharp interface between the *active gas* and the *active liquid* represents an action of the *phase separation* symmetry (6.22). The deterministic term is related to the almost constant dilute volume fraction of the particles in the *active gas* and the *active liquid* and the *active solid* are described by the stochastic term.

A separation into different phases has also been observed in experiments and other numerical studies [24, 36, 193, 195]. For example, Buttinoni et al. [36] observed in experiments the formations of clusters and, with increasing particles density, the formation of separate phases. They found the main reason for the clustering mechanism to be the self-blocking behaviour of opposing particles. In the present work such a behaviour was examined with a simulation of two particles, see Fig. 6.8. In this minimal example, the particles are able to evade and no blocking occurs. Thus, no stable clusters form in the bulk of a dilute suspension (Fig. 6.16a). Due to the low number of particles, most interactions between particles only involve two particles, hence, evasion is possible. By adding more particles to the experiment, the evasion path might get blocked by the additional particles. The joint PDF of the minimal distance and the alignment reveals the blocking mechanism in case of denser suspensions. In Fig. 6.21a a clear maximum for the joint PDF is visible at $(1.2, \pi)$, i.e. for a state where two particles are in contact at their westernmost or easternmost points with opposing orientation vectors. According to Buttinoni et al. [36] the blocking mechanism is the sole reason for the formation of clusters in the case of their experiments with spherical Janus particles. In the case of ellipse shaped particles, alignment effects reinforce the formation of clusters, as indicated by the joint PDF of the minimal distance and alignment for the densest suspension, see Fig. 6.21b. In the current setup, hydrodynamic interactions play a role in the formation of clusters, in contrast to a setup with spherical particles Buttinoni et al. [36]. According to the flow field of a Stokes dipole (1.5) particles with a parallel or opposing orientation attract each other, whereas a perpendicular relative orientation of two particles causes a repulsion. Due to the most likely parallel or opposing alignment of the particles (Fig. 6.21), particles are mostly attracted towards another by the hydrodynamic interactions, especially in the case of denser suspensions. Hence, stronger connections within a cluster are formed. Furthermore, if an additional background flow is present, e.g. the Poiseuille flow caused by the pressure gradient in the case of the experiments presented in Fig. 6.27 and Fig. 6.32, interactions forces between the fluid and the particles have to be taken into account. The difference between the averaged fluid and particle velocities causes lift forces, which in return cause phase separations. In the presented results for the homogenised model, see Sec. 6.3, the Saffman-force was the main cause for the phase separation in Fig. 6.31 and Fig. 6.32. In conclusion, by using the *phase separation* symmetry it is possible to connect a well known phenomenon such as the clustering and phase separation of an active suspension to the underlying theory.

In the introduction to this work (Sec. 1) the term active turbulence was mentioned. While the seemingly chaotic behaviour of an active suspension explains the choice of the term, differences towards classical hydrodynamic turbulence are readily apparent. In a low-Reynolds active suspension no energy cascade exists [4], which is one of the defining features of inertia driven turbulence. Furthermore, clear structures are visible in the results of the simulations, which in a way contradict the previously made assumption of chaotic or turbulent behaviour. These structures are so pronounced that the terms *active gas*, *active liquid* and *active solid* were introduced. These active aggregate states are not products of chance, but are linked to the underlying theory via the *phase separation* symmetry (6.22), (6.23). The PDFs of the velocity and the minimum distance also show a decreasing variance with increasing particle density for the investigated systems. However, especially the particle velocity PDF shows a heavy-tailed behaviour. By this term, a PDF is described, which in the outer areas or tails decreases more slowly than a comparable Gaussian normal distribution. The heavy-tailed nature of the PDF makes comparably large velocities more likely and it can be assumed that intermittency occurs. In this context, intermittency means the sudden outbreak of large velocities in a previously uniform velocity field [135, 206], i.e. chaotic behaviour in a otherwise deterministic system. While emergent structures indicate a deterministic system, the presence of a non-Gaussian particle velocity PDF, where the non-Gaussian behaviour is reinforced by increasing particle densities, and the resulting assumed intermittent behaviour indicate a chaotic state of the active suspension. Both states - chaos and determinism - are present in an active suspension; an active suspension is, thus, a truly intermittent system.

Bibliography

[1] J. Agudo, C. Illigmann, G. Luzi, A. Laukart, A. Delgado, and A. Wierschem. “Shear-induced incipient motion of a single sphere on uniform substrates at low particle Reynolds numbers”. In: *J. Fluid Mech.* 825 (2017), pp. 284–314.

[2] C. Alappat, A. Basermann, A. R. Bishop, H. Fehske, G. Hager, O. Schenk, J. Thies, and G. Wellein. “A Recursive Algebraic Coloring Technique for Hardware-Efficient Symmetric Sparse Matrix-Vector Multiplication”. In: *ACM Trans. Parallel Comput.* 7.3 (2020).

[3] S.-V. Albers and K. F. Jarrell. “The archaellum: how Archaea swim”. In: *Front. Microbiol.* 6 (2015), p. 23.

[4] R. Alert, J. Casademunt, and J.-F. Joanny. “Active turbulence”. In: *Annu. Rev. Condens. Matter Phys.* 13 (2022), pp. 143–170.

[5] R. Alonso-Matilla, B. Ezhilan, and D. Saintillan. “Microfluidic rheology of active particle suspensions: Kinetic theory”. In: *Biomicrofluidics* 10.4 (2016), p. 043505.

[6] A. N. Alsante, D. C. O. Thornton, and S. D. Brooks. “Ocean Aerobiology”. In: *Front. Microbiol.* 12 (2021).

[7] P. W. Anderson. “Absence of diffusion in certain random lattices”. In: *Phys. rev.* 109.5 (1958), p. 1492.

[8] G. R. Andrade, J. L. F. de Araújo, A. Nakamura Filho, A. C. P. Guañabens, M. D. de Carvalho, and A. V. Cardoso. “Functional Surface of the golden mussel’s foot: morphology, structures and the role of cilia on underwater adhesion”. In: *Mater. Sci. Eng. C* 54 (2015), pp. 32–42.

[9] D. N. Arnold. “An interior penalty finite element method with discontinuous elements”. In: *SIAM J. Numer. Anal.* 19.4 (1982), pp. 742–760.

[10] D. N. Arnold, F. Brezzi, B. Cockburn, and L. D. Marini. “Unified analysis of discontinuous Galerkin methods for elliptic problems”. In: *SIAM J. Numer. Anal.* 39.5 (2002), pp. 1749–1779.

[11] I. Babuška. “The finite element method with Lagrangian multipliers”. In: *Numer. Math. (Heidelb.)* 20.3 (1973), pp. 179–192.

[12] I. Babuška. “The finite element method with penalty”. In: *Math. Comput.* 27.122 (1973), pp. 221–228.

[13] I. Babuška and M. Zlámal. “Nonconforming elements in the finite element method with penalty”. In: *SIAM J. Numer. Anal.* 10.5 (1973), pp. 863–875.

[14] D. S. Banks and C. Fradin. “Anomalous diffusion of proteins due to molecular crowding”. In: *Biophys. J.* 89.5 (2005), pp. 2960–2971.

[15] G. Barnocky and R. H. Davis. “Elastohydrodynamic collision and rebound of spheres: experimental verification”. In: *Phys. Fluids* 31.6 (1988), pp. 1324–1329.

[16] A. Baskaran and M. C. Marchetti. “Statistical mechanics and hydrodynamics of bacterial suspensions”. In: *Proc. Natl. Acad. Sci. USA* 106.37 (2009), pp. 15567–15572.

[17] A. Be’er, B. Ilkanaiv, R. Gross, D. B. Kearns, S. Heidenreich, M. Bär, and G. Ariel. “A phase diagram for bacterial swarming”. In: *Commun. Phys.* 3.1 (2020), p. 66.

[18] C. Bechinger, R. Di Leonardo, H. Löwen, C. Reichhardt, G. Volpe, and G. Volpe. “Active particles in complex and crowded environments”. In: *Rev. Mod. Phys.* 88 (4 2016), p. 045006.

[19] L. Beck. “Numerical Integration over implicitly defined Surfaces and Volumes”. MA thesis. Technische Universität Darmstadt, 2018.

[20] C. Beckermann, H.-J. Diepers, I. Steinbach, A. Karma, and X. Tong. “Modeling melt convection in phase-field simulations of solidification”. In: *J. Comput. Phys.* 154.2 (1999), pp. 468–496.

[21] G. v. d. Bergen. “A fast and robust GJK implementation for collision detection of convex objects”. In: *J. Graph. Tools* 4.2 (1999), pp. 7–25.

[22] A. P. Berke, L. Turner, H. C. Berg, and E. Lauga. “Hydrodynamic attraction of swimming microorganisms by surfaces”. In: *Phys. Rev. Lett.* 101.3 (2008), p. 038102.

[23] L. Berthier and J. Kurchan. “Non-equilibrium glass transitions in driven and active matter”. In: *Nat. Phys.* 9.5 (2013), pp. 310–314.

[24] J. Bialké, H. Löwen, and T. Speck. “Microscopic theory for the phase separation of self-propelled repulsive disks”. In: *EPL* 103.3 (2013), p. 30008.

[25] J. R. Blake. “A note on the image system for a stokeslet in a no-slip boundary”. In: *Math. Proc. Camb. Philos. Soc.* 70.2 (1971), pp. 303–310.

[26] J. R. Blake. “A spherical envelope approach to ciliary propulsion”. In: *J. Fluid Mech.* 46.1 (1971), pp. 199–208.

[27] J. R. Blake. “Infinite models for ciliary propulsion”. In: *J. Fluid Mech.* 49.2 (1971), pp. 209–222.

[28] G. Bluman and S. Anco. *Symmetry and integration methods for differential equations*. Vol. 154. Springer Science & Business Media, 2008.

[29] M. Bollhöfer, A. Eftekhari, S. Scheidegger, and O. Schenk. “Large-scale Sparse Inverse Covariance Matrix Estimation”. In: *SIAM J. Sci. Comput.* 41.1 (2019), A380–A401.

[30] M. Bollhöfer, O. Schenk, R. Janalik, S. Hamm, and K. Gullapalli. “State-of-the-Art Sparse Direct Solvers”. In: *Parallel Algorithms in Computational Science and Engineering*. Ed. by A. Grama and A. H. Sameh. Cham: Springer International Publishing, 2020, pp. 3–33.

[31] L. Boltzmann. *Vorlesung über Gastheorie: 2. Teil*. Leipzig: J.A. Barth, 1896.

[32] L. Boltzmann. “Über die Beziehung zwischen dem zweiten Hauptsatz der mechanischen Wärmetheorie und der Wahrscheinlichkeitsrechnung respektive den Sätzen über das Wärmegleichgewicht”. In: *Sitzungsber. d. k. Akad. der Wissenschaften zu Wien II*. Vol. 76. Reprint in Wissenschaftliche Abhandlungen von Ludwig Boltzmann, Band II., S. 164–223, Dr. Fritz Hasenöhrl, Publisher: Johann Ambrosius Barth, Leipzig 1909. Wiener Berichte, 1877, pp. 373–435.

[33] B. van den Bout, T. van Asch, W. Hu, C. X. Tang, O. Mavrouli, V. G. Jetten, and C. J. van Westen. “Towards a model for structured mass movements: The OpenLISEM Hazard model 2.0 a”. In: *Geosci. Model Dev.* 14.4 (2021), pp. 1841–1864.

[34] V. Bratanov, F. Jenko, and E. Frey. “New class of turbulence in active fluids”. In: *Proc. Natl. Acad. Sci. USA* 112.49 (2015), pp. 15048–15053.

[35] F. Brezzi. “On the existence, uniqueness and approximation of saddle-point problems arising from Lagrangian multipliers”. In: *Publ. mathématiques et informatique de Rennes* S4 (1974), pp. 1–26.

[36] I. Buttinoni, J. Bialké, F. Kümmel, H. Löwen, C. Bechinger, and T. Speck. “Dynamical clustering and phase separation in suspensions of self-propelled colloidal particles”. In: *Phys. Rev. Lett.* 110.23 (2013), p. 238301.

[37] V. O. Bytev. “Group properties of the Navier-Stokes equations”. Russian. In: *Chislennye Metody Mehaniki Sploshnoi Sredy (Novosibirsk)* 3 (1972), pp. 13–17.

[38] P. Caussignac and R. Touzani. “Solution of three-dimensional boundary layer equations by a discontinuous finite element method, Part II: Implementation and numerical results”. In: *Comput. Methods Appl. Mech. Eng.* 79.1 (1990), pp. 1–20.

[39] P. Chaikin, A. Donev, W. Man, F. H. Stillinger, and S. Torquato. “Some observations on the random packing of hard ellipsoids”. In: *Ind. Eng. Chem. Res.* 45.21 (2006), pp. 6960–6965.

[40] Y.-C. Chang, T. Hou, B. Merriman, and S. Osher. “A level set formulation of Eulerian interface capturing methods for incompressible fluid flows”. In: *J. Comput. Phys.* 124.2 (1996), pp. 449–464.

[41] G. Chatzipirpiridis, C. de Marco, E. Pellicer, O. Ergeneman, J. Sort, B. J. Nelson, and S. Pané. “Template-Assisted Electroforming of Fully Semi-Hard-Magnetic Helical Microactuators”. In: *Adv. Eng. Mater.* 20.9 (2018), p. 1800179.

[42] G. Chavent and B. Cockburn. “The local projection-discontinuous-Galerkin finite element method for scalar conservation laws”. In: *ESAIM: Math. Model. Numer. Anal.* 23.4 (1989), pp. 565–592.

[43] A. T. Chwang and T. Y.-T. Wu. “Hydromechanics of low-Reynolds-number flow. Part 2. Singularity method for Stokes flows”. In: *J. Fluid Mech.* 67.4 (1975), pp. 787–815.

[44] B. Cockburn, G. Kanschat, and D. Schötzau. “The local discontinuous Galerkin method for the Oseen equations”. In: *Math. Comput.* 73.246 (2004), pp. 569–593.

[45] B. Cockburn, G. Kanschat, and D. Schötzau. “The local discontinuous Galerkin method for linearized incompressible fluid flow: a review”. In: *Comput. Fluids* 34.4-5 (2005), pp. 491–506.

[46] B. Cockburn and C.-W. Shu. “TVB Runge-Kutta local projection discontinuous Galerkin finite element method for conservation laws. II. General framework”. In: *Math. Comput.* 52.186 (1989), pp. 411–435.

[47] M. M. Cross. “Rheology of non-Newtonian fluids: a new flow equation for pseudoplastic systems”. In: *J. Colloid Sci.* 20.5 (1965), pp. 417–437.

[48] R. H. Davis, J.-M. Serayssol, and E. Hinch. “The elastohydrodynamic collision of two spheres”. In: *J. Fluid Mech.* 163 (1986), pp. 479–497.

[49] J. Derksen and R. Larsen. “Drag and lift forces on random assemblies of wall-attached spheres in low-Reynolds-number shear flow”. In: *J. Fluid Mech.* 673 (2011), pp. 548–573.

[50] B. Deußen, A. Jayaram, F. Kummer, Y. Wang, T. Speck, and M. Oberlack. “High-order simulation scheme for active particles driven by stress boundary conditions”. In: *J. Phys. Condens. Matter* 33.24 (2021), p. 244004.

[51] B. Deußen, M. Oberlack, and Y. Wang. “Probability theory of active suspensions”. In: *Phys. Fluids* 33.6 (2021), p. 061902.

[52] B. Deußen. *Theoretical and numerical investigation of active suspensions: Determinism, chaos and intermittency - Homogenised Model*. TUdatalib, Dataset. DOI: 10.48328/tudatalib-986. 2022.

[53] B. Deußen. *Theoretical and numerical investigation of active suspensions: Determinism, chaos and intermittency - Particle resolved model*. TUdatalib, Dataset. DOI: 10.48328/tudatalib-985. 2022.

[54] B. Deußen, Y. Wang, and M. Oberlack. *A deterministic two-phase model for an active suspension with non-spherical active particles using Eulerian spatial averaging theory*. TUdatalib, Dataset. DOI: 10.48328/tudatalib-781. 2021.

[55] B. Deußen, Y. Wang, and M. Oberlack. “A deterministic two-phase model for an active suspension with non-spherical active particles using the Eulerian spatial averaging theory”. In: *Phys. Fluids* 34.2 (2022), p. 023302.

[56] A. Dhar, P. S. Burada, and G. P. R. Sekhar. “Hydrodynamics of active particles confined in a periodically tapered channel”. In: *Phys. Fluids* 32.10 (2020), p. 102005.

[57] M. Dhiman, S. A. Ashutosh, R. Gupta, and K. A. Reddy. “Drag on Sticky and Janus (Slip-Stick) spheres confined in a channel”. In: *J. Fluids Eng.* 142.7 (2020).

[58] D. A. Di Pietro and A. Ern. *Mathematical aspects of discontinuous Galerkin methods*. Vol. 69. Springer Science & Business Media, 2011.

[59] C. Dombrowski, L. Cisneros, S. Chatkaew, R. E. Goldstein, and J. O. Kessler. “Self-Concentration and Large-Scale Coherence in Bacterial Dynamics”. In: *Phys. Rev. Lett.* 93 (9 2004), p. 098103.

[60] A. Donev, I. Cisse, D. Sachs, E. A. Variano, F. H. Stillinger, R. Connelly, S. Torquato, and P. M. Chaikin. “Improving the density of jammed disordered packings using ellipsoids”. In: *Science* 303.5660 (2004), pp. 990–993.

[61] J. Douglas and T. Dupont. “Interior penalty procedures for elliptic and parabolic Galerkin methods”. In: *Comput. Methods Appl. Sci.* Springer, 1976, pp. 207–216.

[62] K. Drescher, J. Dunkel, L. H. Cisneros, S. Ganguly, and R. E. Goldstein. “Fluid dynamics and noise in bacterial cell–cell and cell–surface scattering”. In: *Proc. Natl. Acad. Sci. USA* 108.27 (2011), pp. 10940–10945.

[63] D. A. Drew. “Mathematical modeling of two-phase flow”. In: *Annu. Rev. Fluid Mech.* 15.1 (1983), pp. 261–291.

[64] O. Druzhinin and S. Elghobashi. “Direct numerical simulations of bubble-laden turbulent flows using the two-fluid formulation”. In: *Phys. Fluids* 10.3 (1998), pp. 685–697.

[65] J. Dunkel, S. Heidenreich, M. Bär, and R. E. Goldstein. “Minimal continuum theories of structure formation in dense active fluids”. In: *New J. Phys.* 15.4 (2013), p. 045016.

[66] J. Dunkel, S. Heidenreich, K. Drescher, H. H. Wensink, M. Bär, and R. E. Goldstein. “Fluid Dynamics of Bacterial Turbulence”. In: *Phys. Rev. Lett.* 110 (22 2013), p. 228102.

[67] A. Einstein. “Über die von der molekularkinetischen Theorie der Wärme geforderte Bewegung von in ruhenden Flüssigkeiten suspendierten Teilchen”. In: *Ann. Phys.* 322.8 (1905), pp. 549–560.

[68] A. Einstein. “Eine neue Bestimmung der Moleküldimensionen”. PhD thesis. ETH Zurich, 1905.

[69] A. Einstein. “Berichtigung zu meiner arbeit: Eine neue Bestimmung der Moleküldimensionen”. In: *Ann. Phys.* 339.3 (1911), pp. 591–592.

[70] Erbe, E. and Pooley, C. *Image Number K11077-1*. `https://www.ars.usda.gov/oc/images/photos/mar05/k11077-1/`. Accessed: 2022-08-12. (2005).

[71] F. G. Ergin. “Hydrodynamics of Euglena Gracilis during locomotion”. In: *J. Hydrodynam. B* 33.1 (2021), pp. 120–126.

[72] C. Ericson. *Real-time collision detection*. The Morgan Kaufmann series in interactive 3D technology. Amsterdam and Boston: Morgan Kaufmann Publishers, 2005.

[73] A. A. Evans, T. Ishikawa, T. Yamaguchi, and E. Lauga. “Orientational order in concentrated suspensions of spherical microswimmers”. In: *Phys. Fluids* 23.11 (2011), p. 111702.

[74] B. Ezhilan and D. Saintillan. “Transport of a dilute active suspension in pressure-driven channel flow”. In: *J. Fluid Mech.* 777 (2015), pp. 482–522.

[75] H. Faxén. “Der Widerstand gegen die Bewegung einer starren Kugel in einer zähen Flüssigkeit, die zwischen zwei parallelen ebenen Wänden eingeschlossen ist”. In: *Ann. Phys.* 373.10 (1922), pp. 89–119.

[76] J. Feng and D. Joseph. “The unsteady motion of solid bodies in creeping flows”. In: *J. Fluid Mech.* 303 (1995), pp. 83–102.

[77] G. Frangipane, D. Dell’Arciprete, S. Petracchini, C. Maggi, F. Saglimbeni, S. Bianchi, G. Vizsnyiczai, M. L. Bernardini, and R. Di Leonardo. “Dynamic density shaping of photokinetic E. coli”. In: *Elife* 7 (2018), e36608.

[78] K. Franke and H. Gruler. “Galvanotaxis of human granulocytes: electric field jump studies”. In: *Eur. Biophys. J.* 18.6 (1990), pp. 334–346.

[79] J. Friedrich. “Probability density functions in homogeneous and isotropic magnetohydrodynamic turbulence”. In: *Atmosphere* 11.4 (2020), p. 382.

[80] E. G. Gilbert, D. W. Johnson, and S. S. Keerthi. “A fast procedure for computing the distance between complex objects in three-dimensional space”. In: *IEEE J. Robot. Autom* 4.2 (1988), pp. 193–203.

[81] P. Gondret, M. Lance, and L. Petit. “Bouncing motion of spherical particles in fluids”. In: *Phys. Fluids* 14.2 (2002), pp. 643–652.

[82] D. Gross, W. Hauger, J. Schröder, and W. A. Wall. *Technische Mechanik 3: Kinetik*. Springer-Verlag, 2019.

[83] A. Guttman. “R-trees: A dynamic index structure for spatial searching”. In: *Proceedings of the 1984 ACM SIGMOD international conference on Management of data*. 1984, pp. 47–57.

[84] B. M. Haines, I. S. Aranson, L. Berlyand, and D. A. Karpeev. “Effective viscosity of dilute bacterial suspensions: a two-dimensional model”. In: *Phys. Biol.* 5.4 (2008), p. 046003.

[85] B. M. Haines, A. Sokolov, I. S. Aranson, L. Berlyand, and D. A. Karpeev. “Three-dimensional model for the effective viscosity of bacterial suspensions”. In: *Phys. Rev. E* 80.4 (2009), p. 041922.

[86] E. Hairer, G. Wanner, and S. P. Nørsett. *Solving Ordinary Differential Equations I: Nonstiff problems*. Springer-Verlag, 1993.

[87] A. Halder and Y. Sun. “Biocompatible propulsion for biomedical micro/nano robotics”. In: *Biosens. Bioelectron.* 139 (2019), p. 111334.

[88] T. C. Hales. “A proof of the Kepler conjecture”. In: *Ann. Math.* (2005), pp. 1065–1185.

[89] M. Hamermesh. “Group theory”. In: *Mathematical Tools for Physicists*. Wiley Online Library, 2005, pp. 189–212.

[90] J. Happel and H. Brenner. *Low Reynolds number hydrodynamics: with special applications to particulate media*. Vol. 1. Springer Science & Business Media, 2012.

[91] S. Henkes, Y. Fily, and M. C. Marchetti. “Active jamming: Self-propelled soft particles at high density”. In: *Physical Review E* 84.4 (2011), p. 040301.

[92] Z. D. Hensley and D. V. Papavassiliou. “Drag coefficient correction for spherical and nonspherical particles suspended in square microducts”. In: *Ind. Eng. Chem. Res.* 53.25 (2014), pp. 10465–10474.

[93] J. P. Hernandez-Ortiz, C. G. Stoltz, and M. D. Graham. “Transport and collective dynamics in suspensions of confined swimming particles”. In: *Phys. Rev. Lett.* 95.20 (2005), p. 204501.

[94] J. P. Hernandez-Ortiz, P. T. Underhill, and M. D. Graham. “Dynamics of confined suspensions of swimming particles”. In: *J. Condens. Matter Phys.* 21.20 (2009), p. 204107.

[95] J. S. Hesthaven and T. Warburton. *Nodal discontinuous Galerkin methods: algorithms, analysis, and applications*. Springer Science & Business Media, 2007.

[96] C. Hirt and B. Nichols. “Volume of fluid (VOF) method for the dynamics of free boundaries”. In: *J. Comput. Phys.* 39.1 (1981), pp. 201–225.

[97] S. F. Hoerner. “Fluid-Dynamic Drag. Theoretical, experimental and statistical information”. In: *SF Hoerner Fluid Dynamics, Vancouver, Printed in the USA, Card Number 64-19666* (1965).

[98] A. Hölzer and M. Sommerfeld. “New simple correlation formula for the drag coefficient of non-spherical particles”. In: *Powder Technol.* 184.3 (2008), pp. 361–365.

[99] A. Hölzer and M. Sommerfeld. “Lattice Boltzmann simulations to determine drag, lift and torque acting on non-spherical particles”. In: *Comput. fluids* 38.3 (2009), pp. 572–589.

[100] Hope, M. *Lufthansa | D-AINE | Airbus A320-271NN (neo) | London Heathrow Airport (LHR/EGLL)*. `flickr.com/photos/mitchulhope/38026410891/`. Accessed: 2022-08-12; This work is licensed under the Creative Commons Attribution-ShareAlike 2.0 Generic (CC BY-SA 2.0) licence. To view a copy of this license, visit `https://creativecommons.org/licenses/by-sa/2.0/`. (2017).

[101] A. C. Hortelão, T. Patiño, A. Perez-Jiménez, À. Blanco, and S. Sánchez. "Enzyme-powered nanobots enhance anticancer drug delivery". In: *Adv. Funct. Mater.* 28.25 (2018), p. 1705086.

[102] F. A. Howes and S. Whitaker. "The spatial averaging theorem revisited". In: *Chem. Eng. Sci.* 40.8 (1985), pp. 1387–1392.

[103] J. R. Howse, R. A. Jones, A. J. Ryan, T. Gough, R. Vafabakhsh, and R. Golestanian. "Self-motile colloidal particles: from directed propulsion to random walk". In: *Phys. Rev. Lett.* 99.4 (2007), p. 048102.

[104] J. Hu, M. Yang, G. Gompper, and R. G. Winkler. "Modelling the mechanics and hydrodynamics of swimming E. coli". In: *Soft matter* 11.40 (2015), pp. 7867–7876.

[105] L. Hufnagel, R. Ketzmerick, T. Kottos, and T. Geisel. "Superballistic spreading of wave packets". In: *Phys. Rev. E* 64.1 (2001), p. 012301.

[106] N. H. Ibragimov. *CRC Handbook of Lie Group Analysis of Differential Equations, Volume I: Symmetries, Exact Solutions, and Conservation Laws*. Boca Raton, FL, USA: CRC Press, 1993.

[107] N. H. Ibragimov. *CRC Handbook of Lie Group Analysis of Differential Equations, Volume II: Applications in Engineering and Physical Science*. Boca Raton, FL, USA: CRC-Press, 1995.

[108] B. M. Irons and R. C. Tuck. "A version of the Aitken accelerator for computer iteration". In: *Int. J. Numer. Methods Eng.* 1.3 (1969), pp. 275–277.

[109] M. Ishii and T. Hibiki. *Thermo-fluid dynamics of two-phase flow*. Springer Science & Business Media, 2006.

[110] M. Ishii and N. Zuber. "Drag coefficient and relative velocity in bubbly, droplet or particulate flows". In: *AIChE journal* 25.5 (1979), pp. 843–855.

[111] J. Jaffre, C. Johnson, and A. Szepessy. "Convergence of the discontinuous Galerkin finite element method for hyperbolic conservation laws". In: *Math Models Methods Appl Sci.* 5.03 (1995), pp. 367–386.

[112] M. James and M. Wilczek. "Vortex dynamics and Lagrangian statistics in a model for active turbulence". In: *Eur Phys J E Soft Matter* 41.2 (2018), p. 21.

[113] A. Jayaram, A. Fischer, and T. Speck. "From scalar to polar active matter: Connecting simulations with mean-field theory". In: *Phys. Rev. E* 101.2 (2020), p. 022602.

[114] G. Joseph, R. Zenit, M. Hunt, and A. Rosenwinkel. "Particle–wall collisions in a viscous fluid". In: *J. Fluid Mech.* 433 (2001), pp. 329–346.

[115] B. Jurado-Sánchez, S. Sattayasamitsathit, W. Gao, L. Santos, Y. Fedorak, V. V. Singh, J. Orozco, M. Galarnyk, and J. Wang. "Self-propelled activated carbon janus micromotors for efficient water purification". In: *Small* 11.4 (2015), pp. 499–506.

[116] A. Kanevsky, M. J. Shelley, and A.-K. Tornberg. "Modeling simple locomotors in Stokes flow". In: *J. Comput. Phys.* 229.4 (2010), pp. 958–977.

[117] S. Kim, S. Lee, J. Lee, B. J. Nelson, L. Zhang, and H. Choi. “Fabrication and manipulation of ciliary microrobots with non-reciprocal magnetic actuation”. In: *Sci. Rep.* 6.1 (2016), pp. 1–9.

[118] G. R. Kirchhoff. *Vorlesungen uber mathematische Physik, Vol. 1*. Leipzig: Teubner, 1876.

[119] D. Klingenberg, M. Oberlack, and D. Pluemacher. “Symmetries and turbulence modeling”. In: *Phys. Fluids* 32.2 (2020), p. 025108.

[120] D. Klingenberg. “Development of novel Reynolds-averaged Navier–Stokes turbulence models based on Lie-symmetry constraints”. PhD thesis. Technische Universität Darmstadt, 2022.

[121] D. Klingenberg and M. Oberlack. “Statistically invariant eddy viscosity models”. In: *Phys. Fluids* 34.5 (2022), p. 055114.

[122] S. Kmiecik, D. Gront, M. Kolinski, L. Wieteska, A. E. Dawid, and A. Kolinski. “Coarse-Grained Protein Models and Their Applications”. In: *Chem. Rev.* 116.14 (2016), pp. 7898–7936.

[123] A. N. Kolmogorov. “Dissipation of energy in the locally isotropic turbulence”. In: *Proc. R. Soc. A: Math. Phys. Sci.* 434.1890 (1991), pp. 15–17.

[124] A. N. Kolmogorov. “The local structure of turbulence in incompressible viscous fluid for very large Reynolds numbers”. In: *Proc. R. Soc. A: Math. Phys. Sci.* 434.1890 (1991), pp. 9–13.

[125] D. Krause and F. Kummer. “An incompressible immersed boundary solver for moving body flows using a cut cell discontinuous Galerkin method”. In: *Comput. fluids* 153 (2017), pp. 118–129.

[126] F. Kummer. “Extended discontinuous Galerkin methods for two-phase flows: the spatial discretization”. In: *Int. J. Numer. Methods Eng.* 109.2 (2017), pp. 259–289.

[127] F. Kummer, J. Weber, and M. Smuda. “BoSSS: A package for multigrid extended discontinuous Galerkin methods”. In: *Comput. Math. Appl.* 81 (2021), pp. 237–257.

[128] U. Küttler and W. A. Wall. “Fixed-point fluid–structure interaction solvers with dynamic relaxation”. In: *Comput. Mech.* 43.1 (2008), pp. 61–72.

[129] J. Langer. “Models of pattern formation in first-order phase transitions”. In: *Directions in Condensed Matter Physics*. 1986, pp. 165–186.

[130] E. Lauga and T. R. Powers. “The hydrodynamics of swimming microorganisms”. In: *Rep. Prog. Phys.* 72.9 (2009), p. 096601.

[131] D. Leighton and A. Acrivos. “The lift on a small sphere touching a plane in the presence of a simple shear flow”. In: *Z. Angew. Math. Phys.* 36.1 (1985), pp. 174–178.

[132] D. Leith. “Drag on nonspherical objects”. In: *Aerosol Sci. Technol.* 6.2 (1987), pp. 153–161.

[133] S. Lem. *Der Unbesiegbare*. German. Trans. by R. Dietrich.
Polish original title: *Niezwyciężony*. Frankfurt am Main: Fischer Taschenbuch Verlag, 1971.

[134] P. Lesaint and P.-A. Raviart. “On a finite element method for solving the neutron transport equation”. In: *Publ. mathématiques et informatique de Rennes* S4 (1974), pp. 1–40.

[135] Y. Li and C. Meneveau. “Origin of non-Gaussian statistics in hydrodynamic turbulence”. In: *Phys. Rev. Lett.* 95.16 (2005), p. 164502.

[136] N. P. Library. *Blue whale.* `https://photolib.noaa.gov/Collections/NOAAs-Ark/Whales/emodule/722/eitem/30624/`. Accessed: 2022-08-12. (2018).

[137] S. Lie. *Theorie der Transformationsgruppen I*. Leipzig: Teubner, 1888.

[138] S. Lie. *Theorie der Transformationsgruppen II*. Leipzig: Teubner, 1890.

[139] S. Lie. *Theorie der Transformationsgruppen III*. Leipzig: Teubner, 1893.

[140] B. Liebchen, D. Marenduzzo, and M. E. Cates. “Phoretic Interactions Generically Induce Dynamic Clusters and Wave Patterns in Active Colloids”. In: *Phys. Rev. Lett.* 118 (26 2017), p. 268001.

[141] M. Lighthill. “On the squirming motion of nearly spherical deformable bodies through liquids at very small Reynolds numbers”. In: *Commun. Pure Appl. Math.* 5.2 (1952), pp. 109–118.

[142] T. Lundgren. “Distribution functions in the statistical theory of turbulence”. In: *Phys. Fluids* 10.5 (1967), pp. 969–975.

[143] V. Magar, T. Goto, and T. J. Pedley. “Nutrient Uptake by a Self-Propelled Steady Squirmer”. In: *Q. J. Mech. Appl. Math.* 56.1 (2003), pp. 65–91.

[144] C. Maggi, J. Simmchen, F. Saglimbeni, J. Katuri, M. Dipalo, F. De Angelis, S. Sanchez, and R. Di Leonardo. “Self-assembly of micromachining systems powered by Janus micromotors”. In: *Small* 12.4 (2016), pp. 446–451.

[145] M. Mandø and L. Rosendahl. “On the motion of non-spherical particles at high Reynolds number”. In: *Powder Technol.* 202.1-3 (2010), pp. 1–13.

[146] M. C. Marchetti, Y. Fily, S. Henkes, A. Patch, and D. Yllanes. “Minimal model of active colloids highlights the role of mechanical interactions in controlling the emergent behavior of active matter”. In: *COCIS* 21 (2016), pp. 34–43.

[147] K. Martens, L. Angelani, R. Di Leonardo, and L. Bocquet. “Probability distributions for the run-and-tumble bacterial dynamics: An analogy to the Lorentz model”. In: *Eur. Phys. J. E. Soft Matter* 35.9 (2012), pp. 1–6.

[148] S. O. Mast. “Mechanics of locomotion in amoeba”. In: *Proc. Natl. Acad. Sci. U.S.A.* 9.7 (1923), pp. 258–261.

[149] R. Matas-Navarro, R. Golestanian, T. B. Liverpool, and S. M. Fielding. “Hydrodynamic suppression of phase separation in active suspensions”. In: *Phys. Rev. E* 90 (3 2014), p. 032304.

[150] D. McKenzie. “The generation and compaction of partially molten rock”. In: *J. Petrol.* 25.3 (1984), pp. 713–765.

[151] I. Mema, V. V. Mahajan, B. W. Fitzgerald, and J. T. Padding. “Effect of lift force and hydrodynamic torque on fluidisation of non-spherical particles”. In: *Chem. Eng. Sci.* 195 (2019), pp. 642–656.

[152] R. Metzler, J.-H. Jeon, A. G. Cherstvy, and E. Barkai. “Anomalous diffusion models and their properties: non-stationarity, non-ergodicity, and ageing at the centenary of single particle tracking”. In: *Phys. Chem. Chem. Phys.* 16 (44 2014), pp. 24128–24164.

[153] A. S. Monin. “Equations of turbulent motion: PMM vol. 31, no. 6, 1967, pp. 1057–1068”. In: *J. Appl. Math. Mech.* 31.6 (1967), pp. 1057–1068.

[154] B. Müller, F. Kummer, and M. Oberlack. “Highly accurate surface and volume integration on implicit domains by means of moment-fitting”. In: *Int. J. Numer. Methods Eng.* 96.8 (2013), pp. 512–528.

[155] N. Narinder, J. R. Gomez-Solano, and C. Bechinger. “Active particles in geometrically confined viscoelastic fluids”. In: *New J. Phys.* 21.9 (2019), p. 093058.

[156] J. Nitsche. “Über ein Variationsprinzip zur Lösung von Dirichlet-Problemen bei Verwendung von Teilräumen, die keinen Randbedingungen unterworfen sind”. In: *Abhandlungen aus dem mathematischen Seminar der Universität Hamburg*. Vol. 36. 1. Springer. 1971, pp. 9–15.

[157] E. A. Novikov. “Kinetic equations for a vortex field”. In: *Soviet Physics Doklady*. Vol. 12. 1968, p. 1006.

[158] M. Oberlack and A. Rosteck. “New statistical symmetries of the multi-point equations and its importance for turbulent scaling laws”. In: *Discrete Contin. Dyn. Syst.-S.* 3.3 (2010), p. 451.

[159] M. Oberlack, M. Wacławczyk, A. Rosteck, and V. Avsarkisov. “Symmetries and their importance for statistical turbulence theory”. In: *Mech. Eng. Rev.* 2.2 (2015), pp. 15–00157.

[160] T. Omori, H. Ito, and T. Ishikawa. “Swimming microorganisms acquire optimal efficiency with multiple cilia”. In: *Proc. Natl. Acad. Sci. U.S.A.* 117.48 (2020), pp. 30201–30207.

[161] J. Orozco, L. A. Mercante, R. Pol, and A. Merkoçi. “Graphene-based Janus micromotors for the dynamic removal of pollutants”. In: *J. Mater. Chem. A* 4.9 (2016), pp. 3371–3378.

[162] C. W. Oseen. “Über die Stokes’sche Formel und über eine verwandte Aufgabe in der Hydrodynamik I”. In: *Ark. Mat. Astr. Fys.* 6.29 (1910), pp. 1–20.

[163] S. Osher and R. Fedkiw. *Level Set Methods and Dynamic Implicit Surfaces*. Springer, 2003.

[164] W. Pabst, E. Gregorová, and C. Berthold. “Particle shape and suspension rheology of short-fiber systems”. In: *J. Eur. Ceram. Soc.* 26.1-2 (2006), pp. 149–160.

[165] V. V. Palyulin, G. Blackburn, M. A. Lomholt, N. W. Watkins, R. Metzler, R. Klages, and A. V. Chechkin. “First passage and first hitting times of Lévy flights and Lévy walks”. In: *New J. Phys.* 21.10 (2019), p. 103028.

[166] M. Paoluzzi, R. Di Leonardo, M. C. Marchetti, and L. Angelani. “Shape and displacement fluctuations in soft vesicles filled by active particles”. In: *Sci. Rep.* 6.1 (2016), pp. 1–10.

[167] E. B. Pitman and L. Le. “A two-fluid model for avalanche and debris flows”. In: *Philos. trans., Math. phys. eng. sci.* 363.1832 (2005), pp. 1573–1601.

[168] S. B. Pope. “PDF methods for turbulent reactive flows”. In: *Prog. Energy Combust. Sci.* 11.2 (1985), pp. 119–192.

[169] S. B. Pope and S. B. Pope. *Turbulent flows*. Cambridge university press, 2000.

[170] D. S. Praturi, D. Plümacher, and M. Oberlack. “The hierarchy of multi-point probability density functions and characteristic functions in compressible turbulence”. In: *Phys. Fluids* 32.6 (2020), p. 066102.

[171] E. M. Purcell. “Life at low Reynolds number”. In: *Am. J. Phys.* 45.1 (1977), pp. 3–11.

[172] S. Ramaswamy. “The mechanics and statistics of active matter”. In: *Annu. Rev. Condens. Matter Phys.* 1.1 (2010), pp. 323–345.

[173] W. H. Reed and T. R. Hill. *Triangular mesh methods for the neutron transport equation*. Tech. rep. Los Alamos Scientific Lab., N. Mex.(USA), 1973.

[174] M. C. Reis and Y. Wang. “A two-fluid model for reactive dilute solid–liquid mixtures with phase changes”. In: *Contin. Mech. Thermodyn.* 29.2 (2017), pp. 509–534.

[175] L. Rosendahl. “Using a multi-parameter particle shape description to predict the motion of non-spherical particle shapes in swirling flow”. In: *Appl. Math. Model.* 24.1 (2000), pp. 11–25.

[176] J. M. Rosenholm, C. Sahlgren, and M. Lindén. “Towards multifunctional, targeted drug delivery systems using mesoporous silica nanoparticles–opportunities & challenges”. In: *Nanoscale* 2.10 (2010), pp. 1870–1883.

[177] A. M. Rosteck and M. Oberlack. “Lie algebra of the symmetries of the multi-point equations in statistical turbulence theory”. In: *J. Nonlinear Math. Phys.* 18.supp01 (2011), pp. 251–264.

[178] S. I. Rubinow and J. B. Keller. “The transverse force on a spinning sphere moving in a viscous fluid”. In: *J. Fluid Mech.* 11.3 (1961), pp. 447–459.

[179] R. Rzehak and E. Krepper. “CFD modeling of bubble-induced turbulence”. In: *Int. J. Multiph. Flow.* 55 (2013), pp. 138–155.

[180] P. G. Saffman. “The lift on a small sphere in a slow shear flow”. In: *J. Fluid Mech.* 22.2 (1965), pp. 385–400.

[181] D. Saintillan. “Kinetic models for biologically active suspensions”. In: *Natural Locomotion in Fluids and on Surfaces*. Springer, 2012, pp. 53–71.

[182] D. Saintillan and M. J. Shelley. “Active suspensions and their nonlinear models”. In: *C. R. Phys.* 14.6 (2013), pp. 497–517.

[183] R. Saye. “High-order quadrature methods for implicitly defined surfaces and volumes in hyperrectangles”. In: *SIAM J. Sci. Comput.* 37.2 (2015), A993–A1019.

[184] M. Schäfer. *Numerik im Maschinenbau*. Berlin, Germany: Springer-Verlag.

[185] L. F. Shampine and M. W. Reichelt. “The matlab ode suite”. In: *SIAM J Sci Comput.* 18.1 (1997), pp. 1–22.

[186] L. F. Shampine, M. W. Reichelt, and J. A. Kierzenka. “Solving index-1 DAEs in MATLAB and Simulink”. In: *SIAM review* 41.3 (1999), pp. 538–552.

[187] R. D. Skeel and M. Berzins. “A method for the spatial discretization of parabolic equations in one space variable”. In: *SIAM J. Sci. Statist. Comput.* 11.1 (1990), pp. 1–32.

[188] M. v. Smoluchowski. “Zur kinetischen Theorie der Brownschen Molekularbewegung und der Suspensionen”. In: *Ann. Phys.* 326.14 (1906), pp. 756–780.

[189] M. Smuda. “Direct Numerical Simulation of Multi-Phase Flows using Extended Discontinuous Galerkin Methods”. PhD thesis. Technische Universität Darmstadt, 2021.

[190] M. Smuda and F. Kummer. “On a marching level-set method for extended discontinuous Galerkin methods for incompressible two-phase flows: Application to two-dimensional settings”. In: *Int. J. Numer. Methods Eng.* 123.1 (2022), pp. 197–225.

[191] A. Sokolov and I. S. Aranson. “Physical Properties of Collective Motion in Suspensions of Bacteria”. In: *Phys. Rev. Lett.* 109 (24 2012), p. 248109.

[192] L. Soler and S. Sánchez. “Catalytic nanomotors for environmental monitoring and water remediation”. In: *Nanoscale* 6.13 (2014), pp. 7175–7182.

[193] T. Speck, J. Bialké, A. M. Menzel, and H. Löwen. “Effective Cahn-Hilliard equation for the phase separation of active Brownian particles”. In: *Phys. Rev. Lett.* 112.21 (2014), p. 218304.

[194] J. Spurk and N. Aksel. *Strömungslehre - Einführung in die Theorie der Strömungen*. Berlin, Heidelberg: Springer, 2010.

[195] J. Stenhammar, R. Wittkowski, D. Marenduzzo, and M. E. Cates. “Activity-induced phase separation and self-assembly in mixtures of active and passive particles”. In: *Phys. Rev. Lett.* 114.1 (2015), p. 018301.

[196] G. G. Stokes. “On the Effect of the Internal Friction of Fluids on the Motion of Pendulums”. In: *Trans. Cambridge Philos. Soc.* 9 (1851), p. 8.

[197] H. Su, C.-A. Hurd Price, L. Jing, Q. Tian, J. Liu, and K. Qian. “Janus particles: design, preparation, and biomedical applications”. In: *Mater. Today Bio* 4 (2019), p. 100033.

[198] S. Torquato, T. M. Truskett, and P. G. Debenedetti. “Is random close packing of spheres well defined?” In: *Phys. Rev. Lett.* 84.10 (2000), p. 2064.

[199] F. R. Ulinich and B. Y. Lyubimov. “The statistical theory of turbulence of an incompressible fluid at large Reynolds numbers”. In: *J. Exp. Theor. Phys.* 28 (1969), p. 494.

[200] T. Vicsek, A. Czirók, E. Ben-Jacob, I. Cohen, and O. Shochet. “Novel type of phase transition in a system of self-driven particles”. In: *Phys. Rev. Lett.* 75.6 (1995), p. 1226.

[201] G. Volpe, I. Buttinoni, D. Vogt, H.-J. Kümmerer, and C. Bechinger. “Microswimmers in patterned environments”. In: *Soft Matter* 7.19 (2011), pp. 8810–8815.

[202] M. Wacławczyk, N. Staffolani, M. Oberlack, A. Rosteck, M. Wilczek, and R. Friedrich. “Statistical symmetries of the Lundgren-Monin-Novikov hierarchy”. In: *Phys. Rev. E* 90.1 (2014), p. 013022.

[203] M. Weiss, M. Elsner, F. Kartberg, and T. Nilsson. “Anomalous Subdiffusion Is a Measure for Cytoplasmic Crowding in Living Cells”. In: *Biophys. J.* 87.5 (2004), pp. 3518–3524.

[204] H. H. Wensink, J. Dunkel, S. Heidenreich, K. Drescher, R. E. Goldstein, H. Löwen, and J. M. Yeomans. “Meso-scale turbulence in living fluids”. In: *Proc. Natl. Acad. Sci. USA* 109.36 (2012), pp. 14308–14313.

[205] M. Wilczek, A. Daitche, and R. Friedrich. “On the velocity distribution in homogeneous isotropic turbulence: correlations and deviations from Gaussianity”. In: *J. Fluid Mech.* 676 (2011), pp. 191–217.

[206] M. Wilczek and R. Friedrich. “Dynamical origins for non-Gaussian vorticity distributions in turbulent flows”. In: *Phys. Rev. E* 80.1 (2009), p. 016316.

[207] D. A. Wilson, R. J. Nolte, and J. van Hest. “Autonomous movement of platinum-loaded stomatocytes”. In: *Nat. Chem* 4.4 (2012), pp. 268–274.

[208] C. W. Wolgemuth. “Collective swimming and the dynamics of bacterial turbulence”. In: *Biophys. J.* 95.4 (2008), pp. 1564–1574.

[209] F. Wong, L. D. Renner, G. Özbaykal, J. Paulose, D. B. Weibel, S. van Teeffelen, and A. Amir. “Mechanical strain sensing implicated in cell shape recovery in Escherichia coli”. In: *Nat. Microbiol.* 2.17115 (2017), pp. 1–8.

[210] K.-T. Wu, J. Hishamunda, D. Chen, S. DeCamp, Y.-W. Chang, A. Fernandez-Nieves, S. Fraden, and Z. Dogic. “Transition from turbulent to coherent flows in confined three-dimensional active fluids”. In: *Science* 355 (6331 2017).

[211] X.-L. Wu and A. Libchaber. “Particle diffusion in a quasi-two-dimensional bacterial bath”. In: *Phys. Rev. Lett.* 84.13 (2000), p. 3017.

[212] Y. Wu, R. Dong, Q. Zhang, and B. Ren. “Dye-enhanced self-electrophoretic propulsion of light-driven TiO2–Au Janus micromotors”. In: *Nanomicro Lett.* 9.3 (2017), pp. 1–12.

[213] W. Xue and G. S. Grest. “Shear-induced alignment of colloidal particles in the presence of a shear flow”. In: *Phys. Rev. Lett.* 64.4 (1990), p. 419.

[214] M. Yoneda. “Force Exerted by a Single Cilium of Mytilus Edulis: II. Free Motion”. In: *J. Exp. Biol.* 39.2 (1962), pp. 307–317.

[215] X. Zheng, B. Ten Hagen, A. Kaiser, M. Wu, H. Cui, Z. Silber-Li, and H. Löwen. “Non-Gaussian statistics for the motion of self-propelled Janus particles: Experiment versus theory”. In: *Phys. Rev. E* 88.3 (2013), p. 032304.

[216] H. Zhou, C. C. Mayorga-Martinez, S. Pané, L. Zhang, and M. Pumera. “Magnetically driven micro and nanorobots”. In: *Chem. Rev.* 121.8 (2021), pp. 4999–5041.

[217] A. Zöttl and H. Stark. “Emergent behavior in active colloids”. In: *J. Phys. Condens. Matter* 28.25 (2016), p. 253001.

[218] N. Zuber. “On the dispersed two-phase flow in the laminar flow regime”. In: *Chem. Eng. Sci.* 19.11 (1964), pp. 897–917.

A. Appendix

A.1. Lie symmetries

This section of the appendix contains the proofs for two statements made during the definition of an Lie-symmetry, see Sec. 3.1.

A.1.1. Lie operator

An approximation for the directional derivative of an arbitrary function $f\left(\boldsymbol{x}\right)$ is

$$\mathfrak{X}f\left(\boldsymbol{x}\right)=\lim_{h\to 0}\frac{f\left(\boldsymbol{x}+h\boldsymbol{\xi}\right)-f\left(\boldsymbol{x}\right)}{h}=\xi_i\frac{\partial f\left(\boldsymbol{x}\right)}{\partial x_i} \tag{A.1}$$

Resorting delivers

$$f\left(\boldsymbol{x}+h\boldsymbol{\xi}\right)=\left(1+h\mathfrak{X}\right)f\left(\boldsymbol{x}\right), \tag{A.2}$$

where $h\to 0$ is implied. Hence, by introducing the finite step size $\alpha=Nh$ and applying the operator $\left(1+h\mathfrak{X}\right)$ N-times, one obtains

$$f\left(\boldsymbol{x}^*\right)=f\left(\boldsymbol{x}+\alpha\boldsymbol{\xi}\right)=\left(1+\frac{\alpha}{N}\mathfrak{X}\right)^N f\left(\boldsymbol{x}\right), \tag{A.3}$$

where we made use of the successive property of the one-parameter group $T_\alpha T_\beta=T_{\alpha+\beta}$. With $N\to\infty$ (A.3) becomes

$$f\left(\boldsymbol{x}^*\right)=e^{\alpha\mathfrak{X}}f\left(\boldsymbol{x}\right)=\sum_{n=0}^{\infty}\frac{\left(\alpha\mathfrak{X}\right)^n}{n!}f\left(\boldsymbol{x}\right), \tag{A.4}$$

where $\mathfrak{X}^n=\mathfrak{X}\mathfrak{X}^{n-1}$. Requiring invariance of $f\left(\boldsymbol{x}\right)=f\left(\boldsymbol{x}^*\right)$ under the transformation $x_i^*=x_i+\alpha\xi_i$ delivers

$$\mathfrak{X}^n f\left(\boldsymbol{x}\right)=0, \tag{A.5}$$

as a solution of (A.4). Subsequently, (A.5) is equivalent to the invariance of the function $f\left(\boldsymbol{x}\right)$.

A.1.2. Infinitesimals of derivatives

Using the chain rule on obtains

$$\frac{D\Psi_i}{Dx_j} = \frac{Dy_i^*}{Dx_k^*}\frac{D\Phi_k}{Dx_j} = y^*_{i,x_k}\frac{D\Phi_k}{Dx_j}, \tag{A.6}$$

where D/Dx_i is the total differential operator, see (3.13). Let

$$y^*_{i,x_{k_1},x_{k_2},\dots,x_{k_N}} = \Psi_{i,x_{k_1},x_{k_2},\dots,x_{k_N}} = y_{i,x_{k_1},x_{k_2},\dots,x_{k_N}} + \alpha\eta_{i,k_1,k_2,\dots,k_N} + \mathcal{O}\left(\alpha^2\right) \tag{A.7}$$

be the N-th order derivative of the dependent variable y_i^*. Subsequently, the above chain rule delivers

$$\begin{aligned}&\frac{D}{Dx_{k_{N+1}}}\left(y_{i,x_{k_1},x_{k_2},\dots,x_{k_N}} + \alpha\eta_{i,k_1,k_2,\dots,k_N}\right)\\ &= \left(y_{i,x_{k_1},x_{k_2},\dots,x_j} + \alpha\eta_{i,k_1,k_2,\dots,j}\right)\frac{D}{Dx_{k_{N+1}}}\left(x_j + \alpha\xi_j\right)\end{aligned} \tag{A.8}$$

leading to

$$\begin{aligned}&\frac{Dy_{i,x_{k_1},x_{k_2},\dots,x_{k_N}}}{Dx_{k_{N+1}}} - y_{i,x_{k_1},x_{k_2},\dots,x_{k_{N+1}}}\\ +\alpha&\left(y_{i,x_{k_1},x_{k_2},\dots,x_j}\frac{D\xi_j}{Dx_{k_{N+1}}} + \eta_{i,k_1,k_2,\dots,k_{N+1}} - \frac{D\eta_{i,x_{k_1},x_{k_2},\dots,x_{k_N}}}{Dx_{k_{N+1}}}\right) + \mathcal{O}\left(\alpha^2\right) = 0.\end{aligned} \tag{A.9}$$

Subsequently, one obtains the relation

$$\eta_{i,k_1,k_2,\dots,k_{N+1}} = \frac{D\eta_{i,x_{k_1},x_{k_2},\dots,x_{k_N}}}{Dx_{k_{N+1}}} - y_{i,x_{k_1},x_{k_2},\dots,x_j}\frac{D\xi_j}{Dx_{k_{N+1}}} \tag{A.10}$$

to calculate the infinitesimal $\eta_{i,k_1,k_2,\dots,k_{N+1}}$.

A.2. Invariant solutions

In this section derivations for invariant solutions used in Sec. 6 are given.

A.2.1. Distance PDF

A distance PDF is introduced

$$f^{r^{\min}} = \left\langle\delta\left(\widehat{r}^{\min} - r^{\min}\right)\right\rangle, \tag{A.11}$$

where $\widehat{r}^{\min}$ is the sample space variable corresponding to the physical variable $r^{\min} = \left|\boldsymbol{r}^{\min}\right|$. The vector $\boldsymbol{r}^{\min}$ is intended to describe the distance from the surface of a probing particle towards the closest particle next to the probing particle. Lets consider a two-particle problem, where the first axis of the reference frame is aligned towards the distance vector r_i^{min}. Subsequently, the distance $r^{\text{min}} = \chi_{12} - \chi_{11}$ is defined as the difference between the $\boldsymbol{e}^1$-coordinates of two points $\boldsymbol{\chi}_1$ and $\boldsymbol{\chi}_2$. The one-dimensional position PDF, obtained from (3.75), is

$$\begin{aligned} f^X = \langle \delta\left(X_2 - \chi_2\right)\rangle &= \int \left\langle \delta\left(X_2 - X_1 - r^{\text{min}}\right) \delta\left(X_1 - \chi_1\right)\right\rangle \mathrm{d}X_1 \\ &= \int \left\langle \delta\left(\widehat{r}^{\text{min}} - r^{\text{min}}\right) \delta\left(X_1 - \chi_1\right)\right\rangle \mathrm{d}X_1. \end{aligned} \tag{A.12}$$

Without loss of generality, lets assume that $\chi_1 = 0$ is known and deterministic. Hence, f^X in (A.12) equals $f^{r^{\text{min}}}$. The operator for the constant Galilean symmetry or spatial shift symmetry is

$$\mathfrak{X}_{Gal} = c_{1,G}\left(\frac{\partial}{\partial x_1} + \frac{\partial}{\partial X_1}\right) \tag{A.13}$$

in case of the one dimensional position PDF. The operator for the intermittency symmetry is

$$\mathfrak{X}_{int} = f^{r^{\text{min}}} - \delta\left(X_{12} - X_{11}\right)\frac{\partial}{\partial f^{r^{\text{min}}}} \tag{A.14}$$

Applying the combined operator $\mathfrak{X} = \mathfrak{X}_{Gal} + \mathfrak{X}_{int} = f^{r^{\text{min}}}$ towards the auxiliary function

$$H\left(\boldsymbol{x}, t, r^{\text{min}}; f^{r^{\text{min}}}\right) = f^{r^{\text{min}}} - f^{r^{\text{min}}}\left(\boldsymbol{x}, t, r^{\text{min}}\right) \tag{A.15}$$

delivers the solution

$$f^{r^{\text{min}}} = C\mathcal{H}\left(X_{12} - X_{11}\right)e^{-C(X_{12}-X_{11})} + g\left(-x_1 + x_2, t, -x_1 + X_{12}\right)e^{Cx_1}, \quad C = \frac{1}{c_{1,G}}. \tag{A.16}$$

The first term on the right hand side is an exponential distribution for $C > 0$, hence, the function g necessarily needs to vanish. As the intention was to derive the PDF to describe the position of a particle towards its closest neighbour it is assumed that $bm\chi_1$ is the point at the particle surface, where the distance vector $r_i' = \chi_{12} - \chi_{11}'$ cuts the surface and χ_{11}' is the position of the centre of mass of the probing particle. The second point χ_{12} is the position of the centre of mass the closest neighbour. Subsequently, (A.16) becomes

$$f^{r^{\text{min}}} = C\mathcal{H}\left(r'^{\text{min}}\right)e^{-C\left(r'^{\text{min}}\right)} = C\mathcal{H}\left(r^{\text{min}} - a'\right)e^{-C\left(r^{\text{min}} - a'\right)}, \quad r^{\text{min}} = r'^{\text{min}} + a'. \tag{A.17}$$

Here, r'^{min} is the distance between the two centres of mass and a' accounts for the extensions of the particle. In case of a disk-shaped particle a' is equal to the particle length a, whereas it depends on the orientation of r_i towards the probing particle for arbitrarily shaped particles.

A.2.2. Equally distributed orientation PDF

Active particles posses a geometrical symmetry due to the axisymmetry of the flow field of a Stokes dipole (3.50f). The operator related to this symmetry is (3.47)

$$\mathfrak{X}_{p,\beta} = \frac{\partial}{\partial \beta_p}.$$

The symmetry is valid for single-particle experiments and dilute suspension due to the applicability of the Stokes dipole as an approximation. In case of the PDF the operator needs to be transformed into the sample space, leading to

$$\mathfrak{X}_{p,b} = \frac{\partial}{\partial b_p}. \tag{A.18}$$

Subsequently, differential equation necessary to solve in order to obtain the orientation PDF f^b is

$$\mathfrak{X}_{p,b} H\left(\boldsymbol{x}, t, \boldsymbol{b}; f^b\right)\Big|_{H=0} = 0 \quad \Rightarrow \quad -\frac{\partial f^b}{\partial b_p} = 0. \tag{A.19}$$

Hence, the PDF is constant with respect to the sample space variable. Restricting the possible orientation angles to the interval $[0, \pi]$ delivers

$$f^b = \frac{1}{\pi}. \tag{A.20}$$

I would like to emphasise again that this solution is only valid for single particles and thin suspensions. For more densely packed particles, the assumption of a Stokes dipole is no longer sufficient and it must be assumed that the flow field takes on more complicated forms.

A.3. Joint PDFs

Joint PDFs are formed by the ensemble average of a product of fine-grained PDF. The joint PDF for the minimal distance and the relative angle between two particle

$$f^{\mathfrak{r}\mathfrak{b}} = \left\langle \widehat{f}^{\mathfrak{r}^{\mathrm{min}}} \widehat{f}^{\mathfrak{b}^{\mathrm{min}}} \right\rangle, \tag{A.21}$$

as used in 6.2.3, are presented in Fig. A.1 for all examined suspensions. Apart from the densest suspension $\alpha^S = 0.39$, all PDFs in Fig. A.1 have two distinct maxima at approximately $(0.6, 0)$ and $(1.2, \pi)$. Hence, the most likely state for any particle is a parallel alignment. Parallel particles might either face in the same direction or oppose each other. The configuration examined in Sec. 6.2.1 with two opposing particles as visualised in Fig. 6.8 is related to the second maximum. The first maximum is especially related to the structures visible at the domain walls, see Fig. 6.16. In case of the densest suspension $\alpha^S = 0.39$ both maxima are located at the left corners of the diagram. The next particle to a probing particle is always located in the near field, a property which geometrically requires a parallel orientation.

A second joint PDF can be formed by combining the sample space variable of the minimal distance $\mathfrak{r}^{\mathrm{min}}$ with the sample space variable $\mathfrak{v}^{pq}$ for the relative speed

$$v^{pq} = |\gamma_p \boldsymbol{v}_p - \gamma_q \boldsymbol{v}_q| \tag{A.22}$$

of two particles. The joint minimal distance and relative velocity PDF is, thus,

$$f^{\mathfrak{r}\mathfrak{v}} = \left\langle \widehat{f}^{\mathfrak{r}^{\mathrm{min}}} \widehat{f}^{\mathfrak{v}^{pq}} \right\rangle. \tag{A.23}$$

Opposing particles in a configuration similar to Fig. 6.8 block the way of their opponent, thus, no relative velocity is possible, which explains the maxima at $(1.2, 0)$ in the joint PDFs for the three suspensions in Fig. A.2a-c. Additionally, particles with a parallel orientation, which face into the same direction are most likely to be present at the particle walls for the dilute suspensions $\alpha^S = 0.04$ and $\alpha^S = 0.11$, hence, resulting in a second maximum at $(0.6, 0)$ due to the vanishing velocity. The latter maximum vanishes completely for the suspension $\alpha^S = 0.17$, which does not show any preferred relative velocity for two very close particles. Thus, while cluster emerge and are distinctive due to the parallel alignment of the particles, such clusters tend to be unstable if only particles facing in the same direction are present. The densest suspension is almost frozen, hence, in the closed domain used for the numerical experiment, high values for relative velocities are unlikely.

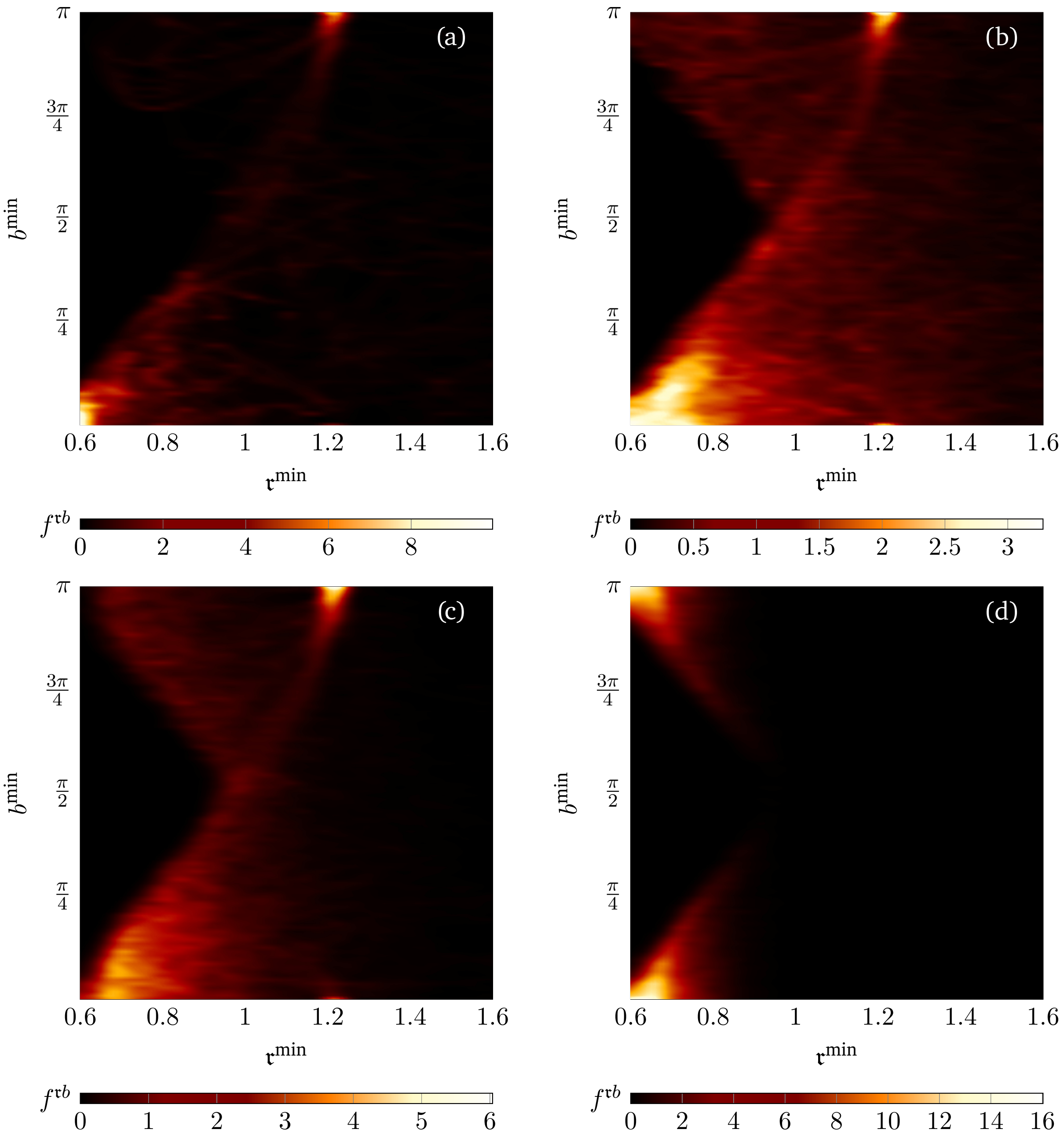

Fig. A.1.: (a) The joint minimal distance and relative angle PDF $f^{\mathfrak{r}b}$ for the dilute suspension $\alpha^S = 0.04$. Two maxima exist; one describes two parallel particles facing in the same direction at $(0.6, 0)$, the other one describes two opposing particles similar to the configuration shown in Fig. 6.8 at $(1.2, \pi)$. (b) The joint PDF for the suspension $\alpha^S = 0.11$. The previously mentioned maxima still exists, additionally a wide range of particle states is possible. (c) The two maxima become more distinct for the suspension $\alpha^S = 0.17$ compared to the case of $\alpha^S = 0.11$. Furthermore, a third maximum is formed at $(0.6, \pi)$, which was not clearly visible before. (d) In the case of the densest suspension $\alpha^S = 0.39$ the maximum at $(1.2, \pi)$ vanishes. All particles are in the closest proximity towards each other.

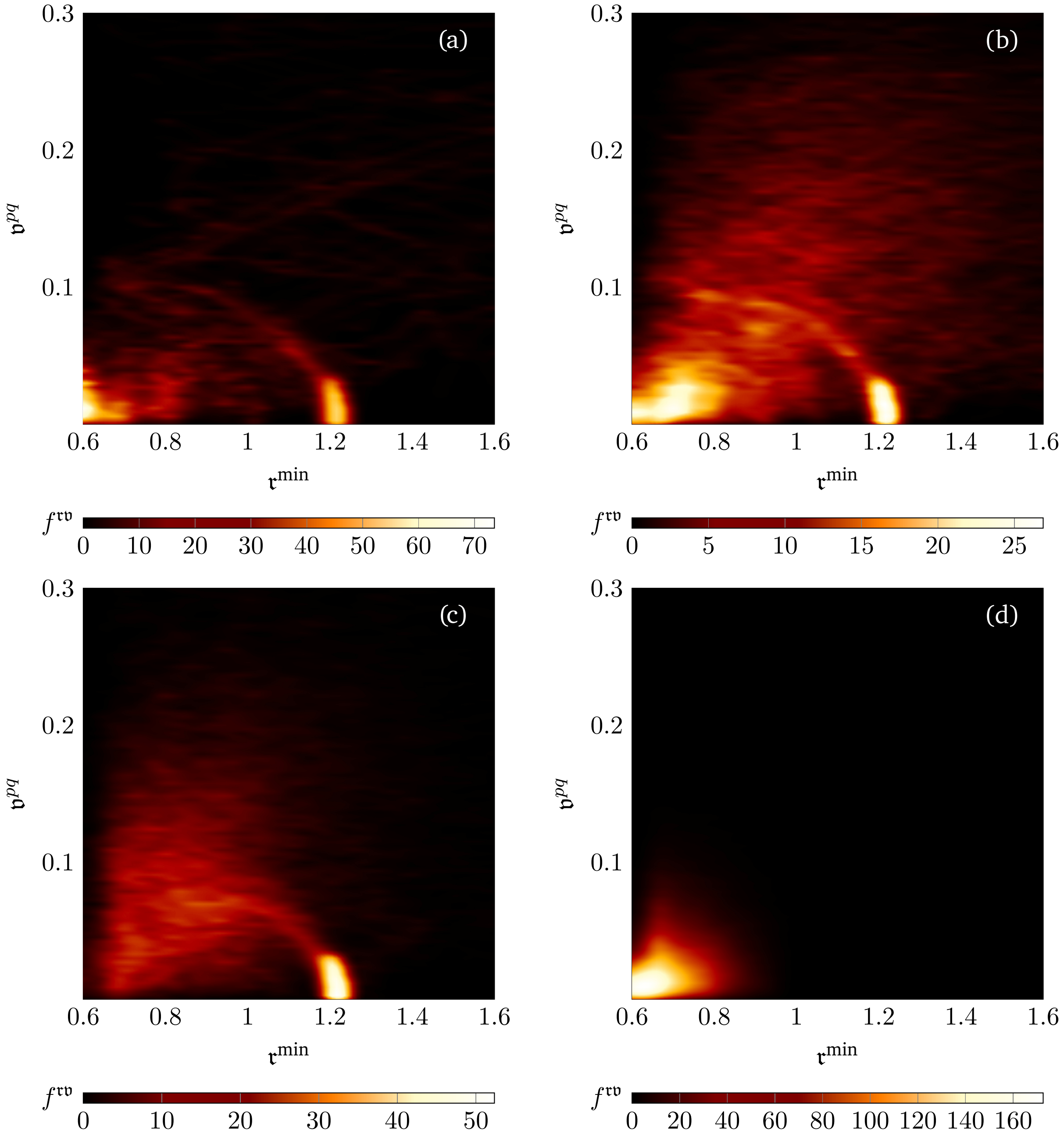

Fig. A.2.: (a) The joint minimal distance and velocity PDF $f^{\mathfrak{rv}}$ for the dilute suspension $\alpha^S = 0.04$. Two maxima exist; one at $(0.6, 0)$, which is related to the situation, where two particles are aligned parallel to each other and facing the same direction. The other one is related to two opposing particles similar to the configuration shown in Fig. 6.8 at approximately $(1.2, 0)$. In the latter case, both particles block the path of their opponent, thus, no relative motion is possible. (b) The joint PDF for the suspension $\alpha^S = 0.11$. The previously mentioned maxima still exists, additionally a wide range of particle states is possible. (c) The maximum at $(0.6, 0)$ vanishes, i.e. for particles in the closest proximity no discrete value for the relative velocity exists. (d)In the case of the densest suspension $\alpha^S = 0.39$ only the maximum in the lower left corner of the diagram remains. The most likely state for a particle pair is, hence, that both have a similar velocity.

Curriculum Vitae

The CV is not included in the online version for data protection reasons.
Der Lebenslauf ist aus Datenschutzgründen in der Online-Version nicht enthalten.

Publications:
B. Deußen, D. Dierkes, & M. Oberlack.
“Statistical theory of helical turbulence.” *Phys. Fluids*, 32(6) (2020), 065109.
B. Deußen, A. Jayaram, F. Kummer, Y. Wang, T. Speck, & M. Oberlack
“High-order simulation scheme for active particles driven by stress boundary conditions.” *J. Phys. Condens. Matter*, 33(24) (2021), 244004.
B. Deußen, M. Oberlack, & Y. Wang.
“Probability theory of active suspensions.” *Phys. Fluids*, 33(6) (2021), 061902.
B. Deußen, Y. Wang, & M. Oberlack.
“A deterministic two-phase model for an active suspension with non-spherical active particles using the Eulerian spatial averaging theory.” *Phys. Fluids*, 34(2) (2021), 023302.